

**SPATIAL-SPECTRUM ESTIMATION AND FILTERING OF RADIO
FREQUENCY ARRAYS VIA ELEMENTAL PHOTONIC
UP-CONVERSION AND COHERENT OPTICAL PROCESSING**

by

Joseph C. Deroba

A dissertation submitted to the Faculty of the University of Delaware in partial fulfillment of the requirements for the degree of Doctor of Philosophy in Electrical Engineering

Fall 2017

© 2017 Joseph C. Deroba
All Rights Reserved

**SPATIAL-SPECTRUM ESTIMATION AND FILTERING OF RADIO
FREQUENCY ARRAYS VIA ELEMENTAL PHOTONIC
UP-CONVERSION AND COHERENT OPTICAL PROCESSING**

by

Joseph C. Deroba

Approved: _____

Kenneth E. Barner, Ph.D.
Chair of the Department of Electrical and Computer Engineering

Approved: _____

Babatunde A. Ogunnaike, Ph.D.
Dean of the College of Engineering

Approved: _____

Ann L. Ardis, Ph.D.
Senior Vice Provost for Graduate and Professional Education

I certify that I have read this dissertation and that in my opinion it meets the academic and professional standard required by the University as a dissertation for the degree of Doctor of Philosophy.

Signed: _____

Dennis W. Prather, Ph.D.
Professor in charge of dissertation

I certify that I have read this dissertation and that in my opinion it meets the academic and professional standard required by the University as a dissertation for the degree of Doctor of Philosophy.

Signed: _____

Mark S. Mirotznik, Ph.D.
Member of dissertation committee

I certify that I have read this dissertation and that in my opinion it meets the academic and professional standard required by the University as a dissertation for the degree of Doctor of Philosophy.

Signed: _____

Christopher A. Schuetz, Ph.D.
Member of dissertation committee

I certify that I have read this dissertation and that in my opinion it meets the academic and professional standard required by the University as a dissertation for the degree of Doctor of Philosophy.

Signed: _____

Olukayode Kami Okusaga, Ph.D.
Member of dissertation committee

”It always seems impossible until it’s done.”

-Nelson Mandela

ACKNOWLEDGEMENTS

I wish to thank all of those whom have guided, challenged and inspired me to start and then complete this doctoral degree. Special thanks are given to my advisor, Dr. Dennis Prather. Without your persistent support and enthusiasm to keep me going, I would not be where I am today. You challenged me to meet your expectations and enabled me to contribute to our growing community of researchers. I am certainly a better engineer because of you; thank you. I look forward to our future research endeavors together.

I wish to thank my colleagues for their support during my quest for an advanced degree. A number of my colleagues must be thanked specifically: Mr. Robert Doto, who convinced me to pursue an advanced degree, without his urging this would never have happened; Ms. Lorraine Kohler, who funded my early research and afforded me the opportunity to begin this endeavor while I worked full-time; Mr. Jonathan Corriveau, who provided me the necessary time away from the office to complete this work; Dr. Shyouyuan Shi, who shared his office with me and was always willing to enlighten me on the finer points of electro-magnetics, photonics and antenna design; Dr. Garrett Schneider, who was vital in the construction and maintenance of many of the prototypes that I have used throughout the course of my research; Dr. Mark Mirotznik, who lent the AWG used in many experiments and was quick to test out my idea for a retro-directive radar reflector based on his line of research; Dr. Olukayode Okusaga, who provided me with my first real introduction to RF photonics; finally, Dr. Christopher Schuetz, who always made time to discuss my ideas and lend careful insight to where I could go wrong, your questions and insight have made all of my experimental results better and more useful. I am truly humbled by all of you.

Finally, I must thank (and in some ways apologize to) my family. I am sorry that the final months of this venture have been so hard on us all. I thank you all for your patience, understanding, support and love. Specific thanks must go out to my son, Joey, who inspires me to better myself as a person and especially as a father. Your amazing questions about the world around you and your willingness to learn the answers along with me will always be cherished memories for me during this time. To my infant twin daughters, Evelyn and Kayla, who have helped me put family, education and career balancing into perspective during this journey. Nothing lifts your spirits after a bad day experimenting like a hug from your children when you get home. Special thanks go to my mother-in-law, Laurel Kenney, who helped with the children while I was busy writing this thesis. Without your help, I would never have gotten to my defense! I must also thank my parents, Joseph and Marian Deroba, for providing me with a solid foundation of love, loyalty, trust, and education. You always believed in me, even when I was failing to believe in myself. Finally, I must thank my wife, Megan Deroba, who always had confidence in me, picked me up when I was down, and sacrificed her own needs so that I could have time to pursue my academic goals. Megan, I would be lost without you.

Truly, I could not have gotten where I am today without the help of my advisor, my colleagues, my family and my friends. I wish to thank you all again for your love, camaraderie and support.

TABLE OF CONTENTS

LIST OF TABLES	xii
LIST OF FIGURES	xiii
ABSTRACT	xx
 Chapter	
1 INTRODUCTION	1
1.1 Radio-Frequency Array Processing	4
1.1.1 Delay and Sum Beam-forming of a Uniform Linear Array	6
1.1.1.1 Delay and Sum Phase Steering	8
1.1.1.2 Element Pattern Effects on Array Response	9
1.1.1.3 Array Beam-width	10
1.1.1.4 Array Grating Lobes	11
1.1.1.5 Weighted Array Factors	12
1.1.1.6 Direction Sines	14
1.1.2 Beam-space Processing of a Uniform Linear Array	15
1.1.2.1 Coordinate Systems and the Array Steering Vector	15
1.1.2.2 Multi-beam Processing and the Beam-space matrix	19
1.1.2.3 Full-Dimension Beam-Space and the Discrete Fourier Transform Matrix	22
 2 PHOTONIC UP-CONVERSION AND FOURIER PROCESSING OF A UNIFORM LINEAR RF ARRAY	 25
2.1 Motivation for Up-converted arrays	25
2.2 Photonic Up-Conversion and Remoting of an Array	26
2.2.1 Antenna Input Voltage	26

2.2.2	MZM Input/Output Analysis	28
2.2.3	Arrayed MZM Output Power Analysis	30
2.2.3.1	Input RF power handling of the Arrayed topology	36
2.2.3.2	System Link Gain of a Two-element Arrayed Topology	37
2.2.4	RF Photonic Link Performance Metrics	38
2.3	Photonic Array Processing	40
2.3.1	Photonic Array Processor Overview	40
2.3.2	Photonic Array Up-conversion	41
2.3.3	Photonic Array Free-Space Optical Processing	45
2.3.3.1	Photonic Array Beam-space Processing Simulation	48
2.3.4	Effects of Up-conversion on RF Angle-of-Arrival (AoA)	49
2.3.5	Apodization of Beams Using the Photonic Beam-space Processor	55
2.3.5.1	Apodization Via Transmissive Film Filtering in the Optical Chain	55
2.3.5.2	Apodization Via Weighted Distribution of a Master Laser	56
2.3.5.3	Master laser Input Power Comparison	59
2.3.6	Beam-Space Down-Conversion and Signal Recovery	63
3	MULTI-FUNCTIONAL PROCESSING OF PHOTONICALLY GENERATED BEAM-SPACES	69
3.1	Imaging of the Continuous Spatial Frequency Spectrum	69
3.1.1	Beam-Squint of Wide-band Signals	72
3.1.2	Analog Re-Steering of the Output Beam-Space	73
3.2	Digitization of a Down-converted Beam-space	76
3.3	Processing the Output of a Single Beam	84
3.3.1	Basic Communications Processing Scheme	84

3.3.2	Basic Radar Processing Scheme	88
3.4	Processing of the Full Beam-space	93
3.4.1	Beam-Space Spatial Spectrum Estimation	97
3.4.1.1	Non-Parametric Spatial Spectrum Estimators	97
3.4.1.2	Sub-space Spatial Spectrum Estimation Techniques	99
3.4.2	Beam-space Adaptive Spatial Spectrum Filtering	102
3.4.2.1	Mean Squared Error (MSE) Optimal Filtering	103
3.4.2.2	Optimal Filtering by Maximizing the Output Signal-to-Noise Ratio	104
3.4.3	Computational Latency of Beam-Space Adaptive Techniques	105
4	EXPERIMENTAL PHOTONIC ARRAY PROCESSOR	108
4.1	Experimental Hardware Overview	108
4.1.1	Photonic Array Processor and Optical Down-converting Cart	108
4.1.2	Signal Generation, Digitization and Processing Cart	114
4.1.3	Radar Test Target Generation	116
4.1.4	QPSK Signal Generation	120
4.2	Experimental Setups	120
5	EXPERIMENTAL RESULTS ON THE GENERATION OF APODIZED BEAM-SPACES VIA PHOTONIC UP-CONVERSION	122
5.1	Motivation for Beam-Space Apodization	122
5.2	Creation of Apodized Beams Using a Prototype Photonic Beam-space Processor	123
5.2.1	Experimental Setup for Spatial Isolation Data Collections	124
5.2.2	Experimental Validation of Apodization Via Weighting of the Master Laser	125
5.2.3	Analysis of Error Sources within the Photonic Array Processing Chain	128
5.2.3.1	Additional Tapering Experiments	129

5.2.3.2	Array Error Analysis for Photonic Array Processor	131
5.2.3.3	Determination of Error Statistics	131
5.2.3.4	Discussion of Error Sources	134
5.2.3.4.1	Sampling Array Effects on Effective Side-lobe Levels	134
5.2.3.4.2	Photonic Phase Modulation Effects on Effective Side-lobe Levels	135
5.2.3.4.3	System Phase Error Budgeting for Low-Side-lobe Performance	138
5.3	Significant Outcomes from the Apodization Experiments	140
6	RECOVERY OF A PHOTONICALLY-GENERATED FULL-DIMENSION BEAM-SPACE FOR MULTI-FUNCTION APPLICATIONS	142
6.1	Dual-Beam multi-function Experiments	142
6.2	Full-Beam-Space Multi-function Experiments	146
6.2.1	Sampling and Calibration of Orthogonal Beam-Space Locations	146
6.2.1.1	Orthogonality of the Sampled Beam-space	153
6.2.1.1.1	Beam-space Whitening	154
6.2.2	Full-Dimension Beam-Space Experimental Setup	155
6.2.3	QPSK Signal Recovery	156
6.2.4	Radar Signal Recovery	158
6.2.5	Estimation of Quantity and Angle-of-Arrival of Interference Sources	160
6.2.5.1	Latency of SWIR-Based AoA Estimates	160
6.2.5.2	AoA Estimation Using the SWIR Measurement of the Spatial Spectrum	163
6.2.6	Beam-Space Adaptivity Via SWIR Measurements of the Interference Spatial Spectrum	170
6.3	Significant Outcomes from Multi-function Experimentation	175

7 CONCLUSIONS AND FUTURE WORK	177
7.1 Future Work	179
7.1.1 Integrated RF-Photonic Receiver Module	180
7.1.2 Reduction of Error Sources	180
7.1.3 Application of real-time laser amplitude control	181
7.1.4 Photonically Driven Adaptive Array Control	181
7.1.5 Foveated Sensing using Coherent Optical Up-Conversion	182
7.1.6 Switched-inputs for Wide-band Operation	183
BIBLIOGRAPHY	184
Appendix	
A DERIVATION OF A CLOSED-FORM ARRAY RESPONSE FOR A UNIFORMLY ILLUMINATED LINEAR ARRAY	191
B DERIVATION OF ARRAY BEAM-WIDTH	193
C JACOBI-ANGER EXPANSION	195
D PERMISSIONS	197

LIST OF TABLES

2.1	Sine-space and Fourier-space locations of 8 Orthogonal Beam Positions for an 8-element array	53
2.2	Ideal and Realized Weights, for Each Modulator Shown in Fig 2.11	59
5.1	Input Laser Weighting for Each Optical Modulator	128
5.2	Table of apodization profiles used in experimentation	129
6.1	Sine-space and Fourier-space locations of 7 Beam Positions for the 7-elements used as the input to the Photonic Beam-Space Receiver. The Fourier plane positions assume unity magnification.	148
6.2	Ideal vs Measured beam locations after sampling via high-speed photo-detectors.	154

LIST OF FIGURES

1.1	Diagram of a Uniform Linear Array of N elements.	6
1.2	Voltage and Power patterns of an 8-element linear array of isotropic elements.	8
1.3	Power patterns of an 8-element linear array, steered in -15 degree increments.	9
1.4	Effects of the element pattern on an 8-element linear array, steered in -15 degree increments.	11
1.5	Comparison of uniform and Taylor array weighting profiles.	12
1.6	Comparison of the power patterns of a uniformly-weighted and Taylor-weighted array.	13
1.7	Sine-space representation of the response of an 8-element linear array.	14
1.8	Array Coordinate Definition	16
1.9	Plots of the beam-responses for a full-dimension beam-space for arrays with even and odd numbers of elements	21
2.1	A schematic drawing of a basic Mach-Zehnder Modulator being fed via an antenna.	28
2.2	Schematic drawing of an optical link behind an antenna array with a traditional RF manifold design.	30
2.3	Schematic drawing of an antenna array with a Mach-Zehnder Modulator being fed by each element of the array.	31
2.4	Diagram of the basic geometry of Beam-space beam-forming of an RF array via optical up-conversion and a Fourier Transforming Lens.	41

2.5	Schematic of the basic form of the proposed photonic, beam-space array processor.	42
2.6	Simulated outputs of the beam-space beam-former for an eight element array.	50
2.7	Two-dimensional graphical depiction of the translation of the input aperture from the RF to the optical domains and its effect on the direction-of-arrival of the incoming RF waves.	52
2.8	Plots of the output Fourier plane for three difference of input fiber beam-waists.	54
2.9	A graphical depiction of an unsteered, spherical, wave being launched from arrays with 3 different element spacings with respect to the launched wave-length.	54
2.10	Example of beam-space apodization via a transmissive filter in the optical path.	57
2.11	A graphical depiction of the fiber coupler layout used for simulation and experimentation using a prototype array.	60
2.12	Example of beam apodization via weighted distribution of the master laser.	61
2.13	Schematic of the Beam-space Array processor with integral optical down-conversion.	65
3.1	Simulated irradiance of the field at the output of the photonic array processor.	70
3.2	Simulated output irradiance patterns for a bore-sight signal overlaid with signals from $\pm 90^\circ$	71
3.3	Simulated output irradiance patterns for a bore-sight signal overlaid with signals from $\pm 45^\circ$	72
3.4	Simulated output of irradiance patterns showing the effects of frequency-dependent, beam-squint.	73
3.5	Example of beam-space steering using optical phase offsets.	74

3.6	Simulated examples for frequency-dependent re-steering of an input array.	75
3.7	Method used for Digital I/Q demodulation of band-limited, real-sampled signals at the output of the proposed array processor.	78
3.8	Example of a sampled output from a single photo-detector after optical down-conversion.	80
3.9	Example base-band translated output from a single photo-detector after optical down-conversion.	81
3.10	Filter Response of the Low-pass filter used for extraction of the base-band spectra of interest during the Digital I/Q generation process.	82
3.11	Example of the final, filtered and decimated output from a single photo-detector after optical down-conversion.	83
3.12	Plot of the time-domain responses for a set of symbols with a raised-cosine response.	86
3.13	Example of the output communications constellation diagram after several stages of digital processing.	87
3.14	Screen Capture from the KeySight VSA software used for real-time digital communication demodulation.	88
3.15	Ideal Linear Frequency Modulated Pulse with the center of the pulse referenced to $t = 0$	89
3.16	Ideal spectrum of a Linear Frequency Modulated pulse.	90
3.17	Received pulse with the time-delay due to a single target in the scene.	91
3.18	Received pulse with the time-delay due to multiple targets in the scene.	91
3.19	Pulse-compressed output for a 3-target scenario.	93
3.20	Example of of an adapted response using the optimal weighting solution for two interference sources.	104

3.21	Family of curves depicting the first order estimate of processing latency when using a covariance-based AoA estimation or adaptive filtering approach for increasing array sizes.	106
4.1	Photograph of the prototype Receiver array with the Radar Transmit horn fixed above it.	109
4.2	Photograph of the prototype gain and up-conversion stage behind each element of the RF array.	110
4.3	Photograph of the prototype optical Array processor.	111
4.4	Plots showing the effects of Carrier Suppression and Leakage.	113
4.5	Screen capture of the LabView interface used to control the photonic receive array components and optical processor.	113
4.6	Photograph of the National Instruments PXIe Chassis with all cards installed.	115
4.7	Screen Capture of the LabView program interface for collection and processing of Radar Data.	117
4.8	Picture showing the RX/TX horns that are part of the photonic radar target generator.	118
4.9	Picture of the Photonic Test Target Generator with the top-cover removed.	119
4.10	Graphical depiction of the equipment used to generate a QPSK signals for experimentation.	121
5.1	Simulated outputs of an 8-channel beam-space beam-former with a large interfering signal along with a low-power desired signal.	123
5.2	Schematic Overview of the Experimental Setup for the Apodization Experiments	124
5.3	Picture of 8-element array used for spatial isolation experiments.	126
5.4	Overlay of simulated and measured data for a bore-sight RF source incident on the 1x8 prototype array.	127

5.5	Measured and ideal array responses when using apodization.	128
5.6	Measured and simulated photonic beam-space beam-former responses with two incident sources.	129
5.7	Overview of the measured and ideal responses for the amplitude profiles listed in Table 5.2.	130
5.8	Measured beam-former output overlaid with simulated response that includes contributions from derived beam-former error sources. . . .	134
5.9	Simulated outputs of aperture patterns for various array sizes, given existing system error budget.	136
5.10	Simulated outputs of captured aperture patterns using detectors with two (2) commercially available pixel pitches.	137
5.11	Measured RF sideband amplitudes, versus time, for a single element’s Mach-Zehnder Modulator and corresponding phase control modulator.	139
6.1	Experimental overview of the Dual-beam multi-function experiments.	143
6.2	AoA measurements from SWIR output of the Photonic Array Processor.	143
6.3	Plots of the waveforms and associated spectra of the captured outputs from the beam directed toward the Radar Test Target Generator. . .	144
6.4	Range/Doppler Processed output of multiple radar pulses from the TTG as sampled from Beam “1.”	144
6.5	Recorded QPSK constellation from the VSA, connected to Beam “0.”	145
6.6	Picture of the beam-sampling photo-detector array used for experimentation.	147
6.7	Simulated, unity magnification output for the experimental setup discussed.	148
6.8	Overview of the Calibration setup and procedure for aligning the beam-sampling photo-detector array.	149

6.9	Simulated, 38% magnification output for the experimental setup discussed.	150
6.10	Beam-sampling photo-detector array outputs over a 140-degree calibration sweep.	151
6.11	Graphical depiction of the potential advantages of the usage of a photo-detector array with smaller pixels.	152
6.12	Comparison of 3 arrays of increasing numbers of elements when scanned to a large angle off bore-sight.	153
6.13	Schematic overview of the experimental setup used for the Full-Dimension Beam-space recovery experiments.	156
6.14	Recovered spectrum and constellation of a QPSK signal incident on the array at the same time as a Radar signal.	157
6.15	The output range/Doppler plots of a single coherent interval for each sampled beam location.	159
6.16	Snapshot of a SWIR measurement of the the output irradiance pattern from the photonic array processor.	161
6.17	Family of curves depicting processing latencies of covariance-based AoA estimation along with the latency of the direct SWIR camera measurements.	162
6.18	Overlay of 50 trials of Angle-Estimation using 11 samples to estimate the sample covariance.	164
6.19	Overlay of 50 trials of Angle-Estimation using 59 samples to estimate the sample covariance.	165
6.20	Overlay of 50 trials of Angle-Estimation using 512 samples to estimate the sample covariance.	166
6.21	Plot showing the measured response at the output of the photonic array processor in the absence of any RF signals.	167
6.22	Comparison of Angle-Estimation performance over multiple trials using two popular estimates of the signal-subspace parameter, D	169

6.23	Plots showing a comparison of various adaptive filtering techniques.	171
6.24	Comparison of sampled waveform data before and after adaptive spatial filtering.	173
6.25	Output spectrum of the quiescent and adapted beams steered toward the direction of the radar signal.	173
6.26	Weighted outputs of the beam-space sampling array.	174
7.1	Graphic depiction of a potential layout for a nested array of photo-detectors.	182

ABSTRACT

A method for imaging Radio-frequency (RF) side-bands about an optical carrier signal, previously devised for passive, non-coherent, imaging of millimeter wave radiation is furthered for use in coherent reception of Radio-frequency signals. Theoretical formulation of a novel photonic beam-space beam-former is presented along with relationships to traditional beam-space array theory. The photonic beam-forming system requires each element of a Radio-Frequency (RF) array be optically up-converted to a laser carrier frequency and fed through a photonic processing system, where the output beam-space is sampled using an array of photo-detectors (or a commercial camera). Specific contributions of this work allow for a more power efficient optical system, amplitude calibration of the optical chain, arbitrary apodization (or tapering) of the output beam-space and application of the receiver system to multiple simultaneous domains (e.g. active sensing and communications in one receive array). Furthermore, a novel adaptive weighting approach is presented that utilizes outputs from both a commercial camera device and an array of high-speed photo-detectors to enable array adaptivity that is shown to be of low-latency when compared to existing techniques. Several experiments are performed using prototype hardware to characterize the system, component and algorithm-level performance enabling more capable designs within future work.

Chapter 1

INTRODUCTION

Since the development of radio broadcast technology, there has been interest in controlling the direction and quality of both radiation and reception of radio waves. Thus, directional array antennas have been discussed by the radio-frequency (RF) community since 1903 [1]. The initial work was performed by Braun, during his early attempts to control the direction of wireless telegraph transmissions. Braun's antenna only allowed for the beam to be steered in 120 degree increments, thus creating three possible transmission locations. The relevance of this work was not fully understood until the early 1930's, when directional array antennas came into wide use for a number of civilian radio applications. The first practical examples were used to solve interference problems between radio stations of neighboring urban centers [2], with later, phase-steerable versions, being used for shortwave radio communications [3]. Military need for large, directive and re-steerable antennas likely began as early as the 1930's with the development of the first practical Radar systems [4], with early scanning systems being used for fire-control purposes [5]. These early phased array antennas used mechanical phase shifters with limited performance and were employed in many radar systems during World War II. However, after the launch of Sputnik, in 1957, the first large-scale phased arrays were developed due to a newly recognized need to detect and track satellites and other, future, space-borne targets [6]. This work led to the development of steering via electronic, ferrite, phase shifters which allowed rapid scanning of the beam and led researchers to investigate methods for placement of a transmitter/receiver pair behind each element of the array [7]. Since the 1960's advancements in array design have led to widespread adoption of electronically steered

antennas for a variety of radio-frequency (RF) sensing and communications applications. The 1980's saw the development of the RF Monolithic Microwave Integrated Circuit (MMIC, pronounced *mim-mick*), principally through the funding of the Defense Advanced Research Projects Agency's (DARPA) MMIC program. Development of a cost-effective MMIC allowed for a significant increase in phased array development and research. With the advent of advanced phased array antennae came advances in array processing techniques such as side-lobe tapering, adaptive nulling of interference and in-situ calibration. Finally, recent advances in digitization and processing technologies have shown promise for fully digital array development in applications where size, weight, and power constraints have previously been too great. However, processing a fully digital array of any reasonable size (i.e. 100's of elements) in real-time is still a challenge [8], particularly when adaptive techniques are involved. In order to reduce the computational burden of large arrays, it is reasonable to assume that only a portion of the field-of-view (FoV) is relevant for any given time-frame, therefore, processing a sub-set of beams, only covering the regions of activity, is of interest. As RF system design complexity has increased steadily over time, antennas that can generate many simultaneous beams have gained significant interest from the community at large [9], with renewed interest being generated by the 5G wireless community [10]. Of particular interest, is the ability of a multi-beam aperture to provide coverage over a wide angular region with a set of high-directivity beams that are generated simultaneously. Typically this beam-fan is steered to a particular region of interest, for radar this is typically the region where the pulses have been transmitted, for communications this could be toward a known, fixed site or geo-stationary satellite. As reviewed in [9, 10], there are typically three general classes of multi-beam antenna, passive multi-beam, active multi-beam and digital multi-beam, with some systems combining a hybrid approach. The array processing system described in this work actually takes advantage of all three classes. Historically, passive beam-forming systems operate at the RF and use quasi-optical or transmission line techniques. Many of these methods utilize bulky lensing materials and/or require RF ports for each individual beam, which, depending

on the RF wavelength of interest, can make mounting of such systems impractical for many applications. Furthermore, beam-forming circuits/networks like those by Butler [11] and Blass [12] have some practical limitations. For example, the Butler matrix is optimal for an even number of beams, and typically these beams exhibit -13 dB sidelobes. The Blass beam-former, on the other hand, contains a number of lossy components. Still, even with these limitations, both are used extensively in a number of systems to this day.

The work described within this thesis concentrates on the theoretical formulation of an RF photonic beam-space array processing technique. This technique allows for the generation of a continuum of beams at the output. Furthermore, these beams can be tailored to have an arbitrary side-lobe level via applications of a number of apodization functions in the optical domain. This capability is seen as a significant advantage of the proposed technique when compared to other beam-space beam-formers like the Butler matrix. The output of the array processing system is a “continuous” beam-space that can be imaged, using techniques initially conceived for passive millimeter wave radiometry, or discretized (i.e. sampled) via introduction of high-speed photo-detectors at the output. Thus, by up-converting the incident RF signal on the antenna array to optical wave-lengths, the associated beam-forming system can be reduced in size by several orders of magnitude when compared to other quasi-optical approaches that operate at the Radio frequency of the antenna (e.g. Luneberg lens, Rotman lens, transmit-arrays, phase-shifting surfaces, etc. [10]). It will be shown in chapter 2 that the output of the photonic beam-space processor is compatible with existing beam-space array theory, when sampled at a set of orthogonal beam-locations via an array of high-speed photo-detectors. Introduction of a separate, coherent, optical Local Oscillator (LO) signal to the output plane further allows the photo-detectors to be used as down-converting mixers so that the outputs can be sent to low-speed analog-to-digital converters (ADCs). The outputs of the ADCs can then be converted to complex samples using digital signal processing techniques. The down-conversion and generation of digital In-Phase and Quadrature (I/Q) samples will be discussed in

Chapter 3. Since the photonic system up-converts the RF signals to the short-wave infrared (SWIR) band, affordable commercial photo-detection devices developed for a variety of high-speed spectroscopy applications can be leveraged directly. The system also features the unique ability to “image” the beam-space directly with a commercial short-wave, infrared (SWIR) camera, this ability was originally devised to “see” black-body radiation in the environment. For active sensing, it is shown that this technique allows the system to determine regions of RF activity within the FoV of the antenna in real-time. Results from several experiments that leverage this visualization are shared in Chapter 4. Finally, the combination of the imaging camera and the sampling photo-detector data creates a powerful digital processing capability that will be discussed in Chapter 5. The sampled beam outputs can be used for a variety of digital beam-space processing techniques, including adaptive nulling and re-steering of a digital beam to any region of interest within the FoV of the sampled beam-space.

The remaining discussion of Chapter 1 presents the necessary background in array processing, such that the reader can more fully understand and appreciate the theory and experimentation discussed in later chapters.

1.1 Radio-Frequency Array Processing

Array processing concepts can be traced back to a call for research on seismic transducer arrays [13]. The principle concern in the late 1950’s was with determination of the precise location of earthquakes and underground nuclear explosions. Further research in the 1960’s included Sound navigation and Ranging (SONAR) applications [14]. These early works look at the array synthesis problem in terms of weighting the array elements such that a single, desired array response is obtained upon summation of the inputs [15–17]. The element level weights can either be deterministic—based on geometry—as in the Delay and Sum beam former, or statistically optimal/adaptive—in the sense of maximizing Signal-to-Noise-Ratio (SNR) across the arrays bandwidth and field-of-view. The seminal study on adaptive arrays

for RF applications is perhaps provided by Applebaum while working for Syracuse University Research Corporation in the 1960s [18], reprinted in the 1970's to allow wider access [19]. Through this early research, adaptive weighting/nulling, side-lobe cancellation and estimation of direction/angle-of-arrival using stored data (off-line processing) are analyzed in context to large arrays. Another popular beam-forming and angle estimation technique, known as Minimum Variance Distortion-less Response (MVDR) beam-forming (i.e. Capon Beam-forming) also has its roots in early seismology. Initially, these early works were not relevant to RF antennas, since it was not yet possible to sample and store the data from array's that operated at radio frequencies. However, once analog-to-digital converter (ADC) and recording technologies became practical for use on higher-frequency RF systems, the techniques optimized for seismic and SONAR beam-forming were investigated for application to RF systems with digital processing. With post-war advancements in phased array technologies and digital processors, many researchers, outside of the military, began implementing adaptive techniques on RF arrays. Beginning in the 1980s several good overviews of beam-forming concepts are provided in the literature [20, 21]. Typically, these techniques are applied across the elements of an array, however, they are equally relevant to an array that performs some beam-forming up-front, as in a Butler array. These arrays are known as beam-space arrays due to the fact that the processing is performed on a set of sampled beam outputs. Beam-space techniques are used exclusively in this thesis and are described in greater detail in later sections.

More recent reviews of array processing show that the adaptive techniques pioneered by Applebaum and Capon maintain relevance with applications that span both spatial and spectral estimation [22–24]. Several estimation techniques will be shown to be compatible with the outputs of the photonic beam-forming system described herein with an in depth discussion of specific techniques used for this research being provided in a later section. For now, it is prudent to review the basic theory behind a delay and sum beam-former. The theory presented concentrates on a uniform linear array, but can be easily extended to multi-dimensional arrays.

1.1.1 Delay and Sum Beam-forming of a Uniform Linear Array

Modern array processing is typically performed using matrix notation and linear algebra. This is done to create a simplified notation, particularly as array sizes become large, however; when beginning one's studies of array processing it is necessary to understand the basic physics of the array beam-forming problem prior to the application of matrix operations. Thus, it is instructive to begin with a simple definition of a uniform linear array as shown in Fig. 1.1. The array is assumed to have a

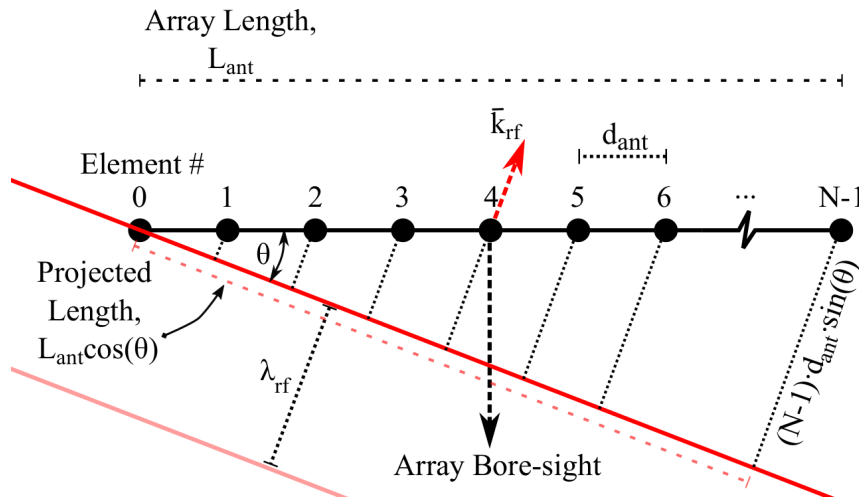


Figure 1.1: Diagram of a Uniform Linear Array of N elements with a single plane wave incident at an angle, θ , relative to the array bore-sight. The parallel wave-fronts of the incident wave are shown in red.

number of elements, N , with a spacing between those elements, d_{ant} , that is uniformly spaced. The spacing of the elements is subject to the same Nyquist/Shannon sampling principles as used in digital signal processing theory. That is to say, any given array must have an element spacing that allows un-ambiguous sampling of the input spatial spectrum. For arrays with elements that possess a wide-field of-view (e.g. $\pm 90^\circ$), the element spacing must be equal to half the wave-length, λ_{ant} , of the desired, highest, frequency of operation. Failure to place elements at the proper spatial sampling intervals will produce aliasing effects. These effects are caused by the inability of the array elements to un-ambiguously sample the phase of a given plane-wave as it crosses the array face. The differential path length between adjacent elements is $d_{ant} \sin \theta$,

where θ is the angle of incidence for a given plane wave. For narrow-band signals, the time-delay of the signal across the elements can be approximated as a phase difference. For the array pictured in Fig. 1.1, the phase difference, $\Delta\phi_n$ that is realized at the n^{th} element of the array due to a plane wave that is incident at an angle, θ , with respect to the array normal is

$$\Delta\phi_n = \frac{2\pi}{\lambda_{rf}} nd_{ant} \sin \theta; \quad 0 \leq n \leq (N - 1), \quad (1.1)$$

where λ_{rf} is the wavelength of the incident RF wave. Each element is imparted with a complex voltage due to the signal. The purpose of the array is to sum these voltages, thus for an un-steered array, the response, or array factor, AF , is defined as the summation of the complex contribution from each element:

$$AF(\theta) = \sum_{n=0}^{N-1} A_n \cdot e^{j\Delta\phi_n} = \sum_{n=0}^{N-1} A_n \cdot e^{j \frac{2\pi}{\lambda_{rf}} nd_{ant} \sin \theta}, \quad (1.2)$$

where A_n is introduced as an amplitude distribution that may be applied across the aperture elements. We can see from (1.2), the array factor has a maximum value of N when $\theta = 0^\circ$. The array factor may be normalized by the number of elements, N , to produce a normalized array response that peaks at 1, rather than N . Normalization is useful when evaluating relative side-lobe levels with respect to the main peak. Without a mechanism to align the elements to a signal incidence angle, other than 0° , we are left with a response, or array factor (AF) over the set of angles $[-90, 90]$ degrees, like that seen in Fig. 1.2a. Additionally, the array's power pattern factor, typically displayed in a decibel format, can be found via the following relationship:

$$AF_{dB}(\theta) = 10 \log_{10} (|AF(\theta)|^2), \quad (1.3)$$

which for the array factor shown in Fig. 1.2a, results in an array power pattern like that shown in Fig. 1.2b. The power pattern shown in Fig. 1.2b is normalized such that the main beam is at 0 dB. It is interesting to note that the array factor of a

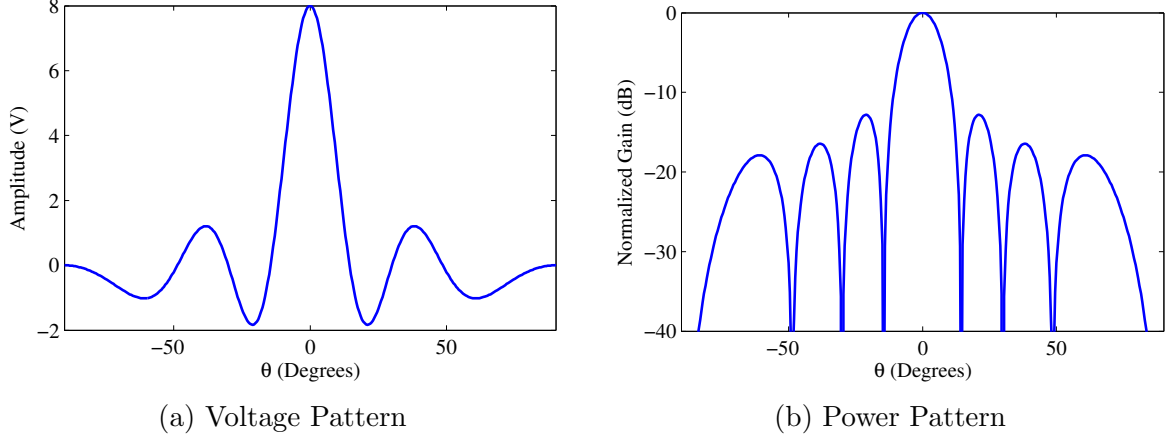


Figure 1.2: Voltage, (a), and Power, (b), pattern responses of an 8-element linear array of isotropic elements.

uniformly illuminated array, that is, $A_n = 1$ for all n , reduces to a sinc-like response that is scaled by the number of elements in the array,

$$\begin{aligned}
 AF(\theta) &= \sum_{n=0}^{N-1} A_n \cdot e^{j\Delta\phi_n} \\
 &= \sum_{n=0}^{N-1} A_n \cdot e^{j\frac{2\pi}{\lambda_{rf}} nd_{ant} \sin \theta} \\
 &= \frac{\sin\left(\frac{\pi N d_{ant}}{\lambda_{rf}} \sin \theta\right)}{\sin\left(\frac{\pi d_{ant}}{\lambda_{rf}} \sin \theta\right)} \\
 &\approx \frac{\sin\left(\frac{\pi N d_{ant}}{\lambda_{rf}} \sin \theta\right)}{\left(\frac{\pi N d_{ant}}{\lambda_{rf}} \sin \theta\right)}
 \end{aligned} \tag{1.4}$$

A full derivation of this relationship is provided in Appendix A.

1.1.1.1 Delay and Sum Phase Steering

Typically, it is desired to steer the array to a desired look direction, θ_s , so that the array response is maximized in the desired direction. In phased arrays, steering is performed via phase shifters behind each element. The array factor can be augmented to include steering via the introduction of a linear phase ramp across the elements,

$$\phi_s = \frac{2\pi}{\lambda_{rf}} nd_{ant} \sin \theta_s, \tag{1.5}$$

which can be inserted directly into (1.2) as a complex phase offset, to arrive at the updated array factor relation:

$$AF(\theta : \theta_s) = \sum_{n=0}^{N-1} A_n \cdot e^{j\Delta\phi_n} e^{-j\phi_s} = \sum_{n=0}^{N-1} A_n \cdot e^{j\frac{2\pi}{\lambda_{rf}} nd_{ant}[\sin\theta - \sin\theta_s]}. \quad (1.6)$$

The effects of steering the array to a given direction are shown in Fig. 1.3, where the beam-broadening effects of steering are evident. The beam broadens in the direction

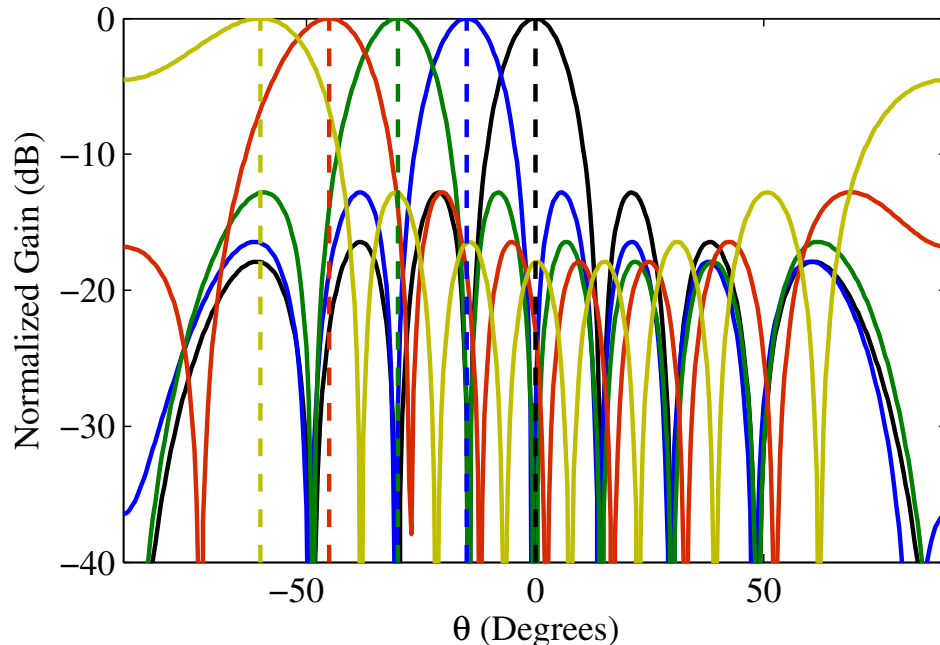


Figure 1.3: Power response of an 8-element linear array of isotropic elements steered in -15 degree increments, displayed in angle-space.

of the scanned angle by approximately $\frac{1}{\cos\theta_s}$. This is due to the fact that as an array scans its beam, the projected length of the array in the direction of the beam varies as the cosine of the angle as shown in Fig. 1.1. Thus as the beam is scanned closer to end-fire, the projected length decreases toward zero.

1.1.1.2 Element Pattern Effects on Array Response

Most arrays do not have iso-tropic elements, thus we must also formulate a pattern response for the elements. A typical element pattern response is given by

$$A_{el}(\theta) = \cos^{\frac{\alpha_e}{2}}(\theta), \quad (1.7)$$

where α_e is a element pattern factor that is used to estimate the shape of the element pattern roll-off with angle. A typical assumed value for α_e is 1.5. Given an element pattern, the total antenna response can then be found via the concept of pattern multiplication, that is the contribution of the element pattern and the array factor are multiplicative. If the array is also sub-divided into sub-arrays, the sub-array pattern must also be multiplied to arrive at a final array output response. Here we will assume that there are no sub-arrays, thus

$$A_{ant}(\theta) = A_{el}(\theta) \cdot AF(\theta : \theta_s) = \cos^{\frac{\alpha_e}{2}}(\theta) \cdot \sum_{n=0}^{N-1} A_n \cdot e^{j \frac{2\pi}{\lambda_{rf}} n d_{ant} [\sin \theta - \sin \theta_s]}, \quad (1.8)$$

where the element pattern contribution is assumed to be identical for all elements. This is a reasonable assumption across a large array that is flat, such that the array normal vector is aligned with the normals of each element. With the element pattern factored in, the steered array response resembles that of Fig. 1.4, which clearly shows the scan loss due to element pattern roll-off along with the beam-broadening due to the smaller projected array length.

1.1.1.3 Array Beam-width

By using the relation in (A.14), one can solve for the beam-width versus angle directly by approximating the array factor with a sinc function as shown in (1.4). For example, a sinc function's -3 dB response point lies when its argument is approximately equal to ± 1.39 . Thus we can solve for an angular offset from θ , θ_{3dB} , that makes the arguments of the sinc function in (1.4) equate to ± 1.39 . Doing so provides the following relation for the 3-dB beam-width of the array:

$$\theta_{3dB} = \frac{0.886 \lambda_{rf}}{L_{ant} \cos(\theta)}, \quad (1.9)$$

where the scalar, 0.866, is specific to the uniformly illuminated array and $L_{ant} = N d_{ant}$, is the length of the array. Interested readers are pointed to Appendix B for a more thorough development of the array beam-width.

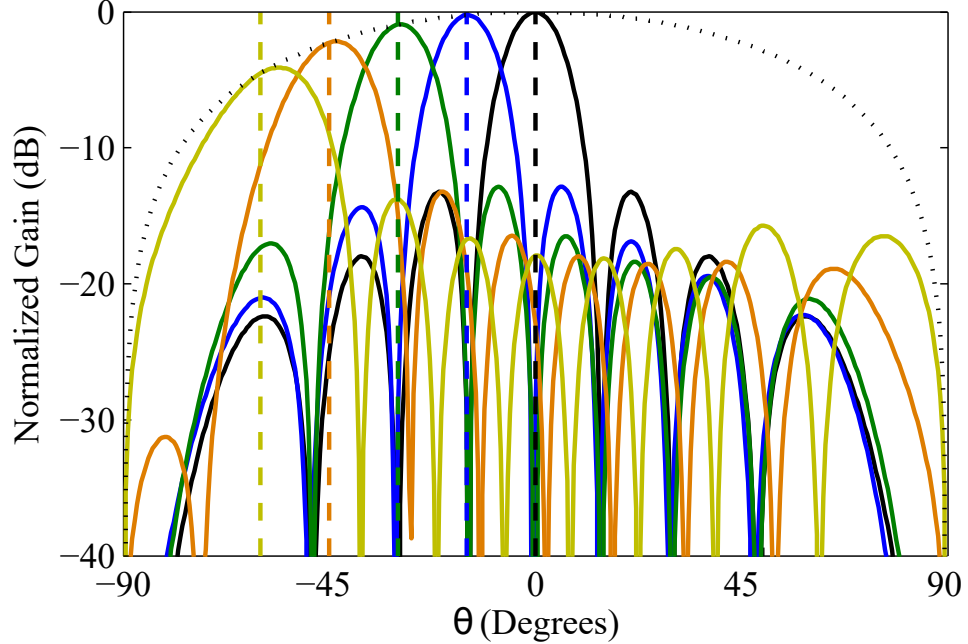


Figure 1.4: Power pattern response of an 8-element linear array of $\cos^{\frac{1.5}{2}}$ elements steered in -15 degree increments, displayed in Angle-space. The element pattern is shown as a black dotted line.

1.1.1.4 Array Grating Lobes

One final concept of importance to cover here is that of Grating Lobes. As mentioned previously, the array elements must be spaced correctly to properly sample the environment. This requirement is due to the fact that an array is a periodic structure in the spatial domain, thus its Array Factor is also periodic. It is desired to ensure that any periodic copies of the main-beam lie well outside the useful field-of-view of the array. Returning for a moment to the closed form solution for the array factor in (A.14),

$$AF(\theta) = \frac{\sin\left(Nd_{ant}\frac{\pi}{\lambda_{rf}}[\sin\theta_s - \sin\theta]\right)}{\sin\left(d_{ant}\frac{\pi}{\lambda_{rf}}[\sin\theta_s - \sin\theta]\right)}, \quad (1.10)$$

we can see that the array factor has maximums where the denominator tends to zero, thus

$$d_{ant}\frac{\pi}{\lambda_{rf}}[\sin\theta_s - \sin\theta] = k\pi,$$

where k takes on any integer value. Rearranging the terms provides the final relationship of grating lobe location to steering angle, wavelength and array element spacing:

$$\sin \theta_{gl} = \sin \theta_s - k \frac{\lambda_{rf}}{d_{ant}}, \quad (1.11)$$

where θ_{gl} is the angle at which the k^{th} periodic grating lobe appears.

1.1.1.5 Weighted Array Factors

Another topic of importance is the effect of application of non-unity weights, A_n , to the array factor response. It may be desired to reduce the sidelobe level of the array, typically on receive, in an effort to reduce the effects of interference that falls outside the main-beam of the antenna. This is usually accomplished via the application of a window function across the array elements. These functions are also known as taper, apodization and/or weighting functions, depending on the specific applications involved.

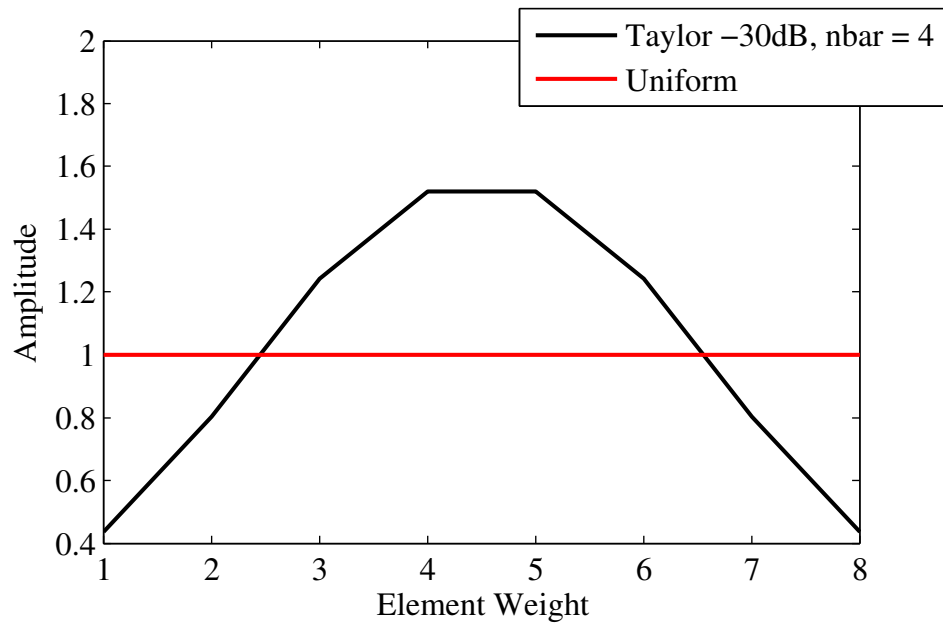


Figure 1.5: Comparison of uniform (un-tapered) array weights with a Taylor weighting scheme that attempts to reduce the side-lobe levels to -30 dB with 4 equal height side-lobes prior to roll-off.

The typical array response is a scaled sinc function response, exhibiting side-lobes that are -13 dB down from the main beam peak. This phenomena is identical to that of a box-car window in spectral analysis. The uniform array can be thought of as a simple spatial box-car filter, thus by smoothing the apparent transition region, one can produce a response with significantly lower side-lobes. An example amplitude profile for an eight element array is shown in Fig. 1.5, with the resulting array response shown in Fig. 1.6. From the result in Fig. 1.6, it is obvious that one must give up some

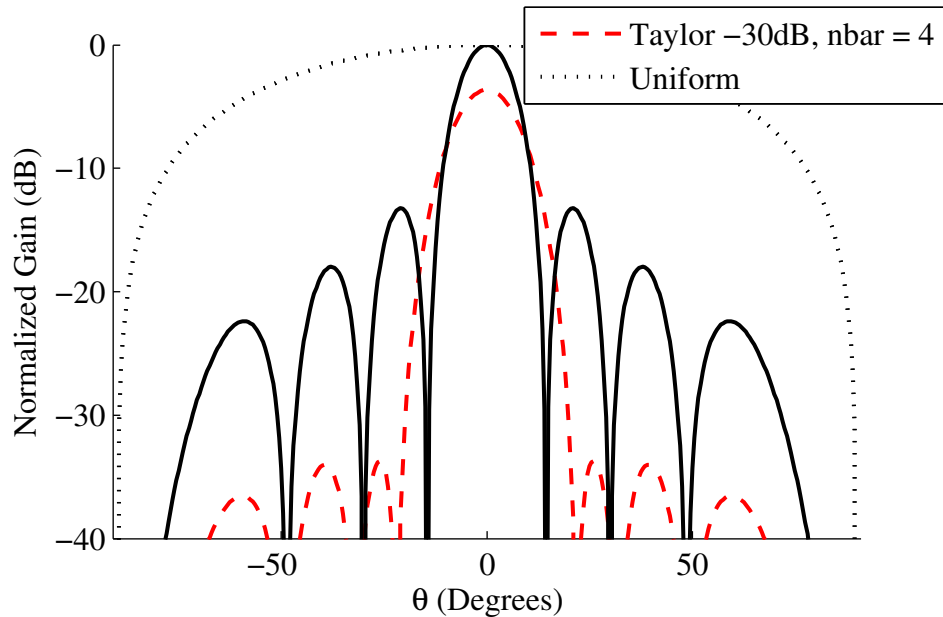


Figure 1.6: Comparison of the power patterns for a uniform (un-tapered) array and one with a Taylor weighting scheme that attempts to reduce the side-lobe levels to -30 dB with 4 equal height side-lobes prior to roll-off.

main-beam gain as well as some angular resolution in order to reduce the side-lobes due to a sharp transition at the edges of the array. Typically, the array is constructed such that the tapered beam meets the necessary resolution and gain requirements, resulting in a slightly larger array.

1.1.1.6 Direction Sines

At this point it is useful to introduce the notion of sine-space coordinates. The direction sine, u , is defined as

$$u = \sin \theta, \quad (1.12)$$

which is simply the sine of the angle of incidence onto any given array. It will be shown later that the sine-space can be transformed into any given coordinate system with relative ease. Thus, the usage of sine-space coordinates is helpful in digital processing since the 180° sector over $[-90^\circ, 90^\circ]$ is normalized to $[-1, 1]$, regardless of the output coordinate system. The ease with which sine-space coordinates are processed and transformed makes it attractive to generate antenna steering commands in the sine-space that are then re-usable across multiple coordinate frames via a simple transformation at the array output. An example of array steering in the sine-space is

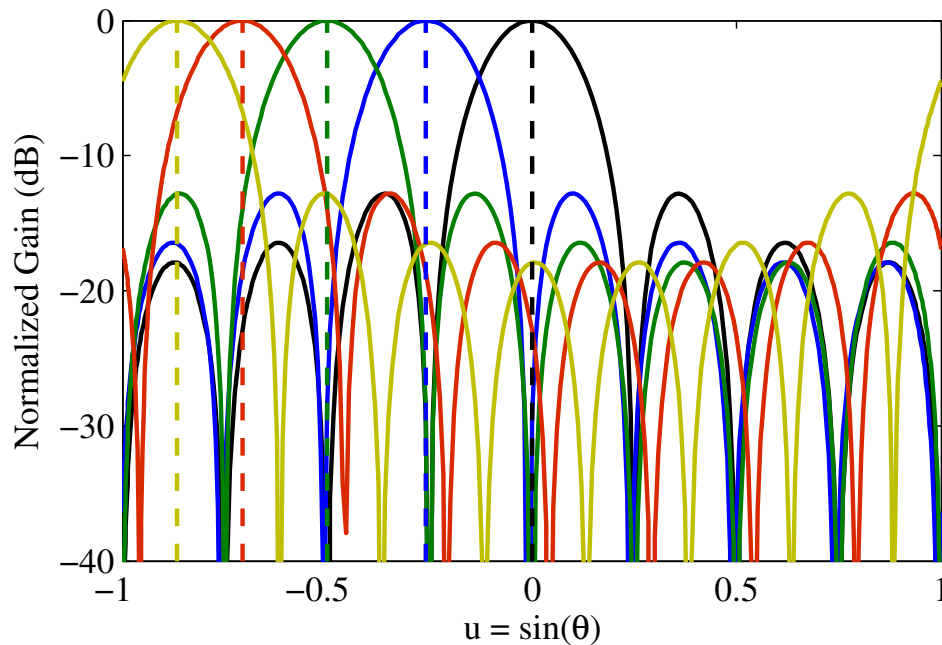


Figure 1.7: Array response of an 8-element linear array of isotropic elements steered in -15° increments, displayed in the sine-space.

shown in Fig. 1.7, where one can notice that the array patterns do not broaden with steering when viewed in the sine-space. The appropriate direction sine can therefore

be directly substituted into any equation derived thus far, and will be used extensively in the discussions of the following sections.

1.1.2 Beam-space Processing of a Uniform Linear Array

As discussed in Section 1, there are various forms of antennae that can provide a beam-space output [9, 10], colloquially referred to as multi-beam antennas. Since the theory presented in the following sections endeavors to show that the output of the photonic array processor is equivalent to a full-dimension beam-space, it is prudent to review the mathematics behind beam-space formation.

1.1.2.1 Coordinate Systems and the Array Steering Vector

The concept of array steering via a linear phase ramp across the elements was introduced in Section 1.1.1.1. The vector of phase delays that are captured by the elements of an array, as a plane wave passes across them, is known as the spatial steering vector. The conjugate of this vector is used to steer the array in a simple delay and sum beam-forming scheme. This concept can be extended to a vector-calculus notation via the introduction of the array coordinate system shown in Fig. 1.8. A modified spherical coordinate system is used so that the antenna coordinates are more compatible with a set of 3-Dimensional simulation environments. There are often disparate coordinate systems for separate RF disciplines, for example, antenna engineers are used to specifying the z-axis as the radiating axis, where as system level users might prefer to use geocentric coordinate systems that likely specify antenna coordinates in azimuth and elevation. For these reasons, it is important to define the coordinate system during any system level simulations, particularly when beam-locations are of interest. The chosen coordinate system defines the azimuth angle about the bore-sight as θ , while ϕ , refers to a positive up, elevation angle from bore-sight. The location of the n^{th} element of the array is defined as a vector, ρ_n . Defining the element positions in this way allows for simulation of arrays that are not located at the origin; useful for simulation of elevated array systems. It is often necessary to define

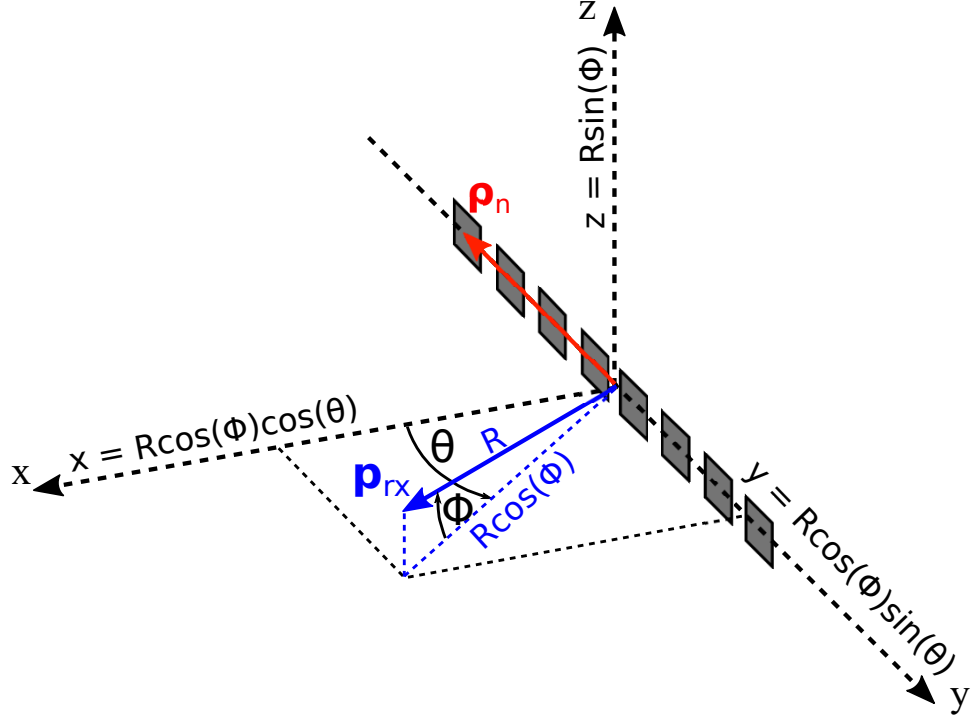


Figure 1.8: Array Coordinate Definition

transformations from the local-angle coordinates of the antenna to the Cartesian space for a vector pointing to a desired receive location, \mathbf{p}_{rx} , with its magnitude defined as, R . With the previous description of \mathbf{p}_{rx} the following coordinate transformations are defined:

$$\begin{aligned}
 x &= R \cos \phi \cos \theta \\
 y &= R \cos \phi \sin \theta \\
 z &= R \sin \phi.
 \end{aligned} \tag{1.13}$$

A set of direction-sines can be similarly generated to aid in conversion of antenna steering commands to the local coordinate system:

$$\begin{bmatrix} u_x \\ u_y \\ u_z \end{bmatrix} = \begin{bmatrix} \cos \phi \cdot \cos \theta \\ \cos \phi \cdot \sin \theta \\ \sin \phi \end{bmatrix}. \tag{1.14}$$

Thus, if we consider an incident signal like that shown in Fig. 1.1, and remember that each element realizes a differential delay as the wave passes the array, we can define

the angle of incidence of the wave via the corresponding sine-space vector, \mathbf{u} . Then by calculating the inner product of a given \mathbf{u} with each element's position vector, $\boldsymbol{\rho}_n$, the projected differential path length in the direction of the incoming wave can be obtained. Usage of vector and matrix notation becomes necessary as the number of terms in the beam-forming equations become large, particularly as array sizes increase to tens of elements or more. For the array pictured in Fig. 1.8, the element position vectors have the form:

$$\begin{bmatrix} \boldsymbol{\rho}_{n,x} \\ \boldsymbol{\rho}_{n,y} \\ \boldsymbol{\rho}_{n,z} \end{bmatrix} = \begin{bmatrix} 0 \\ n \cdot d_{ant} \\ 0 \end{bmatrix}, \quad (1.15)$$

thus the inner product of a given sine-space location and the element positions results in the following:

$$\mathbf{u}^T \boldsymbol{\rho}_n = n d_{ant} \cos \phi \sin \theta. \quad (1.16)$$

If it is desired to determine the relative phase at each element we can introduce the following relation:

$$\mathbf{k} = -\frac{2\pi}{\lambda_{rf}} \mathbf{u}, \quad (1.17)$$

which equates the wave-vector, \mathbf{k} , to the sine-space vector, \mathbf{u} . It is also noteworthy to mention that only the direction of the wave-vector can change with different waves of equal frequency since $|\mathbf{k}| = \frac{\Omega}{c} = \frac{2\pi}{\lambda_{rf}}$, where Ω is the frequency of the wave and c is the speed of light. The phase offset for a given element can now be calculated as

$$\varphi_n = \mathbf{k}^T \boldsymbol{\rho}_n = \frac{2\pi}{\lambda_{rf}} n d_{ant} \cos \phi \sin \theta. \quad (1.18)$$

The result in (1.18) is satisfying since it matches the result in the single dimension case presented in (1.5) when one assumes that no steering in elevation is performed, thereby equating $\cos \phi$ to one.

With the above formulation of the coordinate system complete, and the relations of a particular angular direction to an incoming wave-vector understood, it is possible to formulate the necessary set of vectors used to steer an array. The array steering

vector, \mathbf{v}_s , which is defined as an N dimensional vector of phase delays may be defined as:

$$\mathbf{v}_s(\varphi_n) = \begin{bmatrix} e^{j\varphi_0} \\ e^{j\varphi_1} \\ \vdots \\ e^{j\varphi_{N-1}} \end{bmatrix}, \quad (1.19)$$

where the argument, φ_n , in $\mathbf{v}_s(\varphi_n)$, refers to a definition of the steering vector with respect to a desired elemental phase offset as defined as in (1.18). The steering vector can also be defined with respect to wave-vectors, simple sine-space coordinates or angles using the relations in (1.17) and (1.18). For the array defined in Fig. 1.8, these steering vectors take the following forms:

$$\mathbf{v}_s(\mathbf{u}) = \begin{bmatrix} e^{j \cdot 0} \\ e^{j \frac{2\pi}{\lambda_{rf}} d_{ant} u_y} \\ \vdots \\ e^{j \frac{2\pi}{\lambda_{rf}} (N-1) d_{ant} u_y} \end{bmatrix}, \quad (1.20)$$

and

$$\mathbf{v}_s(\theta, \phi) = \begin{bmatrix} e^{j \cdot 0} \\ e^{j \frac{2\pi}{\lambda_{rf}} d_{ant} \cos \phi \sin \theta} \\ \vdots \\ e^{j \frac{2\pi}{\lambda_{rf}} (N-1) d_{ant} \cos \phi \sin \theta} \end{bmatrix}. \quad (1.21)$$

A steering vector for a particular scan direction will not change for a given array and calibration, thus the steering vectors can be calculated once and stored for use in a real-time system if desired. Forming a steered response is a simple matter of taking the inner product of the conjugate, transpose (sometimes referred to as the Hermitian) of the steering vector with the array inputs. Thus, if we define the input signal at the

n^{th} array element to be $s_n(t)$, an input signal vector across the elements can be defined as,

$$\mathbf{s}(t) = \begin{bmatrix} s_0(t) \\ s_1(t) \\ \vdots \\ s_{N-1}(t) \end{bmatrix}. \quad (1.22)$$

The weight vector for a uniformly illuminated array is simply the hermitian of the steering vector, thus we can arrive at the output of for a single beam-location, $x(t)$ as

$$x(t) = \mathbf{v}_s^T \mathbf{s}(t) = \sum_{n=0}^{N-1} s_n(t) \cdot e^{-j \frac{2\pi}{\lambda_{rf}} n d_{ant} \cos \phi \sin \theta}. \quad (1.23)$$

1.1.2.2 Multi-beam Processing and the Beam-space matrix

For applications where it is desired receive signals over a specific angular interval (e.g. Radar, communications, etc.) but ignore signals elsewhere, it may be beneficial to form a fan of beams that cover the region of interest. For large arrays, when the number of beams in the beam-fan, M , is much smaller than the number of elements, N , digital processing of the beam-fan significantly reduces the dimensionality of any adaptive techniques that may be applied after beam-forming. Two distinct classes of beam-space processing exist, those where $M = N$, known as full-dimension beam-space formation, and those where $M \ll N$, known as reduced dimension beam-space formation [25]. For small arrays, like those used for experimentation throughout the course of this research, a full-dimension beam-space is feasible to process digitally since both M and N are small. Thus, the experimental results described later will focus on utilization of a full-dimension beam-space, however, the techniques described are equally applicable to reduced dimension cases when array sizes are increased.

The construction of a beam-fan can be accomplished via a number of antenna technologies [9,10] however, in general, all beam-forming processes begin with some way of applying a set of steering vectors to a set of input elements. The specific methods for how this is accomplished are what makes each technique unique, for example, a

later section discusses a novel method for generating beams using Fourier processing, a focus of this research. Other antennas may use a Butler or other beam-forming circuit to provide beam-space outputs directly. Regardless of technique, a set of desired beam-locations is generated, the following sections review the processing required to create a beam-fan from a set of input array elements.

Each beam location has a unique beam-space steering vector:

$$\mathbf{b}_m = \mathbf{v}_s(\mathbf{u}_m), \quad (1.24)$$

defined here in the sine-space, with the sub-script, m , denoting the vector for the m^{th} beam. For simplicity in notation, it is assumed that all operations are on a uniform linear array like that shown in Fig. 1.8, thus the sine-space coordinates for any steering vectors presented from here on will only have a single component, u_y , as defined in (1.14), now denoted by u . If it is further assumed that the array has no resolution in elevation, the definition of u can be further altered to ignore the angle, ϕ , leaving a relation similar in form to that presented in Section 1.1.1.1.

Any number of beam-space steering vectors can be formed into a beam-space steering Matrix, \mathbf{B} , defined as

$$\mathbf{B} = [\mathbf{b}_1, \mathbf{b}_2, \dots, \mathbf{b}_{M-1}, \mathbf{b}_M], \quad (1.25)$$

where the columns of the beam-space steering matrix are formed from each of the M beam-space steering vectors making \mathbf{B} an N by M matrix. The beams that compose the steering matrix can be arbitrary in direction; however, there are some advantages to defining the beams such that any two steering vectors are orthogonal [25]. That is to assume that $\mathbf{b}_k^H \mathbf{b}_l = N\delta_{kl}$, which means that the weighting associated with any two beams should have an inner product of zero. This condition creates a set of beams such that when a signal is incident directly on the beam axis of one beam, the signal will not cause a response in any other beam, thus the beams have their main-lobes aligned with the nulls of all the other beams. Two examples of such an orthogonal beam-space are shown in Fig. 1.9a and Fig. 1.9b. The example in Fig. 1.9a is for

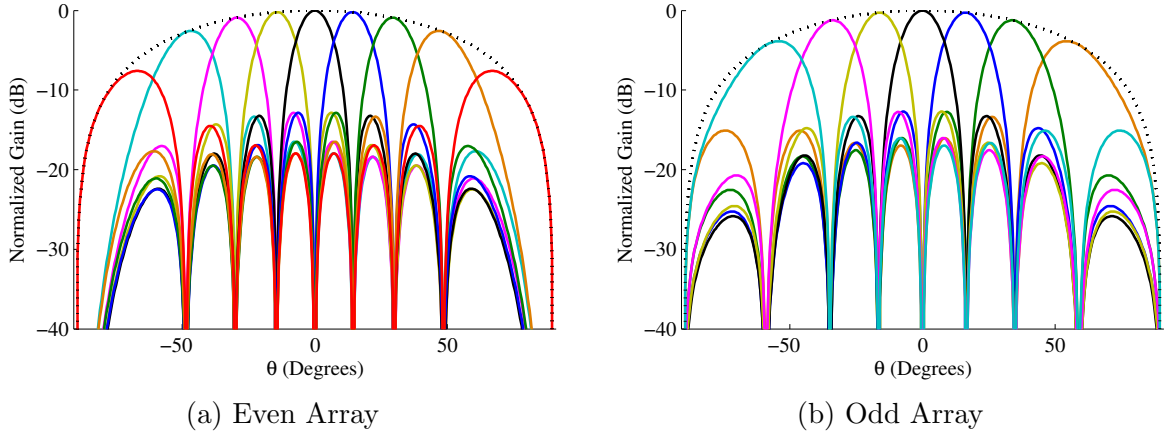


Figure 1.9: Plot of the beam-responses for a full-dimension beam-space of orthogonal beams for an 8-element array, (a), and 7-element array, (b). Notice how the null positions line up perfectly due to the orthogonality constraints on the weights. For even arrays, the final beam position is at end-fire (shown here in red), while for odd-numbered arrays there are no end-fire beams within a full-dimension beam-space.

an 8-element array. All even numbered arrays will have an end-fire beam in the full dimension beam-space, while an odd numbered array will not, as seen in Fig. 1.9b. The full dimension beam-spaces show how the main axis of each beam lies precisely on the nulls of each of the other beams due to the orthogonality constraints placed on the steering/weight vectors. All of the results shown in the later sections utilize either a 7 or an 8 element array configuration, so the beam-spaces of Fig. 1.9a and Fig. 1.9b will be covered in greater depth in later sections.

The set of orthogonal beams are shifted by $\frac{2}{N}$ in the sine-space from a central beam. The central beam of the fan can be steered to center the beam fan on a region of interest in a reduced dimension implementation, but for a full-dimension beam-space, the central beam is aligned with zero. Thus for even arrays, the beam-space steering vector for the m^{th} beam is given by the following:

$$\mathbf{b}_{m,even} = \mathbf{v}_s\left(u - \frac{2m}{N}\right), \quad m = -\frac{N}{2} + 1, \dots, \frac{N}{2}, \quad (1.26)$$

where u is the sine-space location of the central beam. For odd arrays, the orthogonal beam-space steering vectors are given by

$$\mathbf{b}_{m,odd} = \mathbf{v}_s\left(u - \frac{2m}{N}\right), \quad m = -\frac{N-1}{2}, \dots, \frac{N-1}{2}, \quad (1.27)$$

where u is once again defined as the sine-space direction of the central beam.

Once a given beam-space matrix is formed, the responses at the output of each of the M beams can be calculated by multiplying the Hermitian of beam-space matrix and the vector of inputs to each array element, $\mathbf{s}(t)$,

$$\mathbf{x}_{bs}(t) = \mathbf{B}^H \mathbf{s}(t) \quad (1.28)$$

1.1.2.3 Full-Dimension Beam-Space and the Discrete Fourier Transform Matrix

If the desired beam-space is that of a uniformly weighted array, the output, $\mathbf{x}_{bs}(t)$, may be computed via a Discrete Fourier Transform (DFT) (or Fast Fourier Transform (FFT)), across the input elements. Looking at the form of the Hermitian of the beam-space matrix for an odd numbered array we have:

$$\mathbf{B}^H = \begin{bmatrix} \mathbf{b}_{u_{m_1}}^H \\ \mathbf{b}_{u_{m_2}}^H \\ \mathbf{b}_{u_{m_3}}^H \\ \vdots \\ \mathbf{b}_{u_{m_{N-2}}}^H \\ \mathbf{b}_{u_{m_{N-1}}}^H \\ \mathbf{b}_{u_{m_N}}^H \end{bmatrix} = \begin{bmatrix} \mathbf{b}_{\left(\frac{-N+1}{2}\right)}^H \\ \mathbf{b}_{\left(\frac{-N+3}{2}\right)}^H \\ \mathbf{b}_{\left(\frac{-N+5}{2}\right)}^H \\ \vdots \\ \mathbf{b}_{\left(\frac{N-5}{2}\right)}^H \\ \mathbf{b}_{\left(\frac{N-3}{2}\right)}^H \\ \mathbf{b}_{\left(\frac{N-1}{2}\right)}^H \end{bmatrix} = \begin{bmatrix} \mathbf{v}^H \left(-\frac{2}{N} \cdot \frac{-N+1}{2}\right) \\ \mathbf{v}^H \left(-\frac{2}{N} \cdot \frac{-N+3}{2}\right) \\ \mathbf{v}^H \left(-\frac{2}{N} \cdot \frac{-N+5}{2}\right) \\ \vdots \\ \mathbf{v}^H \left(-\frac{2}{N} \cdot \frac{N-5}{2}\right) \\ \mathbf{v}^H \left(-\frac{2}{N} \cdot \frac{N-3}{2}\right) \\ \mathbf{v}^H \left(-\frac{2}{N} \cdot \frac{N-1}{2}\right) \end{bmatrix}, \quad (1.29)$$

which, when fully expanded, provides:

$$\mathbf{B}^H = \begin{bmatrix} 1 & e^{-j\frac{2\pi}{\lambda_{rf}}d_{ant}\frac{N-1}{N}} & e^{-j\frac{2\pi}{\lambda_{rf}}(2)d_{ant}\frac{N-1}{N}} & \dots & e^{-j\frac{2\pi}{\lambda_{rf}}(N-1)d_{ant}\frac{N-1}{N}} \\ 1 & e^{-j\frac{2\pi}{\lambda_{rf}}d_{ant}\frac{N-3}{N}} & e^{-j\frac{2\pi}{\lambda_{rf}}(2)d_{ant}\frac{N-3}{N}} & \dots & e^{-j\frac{2\pi}{\lambda_{rf}}(N-1)d_{ant}\frac{N-3}{N}} \\ 1 & e^{-j\frac{2\pi}{\lambda_{rf}}d_{ant}\frac{N-5}{N}} & e^{-j\frac{2\pi}{\lambda_{rf}}(2)d_{ant}\frac{N-5}{N}} & \dots & e^{-j\frac{2\pi}{\lambda_{rf}}(N-1)d_{ant}\frac{N-5}{N}} \\ & & \vdots & & \\ 1 & 1 & 1 & \dots & 1 \\ & & \vdots & & \ddots \\ 1 & e^{j\frac{2\pi}{\lambda_{rf}}d_{ant}\frac{N-5}{N}} & e^{j\frac{2\pi}{\lambda_{rf}}(2)d_{ant}\frac{N-5}{N}} & \dots & e^{j\frac{2\pi}{\lambda_{rf}}(N-1)d_{ant}\frac{N-5}{N}} \\ 1 & e^{j\frac{2\pi}{\lambda_{rf}}d_{ant}\frac{N-3}{N}} & e^{j\frac{2\pi}{\lambda_{rf}}(2)d_{ant}\frac{N-3}{N}} & \dots & e^{j\frac{2\pi}{\lambda_{rf}}(N-1)d_{ant}\frac{N-3}{N}} \\ 1 & e^{j\frac{2\pi}{\lambda_{rf}}d_{ant}\frac{N-1}{N}} & e^{j\frac{2\pi}{\lambda_{rf}}(2)d_{ant}\frac{N-1}{N}} & \dots & e^{j\frac{2\pi}{\lambda_{rf}}(N-1)d_{ant}\frac{N-1}{N}} \end{bmatrix}. \quad (1.30)$$

If we further assume, $d_{ant} = \frac{\lambda_{rf}}{2}$, and collect some terms, we are left with

$$\mathbf{B}^H = \begin{bmatrix} 1 & e^{-j\frac{2\pi}{N}\frac{N-1}{2}} & e^{-j\frac{4\pi}{N}\frac{N-1}{2}} & \dots & e^{-j\frac{(N-1)2\pi}{N}\frac{N-1}{2}} \\ 1 & e^{-j\frac{2\pi}{N}\frac{N-3}{2}} & e^{-j\frac{4\pi}{N}\frac{N-3}{2}} & \dots & e^{-j\frac{(N-1)2\pi}{N}\frac{N-3}{2}} \\ 1 & e^{-j\frac{2\pi}{N}\frac{N-5}{2}} & e^{-j\frac{4\pi}{N}\frac{N-5}{2}} & \dots & e^{-j\frac{(N-1)2\pi}{N}\frac{N-5}{2}} \\ & & \vdots & & \\ 1 & 1 & 1 & \dots & 1 \\ & & \vdots & & \ddots \\ 1 & e^{j\frac{2\pi}{N}\frac{N-5}{2}} & e^{j\frac{4\pi}{N}\frac{N-5}{2}} & \dots & e^{j\frac{(N-1)2\pi}{N}\frac{N-5}{2}} \\ 1 & e^{j\frac{2\pi}{N}\frac{N-3}{2}} & e^{j\frac{4\pi}{N}\frac{N-3}{2}} & \dots & e^{j\frac{(N-1)2\pi}{N}\frac{N-3}{2}} \\ 1 & e^{j\frac{2\pi}{N}\frac{N-1}{2}} & e^{j\frac{4\pi}{N}\frac{N-1}{2}} & \dots & e^{j\frac{(N-1)2\pi}{N}\frac{N-1}{2}} \end{bmatrix}, \quad (1.31)$$

where the familiar DFT kernel, $e^{-j\frac{kn2\pi}{N}}$, becomes evident across the rows and columns. Here, each row in \mathbf{B}^H represents a single DFT sinusoid, such that upon multiplication of \mathbf{B}^H with a set of elemental inputs from an array, the sampled output for each complex DFT sinusoid in the matrix results. Some texts normalize the beam-space matrix such that the columns become orthonormal and thus the matrix is Unitary. This

normalization is done by dividing the elements by \sqrt{N} and guarantees orthogonality [25].

It has been shown that taking the DFT across an array of inputs is consistent with the generation of a set of orthogonal beams at the output of an array. In the following chapter a novel method to generate the continuous beam-space via photonic up-conversion and Fourier processing will be discussed. It is then hypothesized, and subsequently proven through experimentation that this continuous beam-space can be sampled at the Fourier plane output such that a set of orthogonal beams can be captured and processed using digital beam-space techniques.

Chapter 2

PHOTONIC UP-CONVERSION AND FOURIER PROCESSING OF A UNIFORM LINEAR RF ARRAY

2.1 Motivation for Up-converted arrays

As reviewed earlier, performing analog beam-space processing, for multi-beam antenna applications, at Radio Frequencies requires the use of structures that can be very large and/or heavy as in the case of multi-beam reflector antennas [10], or quasi-optical, lens-like structures that are directly proportional in size to the wave-length of the RF signals of interest [9, 10]. In many cases, such structures are narrow-band with many offering scanning in only a single dimension and in all cases, the structure that performs the phase-shifting or time-delay is larger than the antenna array that feeds it. By first, up-converting the signals behind each element of a given array, one can route the elemental signals via fiber-optic cabling, a significant savings in total system weight when compared to coaxial cable or wave-guide structures. These optical signals can then be processed in the analog domain using lens-based techniques similar to those used directly at the RF, but with significant reductions in size and weight. The array processing optics may also be remoted a great distance from the feeding array via a bundle of optical fibers, making such a technique attractive for elevated applications (e.g. tower-based communications, commercial cellular, 5G, etc.). Furthermore, as photonics integration technologies mature, perhaps through the newly instantiated American Institute for Manufacturing (AIM) in Photonics [26], the potential for integration of optically up-converted signals on multi-function photonic integrated circuits offers even greater savings in size and weight on the RF array itself.

The following sections will begin with a discussion on the advantages of using an arrayed approach to photonic links behind antennas, then continue with a discussion of

the imaging techniques, initially postulated for use in passive millimeter-wave imaging [27] as an efficient way to combine the outputs from an arrayed link. These discussions include the mathematical formulation of the electromagnetic fields at the input and output of the photonic up-conversion system and the subsequent Fourier Transforming lens system. Specific contributions of this work in methods to produce a variety of apodized beam-spaces, precise sampling of the output beam-space to capture a set of orthogonal beams and the usage of digital beam-space processing to extend the techniques described to multi-function apertures will be highlighted. Thus, we begin with a discussion on the conversion of RF signals to optical and the performance of the so-called remoting RF-photonic link.

2.2 Photonic Up-Conversion and Remoting of an Array

Analysis of a single microwave photonic link is well understood and is well defined and described in [28]. However, as photonic architectures become more prevalent and more integrated it will be possible to extend traditional array concepts to tightly integrated photonic systems. In preparation for highly integrated photonic components, it is instructive to analyze the performance of photonic systems within the context of element-level photonic antenna arrays. The potential advantages are shown via an analysis of a simple 2-element array, like that which might be used as an interferometer.

2.2.1 Antenna Input Voltage

In order to derive the link-gain of an intensity modulated direct detection (IMDD) link fed via an RF antenna with specified gain G_{ant} , we must determine the input voltage to the link. We assume a single arm drive Mach-Zehnder Modulator (MZM) with only one output as seen in Fig. 2.1. In its simplest form, a MZM allows an input laser signal to be split into two equal paths, with one path acting as an unperturbed reference while the second path is phase modulated via an electric field. Thus, upon coupling of the two paths at the output, an intensity modulation of the input laser—proportional to the input electric field—is realized. The phase-shift is

typically due to a voltage-induced change to the refractive index of the MZM material (i.e., Pockel's Effect). It is therefore necessary to determine the voltage applied to an MZM due to an incident RF field onto a given antenna or array element.

We start with RF_{in} being an electric field due to the far field propagation of a single tone in free space. This field is propagating toward the antenna in the direction of maximum gain. We assume a 50Ω load and a perfect match at the input to the MZM. With these assumptions in place we will determine the voltage seen at the input to the modulator based on an assumed power density of the incoming wave of $S_{in}[\frac{W}{m^2}]$. Note that $S_{in} = \vec{E} \cdot \vec{H} = \frac{|\vec{E}|^2}{\eta}$ where η is the impedance of free space and is approximately equivalent to 120π or 377Ω . From here we assume an effective aperture of the antenna that collects the incoming power density providing a received power, $P_{RF} = S_{in} \cdot A_{eff}$. The effective area, A_{eff} , has been shown to be related to the gain of the antenna and the wavelength of the design frequency by [29],

$$A_{eff} = \frac{\lambda^2}{4\pi} G_{ant}. \quad (2.1)$$

We will use the effective area of the antenna as a factor for the arrayed analysis later in the paper. With the above relations we find that

$$P_{RF} = \frac{|\vec{E}|^2}{120\pi} \cdot \frac{\lambda^2}{4\pi} G_{ant}. \quad (2.2)$$

We also note that

$$P_{RF} = \frac{V_{RF}^2}{R_L}. \quad (2.3)$$

By substituting (2.2) into (2.3) and solving for the voltage we arrive at

$$V_{RF} = \frac{|\vec{E}| \cdot \lambda}{2\pi} \cdot \sqrt{\frac{R_L}{120} \cdot G_{ant}}. \quad (2.4)$$

The formulation in (2.4) is similar to the approximation for the Antenna Factor (AF) popularized by Ham radio operators:

$$AF_v = \frac{|\vec{E}|}{V} \approx \frac{9.734}{\lambda \sqrt{G_{ant}}}. \quad (2.5)$$

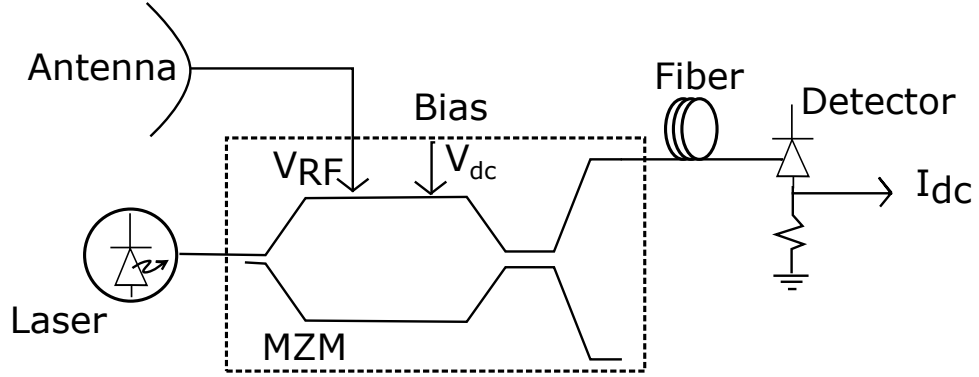


Figure 2.1: A schematic drawing of a basic Mach-Zehnder Modulator (enclosed in the dotted line) being fed via an antenna.

The definition of the Antenna Factor, AF_v , should not be confused with the Array Factor, AF , discussed previously. Next, we describe the basic photonic link setup and begin our analyses of several link topologies within a notional RF array.

2.2.2 MZM Input/Output Analysis

Here it is convenient to define some additional parameters in order to reduce confusion in notation moving forward. The input RF wave's center frequency shall be defined by f , with its radian frequency defined by $\Omega = 2\pi f$. All optical wave center frequencies will be denoted as ν , with optical angular frequencies denoted by $\omega = 2\pi\nu$. We now define the input voltage signal to the MZM behind the antenna due to an RF signal based on the characteristics of the leading RF antenna and any DC bias as

$$V_{in}(t) = V_{dc} + V_{RF} \cos(\Omega t + \alpha_{RF}), \quad (2.6)$$

where V_{RF} is defined in (2.4), Ω is the RF carrier frequency and α_{RF} is any phase function unique to the RF signal. For the MZM we will assume the coupling at the modulator input and output are ideal and that the arms are of equal length. We further assume a loss due to the modulator of \mathcal{L}_m . We can then describe the output electromagnetic fields in each arm of the output coupler by a series of transfer matrices

of the form found in [30, 31]; summarized by [28] as

$$\begin{bmatrix} E_{b1}(t) \\ E_{b2}(t) \end{bmatrix} = \frac{\mathcal{L}_m}{\sqrt{2}} \begin{bmatrix} 1 & j \\ j & 1 \end{bmatrix} \begin{bmatrix} e^{j\phi(t)} & 0 \\ 0 & 1 \end{bmatrix} \begin{bmatrix} 1 & j \\ j & 1 \end{bmatrix} \begin{bmatrix} E_o(t) \\ 0 \end{bmatrix}. \quad (2.7)$$

We note that the phase function $\phi(t)$ introduced in (2.7) is due to the relationship between the input voltage from the antenna, V_{RF} , and the V_π of the modulator as well as any DC voltage bias that is applied to the modulator. The parameter, V_π , describes the necessary applied voltage to shift the phase of the laser signal within an arm of the MZM by π radians. Thus, we can define the induced phase shift, $\phi(t)$, as

$$\begin{aligned} \phi(t) &= \phi_{DC} + \phi_{RF} \cos(\Omega t + \alpha_{RF}) \\ &= \frac{\pi V_{dc}}{V_\pi} + \frac{\pi V_{RF}}{V_\pi} \cos(\Omega t + \alpha_{RF}). \end{aligned} \quad (2.8)$$

The newly defined parameter, α_{RF} , will be important for the analysis of an array where each element feeds an independent modulator and thus each modulator will see a different RF phase. For the case of a signal with normal incidence, α_{RF} then vanishes to zero. We can further define $\phi_{RF} = \frac{\pi V_{RF}}{V_\pi}$ via substitution of (2.4) to arrive at a phase change due to the amplitude of the input field, the antenna (or antenna element) gain and the modulator V_π :

$$\phi_{RF} = \frac{\pi}{V_\pi} \frac{|\vec{E}| \cdot \lambda}{2\pi} \cdot \sqrt{\frac{R_L}{120}} \cdot G_{ant}. \quad (2.9)$$

Inspecting, for a moment, the relationships in (2.9) we notice that when holding all else constant, a change in the input antenna's gain parameter causes a change in the phase applied to the optical field that is proportional to the inverse square of the change to the antenna gain. Typically when remoting a single antenna via an electro-optical link, we wish to determine the average output RF power, P_Ω , at the end of the fiber link. The analysis performed in [28] shows that for a single MZM,

$$P_\Omega = \langle I_{q\Omega}^2(t) \rangle R_o |H_{pd}|^2 = \frac{1}{2} \mathcal{R}^2 \mathcal{L}_m^2 P_o^2 J_1^2(\phi_{RF}) R_o |H_{pd}|^2, \quad (2.10)$$

where $I_{q\Omega}^2(t)$ is the output photo-current due to the first optical sideband when the modulator is biased at quadrature, R_o is the output resistance and H_{pd} is the filter

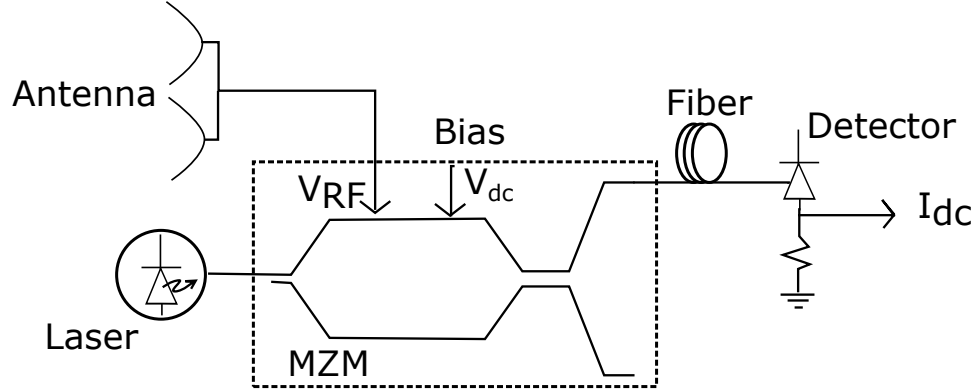


Figure 2.2: Schematic drawing of an optical link behind an antenna array with a traditional RF manifold design.

function of the photo-diode. The result in (2.10) can be used directly for link topologies that are similar to Fig.2.1 or Fig. 2.2. In Fig. 2.2, an array is removed after the array manifold (assumed to be lossless for the purposes of this analysis), which places the antenna's summed RF energy into the optical link. Following a similar derivation as in [28] it can be shown that the photo current at the photo-detector due to the first optical sideband when the modulator is quadrature biased is given by

$$I_{\Omega}(t) = \mp 2I_{dc}J_1(\phi_{RF})\cos(\Omega t + \alpha_{RF}) \quad (2.11)$$

and the small RF signal output photo current in the fundamental sideband is

$$P_{\Omega,ssnon-array} = \frac{1}{8} \mathcal{R}^2 \mathcal{L}_m^2 P_o^2 R_o |H_{pd}|^2 \phi_{RF}^2. \quad (2.12)$$

We now wish to determine the output current for a topology like that of Fig. 2.3 and make some quantitative assessments of the potential advantages and disadvantages of an element-wise optical link approach.

2.2.3 Arrayed MZM Output Power Analysis

Arraying any number of elements as in Fig. 2.3 requires two additional considerations within the optical setup. The first is introduced at point A in Fig. 2.3, where the input laser to the modulators must either be split among the elemental links or separate, locked lasers could be introduced. Regardless of the method, the input

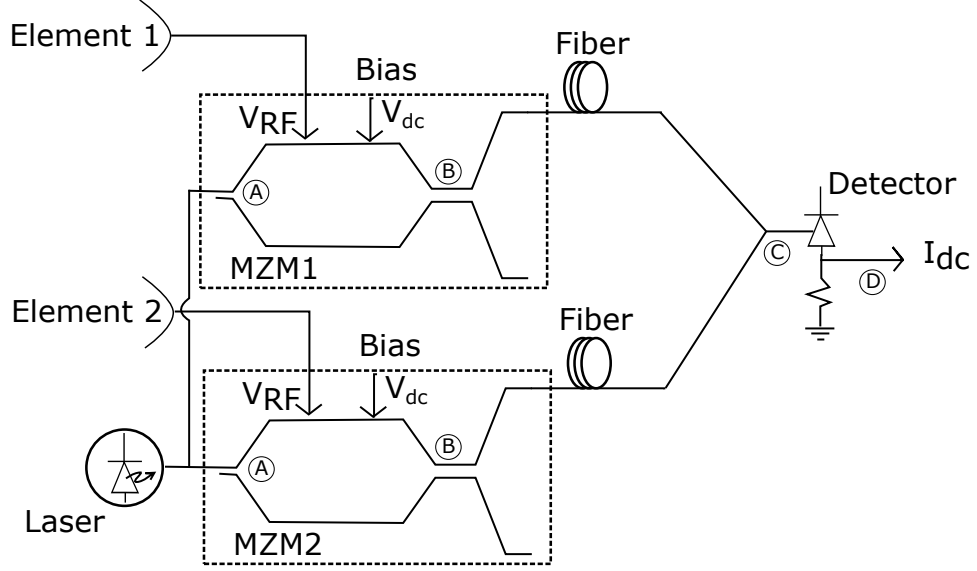


Figure 2.3: Schematic drawing of an antenna array with a Mach-Zehnder Modulator being fed by each element of the array. In this topology the energy must be manifolded in the optical domain.

optical signals must be coherent and the phase must be stable. This extra degree of freedom allows for more total input optical power to be put into the system. Secondly, at point C in Fig. 2.3, we must assume some method of coupling the outputs prior to detection. In practice, it is expected that some additional loss will occur when compared to the simpler antenna remoting link in Fig. 2.2 due to any additional coupling stages. Some further observations with respect to the RF portions of the system are as follows:

1. The total antenna gain, G_{ant} , is proportional to the number of elements, thus the individual element gains,

$$G_e = \frac{1}{N_{elements}} \cdot G_{ant} . \quad (2.13)$$

2. We will assume the input RF field amplitude will be approximately identical at each element due to ideal element gain patterns and an overall small size of the array.

3. Only a bore-sight, or normal incidence angle RF wavefront will result in each element seeing an identical RF phase, all offset angles of arrival will cause a differential phase of the RF signal at each element. This phase offset may be captured by α_{RF} in (2.8).

4. ϕ_{RF} must now include the RF element gain instead of the total antenna gain. Thus, we define

$$\phi_{RF_a} = \frac{\pi}{V_\pi} \frac{|\vec{E}| \cdot \lambda}{2\pi} \cdot \sqrt{\frac{R_L}{120}} \cdot G_e. \quad (2.14)$$

We begin to analyze the topology of Fig. 2.3 in a manner similar to that used in (2.7).

$$\begin{aligned} \begin{bmatrix} E_{B1,1}(t) \\ E_{B1,2}(t) \\ E_{B2,1}(t) \\ E_{B2,2}(t) \end{bmatrix} &= \begin{bmatrix} \frac{1}{\sqrt{2}} & \frac{j}{\sqrt{2}} & 0 & 0 \\ \frac{j}{\sqrt{2}} & \frac{1}{\sqrt{2}} & 0 & 0 \\ 0 & 0 & \frac{1}{\sqrt{2}} & \frac{j}{\sqrt{2}} \\ 0 & 0 & \frac{j}{\sqrt{2}} & \frac{1}{\sqrt{2}} \end{bmatrix} \cdot \\ &\begin{bmatrix} \sqrt{\mathcal{L}_{m_1}} e^{j\phi_1(t)} & 0 & 0 & 0 \\ 0 & \sqrt{\mathcal{L}_{m_1}} & 0 & 0 \\ 0 & 0 & \sqrt{\mathcal{L}_{m_2}} e^{j\phi_2(t)} & 0 \\ 0 & 0 & 0 & \sqrt{\mathcal{L}_{m_2}} \end{bmatrix} \cdot \\ &\begin{bmatrix} \frac{1}{\sqrt{2}} & \frac{j}{\sqrt{2}} & 0 & 0 \\ \frac{j}{\sqrt{2}} & \frac{1}{\sqrt{2}} & 0 & 0 \\ 0 & 0 & \frac{1}{\sqrt{2}} & \frac{j}{\sqrt{2}} \\ 0 & 0 & \frac{j}{\sqrt{2}} & \frac{1}{\sqrt{2}} \end{bmatrix} \begin{bmatrix} \frac{1}{\chi} & \frac{j}{\chi} & 0 & 0 \\ 0 & 0 & 0 & 0 \\ \frac{j}{\chi} & \frac{1}{\chi} & 0 & 0 \\ 0 & 0 & 0 & 0 \end{bmatrix} \begin{bmatrix} \kappa E_o(t) \\ 0 \\ 0 \\ 0 \end{bmatrix} \\ &= \begin{bmatrix} \frac{\sqrt{\mathcal{L}_{m_1}} \kappa}{2} \frac{E_o(t)}{\chi} (e^{j\phi_1(t)} - 1) \\ \frac{\sqrt{\mathcal{L}_{m_1}} \kappa}{2} \frac{E_o(t)}{\chi} (j e^{j\phi_1(t)} + j) \\ \frac{\sqrt{\mathcal{L}_{m_2}} \kappa}{2} \frac{E_o(t)}{\chi} (e^{j\phi_2(t)} - 1) \\ \frac{\sqrt{\mathcal{L}_{m_2}} \kappa}{2} \frac{E_o(t)}{\chi} (j e^{j\phi_2(t)} + j) \end{bmatrix}. \end{aligned} \quad (2.15)$$

It is straightforward to construct the set of matrices in (2.15) for any even number of antenna elements in order to arrive at the output fields for the given set of modulators. An additional parameter introduced in (2.15) is the ratio, $\frac{\kappa}{\chi}$, which allows for variations in the input laser amplitude, via κ , and number of times it is split, via χ . Manipulation of κ and χ enables a comparative analysis between a single antenna remoting link and an arrayed link. We also note that in arrays with N elements, χ and N must be related for equal power distribution to be possible. Since optimal coupling requires equal coupling on the input and output [32], we will assume that $\chi = \sqrt{N}$. In this way, the analysis presented can be applied to arrays with greater than two elements in a straight-forward manner. Thus, in our two-element arrayed case where we have not introduced any additional optical power, $\kappa = 1$ and $\chi = \sqrt{2}$. With the outputs from each arm of the elemental modulators defined in (2.15), we will first take a single output from each modulator and assume they are coupled together with another ideal coupler prior to the photo diode circuit. For simplicity, we will further assume that the modulators are identical and incoming RF wave is at bore-sight which allows the following approximations:

1. $\phi_1(t) = \phi_2(t)$
2. $\mathcal{L}_{m_1} = \mathcal{L}_{m_2}$
3. $\alpha_{RF} = 0$.

Given the assumptions above, we can derive the signal output at point C in Fig. 2.3 due to the upper arms of the modulators (denoted by $E_{Bn,1}$ where n is the antenna element number) as

$$\begin{bmatrix} E_{C1}(t) \\ E_{C2}(t) \end{bmatrix} = \begin{bmatrix} \frac{E_{B1,1}(t)}{\sqrt{2}} + \frac{jE_{B2,1}(t)}{\sqrt{2}} \\ \frac{jE_{B1,1}(t)}{\sqrt{2}} + \frac{E_{B2,1}(t)}{\sqrt{2}} \end{bmatrix} = \begin{bmatrix} 0 \\ \frac{j\sqrt{\mathcal{L}_m} \kappa}{\sqrt{2} \chi} E_o(t) (e^{j\phi(t)} - 1) \end{bmatrix}. \quad (2.16)$$

Taking $E_{C2}(t)$ as the input field to the final photo diode we can find the output photo current as

$$I_{C2}(t) = \mathcal{R}P_{o_{C2}}, \quad (2.17)$$

where \mathcal{R} is the Responsivity of the photo detector and P_{oc2} is the optical power into the detector due to $E_{C2}(t)$. Using definitions of P_o and $E_o(t)$ from [28], we have

$$P_o = \frac{A}{2} \left(\frac{\epsilon}{\mu} \right)^{\frac{1}{2}} E_o^*(t) E_o(t) \quad (2.18)$$

and

$$E_o(t) = \sqrt{\frac{2P_o}{A}} \left(\frac{\mu}{\epsilon} \right)^{\frac{1}{4}} e^{j\omega(t)}, \quad (2.19)$$

such that

$$P_{oc2} = \frac{\kappa^2 \mathcal{L}_m P_o}{\chi^2} [1 - \cos(\phi(t))]. \quad (2.20)$$

Substitution of (2.20) into (2.17) leads us to

$$I_{C2}(t) = \frac{\kappa^2 \mathcal{R} \mathcal{L}_m P_o}{\chi^2} [1 - \cos(\phi(t))]. \quad (2.21)$$

For comparative purposes we wish to derive the photo-current due to the fundamental sideband, since that is where the RF information exists. By substituting (2.8) into (2.21), using the Jacobi-Anger expansion (see derivation in Appendix C) and assuming a proper quadrature bias we can arrive at the following relationship:

$$I_{C2,q}(t) = \frac{\kappa^2 \mathcal{R} \mathcal{L}_m P_o}{\chi^2} + 2 \frac{\kappa^2 \mathcal{R} \mathcal{L}_m P_o}{\chi^2} \sum_{n=0}^{\infty} (-1)^n J_{2n+1}(\phi_{RF_a}) \cos[(2n+1)(\Omega t + \alpha_{RF})]. \quad (2.22)$$

Concerning ourselves only with the first fundamental sideband, when $n = 0$, in (2.22), we arrive at an expression for the output current due to the incident field's fundamental frequency as

$$I_{C2,\Omega}(t) = -2 \frac{\kappa^2 \mathcal{R} \mathcal{L}_m P_o}{\chi^2} J_1(\phi_{RF_a}) \cos(\Omega t + \alpha_{RF}). \quad (2.23)$$

We note that a positive current would be generated from the coupling of the lower outputs of the elemental modulators at point B in Fig. 2.3, which is in agreement with

the formulation used for (2.11). We can now derive the average optical power in the sideband by substituting (2.23) into 2.10 for $I_{q\Omega}^2(t)$ providing us with

$$\begin{aligned}
P_{C2,\Omega} &= \left\langle \left[-2 \frac{\kappa^2 \mathcal{R} \mathcal{L}_m P_o}{\chi^2} J_1(\phi_{RF_a}) \cos(\Omega t + \alpha_{RF}) \right]^2 \right\rangle R_o |H_{pd}|^2 \\
&= 4 \frac{\kappa^4}{\chi^4} \mathcal{R}^2 \mathcal{L}_m^2 P_o^2 J_1^2(\phi_{RF_a}) R_o |H_{pd}|^2 \langle \cos^2(\Omega t + \alpha_{RF}) \rangle \\
&= 2 \frac{\kappa^4}{\chi^4} \mathcal{R}^2 \mathcal{L}_m^2 P_o^2 J_1^2(\phi_{RF_a}) R_o |H_{pd}|^2.
\end{aligned} \tag{2.24}$$

At this point we note that when holding input laser intensity constant from the topology shown in Fig. 2.2 to that shown in Fig. 2.3, $\kappa = 1$ and $\chi = \sqrt{2}$ for the two-way split of the laser, which brings all terms from (2.10) and (2.24) to equilibrium except for the arguments of the Bessel function, which depend on the differing input antenna gain parameters, G_{ant} and G_e . If no additional optical power is introduced into the arrayed topology the small signal power output of the arrayed link is equal to half of the single link case (or $\frac{1}{N}$ for an N-dimensional array). This is due to the fact that the input voltage to the modulators is reduced by the lower elemental gain along with the fact that the modulators themselves are provided with a reduced the laser intensity due to and equal distribution to each of the elements. We instead wish to analyze the case where we use the arrayed topology to introduce a higher laser input intensity into the system. We therefore assume the best case where $E_o(t)$ is doubled by setting $\kappa = 2$ while keeping $\chi = \sqrt{2}$ for a 50-50 split to the dual element array. In this case, we assume that each MZM is being fed with its maximum allowable laser input intensity. Making the necessary substitutions into (2.24), we are left with

$$P_{C2,\Omega,2el} = 8 \mathcal{R}^2 \mathcal{L}_m^2 P_o^2 J_1^2(\phi_{RF_a}) R_o |H_{pd}|^2, \tag{2.25}$$

and assuming small signals we can further reduce to

$$P_{C2,\Omega ss,2el} = 2 \mathcal{R}^2 \mathcal{L}_m^2 P_o^2 \phi_{RF_a}^2 R_o |H_{pd}|^2. \tag{2.26}$$

Brief inspection of (2.12) and (2.26) leads one to believe that there is merit to the arrayed approach, particularly since the arrayed approach allows for additional input

optical power and thus a higher output optical power at the detector. However, we must consider the entire system, especially the differences in ϕ_{RF} and ϕ_{RF_a} , defined in (2.9) and (2.14) respectively, before drawing any definite conclusions. Using the definition in (2.13) and assuming a two element array as in Fig. 2.3, we can manipulate (2.9) and (2.14) in order to define the following relationship:

$$\phi_{RF_{a_{2el}}} = \frac{|\vec{E}| \cdot \lambda}{2\pi} \cdot \sqrt{\frac{R_L}{120} \cdot \frac{1}{2} G_{ant}} = \frac{1}{\sqrt{2}} \phi_{RF}. \quad (2.27)$$

Substitution of (2.27) into (2.26) provides us with

$$\begin{aligned} P_{C2,\Omega_{ss},2el} &= 2\mathcal{R}^2 \mathcal{L}_m^2 P_o^2 \left(\frac{1}{\sqrt{2}} \phi_{RF} \right)^2 R_o |H_{pd}|^2 \\ &= \mathcal{R}^2 \mathcal{L}_m^2 P_o^2 R_o |H_{pd}|^2 \phi_{RF}^2. \\ &= 8P_{\Omega,ssnon-array}, \end{aligned} \quad (2.28)$$

where $P_{\Omega,ssnon-array}$ is defined as in (2.12). We can see from (2.28) that the 2-element array case analyzed provides eight times the output power to the detector. This is due to the ability to drive each modulator with its maximum allowable laser intensity effectively doubling the amplitude of the total system's input laser over the simple antenna remoting case in Fig. 2.2. We further note that by substituting (2.27) into (2.25) we can evaluate the maximum power handling of the arrayed case against that of a single link case.

2.2.3.1 Input RF power handling of the Arrayed topology

Qualitatively, one can see from (2.27) and (2.9) that given the same electric field, \vec{E} , that the arrayed case will provide less input voltage into the modulators due to the lower gain value of the array elements. We wish to calculate the input electric field that would be required to produce the maximum phase shift in the modulators for the arrayed case. From (2.8) we can define a maximum phase shift due to the input RF voltage to be

$$\phi_{max_{RF}} = \frac{V_{RF,max}\pi}{V_\pi}. \quad (2.29)$$

If we assume that we are using identical modulators in both the single link case and the arrayed case, V_π must be held constant, leaving only the RF input voltage to vary the value $\phi_{max_{RF}}$ between the two link topologies under analysis. From (2.27) we can determine that when the input field is constant

$$\phi_{element} = \frac{1}{\sqrt{2}}\phi_{max_{non-array}}. \quad (2.30)$$

We wish to find the input RF field power that would bring the relationship in (2.30) into equilibrium. By substituting (2.4) into (2.30), assuming an identical load resistance, using the relationship for element gain given in (2.13) and solving for the input electric field amplitudes, we arrive at the following relationship:

$$|\vec{E}_{element}|^2 = 2|\vec{E}_{non-array}|^2. \quad (2.31)$$

Therefore we can see that the 2-element arrayed case can handle twice the input RF power before the modulators reach their maximum input voltage. We next analyze the total system gain.

2.2.3.2 System Link Gain of a Two-element Arrayed Topology

The system's small signal RF gain can be defined simply as the ratio of the input RF power at the antenna to the linearized output RF power at the photo-detector, therefore for the 2-element array case

$$G_{system,2el} = \frac{P_{C2,\Omega_{ss},2el}}{P_{RF}}. \quad (2.32)$$

By substituting (2.26) and (2.2) into (2.32) we are left with

$$G_{system,2el} = \frac{2\mathcal{R}^2 \mathcal{L}_m^2 P_o^2 \phi_{RF_a}^2 R_o |H_{pd}|^2}{\frac{|\vec{E}|^2}{120\pi} \cdot \frac{\lambda^2}{4\pi} G_{ant}}. \quad (2.33)$$

We can further simplify (2.33) via substitution of (2.14) and (2.13) for ϕ_{RF_a} and G_e respectively, leaving

$$\begin{aligned} G_{system,2el} &= \frac{2\mathcal{R}^2 \mathcal{L}_m^2 P_o^2 \frac{\pi^2}{2V_\pi^2} \frac{|\vec{E}|^2}{120\pi} \frac{\lambda^2}{4\pi} R_L G_{ant} R_o |H_{pd}|^2}{\frac{|\vec{E}|^2}{120\pi} \cdot \frac{\lambda^2}{4\pi} G_{ant}} \\ &= \frac{\mathcal{R}^2 \mathcal{L}_m^2 P_o^2 \pi^2 R_L R_o |H_{pd}|^2}{V_\pi^2}. \end{aligned} \quad (2.34)$$

Finally, defining the photo-current at quadrature bias as in [28] gives

$$I_{dc} = \frac{\mathcal{R} \mathcal{L}_m P_o}{2}, \quad (2.35)$$

which when substituted into (2.34) provides a final, simplified form of the 2-element arrayed link case as

$$G_{system,2el} = \frac{4I_{dc}^2 \pi^2 R_L R_o |H_{pd}|^2}{V_\pi^2}. \quad (2.36)$$

We can perform a similar analysis starting with (2.12) and assuming the same input RF power to arrive at a gain for the non-array link case as

$$G_{system,non-array} = \frac{I_{dc}^2 \pi^2 R_L R_o |H_{pd}|^2}{2V_\pi^2}. \quad (2.37)$$

Inspection of (2.36) and (2.37) reveals that the arrayed case provides eight times the total system link gain. The greater total gain result is intuitive since the arrayed architecture allows for a higher total input optical power, and thus a higher photo-current at the detector.

2.2.4 RF Photonic Link Performance Metrics

In general, most of the performance of a given RF photonic link depends on just two parameters [28], V_π , and I_{dc} , the modulator V-pi and the output photo-current at the detector, respectively. With this in mind, the following, performance metrics are summarized from [28] for additional context:

$$Gain[dB] = -22.1 + 20 \log_{10} \left(\frac{I_{dc}[mA]}{V_\pi[V]} \right), \quad (2.38)$$

$$P_{o,1dB}[dBm] = -23.5 + 20 \log_{10}(I_{dc}[mA]), \quad (2.39)$$

$$P_{in,1dB}[dBm] = -0.4 + 20 \log_{10}(V_\pi[V]), \quad (2.40)$$

$$OIP3[dBm] = -13 + 20 \log_{10}(I_{dc}[mA]), \quad (2.41)$$

$$IIP3[dBm] = 9.1 + 20 \log_{10}(V_\pi[V]), \quad (2.42)$$

$$NF[dB] = 196.1 - 20 \log_{10} \left(\frac{I_{dc}[mA]}{V_\pi[V]} \right) + N_{out}[dBm/Hz], \quad (2.43)$$

where N_{out} typically consists of input and output thermal noise, shot noise at the photo-detector and any laser Relative Intensity Noise (RIN) contributions at the output and may be defined by

$$N_{out} = \frac{I_{dc}^2}{V_\pi^2} \pi^2 R_i R_o |H_{pd}|^2 k_B T_s + k_B T_s + 2q I_{dc} R_o |H_{pd}|^2 + RIN \cdot I_{dc}^2 R_o |H_{pd}|^2, \quad (2.44)$$

with the final term in (2.44) typically represented via

$$RIN[dBc/Hz] = 13 + N_{opt}[dbm/Hz] - 20 \log_{10}(I_{dc}[mA]) - 2H_{pd}[dB]. \quad (2.45)$$

Two dynamic range metrics are also of interest for most applications:

$$CDR_{1dB}[dB \cdot Hz] = -22.5 + 20 \log_{10}(I_{dc}[mA]) - N_{out}[dBm/Hz], \quad (2.46)$$

and

$$SFDR_3[dB \cdot Hz^{2/3}] = -8.7 + \frac{40}{3} \log_{10}(I_{dc}[mA]) - \frac{2}{3} N_{out}[dBm/Hz]. \quad (2.47)$$

Inspection of the above definitions along with the results in the preceding sections offer some additional insight into the potential advantages of using an arrayed approach to antenna remoting. While a full analysis of each is outside the scope of this work, some motivation may be gained via discussion. For example, the additional total link gain that may be achieved due to the ability to put N -times the optical power into a system with N array elements. When properly coupled at the output, the additional input optical power was shown to produce a greater photo-current at the photo-detector, which from (2.38), increases the overall gain. The increased photo-current can also aid in decreasing the noise-figure and increasing the overall third-order intercept point (OIP3). However, the realizable dynamic ranges may eventually be limited by the intensity noise (i.e., RIN) of the driving laser if careful selection of the lasers and pre-modulator optical amplifier stages are not chosen correctly. The RIN effects on the output are also proportional to the photo-current, thus for a given RIN value there is a maximum useful photo-current before the output reaches a RIN-limited plateau. In any case, there is a practical limit to the amount of additional optical power one

can put into a system before becoming limited by the performance of the underlying optical components themselves. Thus, the relationships between the equations above must be studied and well understood by any prospective system designer.

In addition to the advantages from an RF photonic remoting link perspective discussed above, the elemental up-conversion approach allows for analog beam-forming to be performed in the optical domain. Traditionally, it is desired to do this with photonic true-time delay units (TTDUs), and significant advances in integration techniques for such devices are making them more prevalent [33]. While beam-forming via TTDU is inherently wide-band, it does not allow for multiple simultaneous beams without the need for additional beam-forming networks. We instead approach the challenge of beam-forming via the generation of a continuous beam-space that can be sampled or imaged as described in the next sections.

2.3 Photonic Array Processing

In the previous section it was shown that the up-conversion of each element of an array can allow for additional optical power to be input into the system. This additional optical power may increase the overall link performance of the system, up to any component-limited plateaus. However, the focus of this research is on multi-beam antenna beam-forming and so it is important to be able to produce multiple beam-formed outputs at the termination of the RF-photonic link(s). To this end, it is necessary to describe both physically and mathematically, a method to form an arbitrary beam-space using the up-converted signals. Thus, the theory of operation behind a photonic array processor that uses optical up-conversion and a Fourier Transforming lens will be presented next.

2.3.1 Photonic Array Processor Overview

The photonic array processor assumes that the RF array is placed in a coordinate frame identical to that introduced in Fig. 1.8. Behind each element is an electro-optic modulator that converts the incident RF wave energy into a modulated optical laser

signal. The laser signals for each element are routed from the RF array to a fiber bundle that terminates in a lens-let structure that is a scaled version of the RF array as seen in Fig. 2.4. The optical signals are then re-launched into a free-space optical

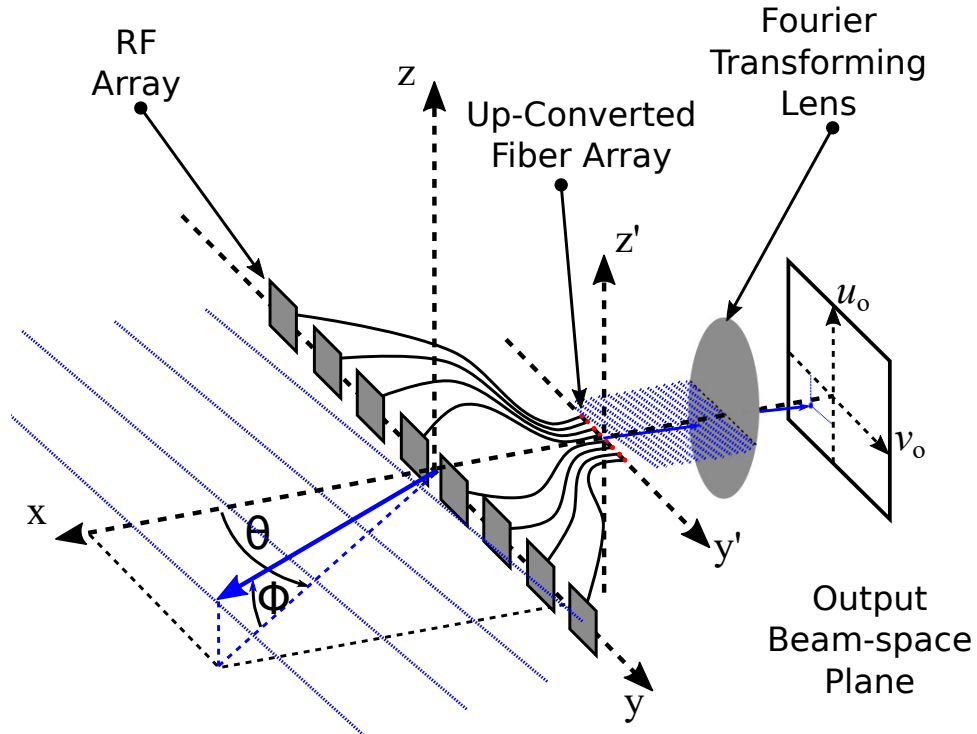


Figure 2.4: Diagram of the basic geometry of Beam-space beam-forming of an RF array via optical up-conversion and a Fourier Transforming Lens.

system that is used to perform the Fourier Transform of the input fiber array. The lens effectively applies a angle-dependent phase shift on the re-radiated waves, such that waves of a particular incidence angle are focused to a spot on the output beam-space plane.

2.3.2 Photonic Array Up-conversion

The photonic array processor discussed here is based on previously proven millimeter-wave imaging techniques, pioneered at the University of Delaware [27, 34]. The schematic in Fig. 2.5, shows that each element of the RF array feeds a Low Noise Amplifier (LNA) and a Mach-Zehnder (Electro-optic) Modulator (MZM). The MZM

is used as an “up-conversion” stage behind each RF element so that the RF signals are converted to optical signals that reside within a set of optical fibers. The fibers are

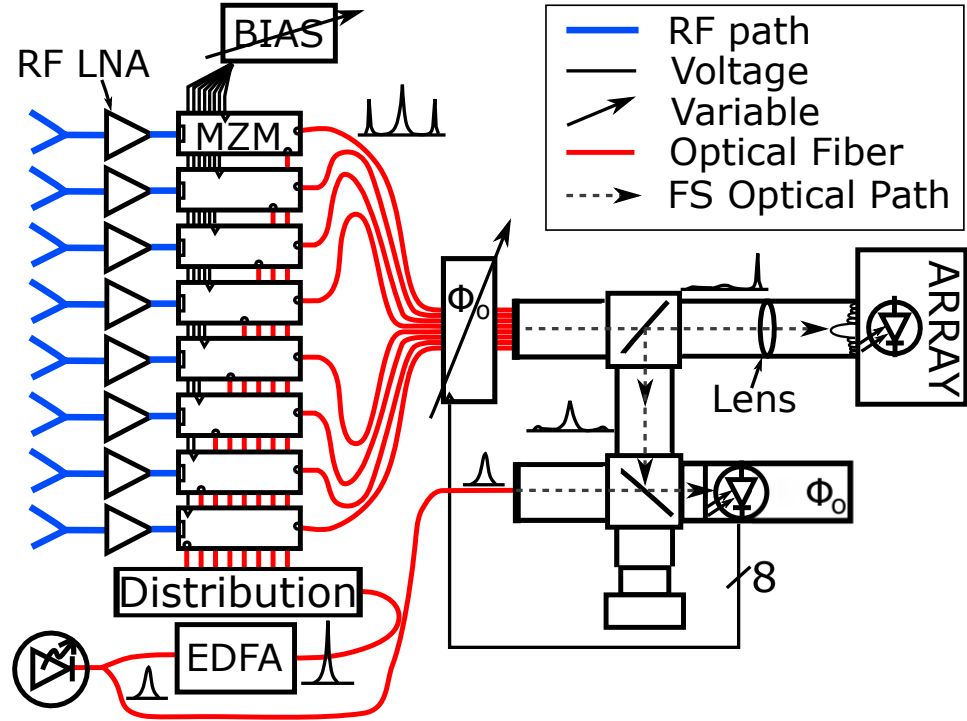


Figure 2.5: Schematic of the basic form of the proposed photonic, beam-space array processor.

then carried to a secondary phase modulator before entering the free-space processing chain. The secondary phase modulator is used to ensure that the optical phases remain coherent, a necessary condition for RF beam-forming and/or signal recovery to be possible at the output.

It is necessary to determine the form of the RF signals of interest as they propagate through the system. Thus we begin with determining the input RF voltage to after the n^{th} array element as

$$V_{RF_e,n} = \frac{|\vec{E}| \cdot \lambda}{2\pi} \cdot \sqrt{\frac{R_L}{120} \cdot G_e G_{LNA}}, \quad (2.48)$$

where it is necessary to consider the gain of any RF amplification stages, behind each element, through the addition of G_{LNA} , to the relation previously derived in (2.4).

Thus we continue with defining the voltage at the input to the electro-optic modulator as before:

$$V_{in}(t) = V_{dc_n} + V_{RF_{e,n}} \cos(\Omega t + \alpha_{RF_n}), \quad (2.49)$$

where V_{dc} is once again a bias voltage that can control the modulator input/output transfer characteristic to achieve a variety of effects on the overall performance of the photonic link [35]. In real applications the bias voltages are likely unique to each modulator, hence the subscripted n . It is equally likely that the element and LNA gain characteristics are slightly different as well, however; for simplicity in notation we will assume that V_{dc_n} and $V_{RF_{e,n}}$ are constant across the array of modulators allowing us to drop the subscripted n moving forward. We do note that the phase seen at each element will be different for any signals that arrive at an angle from the array bore-sight and this relationship is preserved within the phase term, α_{RF_n} . With the input voltage to each MZM defined, we model the phase of the optical carrier signal at the n^{th} element as

$$\begin{aligned} \varphi_n(t) &= \varphi_{dc_n} + \varphi_{RF_n} \cos(\Omega t + \alpha_{RF_n}(t)) \\ &= \frac{\pi V_{dc}}{V_\pi} + \frac{\pi V_{RF_e}}{V_\pi} \cdot \cos(\Omega t + \alpha_{RF_n}(t)). \end{aligned} \quad (2.50)$$

Then, the output optical field from a single element's MZM can then be defined, in a manner similar to (2.7), as

$$E_n(t) = \frac{1}{2} \cdot \sqrt{\ell_n \cdot P_{o_n}} \cdot e^{j\omega t} (e^{j\varphi_n(t)} - 1), \quad (2.51)$$

where ℓ denotes the loss due to the MZM, P_o denotes the input optical power and ω denotes the optical radian frequency. We have assumed a single output MZM, and thus have chosen the upper arm to derive the output relation in (2.51). The choice of output arm is arbitrary as they are equivalent in all aspects but sign. Continuing, we arrive at an initial expression for the optical signal behind each RF antenna element via substitution of (2.50) into (2.51) giving

$$E_n(t) = \frac{1}{2} \cdot \sqrt{\ell_n \cdot P_{o_n}} \cdot e^{j\omega t} \left(e^{j \left(\frac{\pi V_{dc}}{V_\pi} + \frac{\pi V_{RF_e}}{V_\pi} \cdot \cos(\Omega t + \alpha_{RF_n}(t)) \right)} - 1 \right), \quad (2.52)$$

which can be further reduced with an assumption that $\frac{\pi \cdot V_{dc}}{V_\pi} = \frac{\pi}{2}$, a condition known as the quadrature bias, provides us with

$$E_{n,q}(t) = \frac{1}{2} \cdot \sqrt{\ell_n \cdot P_{o_n}} \cdot e^{j\omega t} \left(j e^{j \left(\frac{\pi \cdot V_{RFe}}{V_\pi} \cdot \cos(\Omega t + \alpha_{RFn}(t)) \right)} - 1 \right), \quad (2.53)$$

where the subscript, q , has been added to denote a quadrature bias. From (2.50), we know that $\frac{\pi \cdot V_{RFe}}{V_\pi} = \varphi_{RF}$, thus the exponential with the RF modulation term is of a form that can be reduced to a summation of Bessel functions via the Jacobi-Anger Expansion. After application of the expansion in (C.1) we are left with the following result

$$E_{n,q}(t) = \frac{1}{2} \cdot \sqrt{\ell_n \cdot P_{o_n}} \cdot e^{j\omega t} \left(j \left[\sum_{k=-\infty}^{\infty} j^k J_k(\varphi_{RF}) e^{jk(\Omega t + \alpha_{RFn}(t))} \right] - 1 \right), \quad (2.54)$$

where $J_k()$, represent the Bessel functions of the first kind. The initial result in (2.54) is formidable, but satisfying, since the result of electro-optic conversion of an RF signal is a set of RF side-bands about an optical carrier. Typically, we are concerned with the first optical sideband as this is where the RF signal information resides. Furthermore, the later sidebands fall-off rather quickly making RF signal recovery from those sidebands more challenging. With this in mind, we will concentrate on the result for $k = 1$ giving us

$$\begin{aligned} E_{n,q_1}(t) &= \frac{1}{2} \cdot \sqrt{\ell_n \cdot P_{o_n}} \cdot e^{j\omega t} \left(j \left[j J_1(\varphi_{RF}) e^{j(\Omega t + \alpha_{RFn}(t))} \right] - 1 \right) \\ &= \frac{1}{2} \cdot \sqrt{\ell_n \cdot P_{o_n}} \cdot e^{j\omega t} \left(-J_1(\varphi_{RF}) e^{j(\Omega t + \alpha_{RFn}(t))} - 1 \right), \end{aligned} \quad (2.55)$$

where the subscript, q_1 , on the left hand side of (2.55) denotes the field for the fundamental sideband. We are left with an expression that includes the optical carrier and the first side-band. If we assume that the term, φ_{RF} , is small we can further reduce the result above by using a small signal approximation for the Bessel function in the side-band term. Thus, for small, φ_{RF} ,

$$J_n(\varphi) = \frac{\varphi^n}{2^n n!}, \quad (2.56)$$

which when used in (2.55) provides us with a final form for the signal at the output of the n^{th} element's up-conversion stage as

$$E_{n,q1,ss}(t) = -\frac{1}{4}\sqrt{\ell_n P_{o_n}} \cdot \frac{\pi V_{RF_n}}{V_\pi} \cdot e^{j(\omega+\Omega)t+j\alpha_{RF_n}(t)} - \frac{1}{2}\sqrt{\ell_n P_{o_n}} \cdot e^{j\omega t}, \quad (2.57)$$

where the new subscript, ss , denotes the "small signal" assumption in a manner similar to [28]. Inspection of (2.57) shows two distinct terms, the first is due to the fundamental sideband of the optical input signal to the modulator while the second is due to the optical carrier term. We note in (2.57) that the elemental RF phase, $\alpha_{RF_n}(t)$, due to the incident RF wave sweeping across the elements of the RF array is preserved within the optical side-band. We also point out that the RF signal in the first term of (2.57) must compete with the optical carrier signal within the second term when the combined signals pass through the optical beam-space processor. Each up-converted signal is transported to a Fourier transforming lens via a fiber bundle, which terminates in a lenslet array structure that is a scaled version of the input RF array's elemental configuration as seen in Fig. 2.4. A $2-f$ optical system, where f is the focal-length of the lens in the system, is then used to Fourier transform the input field. This Fourier transform is effectively a Discrete Spatial Fourier Transform (DSFT) of the input array, and is therefore forming a continuous beam-space (i.e., spatial spectrum). In order to show this relationship, we must formulate the input field to the optical system and derive an output relationship for the field once it is propagated through the lens system.

2.3.3 Photonic Array Free-Space Optical Processing

Due to fact that the input RF array is up-converted to optical wavelengths (on the order of 1550 nanometers), a lens-based beam-forming system can be used that is orders of magnitude smaller in overall diameter when compared to a similar system at RF. Thus, we can derive the input/output relationship of the optical processing chain by beginning with the input field.

The field at the input plane (y' and z' axes in Fig. 2.4) of the 2- f optical system is made up of N optical fiber inputs terminated into a micro-lenslet array, where the n^{th} fiber's contribution after the lens-lets is defined as:

$$E_{(y',z')_n}(t) = E_{n,q1,ss}(t) \cdot e^{\left(-\frac{(y'-y'_n)^2+(z'-z'_n)^2}{w_o^2}\right)}. \quad (2.58)$$

Each fiber is given an approximately Gaussian profile with a beam-waist of w_o due to the lenslet array at the termination of the fiber bundle. The y' -axis location of each fiber at the input plane is denoted by the y'_n in this linear array case. For more complex, planar arrays, each element would have components in both the z' and y' axes. We note that this beam-forming system operates on both linear and planar arrays equally well. The total input optical field is then the sum over all N elemental input fields:

$$E_{(y',z')}(t) = \sum_{n=1}^N E_{n,q1,ss}(t) \cdot e^{\left(-\frac{(y'-y'_n)^2+(z'-z'_n)^2}{w_o^2}\right)}. \quad (2.59)$$

By following a derivation similar to [36], the field at the output of the 2- f imaging system is

$$E_{(v,u)}(t) = \frac{e^{jk_o f_l}}{j\lambda_o f_l} \int \int E_{(y',z')}(t) \cdot P(y' + v, z' + u) \cdot e^{-j\frac{2\pi}{\lambda_o f_l}(vy' + uz')} dy' dz', \quad (2.60)$$

where k_o is the optical wave number, λ_o is the optical signal's wavelength, f_l is the focal length of the lens system, and the function $P(y' + v, z' + u)$ represents the effects of the lens pupil function on the output field. When the lens is much larger than the area of the input field and the input field is assumed paraxial, we may assume the effects of the pupil function are small and treat it as a constant equal to one (1). Before continuing, it is convenient to define the variables, E_S and E_C , based on the result in (2.57), as the fields due to the RF-induced sideband and the optical carrier respectively:

$$E_{S_n}(t) = -\frac{1}{4} \cdot \sqrt{\ell_n P_{o_n}} \cdot \frac{\pi V_{RF_n}}{V_\pi} \cdot e^{j(\omega+\Omega)t + j\alpha_{RF_n}(t)}, \quad (2.61)$$

$$E_{C_n}(t) = -\frac{1}{2} \sqrt{\ell_n P_{o_n}} \cdot e^{j\omega t}. \quad (2.62)$$

We also define the Gaussian beam profile function in (2.58) as

$$B_n(w_o) = e^{\left(-\frac{(y'-y'_n)^2+(z'-z'_n)^2}{w_o^2}\right)}. \quad (2.63)$$

We can now expand (2.60) via substitution of (2.61), (2.62), and (2.63) to arrive at the following result:

$$\begin{aligned}
E_{(v,u)}(t) = & \\
& \frac{e^{jk_o f_l}}{j\lambda_o f_l} \int \int \sum_{n=1}^N E_{S_n}(t) \cdot B_n(w_o) \\
& \cdot e^{-j\frac{2\pi}{\lambda_o f_l}(vy'+uz')} dy' dz' \tag{2.64} \\
& + \frac{e^{jk_o f_l}}{j\lambda_o f_l} \int \int \sum_{n=1}^N E_{C_n}(t) \cdot B_n(w_o) \\
& \cdot e^{-j\frac{2\pi}{\lambda_o f_l}(vy'+uz')} dy' dz',
\end{aligned}$$

where the first double integral in (2.64) captures the output due to the energy in the RF-induced optical sideband and the second double integral does the same for the optical carrier signal. Additionally, from (2.64), one can see that the form of the integrals on the right hand side of (2.64) is that of a Fourier Transform. The Fourier transforming capability of a lens stems from its ability to impart a phase delay, to an incident signal, that is quadratic within the perpendicular plane to the paraxial axis. That is to say that any plane wave incident on the input plane of a lens with a wavefront that is tilted in relation the paraxial axis of system is focused to a spot at the output plane, with a position that is directly proportional the tilt angle of the input wave-front. Thus, the output of the photonic beam-space beam-former just described is equivalent to the Discrete Spatial Fourier Transform (DSFT) of the input array, and can be described as a continuous spatial frequency spectrum. Any peaks of the spatial spectrum will coincide with the angles-of-arrival of any plane-waves that are incident on the RF array. With this in mind, we can see from (2.64) and (2.61), that the output due to the “sideband term” of (2.64) is a spatial Fourier transform of the fundamental optical sideband with a tilt angle that is in direct proportion to the angle of the incoming RF waves. The angle of arrival of any incoming RF waves is preserved via the element-to-element phase differences that are captured within the sideband term via the variable, α_{RF_n} , in (2.61). The elemental phase difference causes the generation of off-axis wavefronts on the lens which are focused by the quadratic phase function of

the lens. Similar inspection of the “carrier term” in (2.64) along with the relation in (2.62) shows that the optical carrier output should not have any associated tilt angle. This assumes that the input laser is distributed via a network of equal-length fibers to each optical modulator and that optical phase alignment is maintained after the modulators. For the experimental system discussed later, the optical phase coherence across the channels is controlled via a feedback loop as described in [37].

It has been shown that the input/output relationship of the optical processing chain is that of a Fourier Transform, allowing simulation of the system to be performed with good fidelity via the Fast Fourier Transform (FFT). Thus, a numerical simulation for the proposed processing chain has been developed to allow for visualization of contributions of both the side-band and the carrier to the output spatial frequency spectrum.

2.3.3.1 Photonic Array Beam-space Processing Simulation

We have shown that the RF phase is preserved within the fundamental sideband of the optical carrier so that an RF wave with an incidence angle off of the array’s bore-sight will be shifted in the output Fourier plane proportionally to the angle of incidence. This behavior can be seen from the simulated, solid-colored, “beams” of Fig. 2.6. A significant challenge in the practical application of photonic beam-space beam-forming is in the cancellation of unwanted carrier energy. The lack of any tilt angle associated with the wave-fronts of the carrier’s field causes any uncanceled carrier signal to manifest as a large, bore-sight “beam” response as shown by the black dotted line in Fig. 2.6c and Fig. 2.6d. Thus, the carrier term eclipses any reasonable RF input that would enter the antenna if it is not properly canceled before entering the beam-forming system. From Fig. 2.6d, it is clear that the carrier must be attenuated by more than 35 dB in order for the bore-sight RF signal (in red) to eclipse the carrier signal’s main-lobe for the case simulated here. Furthermore, the carrier term does not contain any useful RF signal information; however, any un-canceled carrier power at the output will produce a non-negligible intensity noise on a receiving photo-detector [38]. For this

reason, uncanceled carrier power becomes another limiting factor for the amount of optical input power that can be put into the up-converted array architecture discussed initially in Section 2.2.3. Carrier rejection—in the experimental beam-space array processor discussed later—is currently accomplished via a combination of reflective, thin-film filtering and use of Mach-Zehnder modulators biased for suppression of the carrier. When properly nulled, one can expect an output like that of Fig. 2.6a and Fig. 2.6b for each signal incident on the array.

Thus, with proper sampling of the output plane, it is hypothesized that one can arrive at an equivalent Beam-space output vector, $\mathbf{x}_{bs}(t)$, to that of the DFT beam-former in (1.28). Furthermore, it is suggested that the signals incident at orthogonal beam positions can be recovered directly at the output of the RF photonic beam-former using high-speed photo-detectors placed at the precise locations. The theory behind determining these locations will be discussed next, with a series of experimental results using the suggested techniques being covered in subsequent Chapters.

2.3.4 Effects of Up-conversion on RF Angle-of-Arrival (AoA)

It is desired to be able to determine the precise locations in the output plane of the optical processing chain that coincide with an arbitrary selection of signal incidence angles. Such a relation would allow for the placement of an array of sampling photo-detectors such that a discrete set of orthogonal beam positions could be recovered. Furthermore, if the output plane intensity is imaged with a camera, the location of any peaks in the image would be able to be converted to angles-of-arrival.

Thus we begin with the formulation by making the simplifying assumption that for the array shown in Fig. 2.4, we do not expect to have any resolution for the angle, ϕ . Therefore, we can consider a “top-down” two-dimensional equivalent geometry for the purposes of mathematical convenience as shown in Fig. 2.7. When an RF plane wave is intercepted by the RF array at an angle, θ , as shown in Fig. 2.7, the total

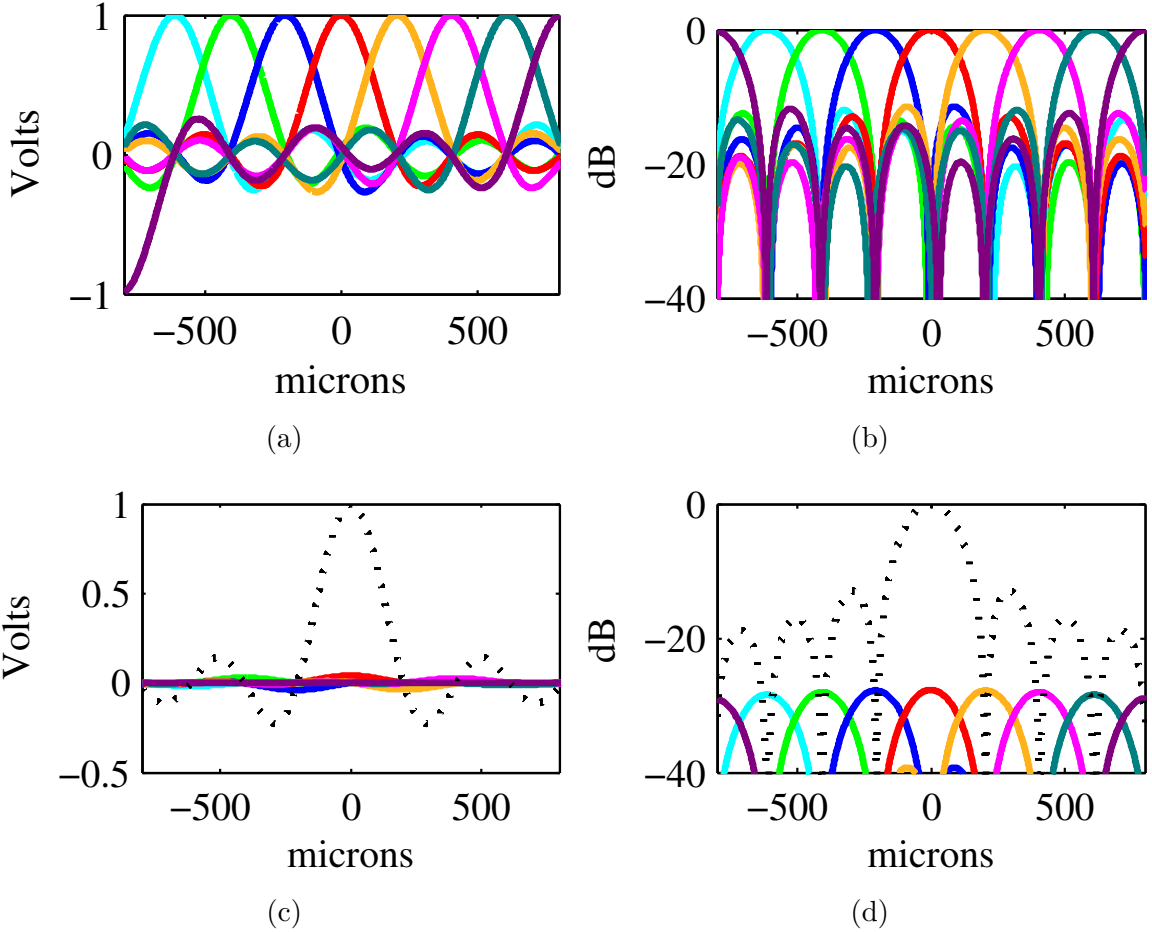


Figure 2.6: Simulated outputs of the beam-space beam-former for an eight element array with RF signals aligned with the main response axis of a single orthogonal beam position. Eight separate signals are shown to illustrate the ability of the photonic system to “image” the entire field-of-view from $[-90^\circ, 90^\circ]$: a) Voltage patterns with optical carrier nulled; b) Power patterns with optical carrier nulled; c) Voltage patterns normalized to optical carrier output; d) Power patterns normalized to optical carrier output. Note colors and line-styles are kept constant for each beam within each subplot.

phase variation across the array is given by:

$$\begin{aligned}\Delta\phi_{RF} &= \frac{2\pi}{\lambda_{RF}} \cdot L_{p_{ant}} \\ &= \frac{2\pi}{\lambda_{RF}} \cdot N \cdot d_{ant} \cdot \sin\theta,\end{aligned}\tag{2.65}$$

where $L_{p_{ant}}$ is the total propagation path length difference across the RF array, N is the number of elements and d_{ant} is the inter-element spacing. The total propagation path length can also be described as the projected antenna length in the direction of travel of the incident wave. The incoming signals are then up-converted to the optical domain where they ride on a side-band of the optical carrier as defined in (2.61). The signals then propagate over equivalent length fibers to the fiber bundle array, where the angle-of-arrival (AoA) is translated such that the entire field of view of the RF array is encompassed within a scaled set of par-axial angles in the optical domain. Since the RF signals are passed to the fiber array without loss of phase (or time of arrival) information the total phase variation and/or time-delay across the fiber array must be equivalent to the total variation across the input RF array as defined in (2.65). We define the total phase variation across the fiber array for any wave launched at a tilt angle, α , relative to the central axis of the optical system as

$$\begin{aligned}\Delta\phi_{fa} &= \frac{2\pi}{\lambda_{SB}} \cdot L_{p_{fa}} \\ &= \frac{2\pi}{\lambda_{SB}} \cdot N \cdot d_{fa} \cdot \sin\alpha,\end{aligned}\tag{2.66}$$

where $L_{p_{fa}}$ is the total propagation path length across the fiber array, λ_{SB} is the wavelength of the first fundamental sideband of the optical carrier, N is the number of elements and d_{fa} is the inter-fiber spacing. Equating (2.66) to (2.65) and solving for α yields

$$\alpha = \arcsin\left(\frac{\lambda_{SB} \cdot d_{ant}}{\lambda_{RF} \cdot d_{fa}} \cdot \sin(\theta)\right).\tag{2.67}$$

From (2.67), we see that the initial RF signal is re-launched from the fiber array at a scaled angle, α , that is proportional to the ratios between the RF and optical wavelengths as well as the RF and optical element spacing. With knowledge of the tilt

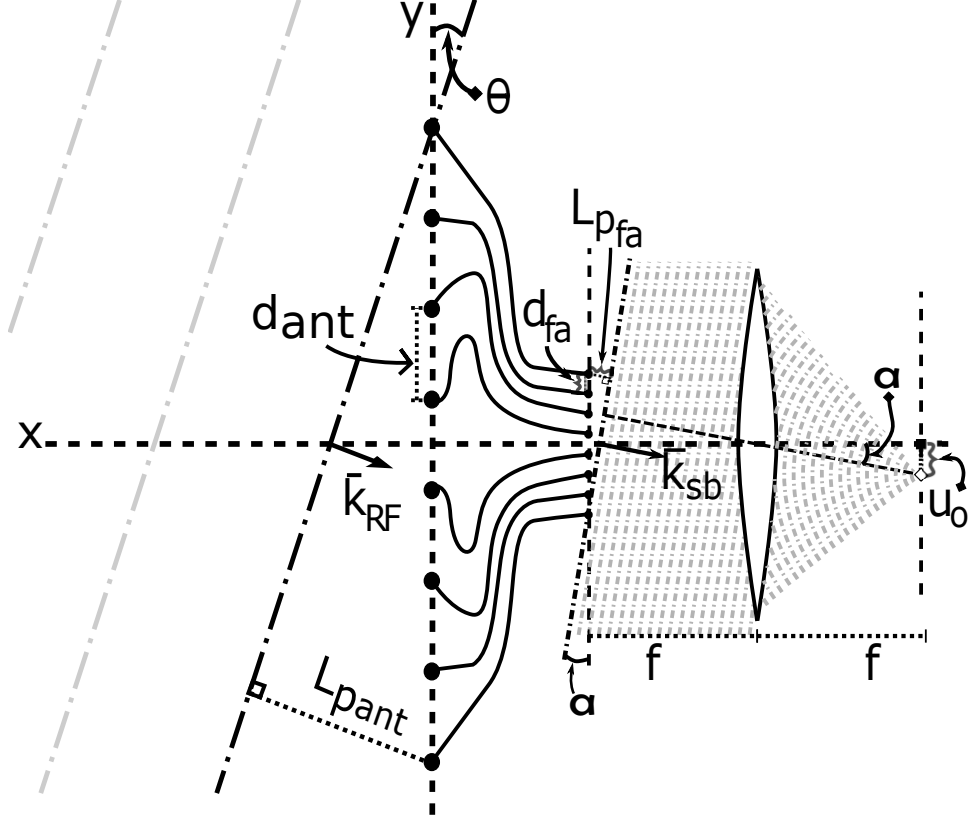


Figure 2.7: Two-dimensional graphical depiction of the translation of the input aperture from the RF to the optical domains and its effect on the direction-of-arrival of the incoming RF waves.

angle of the optical wave-fronts we can determine the output locations on the Fourier plane via simple geometry as

$$u_o = f \cdot \tan(\alpha), \quad (2.68)$$

where u_o is the output plane location and f is the focal-length of the lens as defined in Fig. 2.7. We arrive at a relation between the RF array's sine-space coordinate, u_{sine} , and the output Fourier plane location, u_o , as

$$u_o = f \cdot \tan \left[\arcsin \left(\frac{\lambda_{SB} \cdot d_{ant}}{\lambda_{RF} \cdot d_{fa}} \cdot u_{sine} \right) \right], \quad (2.69)$$

where u_o is defined in meters from the central axis of the output plane. For the simulation outputs shown we have assumed a lens focal-length, f , of 20 centimeters and a fiber spacing, d_{fa} , of 200 microns. If we wish to sample the outputs at eight

Table 2.1: Sine-space and Fourier-space locations of 8 Orthogonal Beam Positions for an 8-element array

Beam (unit-less)	θ_{RF} (degrees)	u_{sine} (unit-less)	u_o (microns)	α (degrees)
1	-48.59	-0.75	-581.2	-0.1665
2	-30	-0.5	-387.5	-0.1110
3	-14.478	-0.25	-193.7	-0.0555
4	0	0	0	0
5	14.478	0.25	193.7	0.0555
6	30	0.5	387.5	0.1110
7	48.59	0.75	581.2	0.1665
8	90	1	775	0.2220

(8) orthogonal beam locations, we can do so by placing high-speed photo-detectors at the required locations in the Fourier plane, as noted in Table 2.1. Just as in the sine-space, grating lobes will appear in the Fourier plane so it is imperative that the RF array is critically sampled to build a proper full-dimension beam-space output. Another important effect of the up-conversion and beam-forming process is that the fiber array cannot physically become small enough to be critically sampled for the chosen optical wavelengths. The spacing is limited by the physical dimension of the optical fiber itself, which is an order of magnitude larger than the optical wave-lengths being carried. The side-effect of this is that there are constant optical grating lobes in the focal-plane, however; the fiber-array is significantly oversampled when compared to the RF signal of interest. Thus the full field-of-view of a properly sampled RF array will lie between the optical grating lobes. The roll-off of the optical grating lobes can be directly affected by altering the beam-shape of the elemental fibers at the input the optical processing system. Currently, each fiber is assumed to have a Gaussian beam shape with beam-waist, w_o , provided via coupling of each input fiber to a lenslet array. The plots in Fig. 2.8 show the simulated Fourier plane output due to a single bore-sight source with varying beam-waist at the input fiber bundle. The graphic in Fig. 2.9 is an additional attempt to visualize grating lobe patterns that result from undersampling the fiber array.

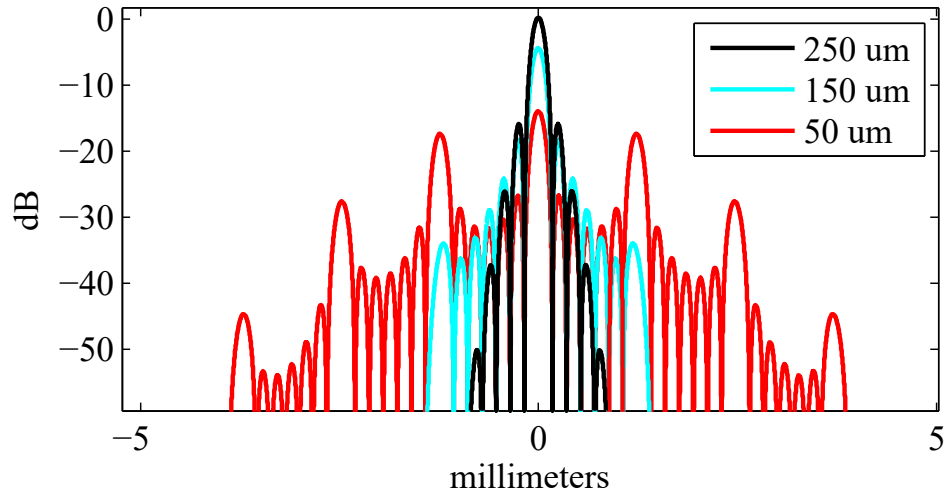


Figure 2.8: Simulated outputs at the Fourier plane of the optical processor for three different assumed Gaussian beam-waists.

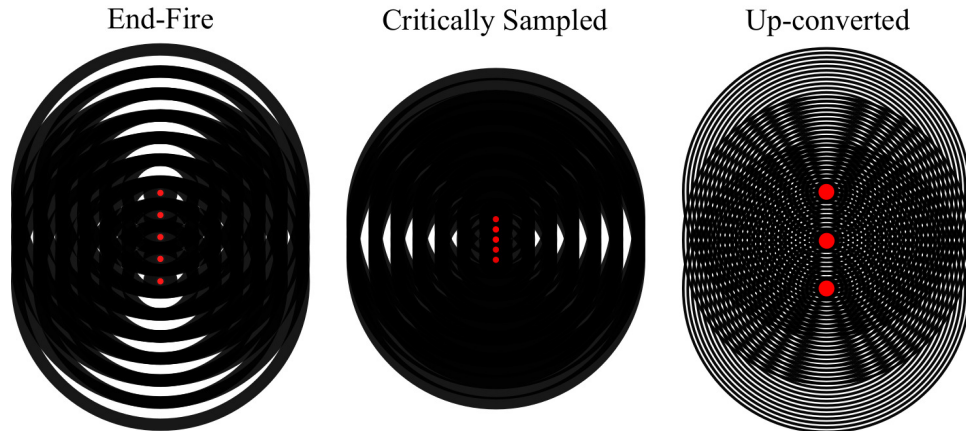


Figure 2.9: A graphical depiction of an unsteered, spherical wave being launched from arrays with 3 different element spacings with respect to the launched wave-length. The launched waves are represented by the light-colored areas. The three array configurations show an End-Fire array, a Critically Sampled Array and an example of an Under-sampled, Up-converted array, with $d_{ant} = \lambda, \frac{\lambda}{2},$ and $10\lambda,$ respectively. The Up-converted case clearly shows the multiple beams/grating lobes that are launched simultaneously as a set of overlapping, light-colored fringes. In the photonic array processor, the RF signals of interest lie in the spaces between the multiple lobes seen in the diagram on the right, allowing them to be recovered un-ambiguously at the output plane.

From inspection of Table 2.1, we see that there is no beam at -775 microns, this is due to the fact that the 8th beam of an even-order array is an end-fire beam that has a grating lobe at -1 in sine-space. This grating lobe is evident in Fig. 2.6 as a purple trace that appears to have main response axes at both -775 and 775 microns in the output plane.

We now have a method to generate a continuous beam-space and calculate locations for the sampling of chosen beams within the output Fourier plane of the beam-former. The example beam-space locations in Table 2.1 would be used for sampling a set of orthogonal inputs such as to further process the beams using beam-space adaptive processing techniques. In some applications there may be the need to directly sample arbitrary beams that exhibit a low-sidelobe response, to mitigate effects of spatially adjacent interference, for example. In order to reduce the output plane sidelobes, a method of apodization or beam-tapering must be employed, as discussed next.

2.3.5 Apodization of Beams Using the Photonic Beam-space Processor

Beam apodization (also known as tapering or windowing) is realized via a pattern of weights across array elements that are typically symmetrical about physical dimensions of the receiving array. In many applications, these weights are applied via physical attenuators within the array beam-former. This method is compatible with the photonic beam-space processor, though it requires an additional RF device to be placed behind the antenna elements. Instead, we apply beam tapering functions within the optical chain, after RF up-conversion has occurred. There are several methods that have been developed, simulated and prototyped.

2.3.5.1 Apodization Via Transmissive Film Filtering in the Optical Chain

A simple, but effective method for beam tapering within the photonic beam-space beam-former is to place an amplitude transmissive profile filter in the free-space optical path of the lens [39]. In order to achieve the desired results, this technique requires precise alignment of the filter with the fiber array's central axis. It is important

that the transmissive filter overlap the input signal support completely. An example optical taper profile that matches a -27 dB Taylor [40] window has been simulated in Fig. 2.10 to show the concept. A consequence of tapering in this manner is the removal of optical power that was put into the system. Amplitude tapering within the optical chain of the beam-space processor effectively lowers the wall-plug efficiency of the system in a manner proportional to the apodization profile that is used on the fiber array. This is due to the fact that the tapering function must be applied via a carefully constructed gradient density filter that blocks the optical signal from the outer fiber array elements, while not altering the phase. For the case of the Taylor function used to generate Fig. 2.10a, the laser signals from the edge elements are attenuated by 70% when compared to the central elements. Another issue with the gradient density tapering method is the actual construction and implementation of the filter itself. The filter must be equal in size to the fiber bundle, which for small arrays will tend to be on the order of millimeters in side length. Precise control of the density gradient may also present a challenge since the approximately linear portion of the function simulated (i.e. the region from ~ 200 to ~ 600 microns in Fig. 2.10b) changes density by 0.11% per micron. Furthermore, switching between tapered and untapered beams requires additional hardware (e.g., a filter wheel) that would complicate the optical system. To circumvent these issues we propose a different method that uses precise control of the input laser power prior to the optical modulators. By limiting the input laser power to each Mach-Zehnder modulator an amplitude taper function can be created that does not “throw away” any input power. This method has the advantage of reducing the total input power of a system when the output of apodized beams is required.

2.3.5.2 Apodization Via Weighted Distribution of a Master Laser

Rather than attenuate the laser amplitudes at the fiber bundle, which can be costly to the overall power efficiency of the system, we wish to limit the initial input laser power to each of the element’s optical modulators. For the purposes of demonstration, a method to “taper” the input laser across an array of eight (8) modulators

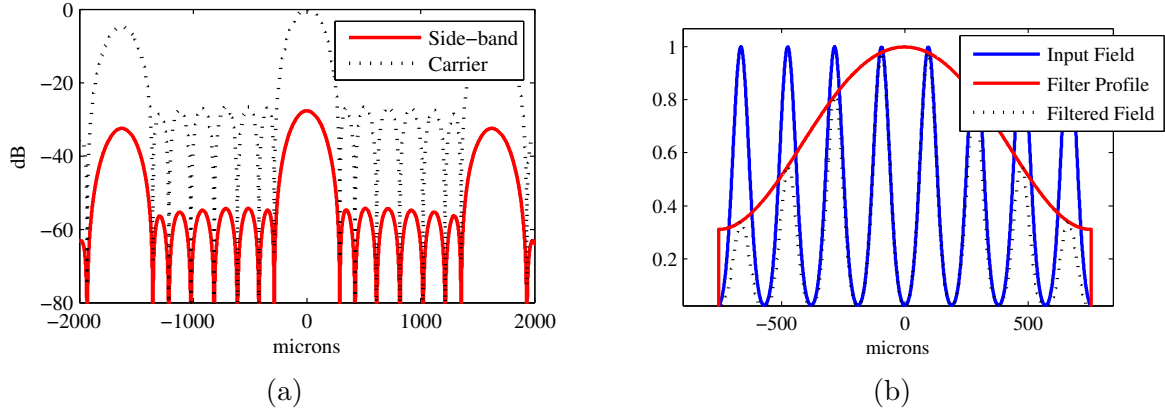


Figure 2.10: Example of Apodization via a transmissive filter in the optical path: a) Fourier plane output showing apodized beam of single bore-sight input (solid, red line) overlaid with un-canceled carrier response (dotted, black line). Note the sidelobe level of the carrier matches that of the -27 dB Taylor weighting applied via the simulated transmissive film over the fiber array. b) Normalized plot of the real-part of the input field showing the filter function and its effect on the elemental Gaussian beam outputs. All optical energy above the red, filter function line is attenuated, lowering the power efficiency of the photonic system.

using commercial fiber couplers was devised as shown in Fig. 2.11. The splitting ratios used are widely available making them easy to procure; however, their limited variability constrains the precision of the apodization profiles that are possible. A total of seven couplers is used in order to split the input laser symmetrically about the center of the modulator array. We wish to approximate the splitting ratio that would be necessary to achieve a -27 dB Taylor with three equal height sidelobes (i.e. $\bar{n} = 3$). The normalized weights applied to the field at each element in order to achieve a perfect 8-sample Taylor window [40] are listed in Table 2.2 along with the weights that can be realized with commercially available fiber couplers as of this writing.

In order to determine the optimal coupling ratio for a given layout a simple tree-like distribution network is assumed. If each 2x2 coupler is treated as an ideal, lossless coupler with a single input, the output can be shown to be of the following

form [28]:

$$\begin{bmatrix} E_{out1} \\ E_{out2} \end{bmatrix} = \begin{bmatrix} \sqrt{1-K} & j\sqrt{K} \\ j\sqrt{K} & \sqrt{1-K} \end{bmatrix} \begin{bmatrix} E_{in} \\ 0 \end{bmatrix}, \quad (2.70)$$

where K is the power coupling ratio. Using the relation in (2.70), a system of equations was created in order to solve for the optimal coupling ratios required to achieve an 8-element Taylor weighting. The equations were set up assuming a splitting layout like that within Fig. 2.11, where one branch from each coupler is further split and the other is split via a 50/50 coupler and fed to a symmetric set of elements. There are three unique branches in the formation, while the others are all assumed to be ideal 50/50 couplers. Assuming the objective is to match the ratios given in the second row of Table 2.2 we can solve for the final input to output coupling ratios for each termination point of the distribution network as labeled in Fig. 2.11 as:

$$\begin{aligned} A_{1,2} &= \frac{1}{\sqrt{2}} \cdot \sqrt{K_1} \cdot A_{in}, \\ A_{3,4} &= \frac{1}{\sqrt{2}} \cdot \sqrt{K_2} \cdot \sqrt{1-K_1} \cdot A_{in}, \\ A_{5,6} &= \frac{1}{\sqrt{2}} \cdot \sqrt{K_3} \cdot \sqrt{1-K_1} \cdot \sqrt{1-K_2} \cdot A_{in}, \\ A_{7,8} &= \frac{1}{\sqrt{2}} \cdot \sqrt{1-K_3} \cdot \sqrt{1-K_2} \cdot \sqrt{1-K_1} \cdot A_{in}, \end{aligned} \quad (2.71)$$

where A_{in} is assumed to be the initial input amplitude from the master laser. Taking the relations in (2.71) and equating their ratios to the normalized weights listed in the second row of Table 2.2 enables a solution for the optimal coupling ratios. For example, from Table 2.2 and Fig. 2.11:

$$\frac{A_1}{A_3} = 0.834, \quad (2.72)$$

therefore,

$$K_2 = \frac{(0.834^2) \cdot K_1}{(1-K_1)}. \quad (2.73)$$

Solving for the remaining coupling ratios based on the Taylor weight values and back substituting leaves the following:

$$\begin{aligned} K_1 &= 0.468 \approx 0.45, \\ K_2 &= 0.612 \approx 0.60, \\ K_3 &= 0.724 \approx 0.70. \end{aligned} \tag{2.74}$$

The values in (2.74) were then approximated with commercially available couplers, to achieve a close estimate of the desired Taylor weighting scheme. The realized weights are listed along with the desired Taylor response in Table 2.2, a graphical comparison is shown in Fig. 2.12b. The output of the ideal and realized weighting functions for the central beam is shown in Fig. 2.12a. As seen in Fig. 2.12, it may be possible to achieve a weighted distribution of the master laser via commercially available couplers that closely resembles an ideal Taylor weighting function. The close-in sidelobes for the achievable distributed laser weightings are approximately 2 dB higher than the ideal case in simulations.

Table 2.2: Ideal and Realized Weights, for Each Modulator Shown in Fig 2.11

MZM_n	1	2	3	4	5	6	7	8
Taylor Weights	.349	.565	.834	1	1	.834	.555	.349
Realized Weights	.383	.585	.856	1	1	.856	.585	.383

2.3.5.3 Master laser Input Power Comparison

If we wish to ensure that the unweighted elements (i.e. central array elements) are fed with the modulators maximum allowable laser power, we must relate the master laser input power to the modulators maximum allowable input power. We start by relating the master laser amplitude to its input power via:

$$A_{in} = \sqrt{P_{oML}}. \tag{2.75}$$

Inspecting the relations in (2.71), we note that the value for $A_{1,2}$ is the maximum output of the distribution system. We will assume that $A_{1,2}$ must not exceed the

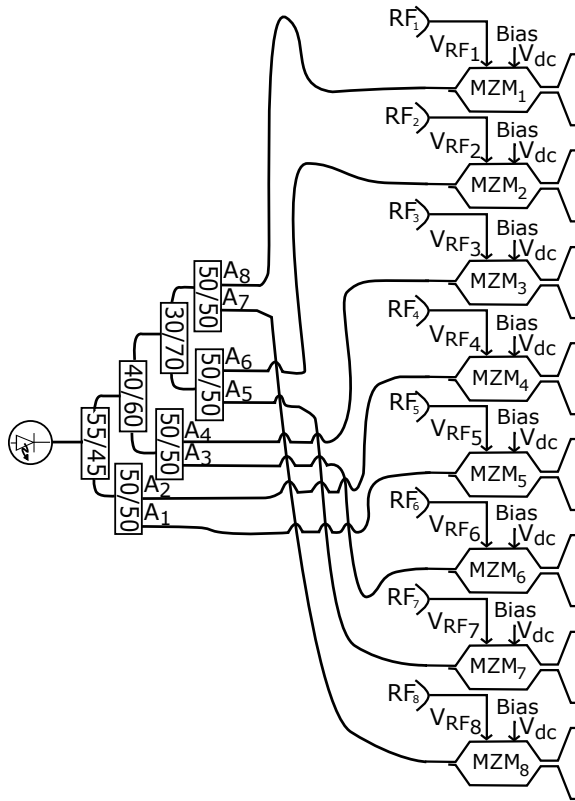
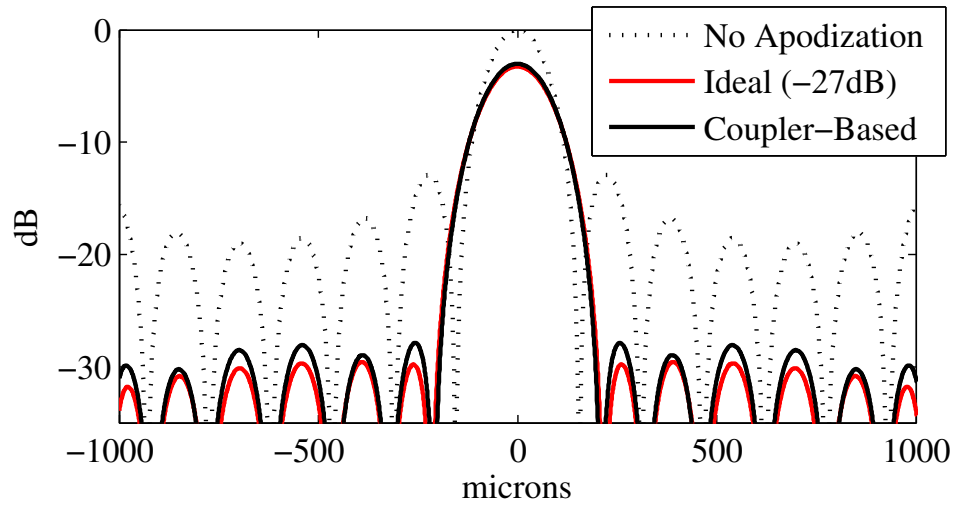
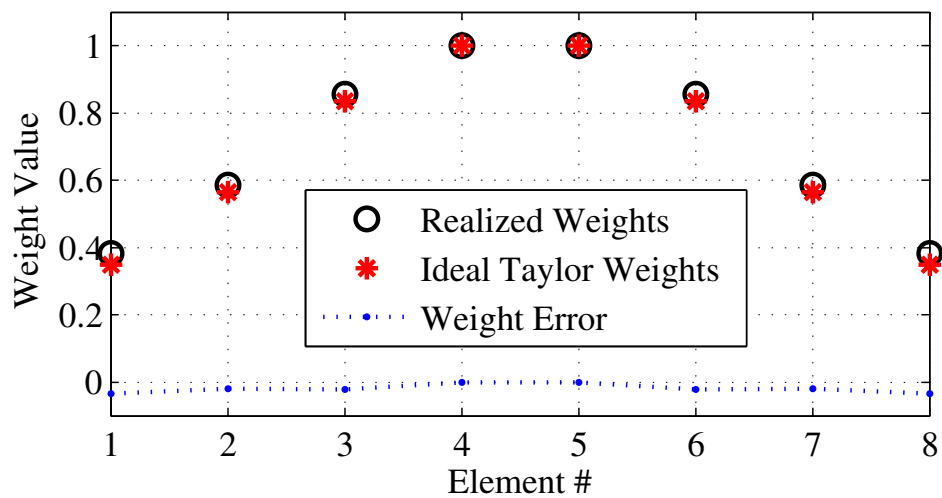


Figure 2.11: A graphical depiction of the fiber coupler layout used for simulation and experimentation using a prototype array. The fiber couplers generate a symmetrical tapering of the input laser amplitude into the Mach-Zehnder Modulators.



(a)



(b)

Figure 2.12: Example of beam apodization of the bore-sight beam via weighted distribution of the master laser: a) Apodized bore-sight beam for the ideal laser weighting (solid red) overlaid with the realized weighting (solid black). Both are compared to the unweighted case (dotted black). Note the ideal case achieves -27 dB sidelobes, while the coupler-based weights yield -25 dB sidelobes with 0.25 dB additional main-lobe gain (barely evident in the plots). b) Comparison of the ideal Taylor (red asterisk) and realized (black circles) weighting functions with the error shown in dotted blue. The slight gain improvement noted in the response plot is intuitive due to the slight decrease in attenuation of the outer elements when using the coupler-based weighting.

maximum allowing input power, $P_{o_{max}}$, for the MZM's used in the array. Substitution of (2.75) into the relation for $A_{1,2}$ and equating to the maximum allowable modulator input power, $P_{o_{max}}$, then provides

$$P_{o_{max}} = \frac{1}{\sqrt{2}} \cdot \sqrt{K_1} \cdot \sqrt{P_{o_{ML}}} . \quad (2.76)$$

Solving for the input power of the master laser leaves us with

$$P_{o_{ML}} = \frac{2 \cdot P_{o_{max}}}{K_1} . \quad (2.77)$$

Finally, substitution of our approximated values for K_1 in (2.74) leaves us with a final relationship between the maximum allowable input power into the modulators and the required input power of the master laser as

$$P_{o_{ML}} = \frac{2 \cdot P_{o_{max}}}{0.45} \approx 4.44 \cdot P_{o_{max}} . \quad (2.78)$$

In comparison to an un-weighted array where we can assume each modulator is driven with a power that is close to $P_{o_{max}}$, the weighted system requires approximately 0.55 of the input power.

$$P_{o_{ML,weighted}} \approx 0.55 \cdot P_{o_{ML,un-weighted}} . \quad (2.79)$$

From (2.79) we can see that the formation of apodized beams via a weighted distribution of the master laser saves approximately 45% in laser power over apodization in the optical domain where excess input power is eliminated via a transmissive filter.

We have shown via simulation that tapering the output beams of the photonic beam-space processor is possible via a weighted distribution of the master feed laser to each modulator. We have also presented a method using commercially available parts to approximate an ideal taper function. As mentioned previously, it is desired to recover the signals within a given beam at it's focused point on the Fourier Plane. This is possible via the introduction of a photo-detector at the precise locations given by the relation in (2.69) for a given optical setup. It is impractical to sample the optical side-band directly at terahertz frequencies in order to recover the lower-frequency RF signal of interest, though significant work in photo-detectors with extremely wide detection

bandwidths exists [41]). For these reasons, we choose to introduce an optical Local Oscillator Signal into the beam-forming processor which allows us to down-convert the optical signals to any arbitrary intermediate frequency for recovery and processing.

2.3.6 Beam-Space Down-Conversion and Signal Recovery

One advantage of sampling a continuous beam-space that is generated via an analog optical processor is that a single LO signal can be used to generate a down-converted beam output for any given sampled beam location. Furthermore, the LO signal can be introduced as part of the fiber-bundle that feeds the photonic array processor. Doing so guarantees that the LO signal will see an identical optical path as each of the array signals, thus remaining fully coherent across the entire useful portion of the focal plane. Care must be taken when designing an optical system that uses photo-detectors as down-converting mixers since it is extremely important that the fields to be mixed arrive at nearly the same incidence angle. Mismatches in angle can cause phase fringes that will reduce the SNR at the detector. Thus, the signals are all introduced at the fiber-bundle in an attempt to mitigate the potential challenges of introduction after the beam-forming lens. The signals arrive at the photo-detector such that a low-frequency beat signal results, the beat frequency must be within the bandwidth of the detector, while the other higher-frequency beat signal should be outside this bandwidth. The concept of detecting beat frequencies between optical signals was introduced in the late 1940's [42] with a large number of experiments following in the literature in an effort to understand the theory of what is now known as optical heterodyning or coherent detection [43–45]. It has been shown [44] that optical heterodyne detection provides a significant conversion gain over direct detection of the optical signal of interest as long as sufficient power is provided to the photo-detector by the LO laser. Furthermore, the LO laser and its spectral performance dominates the noise characteristics of the down-converted signal assuming that a proper LO signal amplitude is chosen so as not to introduce saturation effects [46]. The signal-to-noise ratio out of a PD using coherent heterodyning (when neglecting effects of laser RIN)

may be written in terms of

$$\frac{S}{N} = \frac{\frac{1}{2}i^2 R_{eq}}{2qI_o B \tilde{R}_{eq} + 2qI'_o B \tilde{R}_{eq} + kT_{eq} B}, \quad (2.80)$$

where the three terms in the denominator are due to Shot noise, noise due to background light/dark current and thermal noise, respectively with. The output power has been related to the current via a lumped, equivalent resistance that includes factors due to design parameters of a particular photo-detection device [44]. In practice, the value of the equivalent resistance can be measured for a given device, rather than calculated. If the LO power is strong enough such that, $I_o \gg I'_o$, then the LO induced current dominates the dark current and any currents due to back-ground illumination [44]. It is also desired to set the LO power such that the shot noise is dominant over the thermal noise, creating a fundamentally limited link. Thus, with proper selection of the LO signal power, the signal-to-noise ratio for the coherent optical detector reaches an ideal maximum of

$$\frac{S}{N} = \frac{\beta_o \eta P_s}{h\nu B} = \frac{\beta_o \mathfrak{R} P_s}{Bq}, \quad (2.81)$$

where, β_o is related to the angular overlap of the optical beams, h is Planck's constant of $\approx 6.6 \times 10^{-34} [\frac{m^2 \cdot kg}{s}]$, \mathfrak{R} is the photo-detector Responsivity in amps per watt, P_s is power of the received signal, B is the photo-detector's effective bandwidth and q is the electron charge constant of $\approx 1.6 \times 10^{-19} [Coulombs]$. In the experimental photonic array processor, the optical LO signal is derived from the master laser that feeds each of the electro-optical up-conversion stages behind each element of the RF array. The tapped master laser signal is modulated by a null-biased external modulator that is fed by a tunable RF source as shown in Fig. 2.13. The output of the modulator produces a set of sidebands that are used to injection lock a second, thermally tuned, LO laser to the desired LO frequency. This injection locked signal is then fed into the photonic beam-space beam-forming system so that the, now coherent, LO signal over-lays the beam-space precisely, mitigating losses due to mis-match in incidence angle. This modulation-sideband-injection locking, pioneered at the University of Delaware, has been shown to produce coherent LO signals across several octaves of bandwidth [47],

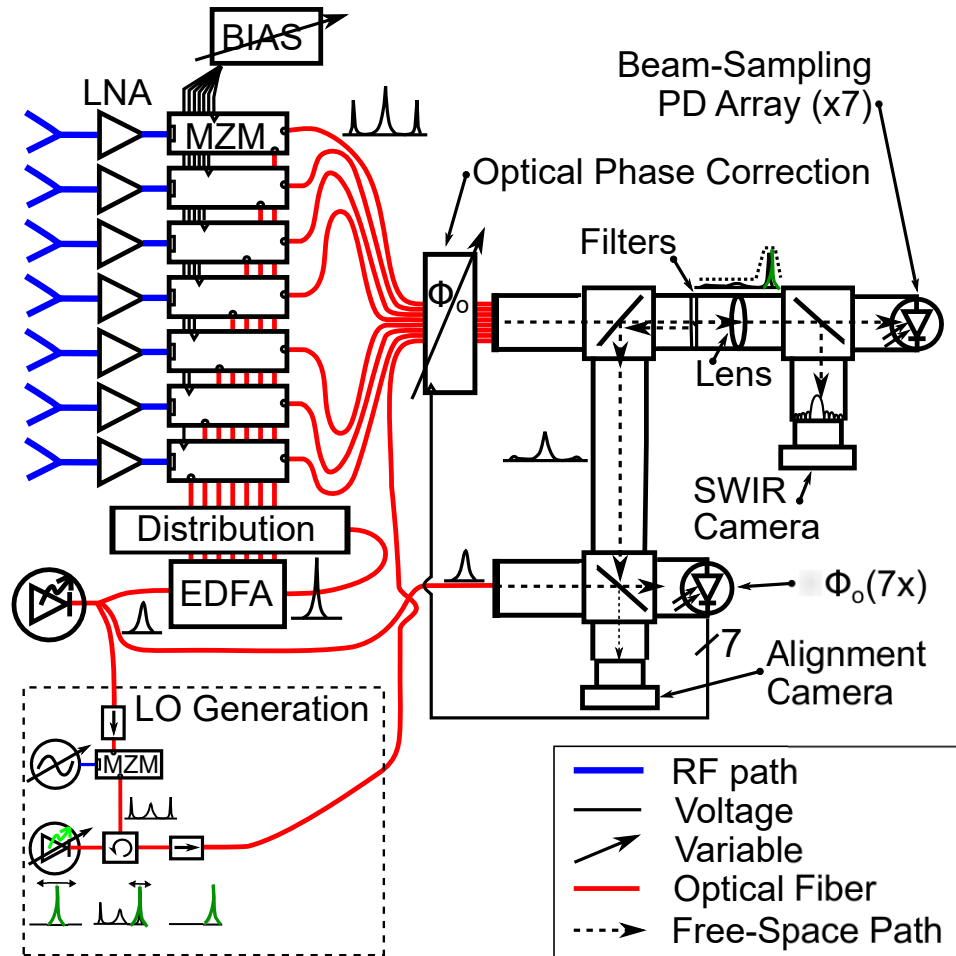


Figure 2.13: Schematic of the Beam-space Array processor with integral optical down-conversion.

allowing the photonic array processor to down-convert signals across its entire accessible bandwidth to any chosen intermediate frequency (IF).

At any given beam-location in the output plane of the photonic array processor we will have the superposition of the up-converted RF signal fields with that of the LO laser. For a single incident RF field we would have a superposed field at the photo-detector array of the following form:

$$E_{PD} = A_{LO} \cdot e^{j\omega_{LO}t} + A_s \cdot e^{j\omega_s t}, \quad (2.82)$$

with

$$\omega_{LO} = \omega_o + \omega_{RF} + \omega_{IF} \quad (2.83)$$

and

$$\omega_s = \omega_o + \omega_{RF}, \quad (2.84)$$

where ω_o is the radian frequency of the optical carrier, ω_{RF} is the radian Radio frequency and ω_{IF} is the desired output intermediate frequency. We can then define the intensity of the combined field at the photo-detector as

$$\begin{aligned} I_{PD} &= \frac{E_{PD}E_{PD}^*}{Z_o} \\ &= \frac{1}{Z_o} [(A_{LO} \cdot e^{j\omega_{LO}t} + A_s \cdot e^{j\omega_s t}) (A_{LO} \cdot e^{-j\omega_{LO}t} + A_s \cdot e^{-j\omega_s t})], \end{aligned} \quad (2.85)$$

where the * indicates the complex conjugate and Z_o is the characteristic impedance.

Simplification of the relation in (2.85) yields

$$\begin{aligned} I_{PD} &= \frac{1}{Z_o} [(A_{LO} \cdot e^{j\omega_{LO}t} + A_s \cdot e^{j\omega_s t}) (A_{LO} \cdot e^{-j\omega_{LO}t} + A_s \cdot e^{-j\omega_s t})] \\ &= \frac{1}{Z_o} [A_{LO}^2 \cdot e^{j(\omega_{LO}-\omega_{LO})t} + A_{LO}A_s \cdot e^{j(\omega_{LO}-\omega_s)t} + \dots \\ &\quad A_{LO}A_s \cdot e^{-j(\omega_{LO}-\omega_s)t} + A_s^2 \cdot e^{-j(\omega_s-\omega_s)t}] \\ &= \frac{1}{Z_o} [A_{LO}^2 + A_s^2 + A_{LO}A_s (e^{j(\omega_{LO}-\omega_s)t} + e^{-j(\omega_{LO}-\omega_s)t})] \\ &= \frac{1}{Z_o} \cdot [A_{LO}^2 + A_s^2 + 2A_{LO}A_s \cos [(\omega_{LO} - \omega_s) t]]. \end{aligned} \quad (2.86)$$

We can then write the output photo-current as

$$\begin{aligned} i_{PD} &= \Re I_{PD} \\ &= \Re \left[P_{LO} + P_s + 2\sqrt{P_{LO}P_s} \cos(\omega_{LO} - \omega_s) t \right], \end{aligned} \quad (2.87)$$

where P_{LO} and P_s are the incident optical powers of the LO and sideband signals respectively. Inspecting the result in (2.87), we have a DC term, i_{dc} and a signal term, i_s ,

$$i_{dc} = \Re \cdot (P_{LO} + P_s), \quad (2.88)$$

and

$$i_s = 2\Re \sqrt{P_{LO}P_s} \cos[(\omega_{LO} - \omega_s) t]. \quad (2.89)$$

When $P_{LO} \gg P_s$, as should be the case when maximizing output SNR, the DC photo-current reduces to

$$i_{dc} = \Re \cdot P_{LO}. \quad (2.90)$$

Finally, substitution of the definitions in (2.83 - 2.84) provides us with the output signal current at the IF as

$$\begin{aligned} i_{s,IF} &= 2\Re \sqrt{P_{LO}P_s} \cos[(\omega_o + \omega_{RF} + \omega_{IF} - \omega_o - \omega_{RF}) t] \\ &= 2 \cdot \Re \cdot \sqrt{P_{LO}P_s} \cos(\omega_{IF} t). \end{aligned} \quad (2.91)$$

From the result in (2.91) we can see that it is possible to down-convert the RF signal within the fundamental optical sideband to any desired IF via introduction of a coherent laser LO signal that is offset from the sideband by the desired IF. Hence, the center of the IF band can be precisely selected by generation of the coherent LO via the technique described in [47]. We note that for wide-band inputs, a single LO stage like that described makes it is possible for more than one RF signal to alias into the IF band of interest. Therefore, some care must be taken to ensure that only the signal of interest is down-converted. During experimentation, this is done via the use of a narrow-band array at the input. Thus, assuming proper frequency planning, the desired IF signal for any given beam-location can be conditioned and sampled at the output of the beam-sampling PD array.

In this chapter, it has been shown that the proposed methods of array remoting, photonic beam-forming and beam-space sampling can allow for the sampling and down-conversion of an arbitrary beam-space. The beam-space that is generated is continuous across the full-field-of-view of an input RF antenna array. The importance of using a critically sampled RF antenna was discussed and a method to determine precise optical sampling locations in the output plane of the optical processor was derived. Thus, any arbitrary angular region in the field of view of an input antenna can be collected using a precisely positioned, high-speed photo-detector. For applications that require low-sidelobes for reduced spatial interference at the sampled beam-location, a method to apodize the output beam-space was presented. Finally, the entire beam-space can be simultaneously down-converted via the introduction of a single, coherent Local Oscillator signal. This technique mitigates the need for complex LO distribution across large arrays as one might need for a traditionally digitized beam-space array or an elemental digital array and allows for a full-dimension orthogonal beam-space to be down-converted upon sampling. The next chapter discusses an experimental photonic system that allows for the visualization of the incident spatial frequency spectrum while simultaneously providing a set of down-converted, orthogonal beam outputs that can be used for digital processing of multiple signal types.

Chapter 3

MULTI-FUNCTIONAL PROCESSING OF PHOTONICALLY GENERATED BEAM-SPACES

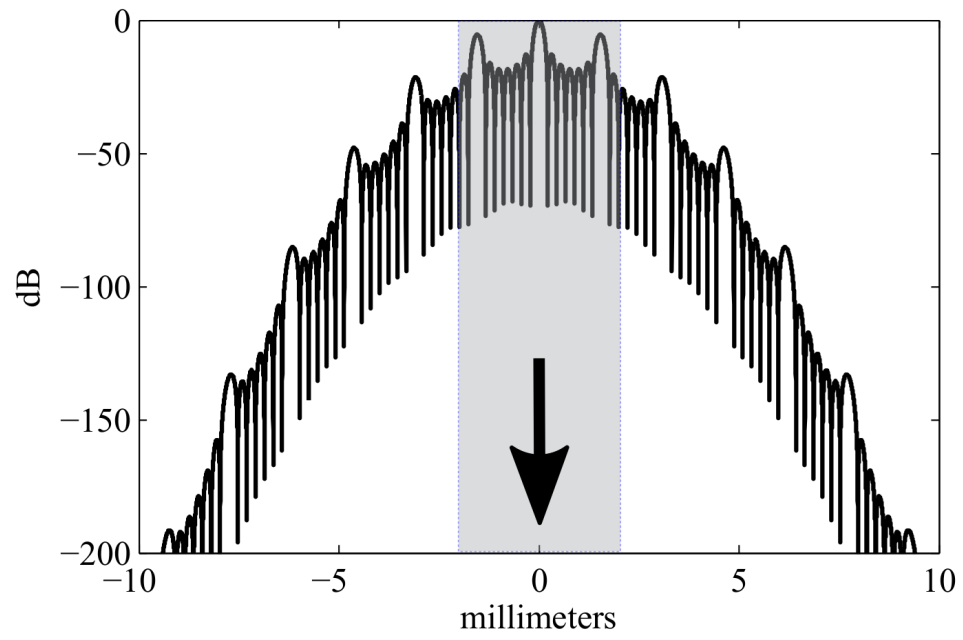
As discussed in Chapter 2, the output of the proposed photonic array processor is a continuous spatial frequency spectrum. This spectrum is generated via analog means, and is therefore processed in real-time, regardless of the input array size. It is desirable to utilize the output for multiple simultaneous functions, also in real-time (or as close to real-time as modern processing will allow). Thus, there are two distinct methods to capture and process the spectral output, one is via traditional, camera-type devices, while the other is via high-speed photo-detectors, perhaps using coherent detection as discussed in the previous chapter. Both methods have significant merit, particularly if used in tandem.

3.1 Imaging of the Continuous Spatial Frequency Spectrum

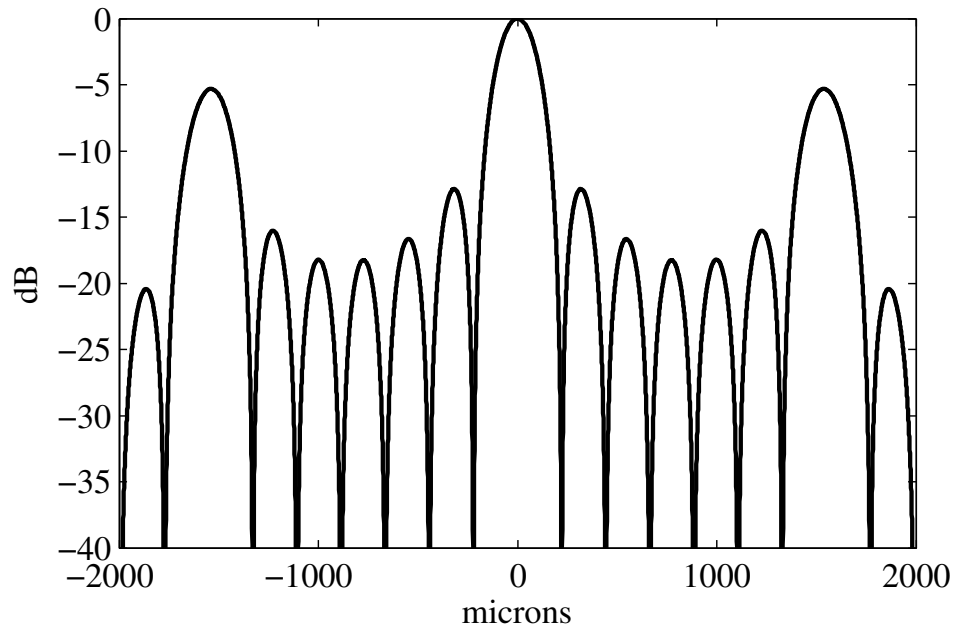
When the photonic array processor is utilized without a down-converting LO signal, as shown in Fig. 2.5, detection of the output plane irradiance (also called the intensity) would allow for visualization of the spatial spectrum. A commercial camera is too slow to follow the oscillations of the optical signal directly, but instead responds to the time-averaged intensity. The camera must be matched to the wavelength of the sidebands of interest and have sufficiently fast integration times, such that an image can be generated at video rates. The irradiance of a field is defined as the flux, in watts, per unit area on a given output plane and may be modeled via

$$I_r(v, u) = \frac{1}{2\eta_0} E_{t_1}(v, u) E_{t_1}^*(v, u) = \frac{1}{2\eta_0} |E_{t_1}(v, u)|^2, \quad (3.1)$$

where $E_{t_1}(v, u)$ is the output plane electric field given in (2.64) at a given time instant, $t = t_1$, and η_0 , the characteristic impedance of the medium. For the purposes of imaging



(a)



(b)

Figure 3.1: Simulated irradiance of the field at the output of the photonic array processor with, (a), full plane, and, (b), zoomed portion of plane, covered by gray box in (a), that is practical to image with a commercial detector array or camera.

the the spatial spectrum of a set of incident RF fields, only the relative form of the irradiance is necessary allowing multiplier, $\frac{1}{2\eta_0}$, in (3.1) to be ignored. With that, some simulated outputs for a single, bore-sight, plane wave are shown in Fig. 3.1. The result in Fig. 3.1a shows the grating lobe structure due to the spacing of the fiber array. This result is in agreement with the cartoon example shown in Fig. 2.9. The roll-off is due to the Gaussian beam shape at the output of the system. In practice, it is only useful to image, or sample, a portion of the region between two opposing optical grating-lobes. All desired RF signal angle-of-arrival information is preserved unambiguously in between the optical grating lobe region, as shown in Fig. 3.2, where two opposing signals are simulated as incident at $\pm 90^\circ$. In many cases, the RF array's field-of-view

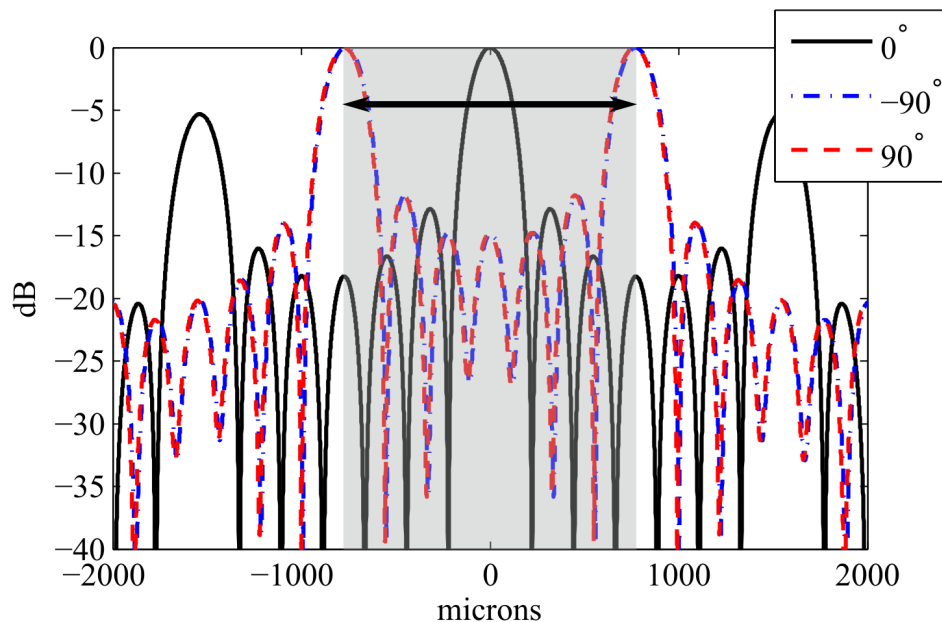


Figure 3.2: Simulated output irradiance patterns for a bore-sight signal overlaid with signals from $\pm 90^\circ$, showing that even though there are optical grating lobes, they do not interfere with recovery of signals from a critically sampled RF array at the input. The region unambiguous measurement of input RF signal angle is shown by the gray overlay.

will be limited to less than the region over $[-90^\circ, 90^\circ]$, often by the element pattern, as discussed in Section 1.1.1.2. We also show an example of opposing signals at $\pm 45^\circ$ in Fig. 3.3. In the case simulated here, we have assumed a reasonable optical setup with

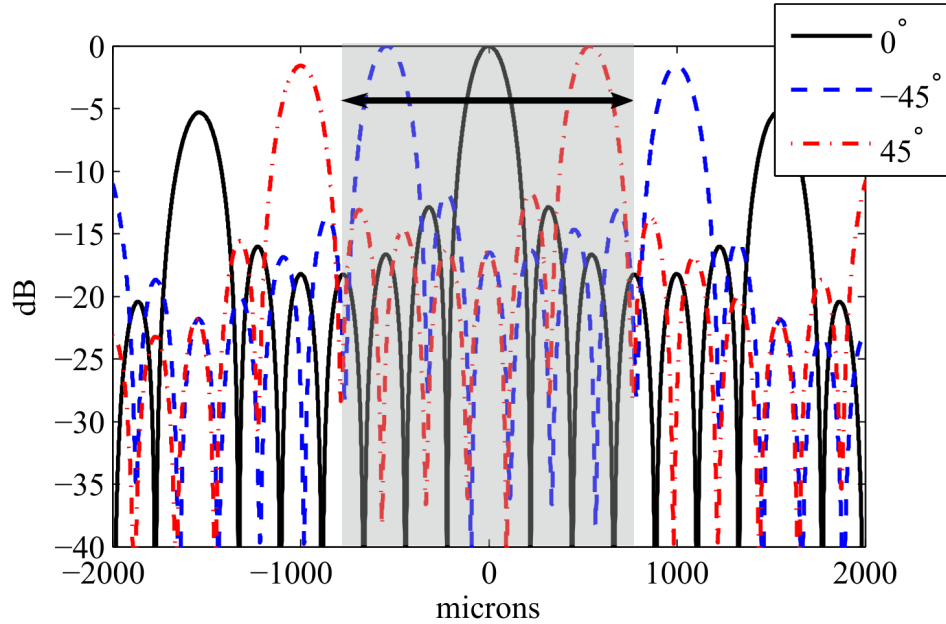


Figure 3.3: Simulated output irradiance patterns for a bore-sight signal overlaid with signals from $\pm 45^\circ$. The region unambiguous measurement of input RF signal angle is shown by the gray overlay.

a lens focal length of 20cm , a lens diameter of 2cm , an optical wavelength of 1550nm (in the Short-Wave Infrared Detector Range), an optical fiber spacing of $200\mu\text{m}$ and an elemental beam-waist of $50\mu\text{m}$. Therefore, for the simulation parameters used here, one can visualize the entire field of view of any critically sampled (i.e. $d_{ant} = \frac{\lambda_{RF}}{2}$) RF array with an image sensor less than 2 millimeters in diameter.

3.1.1 Beam-Squint of Wide-band Signals

The Fourier operation that is performed on the input signal field is not wide-band in a true-time delay sense. The lens is effectively imparting an angular dependent phase offset to the incident fields, thus the angular translation is subject to dispersive effects. These effects manifest themselves as a frequency dependent steering of the output beams, known as beam squint/dispersion. This phenomena is evident in traditional phased arrays that do not use true-time-delay in their beam-steering systems. An example output of a set of signals incident from identical angles, but at frequency offsets of 1 GHz relative to one another is shown in Fig. 3.4. It is interesting to note

that the apparent “beam-width” of the output field irradiance patterns is determined solely by the optical fiber array size and the side-band frequencies, while the angle is determined by the relative RF phases across the fiber array elements. While a 6 GHz span is quite large for a typical RF array, it is orders of magnitude smaller in percent bandwidth at the up-converted frequencies, thereby generating a set of “beams” that do not appear to broaden significantly with frequency when viewed in the output optical plane.

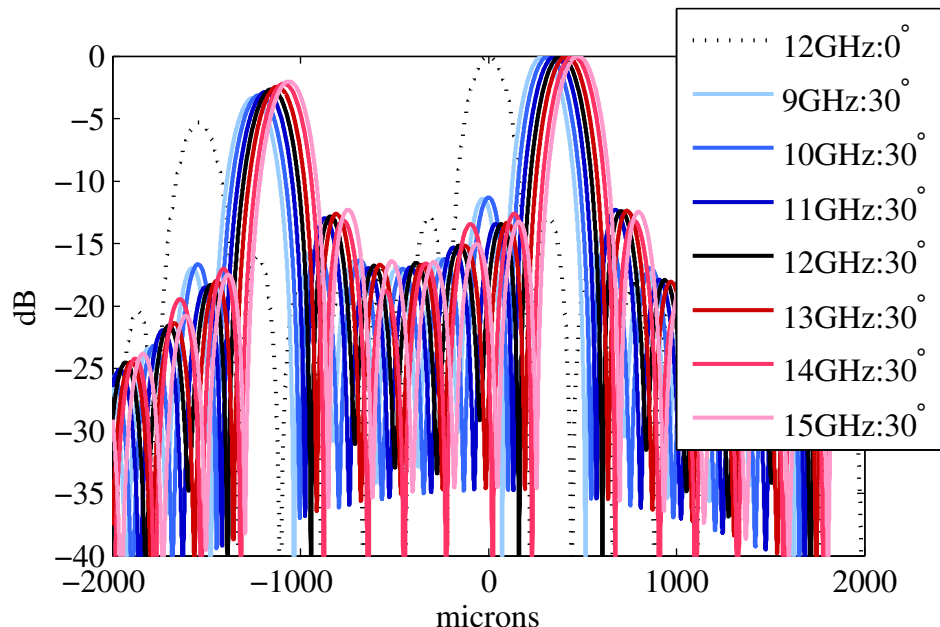


Figure 3.4: Simulated output irradiance patterns for a set of 30° offset signals of various frequencies. The typical beam-broadening effects are not seen due to the fact that the output irradiance “beams” are dependent only on the optical array size and corresponding side-band frequencies, which have extremely small differences in terms of percentage bandwidth across the RF signal span shown.

3.1.2 Analog Re-Steering of the Output Beam-Space

If we apply a frequency-dependent steering vector to the elements prior to the photonic array processor, we can re-steer the entire beam-space. The necessary phase offset across the RF elements has the following form:

$$\Delta\phi_{RF} = \frac{2\pi}{\lambda_{str}} n d_{ant} \sin(\theta_d), \quad (3.2)$$

where λ_{str} is the wavelength of signal that we wish to steer toward in the direction, θ_d , and is presumed different from the design wavelength of the antenna. Applying this phase offset in either the RF domain, prior to up-conversion, or in the optical domain, prior to the lens-let array, will re-steer the beam-space such that a signal incoming from the angle, θ_d , will be output at the center of the focal plane. In this way, a beam-fan of a particular size may be sampled via a set of specialized photo-detectors, potentially embedded within a traditional camera focal plane array, a so called ‘‘Foveal’’ detector array. While creation of such a device is not the focus of this work, it is perhaps an interesting system-level approach to applying the photonic array processing scheme discussed here. Nonetheless, for the existing experimental system, application of a steering vector that is keyed to a particular frequency and angle of signal can be used to steer a beam-fan, as shown in Fig. 3.5.

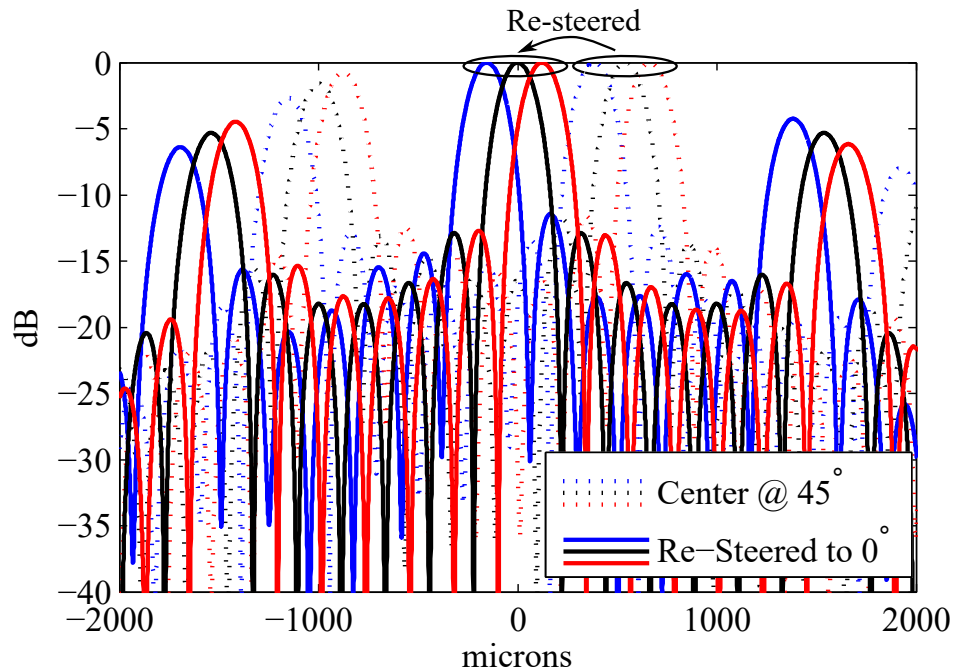


Figure 3.5: Simulated output irradiance patterns for a set of 3 offset signals, or beam-positions. The beam-fan is then shown in a re-steered configuration which has centered the outputs at the origin of the focal plane. This technique would be especially useful for implementing reduced-dimension beam-space systems.

It is also possible to apply a steering vector, such that a particular frequency of

interest can be centered on the array. In certain cases this may mitigate ambiguities in angle-of-arrival of two signals with widely offset frequencies; however, any technique to determine frequency, without a-priori knowledge, would require a structured search that would undoubtedly require signals that were persistent in angle for the duration of the search routine. Therefore, without the use of known-angle, pilot-tone types of signals, it is unlikely that a frequency-dependent phase steering technique would be practical in determining true frequency of multiple arriving signals in a real-time operation. Nonetheless, in situations where the frequencies of likely signals are known, as in communications or RF sensing applications, frequency-dependent phase shifting in the RF domain can compensate for dispersive effects. An example is shown in Fig. 3.6.

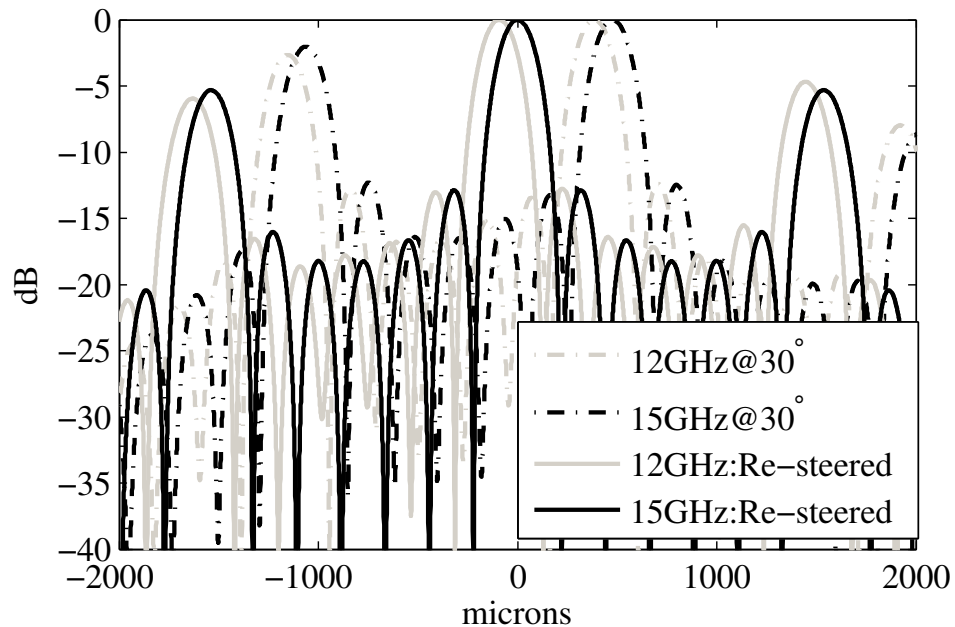


Figure 3.6: Simulated output irradiance patterns for a signal at 15GHz incident on an array at 30 degrees. The Array is designed for a 12GHz center frequency, which causes the 15GHz signal to appear at an angle of approximately 38.5 degrees. The pattern for a 12GHz signal at 30 degrees is shown as a light gray dash-dotted line. Application of a steering vector such that $\lambda_{str} = \frac{c}{15GHz}$ and $\theta_d = 30^\circ$ results in the 15GHz signal being centered on the focal-plane, even though it originally appeared at 38.5°. We note that a 12GHz signal incident at θ_d is now pushed off-center as shown by the solid light gray line.

3.2 Digitization of a Down-converted Beam-space

When performing a simple imaging operation on the spatial spectrum of the environment given an input RF array that is collecting signals, a simple camera can be used to capture and digitize the entire intensity map of the spatial spectrum. In this manner, all digitization is performed via the analog to digital read-out circuits on the camera itself. However, when it is desired to capture and digitize a set of beam-positions such that the signal phase can also be recovered, a more sophisticated sampling architecture with high-speed photo-detectors and an integral optical LO, like that discussed in Section 2.3.6, is required.

From Section 2.3.6, the output signal from a coherent, heterodyned, photo-detector will be an analog signal centered at the desired IF. Methods for determining the placement of such photo-detectors were described via the relations in Section 2.3.4. Thus, for a given set of detectors placed at the focal plane of the optical array processing chain, we wish to digitize the outputs such that both In-phase and Quadrature (I/Q) signal components can be recovered.

Recovery of I/Q signal samples is vital for the processing of nearly all modern communications signals. Most signals rely on the transmission of two-orthogonal carriers that are used to generate a constellation of points within the complex plane. Thus, failure to recover one of the orthogonal carriers (namely the I or Q signal) would prevent reconstruction of the signal constellation entirely. Similarly, for radar processing, both I and Q inputs are required in order to determine the velocity of an object. Failure to have both components would only allow for the direct recovery of the speed, or absolute value of the velocity. Typically, it is desirable to determine whether a target signal is encroaching or receding upon detection.

Traditional coherent receivers perform I/Q signal demodulation via a matched set of receiver paths, each fed via the same LO, but with one LO signal being out of phase with the other by 90° . Doing so allows for digitization of matched sinusoidal and co-sinusoidal signals at an intermediate or even baseband frequency. The two digitized

signals are then summed to form a single complex signal record as $x_s = I + jQ$. Down-converting a signal using a set of signal paths that are at quadrature requires a great amount of calibration. The amplitude and phase of both the In-phase and Quadrature signal paths must be matched precisely. To avoid the additional complications of a quadrature demodulation design, multiple methods for sampling a band-limited signal in order to recover the complex In-phase and Quadrature components without the need for an analog I/Q receiver structure have been analyzed since the early 1980's [48–51]. All, so-called “Digital I/Q,” techniques take advantage of the sampling theorem in an effort to ensure that the band-limited signal of interest is converted to an IF that can be sufficiently oversampled. The oversampling enables digital filtering and decimation procedures to bring the real-sampled bandpass signal down to a complex baseband representation where it can be filtered without aliasing. Thus, in order to avoid the complexities of analog I/Q demodulation, one must design the digital demodulation receiver with an analog-to-digital converter (ADC) that is up to 4 times faster than its in an analog quadrature demodulation receiver design.

For the system concept presented herein, we utilize a set of 14-bit ADCs with a sampling rate of 250 Msps. Due to the desire to maximize the recoverable RF bandwidth, a digital demodulation technique similar to [52] was chosen. The technique in [52] allows for an RF bandwidth of $\beta = 0.4 \cdot f_{samp}$ to be recovered without aliasing and was initially proposed for digitization of wide-band Synthetic Aperture Radar data. The implementation is quite simple and requires that the band-limited signal be down-converted to an IF that is $0.625 \cdot \beta$ and then sampled at a rate that is $2.5 \cdot \beta$. A scale, pictorial representation of the technique is shown in Fig. 3.7. For the photonic array processor experiments discussed in later sections, $f_{samp} = 250$ MHz and $\beta = 100$ MHz, thus requiring an IF of 62.5 MHz. The sampled signal is then multiplied by a complex modulation of $e^{\frac{j\pi n}{2}} = j^n$ to shift the signal to base-band. The baseband spectrum now encompasses the normalized frequency band of $(-0.4\pi, +0.4\pi)$. In order to reject any unwanted signals a low-pass filter is applied to the baseband data, followed by a decimation by 2. Since filtering essentially eliminates any signals outside

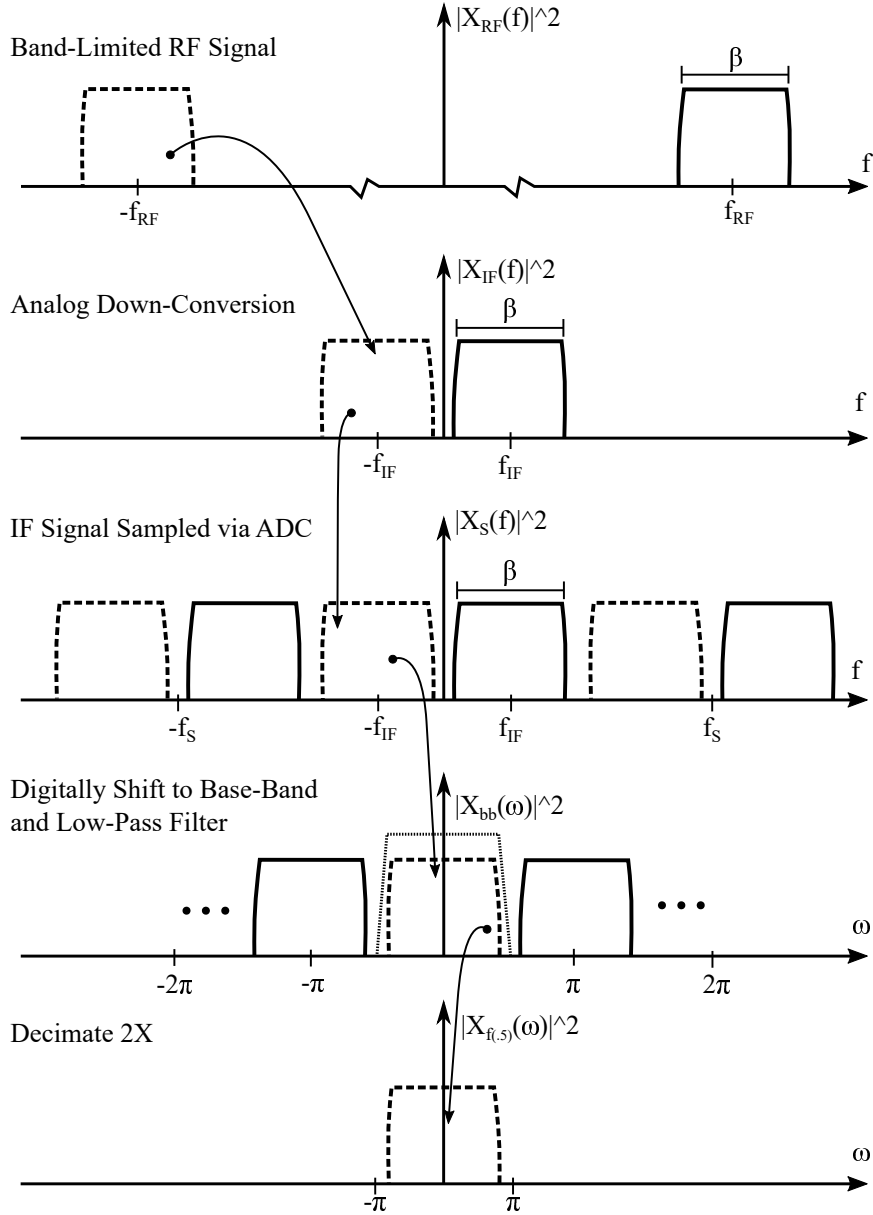


Figure 3.7: Digital I/Q demodulation of a band-limited, real-sampled signal captured at the output of the array processor. The technique begins with an analog down-conversion stage to bring the RF signal to a lower IF. For the photonic system, analog down-conversion is performed via an optical LO at the focal plane of the array processor. The signal at the output of each photo-detector is sampled via an ADC. The sampling rate of the ADC must be at least 2.5β . Oversampling ensures mitigation of aliasing effects upon digitization and translation to base-band. The digitized IF signal is multiplied by a complex phasor to translate one of the side-bands to baseband and create complex data samples. The digital baseband signal is filtered via an FIR filter and decimated by two leaving a final complex signal sampled at 1.25β .

of the band of interest the effective sampling rate can be reduced to that needed only to represent the final output spectrum. Thus, the decimation operation reduces the sampling rate by half, leaving the digital I and Q signals sampled at a final rate of $1.25 \cdot \beta$ where they are ready for further digital processing. The slight over-sampling of the final signal is not seen as detrimental to further processing, in fact, it concedes some headroom for any further filtering operations. This technique was chosen due to its simplistic implementation within digital hardware. For example, the filtering and decimation can be performed together within a field-programmable gate array (FPGA) using commercially available development tools. The final output I/Q samples are then ready to be processed for any application with signals within the down-converted bandwidth of β (e.g. Radar and/or communications waveforms).

Thus, we can consider the output of a single photo-detector to be that of a single beam-space data vector, more specifically a single row of $\mathbf{x}_{bs}(t)$, as defined in (1.28). For a single time-instant, \mathbf{x}_{bs} is an M by 1 vector, however, for a given time interval, $[t_0, T_s]$, each row in the beam-space data matrix contains a continuous-time signal. These signals are sent to an ADC for digitization where we obtain a sampled beam-space data matrix, \mathbf{X}_{bs} , such that

$$\mathbf{X}_{bs} = [\mathbf{x}_{bs}[t_0]; \mathbf{x}_{bs}[t_0 + \Delta t]; \cdots \mathbf{x}_{bs}[T_s]], \quad (3.3)$$

where T_s is a total sampling interval that depends on application and

$$\Delta t = \frac{1}{f_s}, \quad (3.4)$$

and f_s is the sampling frequency of the ADC used for digitization. Therefore, after sampling we have a matrix of sampled data values for each channel. Each ADC channel is digitizing signals that are contained within a single beam-position, creating a bit-stream for each beam that is sampled at the focal plane. If multiple sample periods, P , are taken for a total time span of PT_s , the output matrix takes the form of a 3-dimensional cube. This method of sampling is common in pulsed systems like Radar and the sampled data matrix is often referred to as a data cube.

Taking a single beam output as an example, Fig. 3.8 shows the sampled waveform and its spectrum. Since the samples are real-valued, the aforementioned Digital

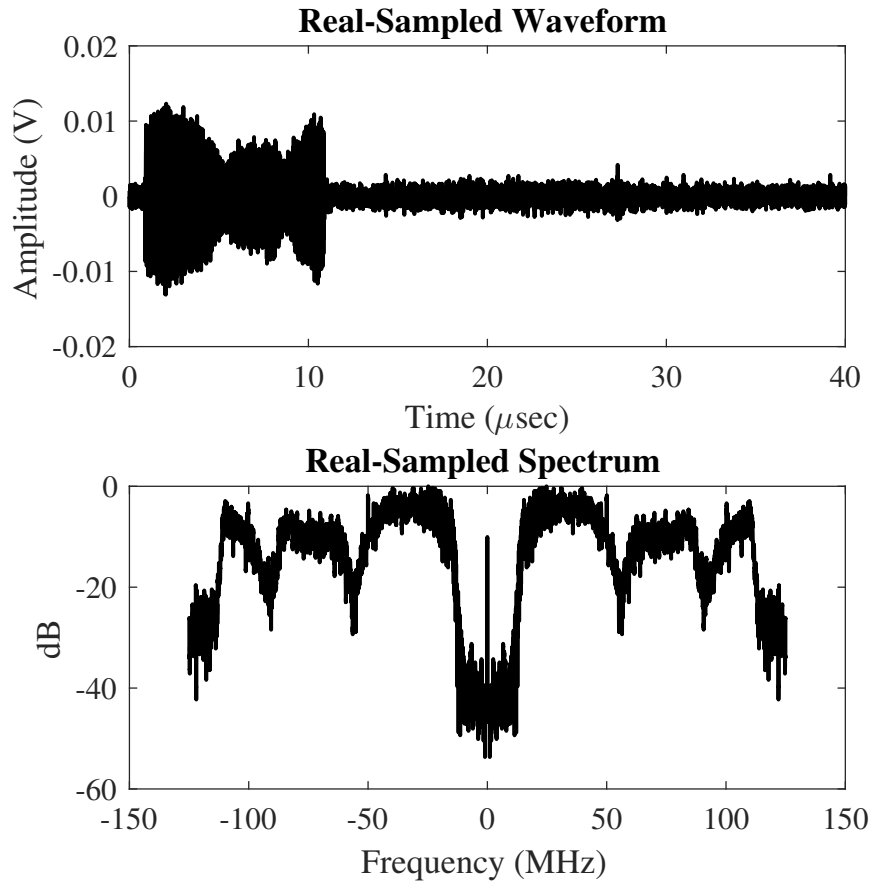


Figure 3.8: Example of a sampled output from a single photo-detector after optical down-conversion. The signal waveform contains a set of 3 echo pulses from a test target generator.

I/Q demodulation technique is performed on every channel to produce a complex base-band result as shown in Fig. 3.9. The base-band waveform shown in Fig. 3.9 now has complex components due to the complex digital base-band translation operation. We also see how the lower-frequency spectral component has been translated to be centered at DC in the spectrum plot shown in Fig. 3.9. We still require application of a low-pass filter to remove the unwanted, redundant spectral content at the edges of the sampled spectral band. We will also, likely be able to remove the LO leakage signal seen as a large spur at 62.5 MHz in Fig. 3.9 and at DC in Fig. 3.8. For the

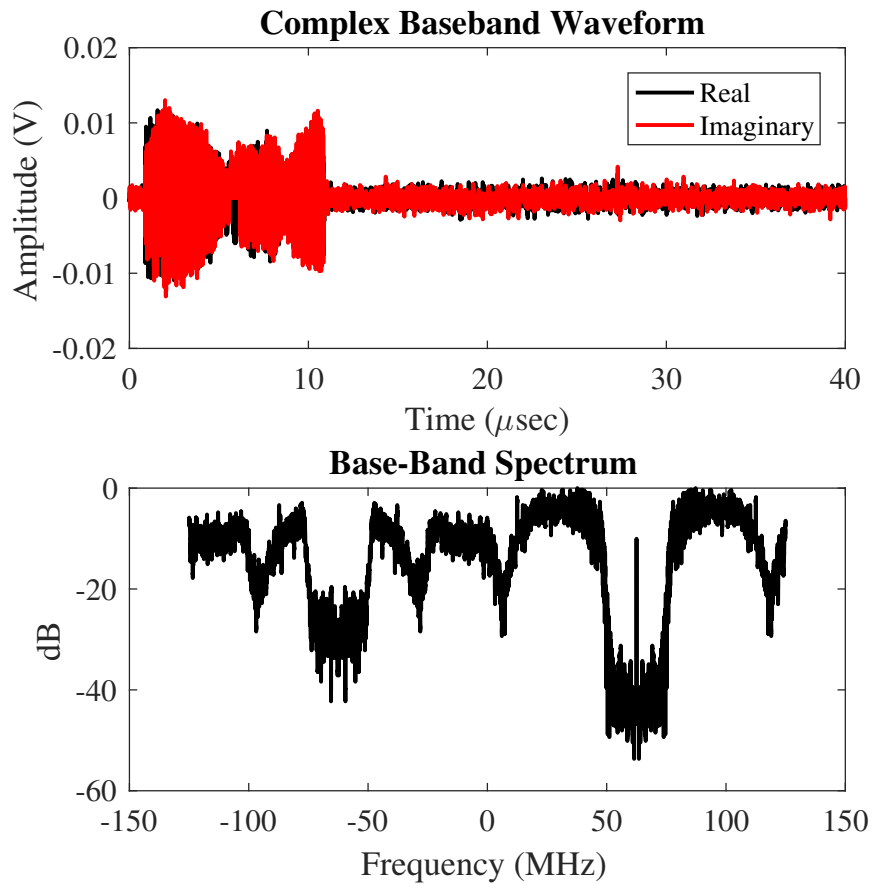


Figure 3.9: Example base-band translated output from a single photo-detector after optical down-conversion. The signal waveform contains a set of 3 echo pulses from a test target generator. The base band translated signal now contains a complex spectrum.

filtering operation a finite-impulse-response (FIR) filter was designed using the Parks and McClellan algorithm [53], a widely used technique for optimum digital filter design. The filter’s response is shown in Fig. 3.10. The filter is applied to the digital

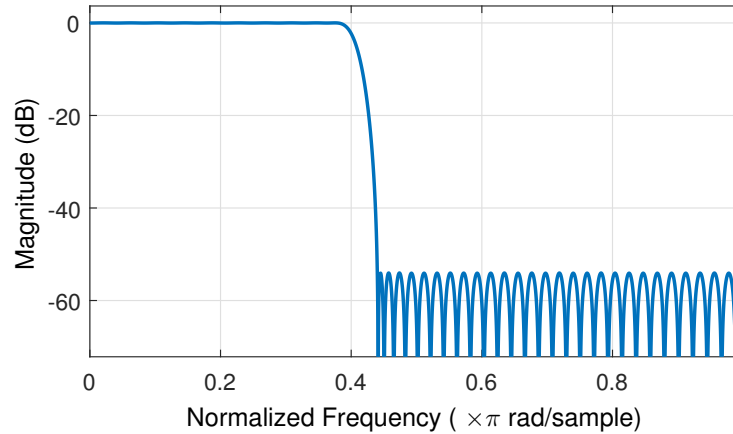


Figure 3.10: Filter Response of the Low-pass filter used for extraction of the base-band spectra of interest during the Digital I/Q generation process. The filter has ≈ 54 dB of rejection in the stop band.

base-band data stream to arrive at the final complex I/Q signal result. If being done in a real-time system the decimation and filtering can be performed in tandem for some computational savings [52]. After the filtering and decimation operations we arrive at the final complex result shown in Fig. 3.11. The result in Fig. 3.11 has isolated the relevant 100 MHz of spectrum. The examples shown have a 100 MHz bandwidth Linear Frequency Modulated (LFM) (i.e. chirp) waveform filling the entire spectrum. The process shown in Fig. 3.8, Fig. 3.9, and Fig. 3.11 is performed on each sampled beam-location at the output of the photonic array processor described in the previous section.

The beam-space imaging, LO generation, and digital beam-space demodulation techniques described have been utilized along with an prototype photonic array processor to collect a number of experimental datasets that will be described in the following Chapters. However, prior to discussing the experimental results, it is helpful to gain an understanding of the types of processing that can be applied to the sampled outputs.

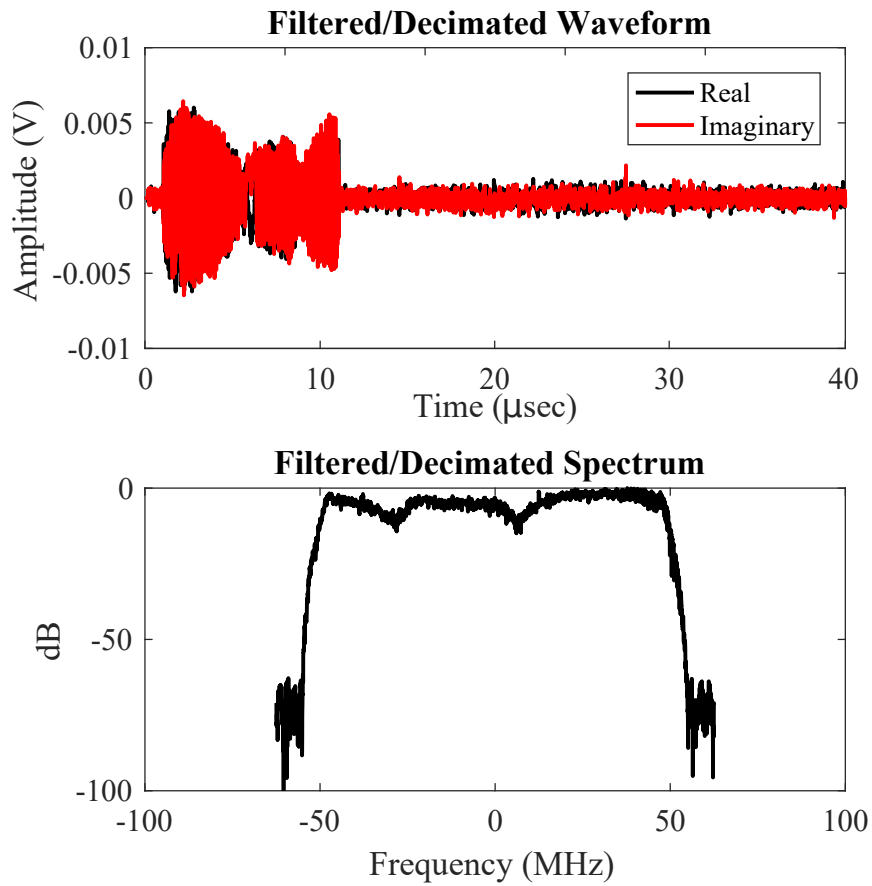


Figure 3.11: Example of the final, filtered and decimated output from a single photo-detector after optical down-conversion. The filtered spectrum appears as a plateau with a shape similar to that of the filter response.

3.3 Processing the Output of a Single Beam

In the most straightforward application of the beam-space generation techniques discussed in the previous sections, each beam can provide spatial coverage of a predefined region of interest and can therefore be processed directly, without consideration of the signals in the other beams. This may be used in a next generation wireless communication system to provide additional spectral re-use. This may be possible by the usage of “beams” rather than “cells”, with the beams having a much more tightly controlled spatial response. This application is a good example where a low-sidelobe beam-space might be of interest. Some initial results in forming a beam-space with high spatial isolation of the beams was presented in [54]. Additional low-sidelobe beam-space results will be presented in a later Chapter as well. This type of application may be thought of as a non-adaptive approach, that is, each beam is processed separately and no attempt is made to use other adjacent beams to form a more optimal output. In general, each beam can be processed for any signal that is within the down-converted bandwidth of the sampling system. Here we have chosen to concentrate on two specific applications, Radar and Communications.

3.3.1 Basic Communications Processing Scheme

In order to show that the signals can be processed for multiple applications simultaneously, a digital communications receiver system was created to perform filtering, demodulation and display of constellation diagrams. Typically, communications signals are formed by modulating a series of data samples onto a set of orthonormal basis functions. Thus, for a given data symbol, \mathbf{d} , the corresponding modulated waveform can be described as [55]:

$$x_c(t) = \sum_{n=1}^N d_n \varsigma_n(t), \quad (3.5)$$

where $\varsigma_n(t)$ is to the n^{th} orthonormal basis function onto which the n^{th} data value is modulated. A simple set of orthonormal basis functions are the sine and cosine, thus a simple communications modulation is that of Quadrature Phase Shift Keying (QPSK)

where the data symbols are modulated onto the In-phase and Quadrature components of a transmitted carrier. This allows for the reception of four (4) distinct signal levels, one for each quadrant in the real/imaginary plane. While the concept is simplistic, reception of the signal constellation involves several steps as outlined below.

Recovery of any given Communications signal begins with a gain equalization and filtering stage, typically, a raised-cosine filter shape is used to shape the spectrum of the communications signal. This is necessary since the amplitude and phase modulation that is inherent to a number of communications protocols causes an extreme widening of the spectral bandwidth, outside that which is useful to the communications receiver. This spectral, spillage or leakage is often termed Adjacent Channel Interference (ACI), and can be controlled to some degree with spectral filtering. Another benefit of the filtering stage is in the reduction of inter-symbol interference (ISI), this is typically due to coherent effects within the channel (i.e., multipath), or any other misalignment in sampling, such that a given symbol interferes with its neighbors. The usage of a paired transmit and receive filter, like a root-raised cosine filter, allows for matched filtering of the symbols on receive. The final output filter can be made to match that of a Raised cosine filter, which meets the conditions of the Nyquist ISI criterion in [55] when sampled at the proper time intervals, as shown in Fig. 3.12. Inspection of the symbols in Fig. 3.12 show that they have a form that is identical to the orthogonal beams shown in Fig. 2.6, and we are once again reminded of the importance of proper sampling and filter design, whether in the temporal, spatial, or spectral domains. Thus, for a communication only application, the desire would be to have spatial channels from the photonic array processor that have little interference (i.e., orthogonal or low-sidelobe beams), with each channel then being able to receive communications symbols with little interference (i.e., ISI). The communications receiver/processor assumes a root-raised-cosine filter for its matched filtering stage. Just prior to matched-filtering, the sampled data is put through an automatic gain control process that attempts to ensure that the signal level from sample-to-sample is flat. The signal is then filtered, however; direct attempts at recovering a constellation at this stage are typically fruitless as seen

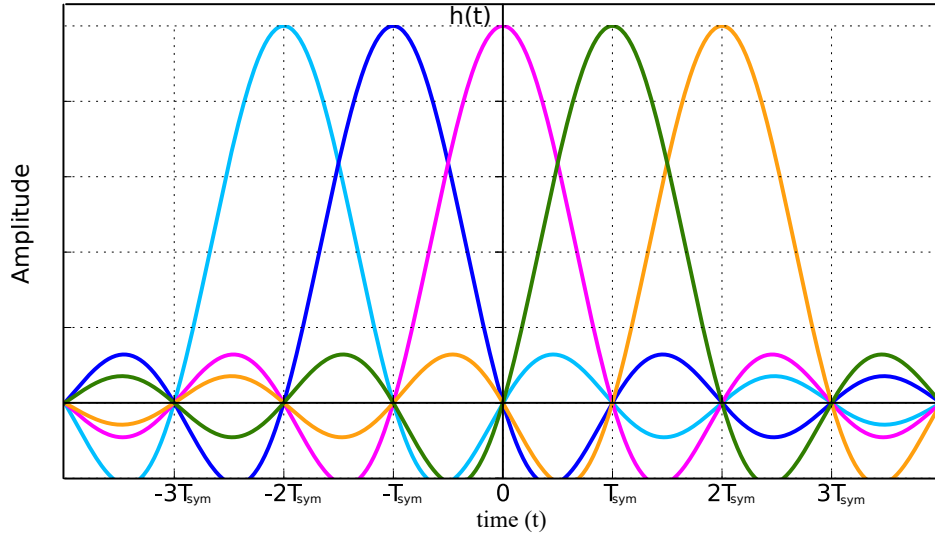


Figure 3.12: Plot of the time-domain responses for a set of symbols with a raised-cosine response. Each symbol can be sampled at the symbol rate, such that its response is maximum, while the adjacent symbols are minimum.

from the cyan dots of the I/Q plot in Fig. 3.13. The communications receiver is not yet synchronized in phase or frequency with the received data. A synchronization process is performed to estimate the timing error in the sampling of the symbols. This can be performed in many ways and the implementation here is likely not optimum as it is not the focus of this research. However, a simple “zero-crossing” timing error detector scheme is implemented such that the In-phase and Quadrature samples are compared to find instances where an “eye-diagram” crosses zero. Other popular techniques exist with slightly more complex implementation of the feed-back mechanisms such those offered by Gardner [56] and Mueller [57]. Regardless of the timing error estimator, estimated offsets of the samples from the ideal locations are used to interpolate the data samples such that they align with the proper sampling locations. The coarsely aligned result is shown as the red dots on the constellation diagram in Fig. 3.13. The remaining steps utilize an adaptive linear equalization technique to reduce the effects of multi-path and other dispersive channel effects. The effect of this step can be seen in Fig. 3.13 as the drastic tightening of the constellation points from the red to the green dots. The phase errors associated with the dispersive channel have been equalized via

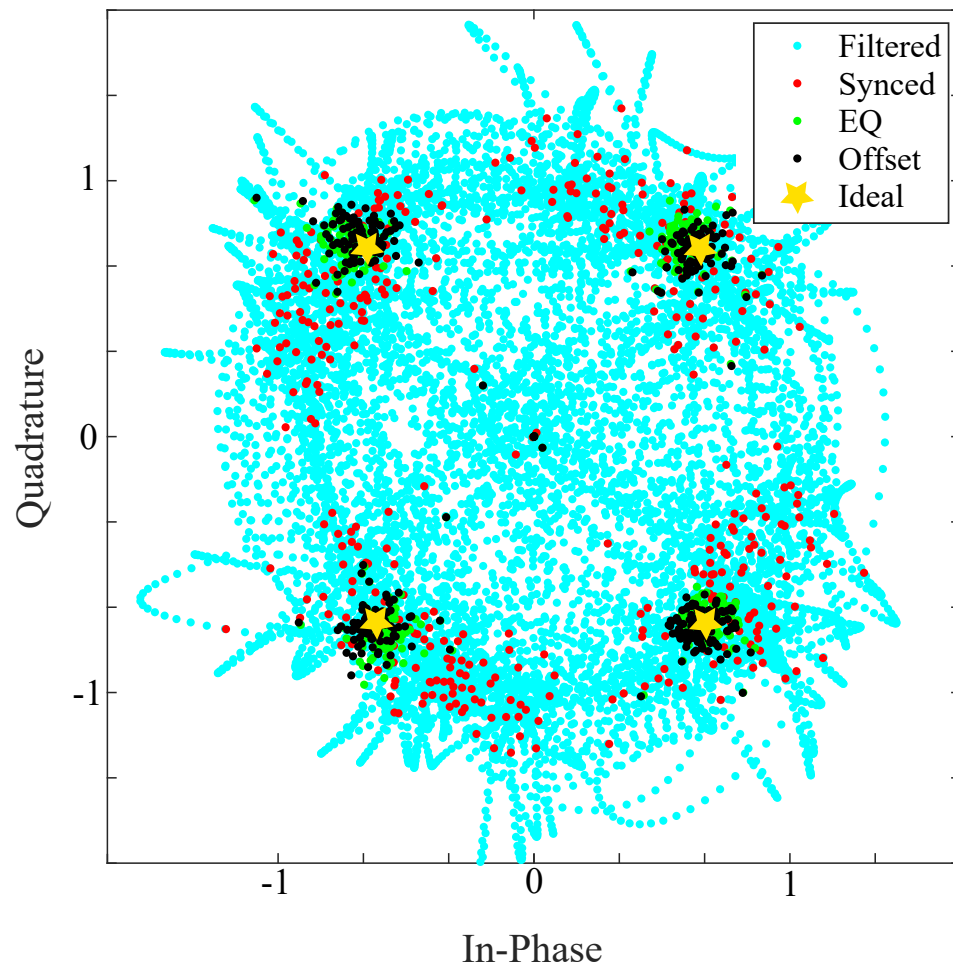


Figure 3.13: Example of the output communications constellation diagram after several stages of digital processing.

a set of complex filter weights. Finally, any deviations from the carrier are detected via use of an FFT based spectral analysis approach. This allows for corrections due to slight Doppler-shifts or other channel-related carrier offsets. Thus, the final output constellation is shown in black within Fig. 3.13, where it is seen to have good agreement with the ideal constellation, shown as a set of stars for this particular QPSK data-set. At this point a threshold detector can be used to determine which quadrant, of the I/Q plane, the samples lie within so that the bit-stream can be reconstructed. Each point on the constellation corresponds to a set of bits (i.e., one symbol). The digital communications receiver reviewed here is not a real-time implementation, but

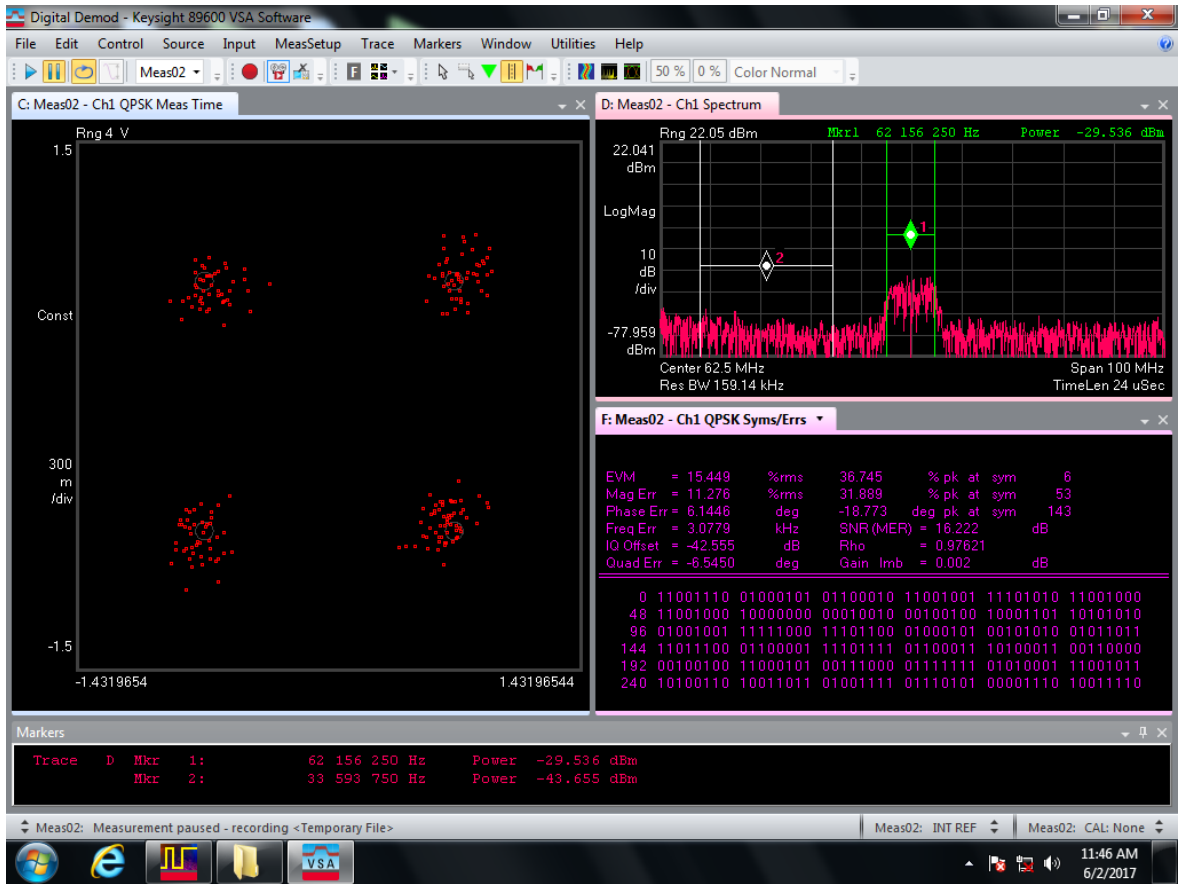


Figure 3.14: Screen Capture from the KeySight VSA software used for real-time digital communication demodulation.

is instead post processed. Non-real-time operation is not ideal, therefore, a Vector Signal Analyzer (VSA) using a digital communication demodulation software package is used for most of the experiments presented in subsequent Chapters. A screen capture of the VSA software is shown in Fig. 3.14. For multi-function experimentation, the VSA is provided a direct feed from one of the output beam-sampling photo-detectors for communications processing in real-time, while the other outputs are provided to a radar processor built around a National Instruments PXI-e chassis.

3.3.2 Basic Radar Processing Scheme

Another primary RF function of interest to this research is that of Radar processing. For any given beam-output a matched filtering operation can be performed,

such that, a known transmit signal can be pulled from a noisy background. The transmit signaling for radar operations can be widely varied [58], we therefore choose to focus on systems that use a Linear Frequency Modulation (LFM) waveform (i.e., Chirp Waveform). Thus, a transmitted LFM radar signal will have a form similar to the following:

$$x_r(t) = A_r e^{j(\Omega t + \frac{\gamma}{2} t^2 + \phi_r)}, \quad (3.6)$$

where the radian chirp parameter, γ is defined as

$$\gamma = \frac{2\pi\beta_r}{\tau_r}, \quad (3.7)$$

with β_r being the transmission bandwidth of the pulse and τ_r the pulse length. The complex output of a baseband chirped Pulse of 10 μ secs with a 10 MHz bandwidth is shown in Fig. 3.15. When up-converted to a center frequency of 12 GHz, the spectrum

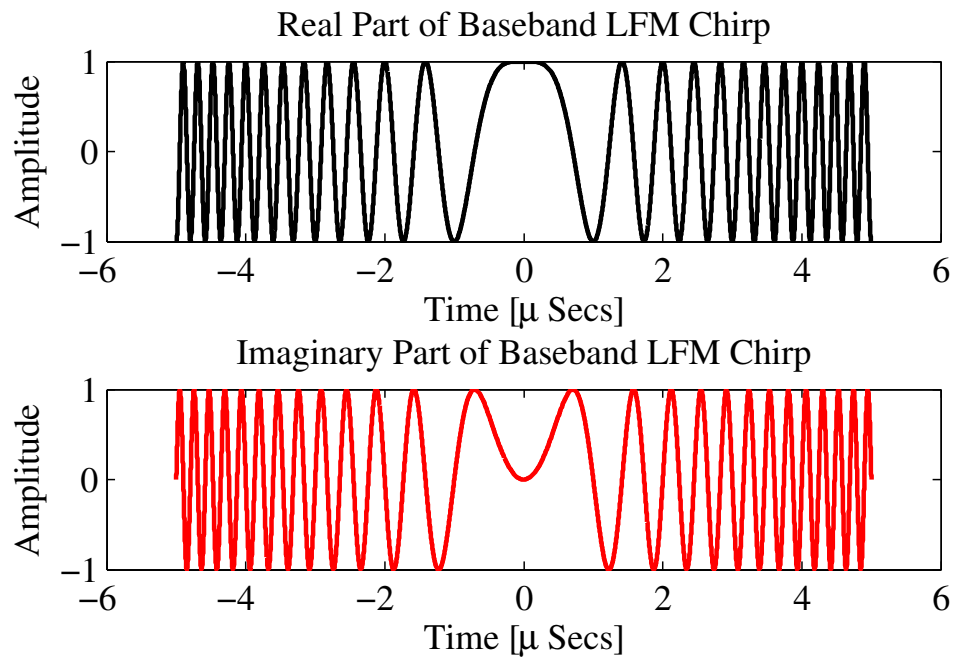


Figure 3.15: Ideal Linear Frequency Modulated Pulse with the center of the pulse referenced to $t = 0$.

of the base-band LFM pulse is shifted in frequency as shown in Fig. 3.16. Upon reception a similar shift is performed during down-conversion to get the signals back to

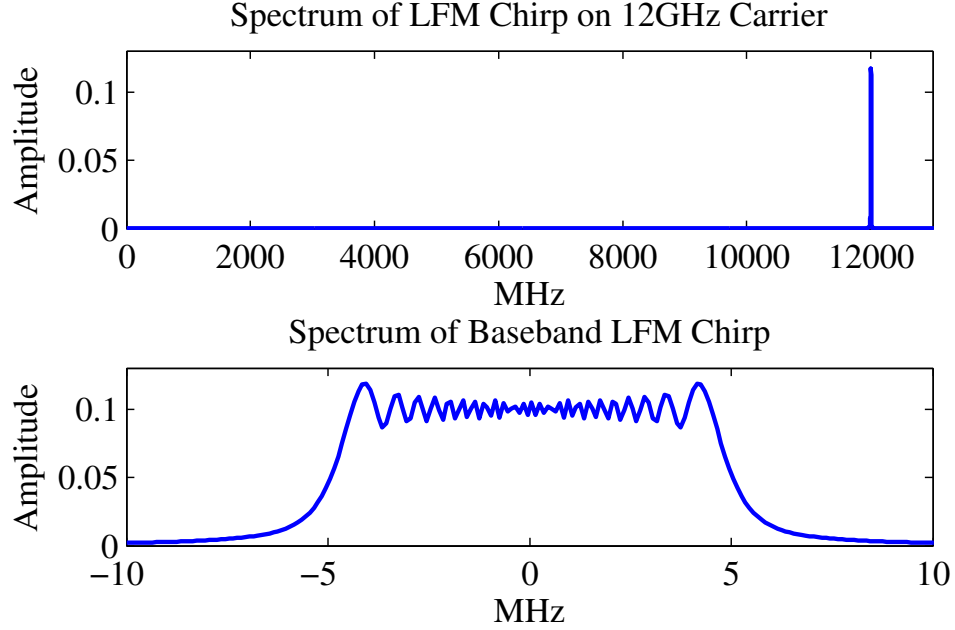


Figure 3.16: Ideal spectrum of a Linear Frequency Modulated pulse.

a base-band representation as discussed in Section 3.2. The pulse is transmitted where it will react with the environment such that a set of delayed replicas will return to a receiving station. The received signal can therefore be represented as

$$s_{r,n}(t) = A_{r,n} e^{j(\Omega(t-t_{d,n}) + \frac{\gamma}{2}(t-t_{d,n})^2 + \phi_r)}. \quad (3.8)$$

Reviewing the case where there is a singular target return, $n = 1$, allows for straightforward visualization of the time-delay, t_d , in the down-converted received signal as shown in Fig. 3.17. The time-delay represents a round-trip delay and must be divided by two when converting received time-delay to radar range. Therefore,

$$t_d = \frac{2R}{c}, \quad (3.9)$$

where R is the range to a given target and c denotes the speed of light. Radar returns rarely have single target returns due to reflections from the surrounding ground, often called clutter returns. When multiple targets are present in a received signal, the superposition of those echoes results in a highly modulated return pulse. An example for just 3 targets is shown in Fig. 3.18. This modulation is due to the fact that the

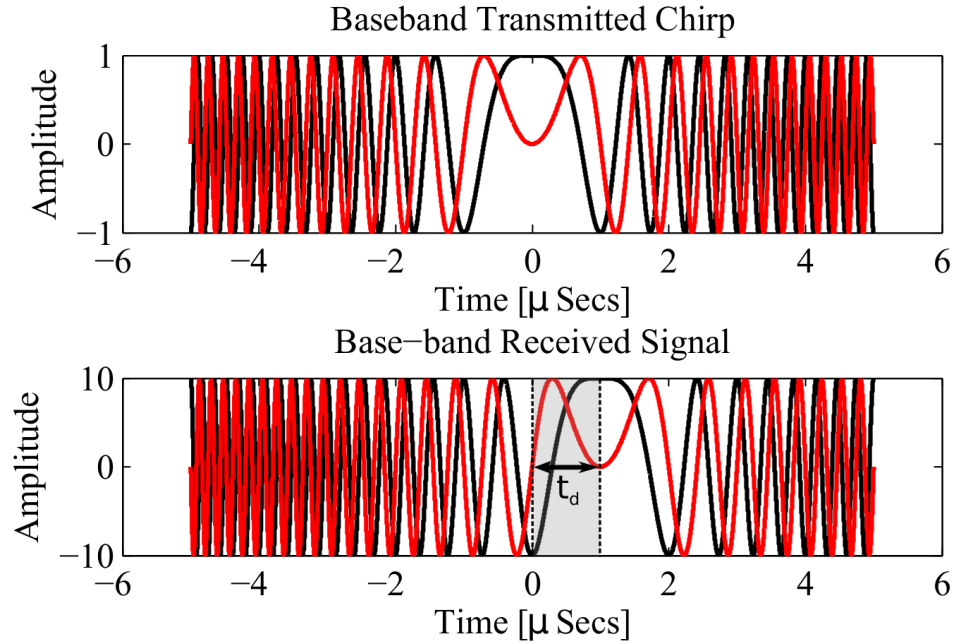


Figure 3.17: Received pulse with the time-delay due to a single target in the scene.

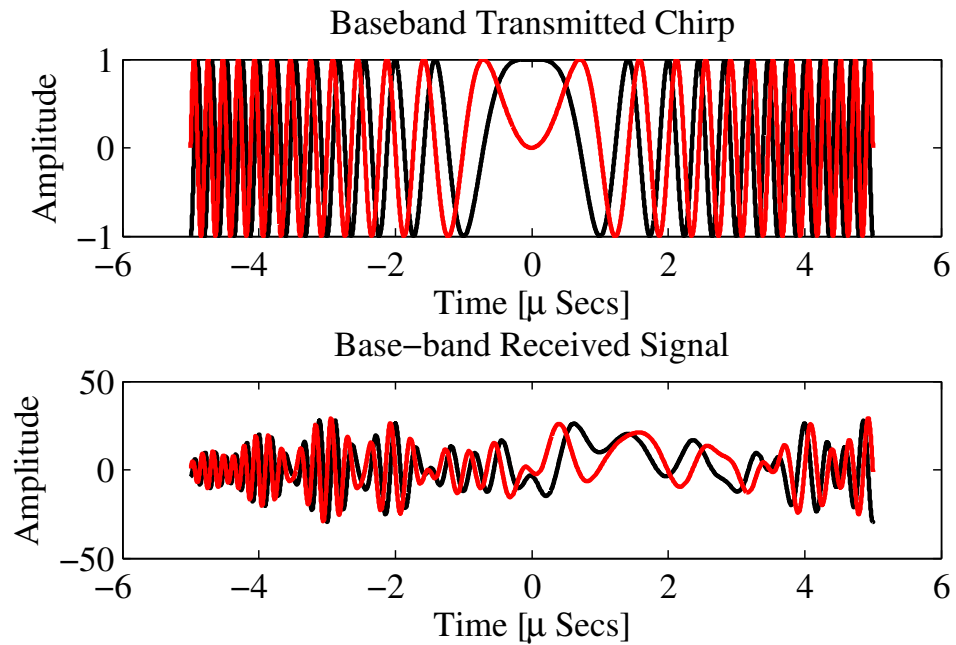


Figure 3.18: Received pulse with the time-delay due to multiple targets in the scene, individual delays are now very difficult to visualize and detect.

transmitted pulse has an extremely long spatial length. When considered the round-trip aspect of radar, the spatial length of the pulse is equal to $\frac{c\tau_p}{2}$, thereby making the 10 μ Sec pulse in the examples equivalent to 1500 meters in range. In fact, a good rule of thumb to remember is that 1 μ Sec is equivalent to 150 meters of range. In order to detect the time delays of each of the targets within the spatial pulse, the properties of the LFM are used to “compress” the intrapulse resolution. Since the pulse appears to be “different” with time, a correlation operation will result in peaks where the received signal matches well with the transmitted pulse. This operation effectively “compresses” the pulse by a factor that is proportional to the pulse width and bandwidth of the chirp. This type of radar pulse compression processor is often referred to as a range correlator in the literature. It makes use of the properties of the matched filter to optimize the signal to noise ratio of the returns [58], while also providing a range resolution, ρ_r , that is proportional to the bandwidth of the transmitted chirp signal, thus,

$$\rho_r = \frac{c}{2\beta_r}. \quad (3.10)$$

The operation is simple; the transmit pulse modulation is known and, thus, a replica of the transmitted pulse is used to perform a cross-correlation with the received signal. This is typically done via a fast convolution process that uses the FFT. Remembering that the convolution of two signals in the time domain is equivalent to a multiplication of those signals in the frequency domain gives the following form of the range-correlator:

$$y_r(t) = FFT^{-1} \{ S_{r,bb}(\Omega) X_{r,bb}^*(\Omega) \}, \quad (3.11)$$

where $X_{r,bb}^*(\Omega)$ is the baseband matched filter form of the initial transmitted signal and $S_{r,bb}(\Omega)$ is the FFT of the baseband received signal. An example of the compressed pulse output for the 3 target case presented earlier can be see in Fig. 3.19. The experiments discussed later use a range-correlator processor that is implemented on a National Instruments PXIe- chassis that utilizes an FPGA and a single-board computer for processing.

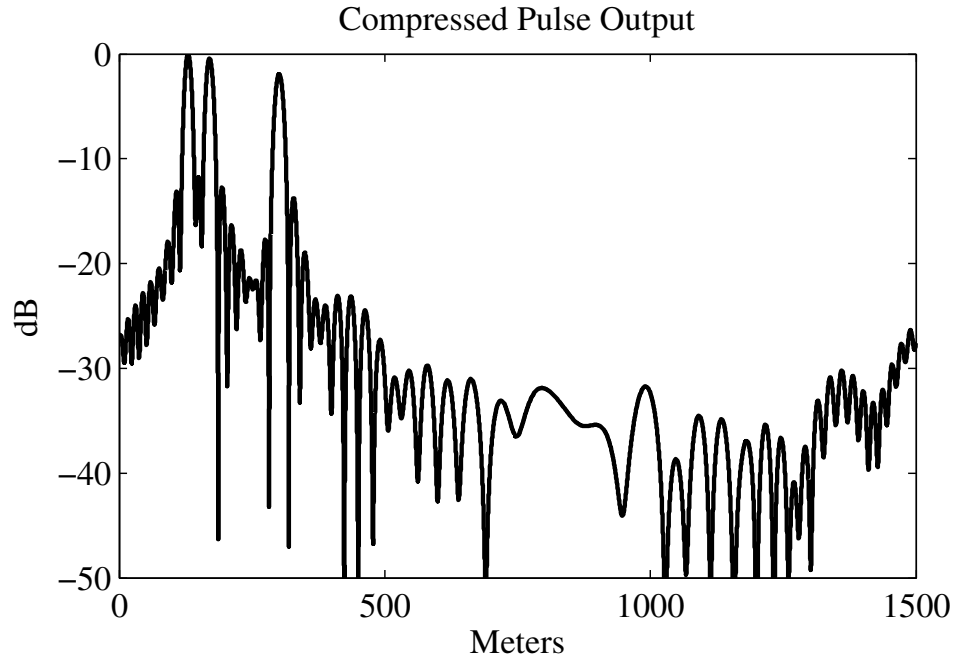


Figure 3.19: Pulse-compressed output for the 3-target echo signal shown in Fig. 3.18. Targets were placed at 130, 170 and 300 meters.

3.4 Processing of the Full Beam-space

The previous sections described processing that can be performed on a single row of the sampled and digitized beam-space data matrix defined in (3.3). However, a multitude of beam-space processing techniques can be readily applied if we consider the columns of the beam-space data matrix. The concepts of array processing were introduced in Section 1.1, where much of the early research was performed across the elements of a given array. Here, we assume to have properly sampled the continuous spatial frequency spectrum at the output of the photonic array processor, as described in Section 2.3.3, such that we have effectively captured a set of orthogonal beam outputs as initially described in Section 1.1.2. By doing so, many of the so-called “element-space” array processing techniques are easily converted to application in the beam-space regime proposed here. In practice, the sampling of the beam-space requires precise alignment along with significant calibration, as will be discussed in a later section. For now, we assume to have a set of output samples from the beam-sampling

photo-detector array that are a set of down-converted beam-space signals from a set of orthogonal beams such that,

$$\mathbf{X}_{bs} = \mathbf{B}^H \mathbf{X}_{es}, \quad (3.12)$$

where \mathbf{X}_{bs} and \mathbf{X}_{es} denote the beam-space and element-space data matrices, respectively. The structure of the element-space data matrix is such that each row contains a set of time-sampled values of the superposition of the incident RF signals and noise. In the noiseless case, each column of the element-space matrix is a separate time-snapshot of the vector, $\mathbf{s}(t)$, introduced in (1.28). With the addition of a noise signal term, element data vector can be defined for an arbitrary number of signals as

$$\mathbf{x}_{es}(t) = \mathbf{V}(\theta)\mathbf{s}(t) + \mathbf{n}(t), \quad (3.13)$$

which allows for

$$\mathbf{x}_{bs}(t) = \mathbf{B}^H \mathbf{V}(\theta)\mathbf{s}(t) + \mathbf{n}(t) = \mathbf{V}_{bs}(\theta)\mathbf{s}(t) + \mathbf{n}(t), \quad (3.14)$$

where $\mathbf{V}(\theta)$ is a matrix containing the steering vectors toward the signals incident on the array, $\mathbf{s}(t)$ is a vector of those signals, and $\mathbf{n}(t)$ is a noise vector assumed to be white with variance σ_n^2 and uncorrelated with the signals in $\mathbf{s}(t)$. The newly defined beam-space steering matrix, \mathbf{V}_{bs} , contains the element-space steering vectors for the signals as augmented by the beam-space matrix, \mathbf{B} . It is noted that $\mathbf{v}(\theta)$ is substituted with the beam-space augmented version, $\mathbf{v}_{bs}(\theta)$, when performing the described operations on beam-space data vectors. The continuous-time signals are assumed to be sampled via an ADC such that the beam-space matrix becomes an M by L matrix, $\mathbf{X}_{[bs]}$, where $L = f_s \cdot T_s$ is the total number of samples acquired at the sampling rate, f_s , during the sampling duration, T_s . This matrix is some-times referred to as a ‘‘Space-Time’’ data matrix since the rows correspond spatial locations while the columns correspond to time-samples or ‘‘snapshots.’’

It is worth reminding the reader that the transformation in (3.12) is equivalent to sampling the Discrete Spatial Fourier Transform of the input elements at the sample

intervals provided by a Discrete Fourier Transform, and is therefore an invertible operation [25]. This implies that one could retrieve the element-space data vector from the beam-space output of the photonic array processor if desired. We further emphasize the capability of the Photonic Beam-space Array processor to directly sample \mathbf{X}_{bs} without any digital computation, all beam-space beam-forming and sampling is performed in real-time regardless of the number of elements in the RF array.

Two primary uses for the application of element-space or beam-space array processing techniques are to determine the directions, or angles-of-arrival (AoAs) of a number of unknown signals that are incident on the array and/or steer the array such that only signals from a desired AoA are sampled. In general, all of these techniques attempt to perform a calculation that is optimum in the sense of minimizing the mean square error with a desired signal and/or maximizing the signal-to-noise ratio [59]. Often, a given spatial spectrum estimator or adaptive array weight calculation will rely on knowledge of the covariance matrix, \mathbf{R}_x , of the received spatial environment. Typically, the true, or clairvoyant, covariance is unknown and an estimate must be made from the data samples that are collected by the array. Thus, for a given array output that is derived via a weighted sum on input samples (in either the element-space or the beam-space) we have

$$y = \mathbf{w}^H \mathbf{x}, \quad (3.15)$$

where \mathbf{w}^H is the weight vector applied to the array outputs that steers (or adapts) the baseline array response in order to detect the specific, $s(t)$, per the definition in (3.13). It has been shown that the expected output power from the array is of the following form [59],

$$E[|y|^2] = \mathbf{w}^H E[\mathbf{x}\mathbf{x}^H] \mathbf{w}. \quad (3.16)$$

The expectation of the data vector in (3.16) is equal to the covariance such that

$$\mathbf{R}_x = E[\mathbf{x}\mathbf{x}^H]. \quad (3.17)$$

If it is further assumed that the desired signal, noise and any interference signals are mutually uncorrelated, we can define

$$\mathbf{R}_x = E [\mathbf{x}\mathbf{x}^H] = |A_s|^2 \mathbf{v}(\theta_s)\mathbf{v}(\theta_s)^H + \sum_{z=1}^Z |A_z|^2 \mathbf{v}(\theta_z)\mathbf{v}(\theta_z)^H + \sigma_n^2 \mathbf{I}, \quad (3.18)$$

where the subscripted, s , defines the values for the desired signal, while z delineates the contributions from Z possible interfering sources. The result in (3.18) may be termed the clairvoyant covariance. If we assume isotropic noise, the noise will only contribute to the diagonal of the covariance matrix while the off-diagonal terms are due to correlations across the array from incident plane-wave sources and thus contain information about angles of arrival. Since the clairvoyant covariance is not likely to be known, a good estimate of the covariance must be made from the sampled data, known as the sample covariance matrix, $\hat{\mathbf{R}}_x$. The sample covariance matrix is often calculated via the following formula:

$$\hat{\mathbf{R}}_x = \frac{1}{K} \sum_{k=0}^{K-1} \mathbf{x}_k \mathbf{x}_k^H, \quad (3.19)$$

where $\hat{\mathbf{R}}_x$ converges to the maximum likelihood estimate of \mathbf{R}_x when K is large [60].

Once the sample covariance is formed, a number of techniques can be applied to the data. These techniques are broken into two classes for the purposes of this discussion:

1. Methods that attempt to estimate the Spatial Spectrum and thereby determine possible Angles-of-Arrival of incident sources.
2. Methods that attempt to form an adapted array response such that the desired signal is captured and unwanted interference is attenuated.

We begin with a discussion on the estimation of the array spatial spectrum, followed by an example of array adaptation that is used for experimentation.

3.4.1 Beam-Space Spatial Spectrum Estimation

Estimation of the spatial frequency spectrum is equivalent to searching over all possible array steering vectors for locations where the array response peaks. Significant research has been performed in this area for decades, with several comprehensive reviews existing in the literature [22–24]. Here, only the necessary foundations of the relevant techniques will be reviewed. The discussion begins with a basic form of spatial spectral estimation that is non-parametric in nature. That is, the estimation techniques are not based on any particular spectral/signal model.

3.4.1.1 Non-Parametric Spatial Spectrum Estimators

The most straightforward spatial spectrum estimator is the Fourier Spectral estimator, also called the Bartlett Beam-former [61], which takes advantage of the relation in 3.16, to search for peaks in the array response. Thus, AoA estimates are associated with the peaks of the following spectral function:

$$P_{Bartlett}(\theta) = \mathbf{v}(\theta)^H \hat{\mathbf{R}}_x \mathbf{v}(\theta). \quad (3.20)$$

We can see from (3.20) that the estimate is formed from a rigorous search across all potential steering vectors. For the sampled beam-space output that is retrieved from the photonic array processor we must convert the relation in (3.20) to one that will operate in the beam-space using the relation in (3.14). Thus, we apply the beam-space steering matrix, \mathbf{B}^H , to any element-space steering vectors to arrive at the beam-space Bartlett estimator:

$$\begin{aligned} P_{Bartlett}(\theta) &= (\mathbf{B}^H \mathbf{v}(\theta))^H \hat{\mathbf{R}}_x (\mathbf{B}^H \mathbf{v}(\theta)) \\ &= \mathbf{v}_{bs}(\theta)^H \hat{\mathbf{R}}_x \mathbf{v}_{bs}(\theta). \end{aligned} \quad (3.21)$$

The relation of element-space estimators to beam-space datasets will be used throughout this thesis. In practice the steering vectors can be calculated once and stored as large matrix, allowing a single set of matrix multiplications to provide $P_{Bartlett}(\theta)$ directly. It will be shown in a later section that the “imaged” output of the photonic array processor is essentially equivalent the Bartlett beam-former.

The next estimator that is used is known as the Minimum Variance Distortionless Response (MVDR) or Capon Beam-former [62]. The Capon formulation takes the basic concept of the Bartlett method and applies several constraints in an effort to optimize the result. Noticing that the relation in (3.16) is equivalent to the variance of the array response, Capon wished to find a set of optimal weights, $\mathbf{w}_o(\theta)$, such that the variance is minimized by

$$\mathbf{w}_o(\theta) = \arg \min \{ E [|y(\theta)|^2] \}, \quad (3.22)$$

but the response in a desired direction was left undistorted by

$$\mathbf{w}_o^H(\theta) \mathbf{v}_{bs}(\theta) = 1. \quad (3.23)$$

When the constrained optimization problem is solved the resulting optimal weights are found via

$$\mathbf{w}_{capon}(\theta) = \frac{\hat{\mathbf{R}}_x^{-1} \mathbf{v}_{bs}(\theta)}{\mathbf{v}_{bs}^H(\theta) \hat{\mathbf{R}}_x^{-1} \mathbf{v}_{bs}(\theta)}, \quad (3.24)$$

with the spatial spectrum then given by

$$P_{Capon}(\theta) = \frac{1}{\left| \mathbf{v}_{bs}^H(\theta) \hat{\mathbf{R}}_x^{-1} \mathbf{v}_{bs}(\theta) \right|}, \quad (3.25)$$

where the result is once more augmented to operate within the desired beam-space.

The final non-parametric method to be discussed is that of the Maximum Entropy Method (MEM) [63]. The aim of MEM was to augment the existing Fourier Methods by attempting to extrapolate data outside of the aperture. This extrapolation essentially widens the aperture, which theoretically improves the resolution. The key to MEM is in how it attempts to guarantee the validity of the extrapolated data when there seems to be an infinite number of possible extrapolations. Thus, the MEM technique constrains the extrapolation in an effort to maximize the randomness (or minimize the structure) of the data. This, in turn, acts to maximize the flatness of the spectral response outside of the measured array region. The maximum entropy spatial spectrum is given by

$$P_{MEM}(\theta) = \frac{\mathbf{e}_1 \hat{\mathbf{R}}_x^{-1} \mathbf{e}_1^T}{\left| \mathbf{e}_1 \hat{\mathbf{R}}_x^{-1} \mathbf{v}_{bs}(\theta) \right|^2}, \quad (3.26)$$

where $\mathbf{e}_1 = [1 \ 0 \ \cdots \ 0]$ is a 1 by M vector known as the first standard basis vector.

Thus, with only a sample covariance matrix, a great number of angle-of-arrival estimation techniques can be performed, with many offering significant performance increases over simplistic Fourier techniques. The next set of techniques rely on an Eigen-analysis of the covariance and will be referred to collectively as “sub-space” estimators.

3.4.1.2 Sub-space Spatial Spectrum Estimation Techniques

Sub-space methods begin with an Eigen-decomposition of the sample covariance matrix such that

$$\hat{\mathbf{R}}_x \mathbf{q}_i = \lambda_i \mathbf{q}_i \text{ for } i = 1, 2, \cdots, M, \quad (3.27)$$

where the λ_i are found to be roots of the characteristic equation given by

$$\det [\hat{\mathbf{R}}_x \mathbf{q} - \lambda \mathbf{I}] = 0. \quad (3.28)$$

For our beam-space outputs of M beams, there will be M roots. These roots, λ_i , are known as the Eigenvalues, each with an associated Eigenvector, \mathbf{q}_i . An important property of the Eigenvectors is that any two Eigenvectors associated with two distinct Eigenvalues will be orthogonal such that the eigen matrix, $\mathbf{Q} = [\mathbf{q}_1 \mathbf{q}_2 \cdots \mathbf{q}_M]$, is unitary making

$$\mathbf{Q}^H \mathbf{Q} = \mathbf{I}. \quad (3.29)$$

We may also factor the sample covariance matrix in terms of the eigen matrix and a diagonal matrix of the Eigenvalues, $\mathbf{\Lambda}$, such that

$$\hat{\mathbf{R}}_x = \mathbf{Q} \mathbf{\Lambda} \mathbf{Q}^H, \quad (3.30)$$

which is an identity that is often useful in estimating the inverse of the covariance matrix as $\hat{\mathbf{R}}_x^{-1} \approx \mathbf{Q} \mathbf{\Lambda}^{-1} \mathbf{Q}^H$, particularly when a technique uses a sub-space covariance estimate.

Returning to the Eigenvalues, λ_i , for a given sample covariance matrix, if the noise is assumed to be white Gaussian, the Eigenvalues may be sorted such that the

largest, $i = 1, 2, \dots, D$, Eigenvalues are associated with, D , incident signals, while the remaining, $M - D$, Eigenvalues are associated with noise. In an ideal case, the noise Eigenvalues would all be equal to the noise power, however, this is rarely the case due to the fact that the covariance is estimated from a finite number of data snapshots. Thus, determining a proper Eigenvalue threshold for, D , is of interest and is typically done based on some statistics of the eigenvalues or eigenvectors of the sample covariance matrix. Often, an estimate of the multiplicity of the smallest eigenvalue is used [23]. Other popular algorithms include Akaike's Information-Theoretic Criterion (AIC) and the Minimum Description Length (MDL) [64] from the information theory community, which form an estimate of D via the following minimizations:

$$\hat{D}_{AIC} = \arg \min \left\{ \hat{D}_{AIC}(2M - \hat{D}_{AIC} + 1) - (M - \hat{D}_{AIC})L_s \log_e \left[\frac{\left(\prod_{i=\hat{D}_{AIC}+1}^M \lambda_i \right)^{\frac{1}{M-\hat{D}_{AIC}}}}{\sum_{i=\hat{D}_{AIC}+1}^M \frac{\lambda_i}{M-\hat{D}_{AIC}}} \right] \right\}, \quad (3.31)$$

and

$$\hat{D}_{MDL} = \arg \min \left\{ \frac{1}{2} \hat{D}_{MDL}(2M - \hat{D}_{MDL} + 1) \log_e(L_s) - (M - \hat{D}_{MDL})L_s \log_e \left[\frac{\left(\prod_{i=\hat{D}_{MDL}+1}^M \lambda_i \right)^{\frac{1}{M-\hat{D}_{MDL}}}}{\sum_{i=\hat{D}_{MDL}+1}^M \frac{\lambda_i}{M-\hat{D}_{MDL}}} \right] \right\}, \quad (3.32)$$

where L_s is the number of time-samples (i.e., snapshots) used in forming the sample covariance matrix. Another method, germane to the photonic array processing scheme presented here, is to threshold the peaks that are detected when using a camera to image of the irradiance pattern of the continuous spatial spectrum formed at the output focal plane. This particular technique will be discussed in detail within Chapter 6.

Assuming that a proper estimate of the number of signals can be made, the covariance matrix can be divided into two orthogonal sub-spaces, one associated with only signals and the other associated with only noise. The signal sub-space, \mathbf{Q}_s , is a

matrix of eigenvectors that are associated with the incident signals, while the noise sub-space, \mathbf{Q}_n , is a matrix formed from the eigenvectors associated with noise only. It is therefore possible to form a new covariance estimate that uses only the signal sub-space, a so-called covariance of the Principle Components. The Principle Components covariance, $\hat{\mathbf{R}}_{x,PCA} = \mathbf{Q}_s \mathbf{\Lambda}_s \mathbf{Q}_s^H$ can be directly substituted into the non-parametric methods discussed in Section 3.4.1.1. Usage of a properly estimated signal-subspace covariance affords a reduction in the noise-floor along with the number of false peaks in the previously mentioned techniques. The remaining sub-space methods concentrate on the noise-subspace and various weighted projections onto it, in order to determine angles-of-arrival.

The simplest of the noise sub-space methods is likely that given by Pisarenko [65], where a pseudo-spectrum is formed based on the projection of candidate steering vectors onto the eigenvector, \mathbf{q}_{min} , that is associated with the smallest eigenvalue. The theory being that the minimum eigenvector represents the noise, which should be orthogonal to any steering vector that represents a signal location, thus,

$$P_{Pisarenko}(\theta) = \frac{1}{|\mathbf{q}_{min}^H \mathbf{v}_{bs}|^2}. \quad (3.33)$$

A natural follow-on to the Pisarenko method is that of the Multiple Signal Classification (MUSIC) method which projects candidate steering vectors onto the entire noise subspace, \mathbf{Q}_n , with the output MUSIC spectra given by

$$P_{MUSIC}(\theta) = \frac{1}{\mathbf{v}_{bs}^H(\theta) \mathbf{Q}_n \mathbf{Q}_n^H \mathbf{v}_{bs}(\theta)} = \frac{1}{|\mathbf{Q}_n^H \mathbf{v}_{bs}(\theta)|^2}, \quad (3.34)$$

or alternatively by

$$P_{MUSIC_N}(\theta) = \frac{\mathbf{v}_{bs}^H \mathbf{v}_{bs}(\theta)}{\mathbf{v}_{bs}^H \mathbf{Q}_n \mathbf{Q}_n^H \mathbf{v}_{bs}(\theta)}, \quad (3.35)$$

where the numerator serves to normalize the array response vectors in the case of beam-space operation [66]. Several other estimators that are closely related to MUSIC are of interest, namely the Minimum Norm [67] and Eigenvector Methods [68]. The Minimum Norm method has been shown to have less bias and better detection performance in low SNR environments as the cost of some level of increased estimation variance [69], while

the eigenvector method is more tolerant of non-whitened noise and is less susceptible to errors in the estimation of the size of the signal sub-space, D . The Min-Norm method projects candidate steering vectors onto a portion of the noise sub-space with the constraint that the steering vectors must be minimized in length (i.e. norm) and the weight associated with the first element of the array must be unity. The min-norm spatial spectrum is provided by

$$P_{MNM}(\theta) = \frac{1}{|\mathbf{d}^H \mathbf{v}_{bs}|^2}, \text{ where } \mathbf{d} = \frac{\mathbf{Q}_N \mathbf{Q}_N^H \mathbf{e}_1}{\mathbf{e}_1^H \mathbf{Q}_N \mathbf{Q}_N^H \mathbf{e}_1}. \quad (3.36)$$

The eigenvector method uses the eigenvalues associated with the noise sub-space as a set of weights against the subspace vectors. The eigenvalue method spatial spectrum is given by

$$P_{EVM}(\theta) = \frac{1}{\mathbf{v}_{bs}^H \mathbf{Q}_n \mathbf{\Lambda}_n^{-1} \mathbf{Q}_n^H \mathbf{v}_{bs}}. \quad (3.37)$$

The angle estimation methods discussed here will be used extensively with the sampled beam-space outputs of the photonic array processor presented in the previous Chapters. A comparison of their relative performance during experimentation will also be discussed. It will be shown that the beam-space generated by the photonic array processor can be made orthogonal such that these super-resolution techniques can be applied for increased angular estimation performance.

3.4.2 Beam-space Adaptive Spatial Spectrum Filtering

If we recall the relation in (3.15) and augment it with our Beam-space matrix we have

$$y(t) = (\mathbf{B}^H \mathbf{w})^H \mathbf{x}_{bs}(t) = \mathbf{w}_{bs}^H \mathbf{x}_{bs}(t). \quad (3.38)$$

Typical weights for beam-steering are simply a set of steering vectors toward a desired set of locations, however; if there is significant interference within the environment it is desirable to apply weights to the array response such that the error between the beam-former output and the desired signal is minimized. This optimization effectively uses the degrees of freedom of the array to produce an optimal array pattern such that unwanted signals are aligned with nulls in the patter. For the beam-space processing

discussed here, the number of degrees of freedom is equal to the number of beams in the beam-space, M . There are two formulations that are popular, one is in minimizing the mean square error and the other is in maximizing the signal-to-noise ratio.

3.4.2.1 Mean Squared Error (MSE) Optimal Filtering

The optimal set of filter weights that minimize the MSE generate what is known as a Wiener filter (also called Wiener-Hopf or Wiener-Kolmogorov solutions in some texts). If we define the error at the output of the beam-former as

$$\epsilon(t) = s_d(t) - y(t) = s_d(t) - \mathbf{w}_{bs}^H \mathbf{x}_{bs}(t), \quad (3.39)$$

where $s_d(t)$ is the desired signal output. Then, the squared error becomes

$$|\epsilon(t)|^2 = |s_d(t)|^2 - s_d^*(t) \mathbf{w}_{bs}^H \mathbf{x}_{bs}(t) - \mathbf{x}_{bs}^H(t) \mathbf{w}_{bs} s_d(t) - \mathbf{w}_{bs}^H \mathbf{x}_{bs}(t) \mathbf{x}_{bs}^H(t) \mathbf{w}_{bs}, \quad (3.40)$$

with the expectation or mean of the squared error being given by

$$\begin{aligned} \epsilon_{MSE}(t) &= E [\epsilon^2(t)] \\ &= E [s_d^2(t)] - \mathbf{w}_{bs}^H E [s_d^*(t) \mathbf{x}_{bs}(t)] \cdots \\ &\quad - E [\mathbf{x}_{bs}^H(t) s_d(t)] \mathbf{w}_{bs} - \mathbf{w}_{bs}^H E [\mathbf{x}_{bs}(t) \mathbf{x}_{bs}^H(t)] \mathbf{w}_{bs} \\ &= \overline{s_d^2(t)} - \mathbf{w}_{bs}^H \mathbf{r}_d - \mathbf{r}_d^H \mathbf{w}_{bs} - \mathbf{w}_{bs}^H \mathbf{R}_x \mathbf{w}_{bs}, \end{aligned} \quad (3.41)$$

where the over-bar accent on $\overline{s_d^2(t)}$ denotes the mean. The Wiener solution to minimizing the error with respect to the weights gives

$$-2\mathbf{r}_d + 2\mathbf{R}_x \mathbf{w}_{bs} = 0, \quad (3.42)$$

which is obtained by setting the gradient of the MSE with respect to the weights equal to zero. When solved for the weights, the relation in (3.42) provides the optimal weight vector as

$$\mathbf{w}_{opt} = \mathbf{R}_x^{-1} \mathbf{r}_d. \quad (3.43)$$

In practice, it is unreasonable to expect that the desired signal is completely known. Remembering the relation in (3.13) allows substitution of $s(t)$ in for the desired signal, which leaves us with

$$\begin{aligned}\mathbf{w}_{opt} &= \mathbf{R}_x^{-1} \mathbf{r}_d = \mathbf{R}_x^{-1} E [s^*(t)s(t)\mathbf{v}_{bs}(\theta)] \\ &= |s(t)|^2 \mathbf{R}_x^{-1} \mathbf{v}_{bs}(\theta),\end{aligned}\tag{3.44}$$

where the signal power, $|s(t)|^2$, is often replaced by a simple scaling parameter with little effect to the output signal-to-interference-plus-noise ratio (SINR). An example of how a pattern is adapted in this way is shown in Fig. 3.20. The other method of

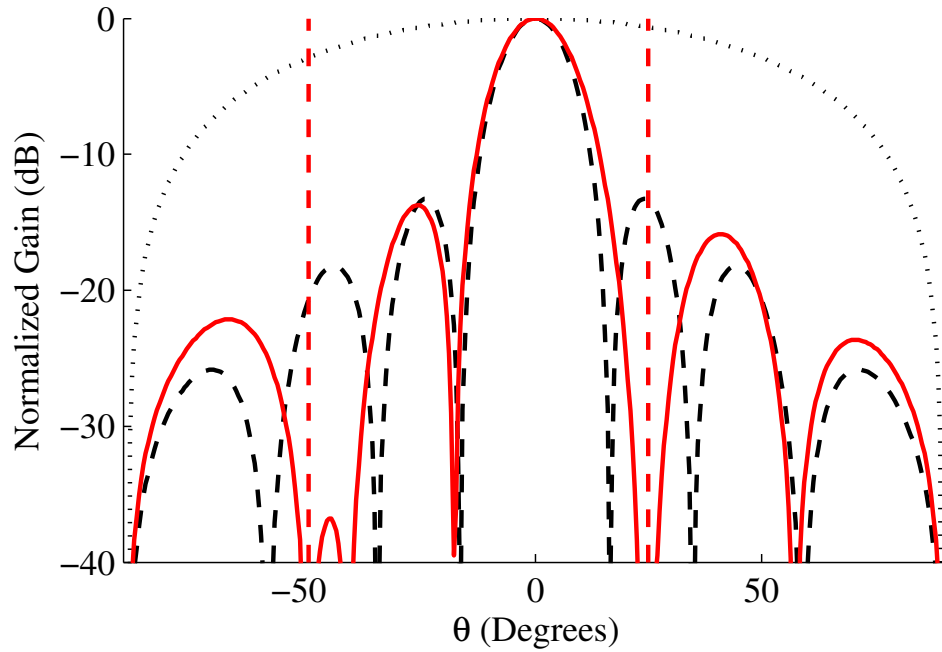


Figure 3.20: Example of of an adapted response using the optimal weighting solution for two interference sources, shown as dotted-red lines. The adapted response is shown in red.

solving for the optimal weights is in maximizing the SNR at the output.

3.4.2.2 Optimal Filtering by Maximizing the Output Signal-to-Noise Ratio

The output SNR for a given set of weights can be written as

$$\frac{S}{N} = \frac{\mathbf{w}_{bs}^H \mathbf{R}_s \mathbf{w}_{bs}}{\mathbf{w}_{bs}^H \mathbf{R}_{i+n} \mathbf{w}_{bs}} = \frac{|\mathbf{w}_{bs}^H s \mathbf{v}_{bs}(\theta)|^2}{\mathbf{w}_{bs}^H \mathbf{R}_{i+n} \mathbf{w}_{bs}}.\tag{3.45}$$

A similar derivation as that performed for the MMSE case can be done here by setting the gradient, with respect to the weight vector, of the result in (3.45) equal to zero. The final relation for the weights that optimize the SNR can be written as [21, 25]:

$$\mathbf{R}_{i+n}^{-1} \mathbf{R}_s \mathbf{w}_{bs} = \lambda_{max} \mathbf{w}_{bs}, \quad (3.46)$$

which can be reduced to

$$\mathbf{w}_{SNR} = \alpha \mathbf{R}_{i+n}^{-1} \mathbf{v}_{bs}(\theta). \quad (3.47)$$

The results in (3.44) and (3.47) are seen to be equivalent to within a scale factor. It is noted that the optimal MVDR result given in (3.24) is also equivalent—within a scale factor—to the results given in (3.44) and (3.47). The scaling does not effect the output SINR since all signals scale proportionally.

Thus, if the signal and/or noise subspaces are known or can be well estimated an optimally adapted response can be obtained via the application of the weights given by (3.24), (3.44) or (3.47). It will be shown later that the ability of the photonic array processor to measure the irradiance pattern of the continuous spatial spectrum of an array directly (and in real-time), allows for the generation of a direct estimate of the interference covariance. This estimate can be used to form a set of weights that effectively null any unwanted interference in the spatial spectrum.

3.4.3 Computational Latency of Beam-Space Adaptive Techniques

Later sections will show the ability of the proposed system to perform several estimates of importance in adaptive processing via simple calculations, thus potentially improving overall latency of adaptive techniques. For this reason it is instructive to discuss the notional latencies that might be expected when performing the calculations described above.

The latency associated with any adaptive operations is largely dependent on the size of the sample covariance matrix. The estimation convergence time is directly dependent on the sample rate of the input data vectors, the total degrees of freedom, the required accuracy of the estimate and the processing capability of the system.

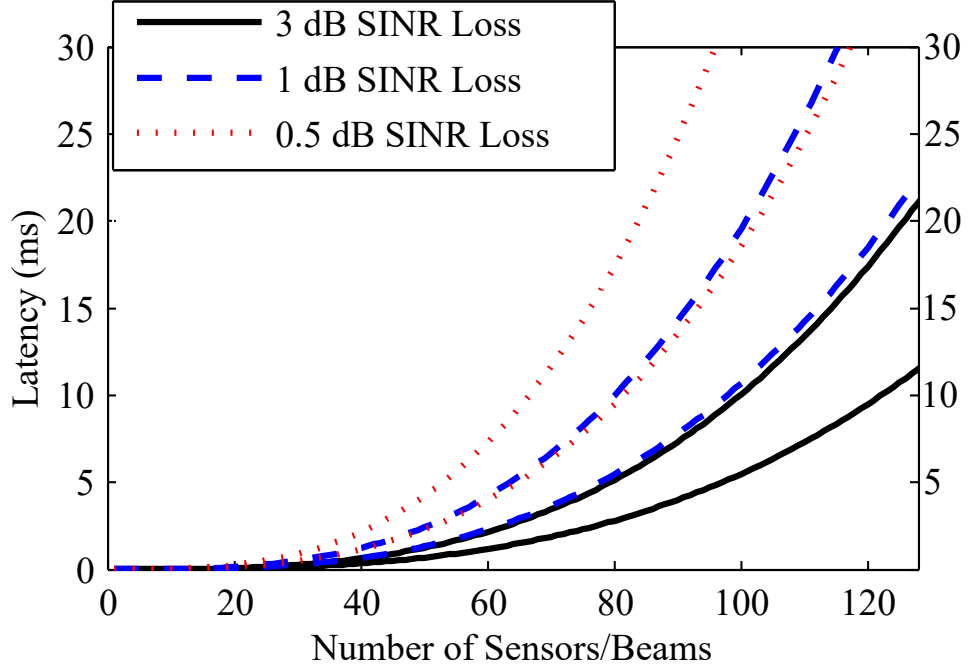


Figure 3.21: Family of curves depicting the first order estimate of processing latency when using a covariance-based AoA estimation or adaptive filtering approach for increasing array sizes. Each pair of curves depict a bounded region of expected latency assuming use of a Virtex-7 class of FPGA.

In practice, an upper limit on the accuracy required is chosen to limit latency and computation. For an array with N sensors, the Signal-to-Interference-Plus-Noise Ratio (SINR) loss (in dB) associated with the number of samples (or snapshots) used to form the sample covariance matrix is related by [70],

$$loss_{SINR} = -10 \cdot \log_{10} [(K + 2 - N)/(K + 1)]. \quad (3.48)$$

A typically chosen limit of 3 dB results in $K = 2N - 3$ samples, while a more stringent 1 dB requirement would result in $K = 5N - 6$ samples. The samples must then be processed via a matrix operation involving the input data matrix and its hermitian transpose, which requires $O(M^2K)$ complex operations. The matrix is inverted ($O(M^3)$) for use in either adaptive weight calculations ($O(M^2)$) and/or generation of the spatial spectral estimates ($O(MA)$, where A is the number of angles to estimate). In a real-time implementation the final step can be done in parallel effectively making

$A = 1$ for any latency calculations. For the case provided, a modern Xilinx Virtex 7 can be expected to perform the required complex multiply/add operations with output rates varying between 297 MHz and 544 MHz depending on the particular implementation design [71]. For $M = 7$ and $K = 11$, we have $O(M^2K + M^3 + M^2 + MA) \approx 938$ operations, which results in a rough estimate of the lower bound on total latency as $3.16\mu\text{s}$. However, as M increases linearly, the processing latency does so exponentially, as shown in Fig. 3.21. The curves shown in Fig. 3.21 should be taken to represent the minimum requirement for calculations and estimation samples. Often, a given estimator may require further operation on the covariance matrix (e.g. singular value decomposition) in order to weight the estimates or to generate a projected sub-space to improve performance over a region of interest [66]. Additional steps to the AoA estimation process will only add latency.

Chapter 4

EXPERIMENTAL PHOTONIC ARRAY PROCESSOR

4.1 Experimental Hardware Overview

A set of prototype components were developed at the University of Delaware in order to test the hypothesized ability—of the photonic up-converted array processor described in the preceding Chapters—to allow for imaging of the continuous spatial frequency spectrum from an RF array while simultaneously enabling the discretization and digitization of an orthogonal subset of the spatial spectrum for further, digital processing.

4.1.1 Photonic Array Processor and Optical Down-converting Cart

The collection of hardware that makes up the prototype array and photonic up-conversion stages, introduced via the schematic diagram of Fig. 2.13 is housed in a mobile rack. The entirety of the aforementioned “receiver cart” is pictured in Fig. 4.1. The top of the cart includes a critically sampled RF array with a center frequency of 12 GHz, with an up-conversion stage behind each RF element. The array assembly sits on a rotational stage for precise angular steering of the entire system. The up-conversion stages behind each element utilize an Agile Microwave Technology, AMT-A0253, LNA that offers a noise figure of less than 3 dB (typical), followed by a Mach-Zehnder Electro-optic Modulator by Optilab. The OptiLab, IM-1550-40-PM-HER, modulators will operate at frequencies up to 40 GHz, while the LNA’s used are only able to operate at frequencies up to 20 GHz. At the termination of the gain and up-conversion stages, each RF array element’s input signal resides on an optical sideband that is transported via an optical fiber as seen in Fig. 4.2. The inside of the cart houses several laser sources, a master laser that is used to feed each of the MZMs, an Erbium Doped Fiber

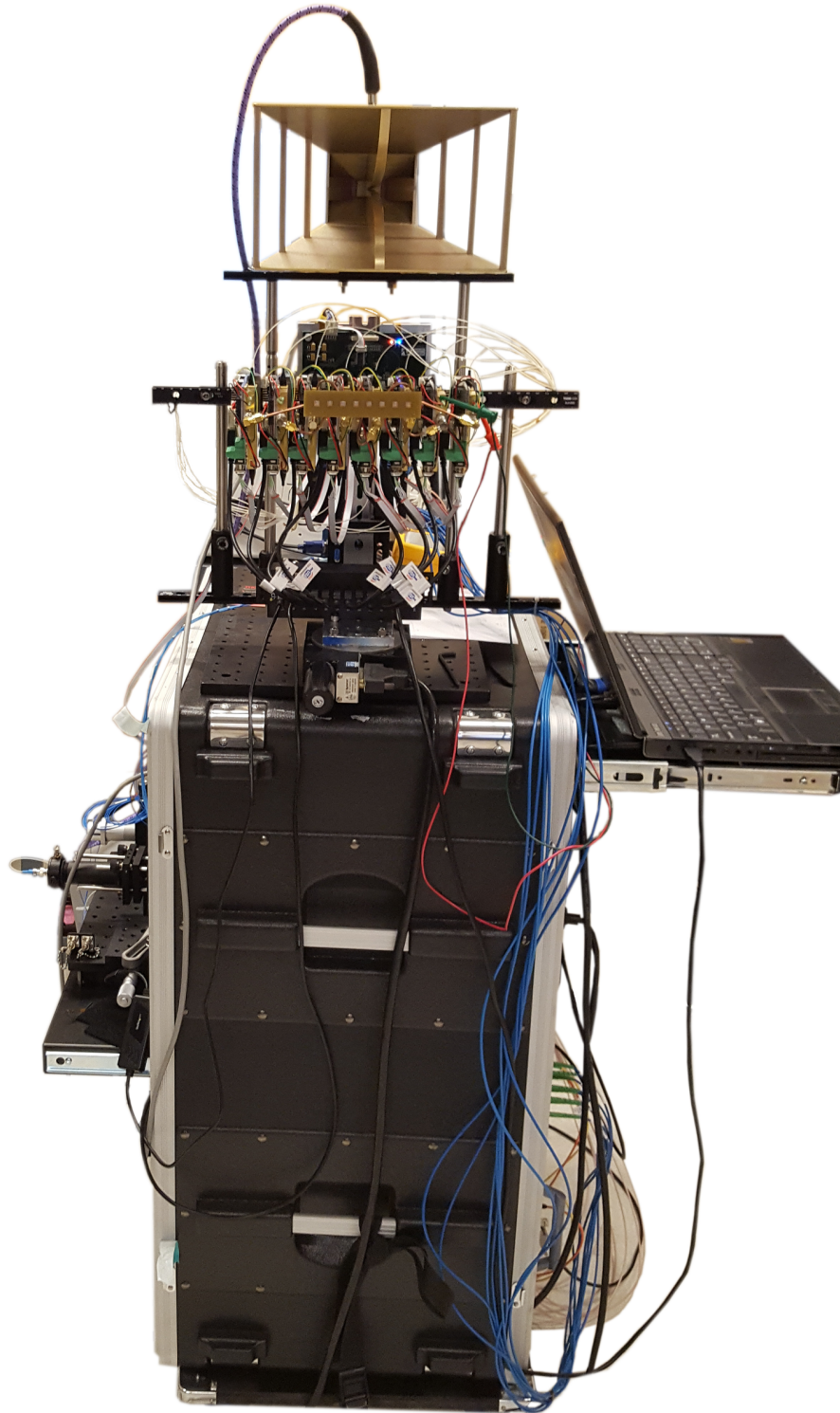


Figure 4.1: Photograph of the prototype Receiver array with the Radar Transmit horn fixed above it. The box below the array houses the optical array processing chain along with a number of laser sources and power conditioning devices.

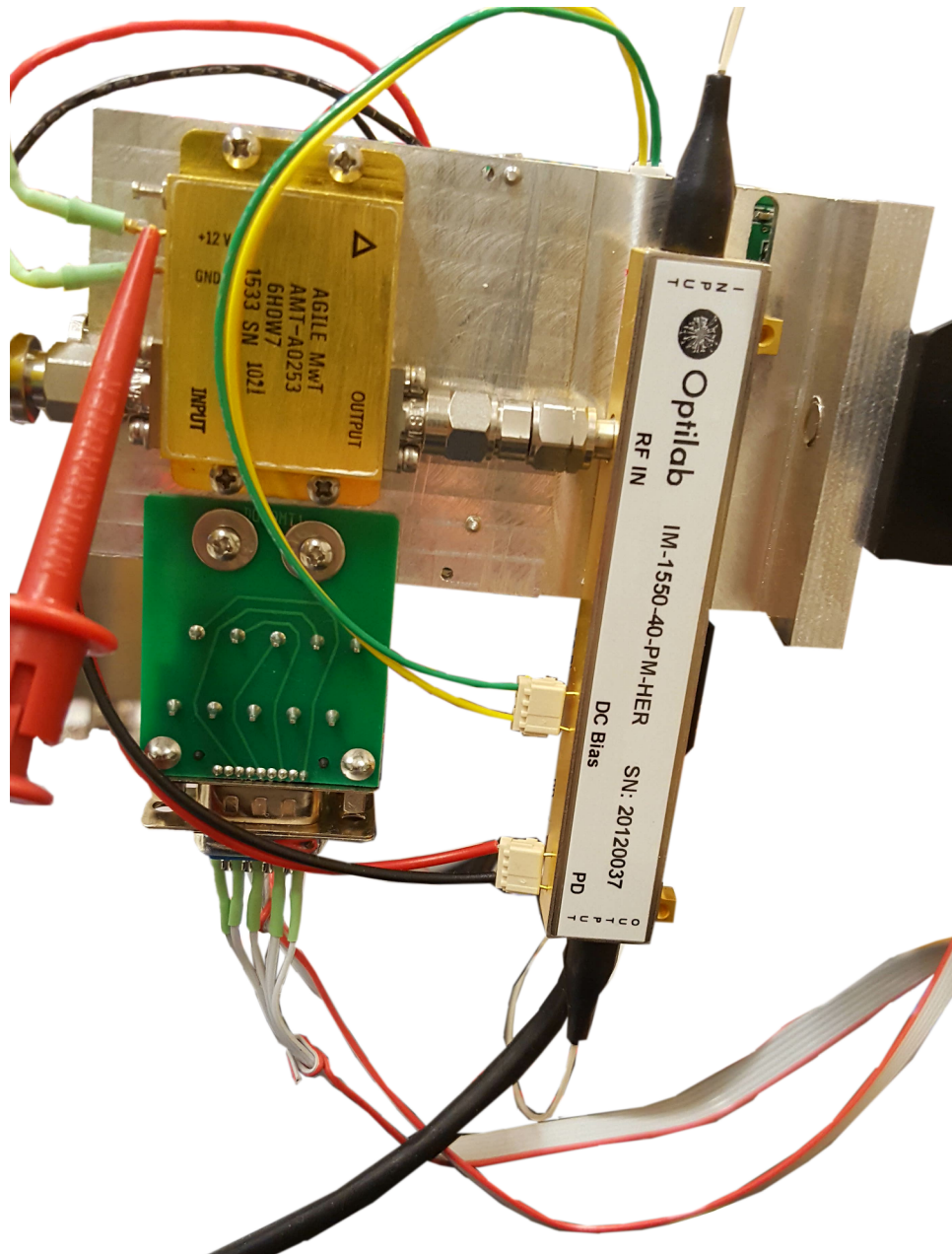


Figure 4.2: Photograph of the prototype gain and up-conversion stage behind each element of the RF array that feeds the array processing system. Not shown in the image is the back side of the unit where a circuit card assembly (CCA) is held for controlling the MZM bias.

Amplifier (EDFA) that is used to amplify the master laser prior to the MZMs and a local oscillator (LO) laser source that is used for optical heterodyning at the output of the beam-space. Also inside the cart are several electro-optic phase modulators that are used to apply the necessary phase shifts to the optical fibers such that they can maintain coherence. The phase offsets are measured via photo-detector board that resides as part of the optical array processor. The schematic of the array processor is shown in Fig. 2.13, while the prototype optical chain is pictured in Fig. 4.3. An

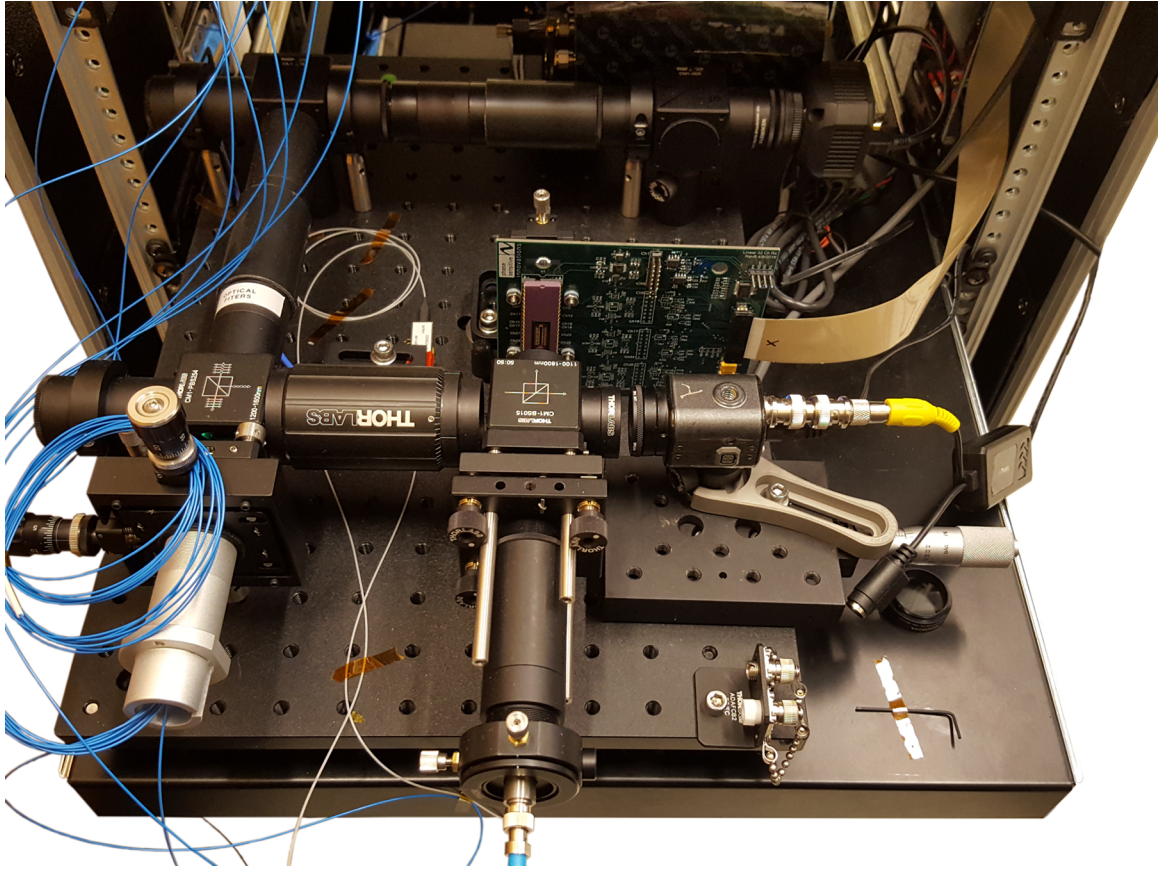
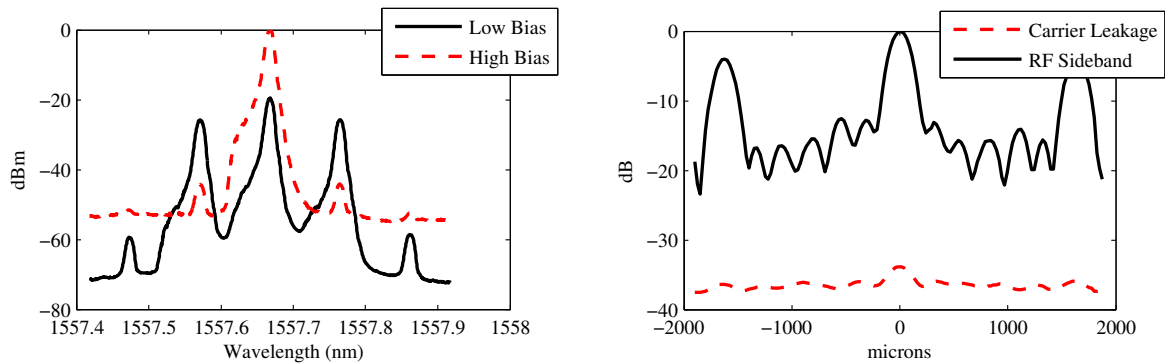


Figure 4.3: Photograph of the prototype optical Array processor.

important function within the optical processing chain is that of carrier tracking and suppression. The photonic array processor has the unique need for the carrier to be left unsuppressed until after phase-offsets between the channels can be measured. However, failure to suppress the carrier prior to output of the beam-forming optical system results in the large carrier response simulated in Fig. 2.6d.

A number of carrier suppression methods have been proposed in the literature with two main classes of techniques evident: optical filtering and modulator biasing [28]. For the experimental photonic array processor described within this thesis, carrier suppression is achieved via a combination of low-biasing of the front-end modulators with additional carrier rejection in the beam-space processor via a stack of thin-film optical filters. To the knowledge of the author, this is the first system to use both classes of suppression techniques in series within a multi-channel photonic link architecture. The first level of suppression is done at the elements of the array via a MZM that is biased between “null” and “quadrature.” The measured output of a single MZM at high and low bias points is shown in Fig. 4.4a. In other applications, the modulators may be biased at “null,” further reducing the output at the carrier wavelength; however, some carrier signal is required for the maintenance of phase coherency across the channels within the beam-former. It is therefore desired to allow just enough carrier power through to the first stage of the optical system, where channel-to-channel phase offsets are measured. The remaining carrier signal is then filtered via a stack of thin-film filters prior to the Fourier transform lens. It is necessary for the filtering operation to provide sufficient cancellation so that the RF sideband dominates the output as shown in Fig. 4.4b. The addition of the filter stack also aids in rejection of some increased 2nd and 3rd order spurs that can be introduced due to biasing the modulators away from the quadrature point (i.e. the center of the linear region of the transfer function).

Finally, a variable RF source used to tune the LO laser is the only non-photonic/optical component other than the various digital logic and control boards used to interface with all of the components via the laptop, pictured on the right side in Fig. 4.1. A LabView interface was previously developed to allow for control of the electro-optic modulators, phase-control and the LNAs of the up-conversion stage. Several SWIR cameras are also able to be viewed, one for alignment of the fiber-array and the other for imaging of the continuous spatial spectrum as discussed earlier. Typically, the latter camera output is of interest during experiments and can be viewed and recorded in real-time via the LabView interface depicted in Fig. 4.5. Finally, the large horn seen



(a) Comparison of a single element’s MZM output at both a “high” bias (offset below Peak bias) and a “low” bias (offset above Null bias). Note: The signal floor at -53 dBm is a limitation of the the analyzer used to collect the data and is therefore artificially raised in the “high” bias plot.

(b) A measured beam output using a SWIR camera at the focal-plane of the beam-space processor. The “beam” pattern generated by the leakage of the optical carrier signal is shown to be approximately 34 dB down from the peak of desired RF signal for the case shown.

Figure 4.4: Plots showing the effects of Carrier Suppression and Leakage.

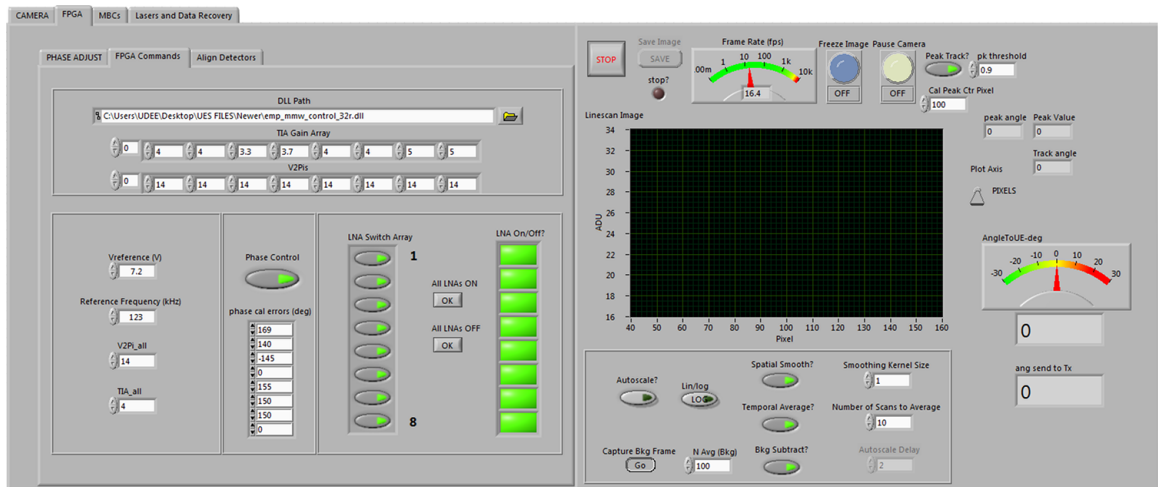


Figure 4.5: Screen capture of the LabView program that allows for control of the photonic up-conversion and phase control stages along with collection and processing of the beam-space imaging SWIR camera.

in Fig. 4.1 is a wide-band transmit horn that is fed by the “PXIe cart,” as discussed next.

4.1.2 Signal Generation, Digitization and Processing Cart

The second cart used for experimentation contains the signal generation, digitization and processing components all contained within a single National Instruments PXIe chassis. The “PXIe Cart” is used to generate the radar waveforms that are transmitted via the wide-band horn pictured above the receive array in Fig. 4.1. The PXIe chassis contains a base-band RF signal generator with a high-speed, dual-channel 16-bit Digital-to-Analog Converter (DAC). The signals are generated via the use of an Arbitrary waveform generation capability built into the National Instruments PXIe-7972R FPGA Card. The DAC is contained within a National Instruments 5782 Input/Output module that is seen as the protruding card on the left side of the chassis pictured in Fig. 4.6. The DAC card is configured to output a base-band I/Q signal. For the purposes of experimentation, it was desired to maximize the range resolution that could be sampled on receive. Thus, based on the discussions in Section 3.2, a Linear Frequency Modulated Chirp of 100 MHz was programmed. The pulse width, pulse rate and transmit and receive gating was performed via the on-board FPGA within the 7972R. The maximum pulse width of the signal is limited by on-board memory within the FPGA to something on the order of a second, however; the limit was never approached during experimentation since typical radar pulse lengths are measured in microseconds. All signaling and clocks were derived from a single high-fidelity clock that is generated by a NI-6674T, timing and synchronization module. The 6674T was also used to route all of the triggers, generated via the 7972R, to the other cards within the system using an equal trace-length bus. Thus, upon receipt of the transmit trigger, the I/Q outputs from the DAC card are fed to a Programmable Signal Generator (PSG) that serves as an I/Q mixer. The PSG is configured to accept wide-band I/Q inputs and is used as an up-converter stage for the 12 GHz transmit signal. The 6674T can also be used to route a pulse-on gate signal to the PSG for pulsed operation. The output of the PSG

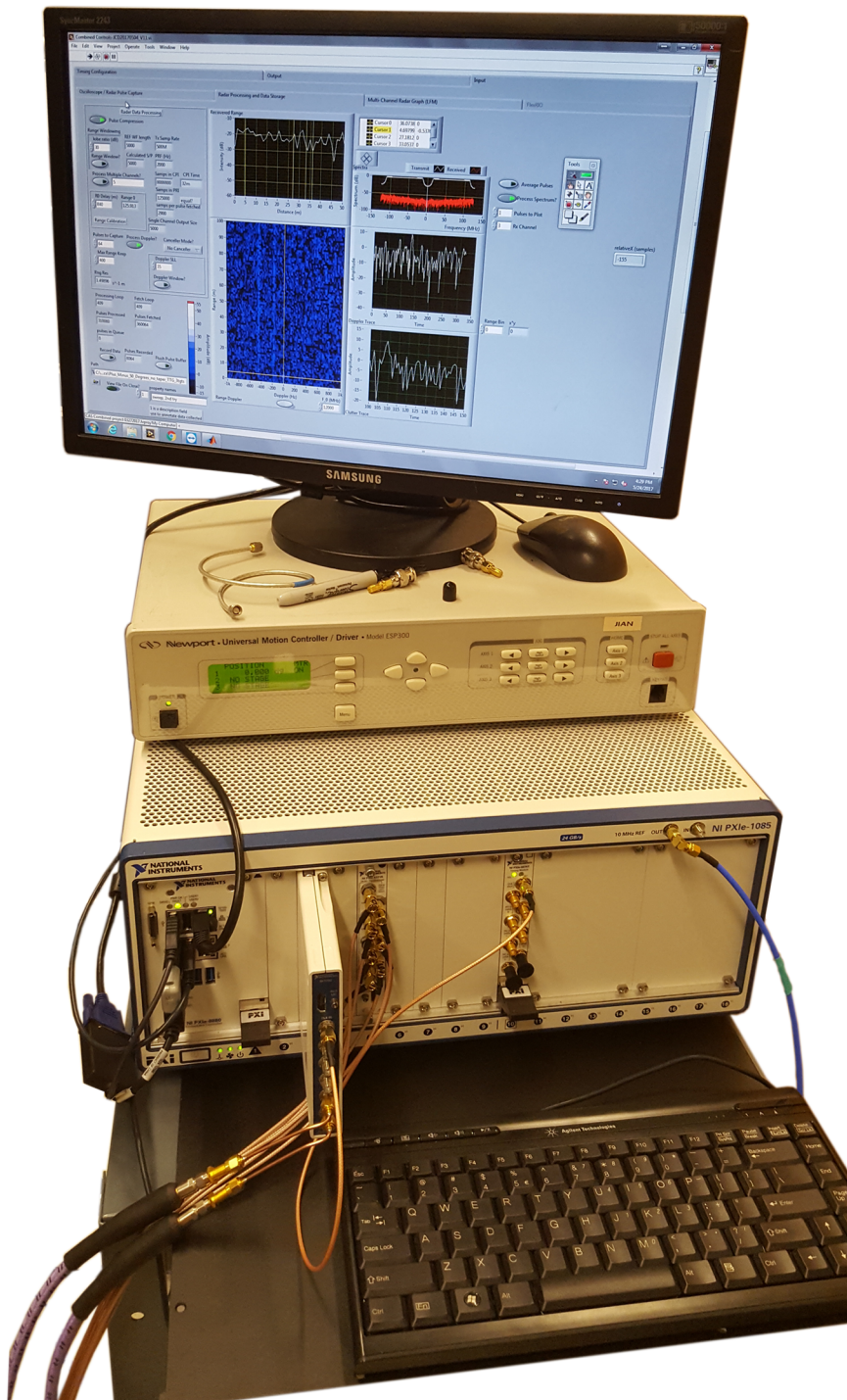


Figure 4.6: Photograph of the National Instruments PXIe Chassis with all cards installed. The box just below the monitor is the controller for the angular positioning stage that is beneath the RX array, used for calibration sweeps.

is fed to an external amplifier, if necessary, prior to being radiated via the wide-band horn. For laboratory experiments, the transmit horn is directed toward a photonic test target generator (TTG) that is used to generate a set of return echoes that would not otherwise be possible within the confined space of the laboratory environment.

Upon reception of the returned radar signals, along with any other RF signals within the field-of-view of the receive array, the photonic array processor described in Chapter 2 is used to down-convert and sample an orthogonal set of beams as detailed in Sections 2.3.6 and 6.2.1, respectively. The output of the beams are sent to a National Instruments Reconfigurable Oscilloscope (NI PXIe-5171R) with eight (8), 14-bit channels capable of sampling at 250 Msps. The 5171R is used to digitize the each beam's down-converted output. The on-board FPGA within the 5171R allows for real-time signal conditioning and has plenty of room left for performing digital-IQ generation on the fly. For the purposes of experimentation here, the digital I/Q generation was done using the single board computer (SBC) that is seen as the left-most, quadruple-wide, card in the PXIe chassis. Each channel results in a digitized complex, base-band dataset that can be recorded to a hard-disk that is part of the PXIe Chassis. Simultaneously, a LabView program is used to capture, and view Radar processing results in real-time. An example of the real-time radar display from the LabView program is shown in Fig. 4.7. The output beams can be processed individually for separate functions as described in Section 3.3, or processed together to perform spatial spectrum estimation or to form adaptive beams as discussed in Section 3.4.

4.1.3 Radar Test Target Generation

For the purposes of experimentation it is desired to have a controlled environment with known targets. In order to allow for the generation of actual radar return echoes of arbitrary amplitude and time-delay, a radar test target generator was built using components formerly used in an attempt to model a multi-path channel. The radar signal is radiated toward the photonic test target generator (TTG) where the transmitted waveform is received by a horn antenna, time-delayed and re-radiated

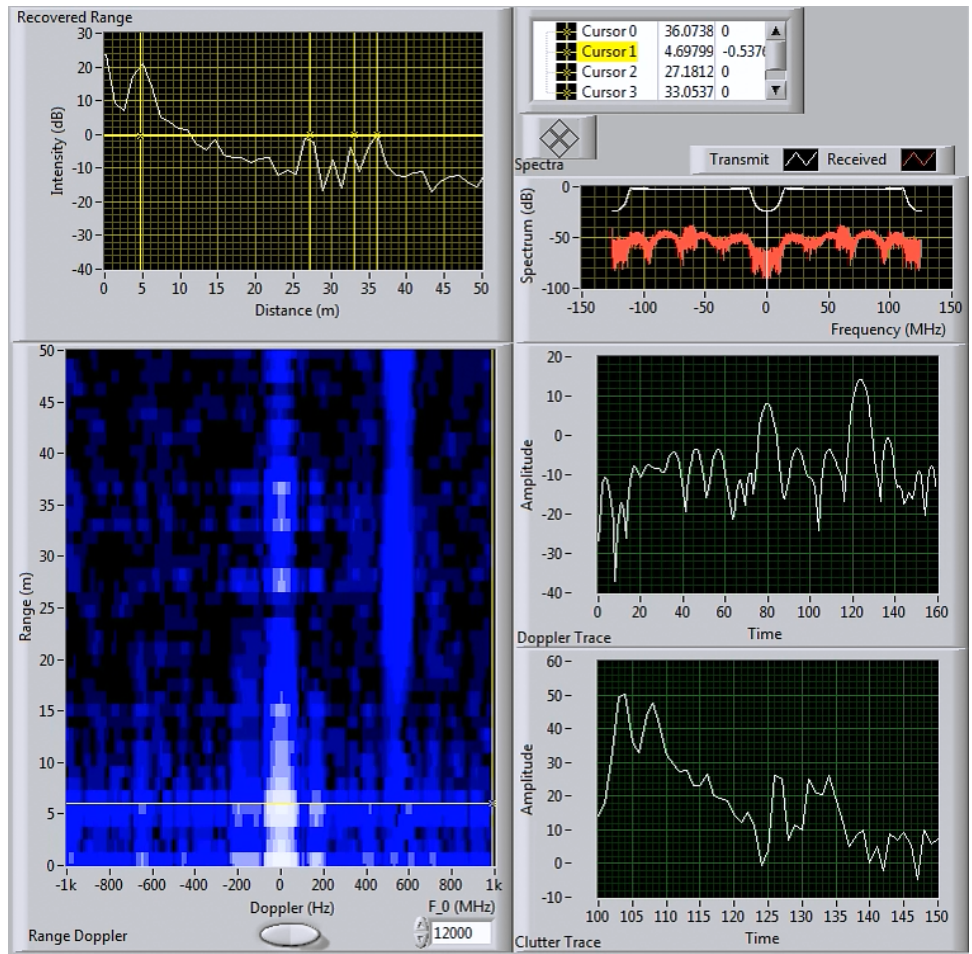


Figure 4.7: Screen Capture of the LabView program interface for collection and processing of Radar Data using the photonic array processor and down-converting receiver.

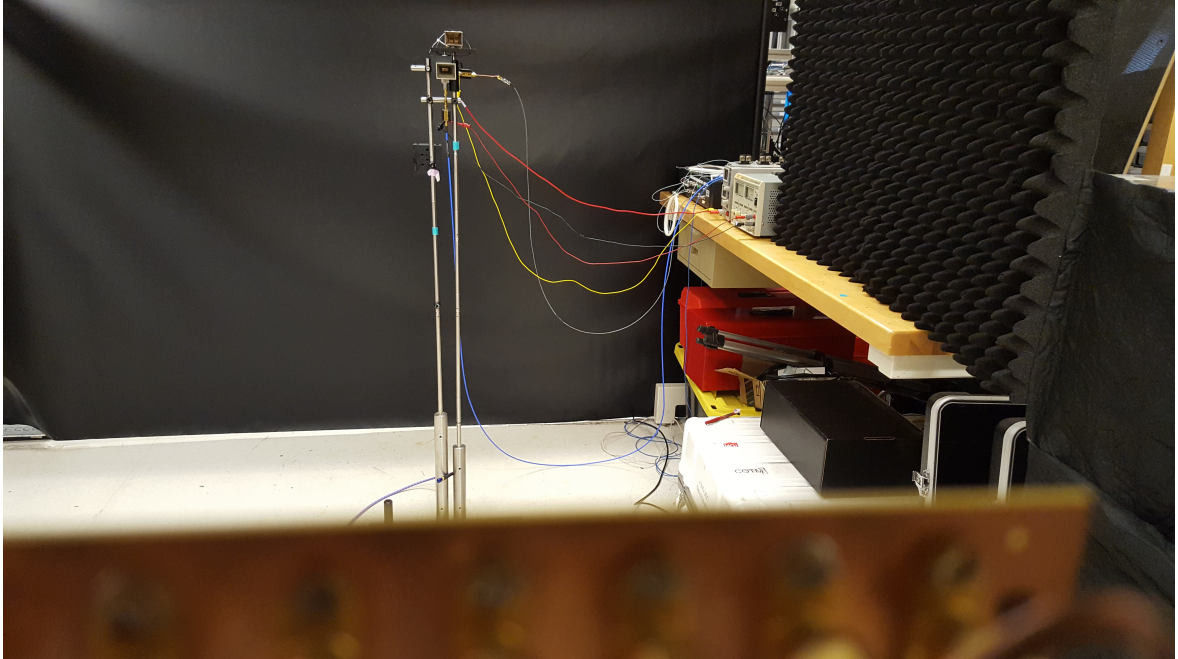


Figure 4.8: Picture showing the RX/TX horns that are part of the photonic radar target generator built for simulating radar targets at ranges that are un-obtainable within the laboratory environment. The picture is taken from the point of view of the Receive Array, showing the relative distance of the TTG receive and transmit horns from the receiver. The TX horn is also used during Calibration to transmit a calibration signal.

back toward the radar via a second horn. The distance of the TTG antennas to the radar system can be made arbitrary, with all of the “range” coming from the ability to change the time-delay of the returns using a set of switch-able optical fibers. The relative distance of the horns can be seen in Fig. 4.8 since the same set of horns were also used for calibration. The TTG used has the ability to create up to 4 synthetic targets (though only 3 were used in the experiments presented here), each with its own range and amplitude. A picture of the TTG is shown in Fig. 4.9, where the three fiber spools that generate the relative time-delays between targets can be seen on the right. Test target generation begins with a set of multiplexed lasers, driven by Thorlabs CLD1015s, that feed a high-speed intensity modulator by Codeon that responds to signals at center frequencies up to 40 GHz. The resultant optical signal is then de-multiplexed allowing each laser to travel through separate optical delay lines.

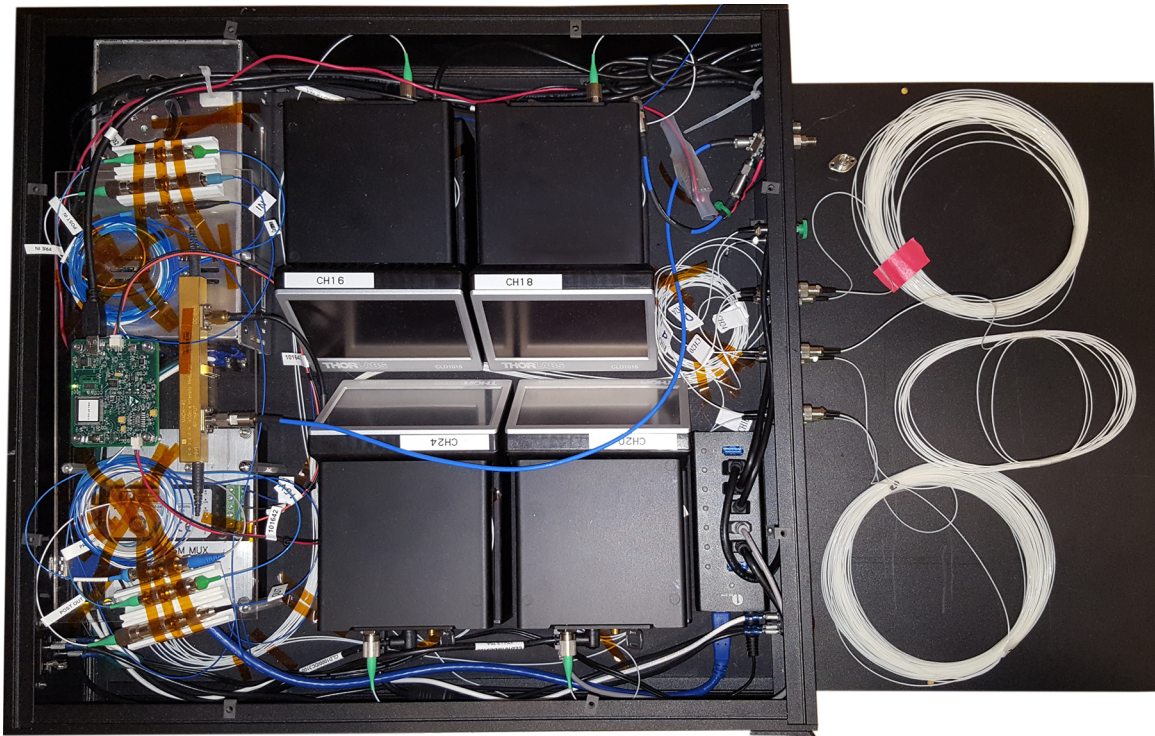


Figure 4.9: Picture of the Photonic Test Target Generator with the top-cover removed. The TTG is used to provide radar target returns for reception and processing during experimentation. The three fiber spools used to generate relative target delays are seen to the right. The 4 Thorlabs CLD1015 laser drivers are seen in the center (labeled Ch16, Ch18, Ch20, Ch24). Each laser can generate one target signal. The MUX and DEMUX equipment along with the Codeon 40GHz intensity modulator are shown to the left of the laser drivers.

The signals can then be separately detected and re-radiated or multiplexed again so that all target returns are radiated from a signal source. Varying the length of each fiber spool allows for precise time-delays to be selected for each generated target, while varying the laser power for each signal changes the apparent target amplitude. The photo-detectors used within this device must be sensitive to the RF frequency, thus the final output PD that generates the signals to be sent to the TTG transmit horn is a μ^2t (now Finisar) 50 GHz bandwidth photo-detector. Thus, the target generator, as configured, can generate synthetic targets for any signal that is under the 40 GHz limit of the first stage intensity modulator. The TTG's output photo-detector signal is fed directly to an amplifier after which it is radiated via an x-band horn antenna back towards the receive array.

4.1.4 QPSK Signal Generation

In order to show multiple functions, a second signal source consisting of a QPSK signal of random values is set up according to Fig. 4.10. The signal is generated at an IF by a 10-bit Arbitrary Waveform Generator (AWG). The AWG is set to generate an I/Q output that is then mixed up to RF using a Mixed Signal Generator (MXG) as the local oscillator. The MXG is fed directly into the LO port of a double balanced mixer configuration, where it is mixed with the combined I and Q signals from the AWG. The communications signal is then amplified and radiated from a second horn antenna. The QPSK signal is configured to output a spectrum shaped by a Root-Raised Cosine Filter on transmit. The total radiated bandwidth can be varied from 1 to 100 MHz and is well contained via the applied Root-Raised Cosine filtering.

4.2 Experimental Setups

Two distinct sets of experiments were performed. The initial experiments were designed to test the theory introduced in Section 2.3.5 and determine the limits of apodization performance for the photonic system. This early work in apodization was focused on applications where beams could be assumed stationary and separated by at

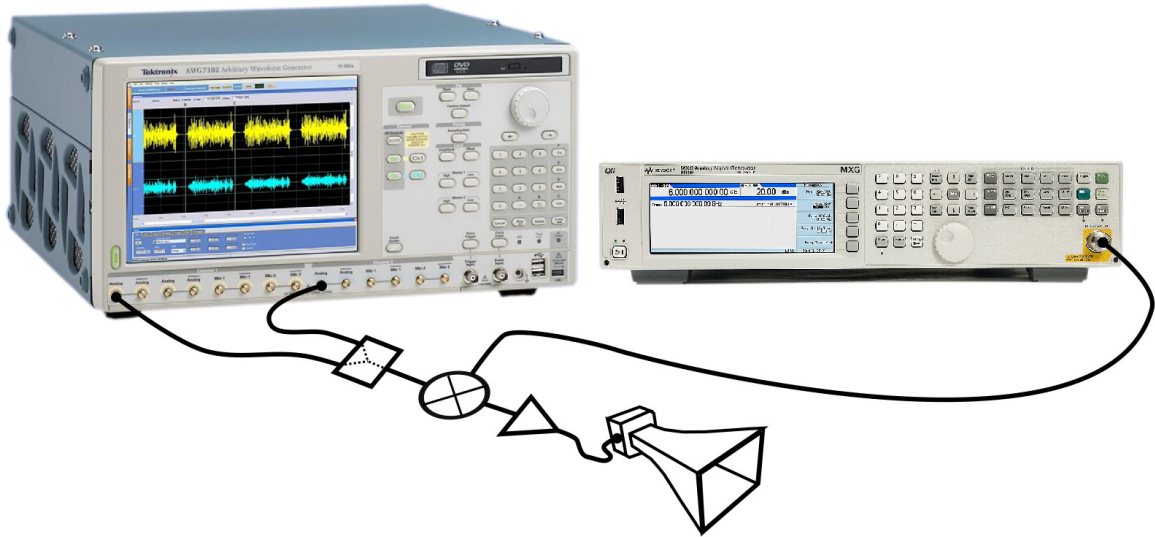


Figure 4.10: Graphical depiction of the equipment used to generate a QPSK signal at various center frequencies for experimentation. The complex QPSK signal was generated at an IF using a 10-bit Tektronix AWG. The I/Q signals were combined and then mixed up to RF using an Agilent MXG as the variable Local Oscillator Source. The communications signal was then radiated via an amplified and horn antenna toward the Receive array.

least a null-to-null beam-width. Thus, the intent was to generate a set of output beams that had extremely low side-lobes to improve the spatial isolation between adjacent spatial channels [54]. These experiments utilized a set of CW sources of differing power levels, such that both could be detected upon application of apodization profiles across the master-laser inputs to the modulator array. These experiments are the focus of the discussion in Chapter 5.

The follow-on experimentation endeavored to prove the theory developed in Sections 2.3.4 and 2.3.6. During these experiments, the Radar and QPSK signal generators described in Sections 4.1.2, 4.1.4 and 4.1.3 are used extensively in order to show the ability of the system to operate on multiple functions simultaneously. The experiments begin with the capture and calibration of a full dimension beam-space and end with the simultaneous processing of a Radar and QPSK signal at the array processor output. The discussions in Chapter 6 focus on these multi-functional experiments.

Chapter 5

EXPERIMENTAL RESULTS ON THE GENERATION OF APODIZED BEAM-SPACES VIA PHOTONIC UP-CONVERSION

5.1 Motivation for Beam-Space Apodization

An unweighted array will possess a power pattern resembling that shown in Fig. 1.2b. The “beam” in Fig. 1.2b possesses a sinc-like response, typical of a sampled periodic aperture. An individual beam possesses a decaying side-lobe structure with peak side-lobes nominally occurring 13.3 dB down from the main response. We can see a similar result, simulated for the photonic array processor output in Fig. 2.6. However, in many applications, the input signals of interest can be small compared to interference or other unwanted signals in adjacent beam positions. Thus, if a signal of interest and an interference signal enter the array from adjacent spatial locations it is highly probably that the side-lobes of each individual beam will interact. This issue is particularly troublesome when one signal’s side-lobes are of equal power to an adjacent signal’s main-lobe. This effect can be visualized quite easily with the optical beam-space processor because the lens system produces a continuous Fourier spectrum at the output. With a peak side-lobe level of -13.3 dB, a desired signal must be of a large enough magnitude to provide sufficient signal-to-interference ratio for reliable isolation and subsequent error-free processing. In instances where one spatial channel is masked by a large interference source incident in the adjacent spatial channel, lowering of the array output side-lobes may provide enough isolation to allow detection of the desired signal. An example is shown in Fig. 5.1, where the desired signal, in black, is 17 dB below a interfering signal slightly off bore-sight. To improve isolation of signals in the presence of high-amplitude signal sources, we wish to limit the side-lobe levels of the spatial receive channels at the output of the photonic array processor.

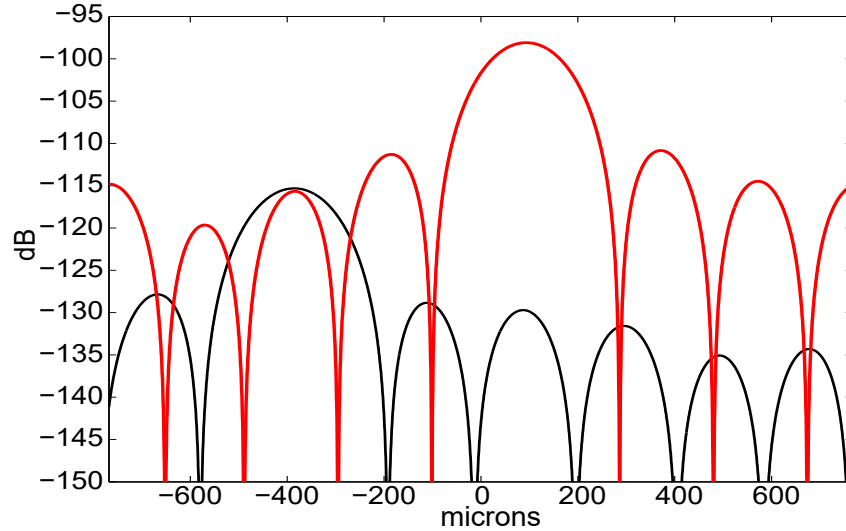


Figure 5.1: Simulated outputs of an 8-channel beam-space beam-former with a large interfering signal (red) entering the array slightly off-bore-sight along with a desired signal (black) entering in an adjacent spatial channel [54]. © IEEE 2017.

5.2 Creation of Apodized Beams Using a Prototype Photonic Beam-space Processor

As in any apodization scheme the effects are realized via a pattern of weights that are applied across the physical dimensions of the receiving aperture. A method for tapering via a transmissive film in the optical path of a photonic beam-space processing chain was introduced in [39]. An important negative side effect of tapering in the free-space optical domain is the removal of optical power that was put into the system. In order to avoid the unnecessary loss of input optical power the techniques discussed in Section 2.3.5 were developed. The tapering or weighting functions used for experimentation are real-valued, and thus only operate on the relative amplitudes of the array elements. A subsequent chapter discusses the usage of complex weightings that allow for generation arbitrary array responses (within the limits of the array’s available degrees of freedom).

For this reason, the apodization experiments began with applying an optical amplitude profile across the master laser feeds to the photonic up-conversion stage

behind each element of a wide-band array. The array of wide-band elements can be seen in Fig. 5.3, where all 8 elements are used in the tapering experiments.

5.2.1 Experimental Setup for Spatial Isolation Data Collections

The experimental setup includes two RF sources within the field of view of the RF antenna. The wide-band antenna used for these initial experiments could not be critically sampled, thus the field-of-view of the photonic array system is significantly constrained. For this reason the sources were placed offset from one another with one at bore-sight to the antenna array and another placed 22.5 degrees off-bore-sight as shown in Fig. 5.2. Initially only the bore-sight source is turned on so that proper calibration

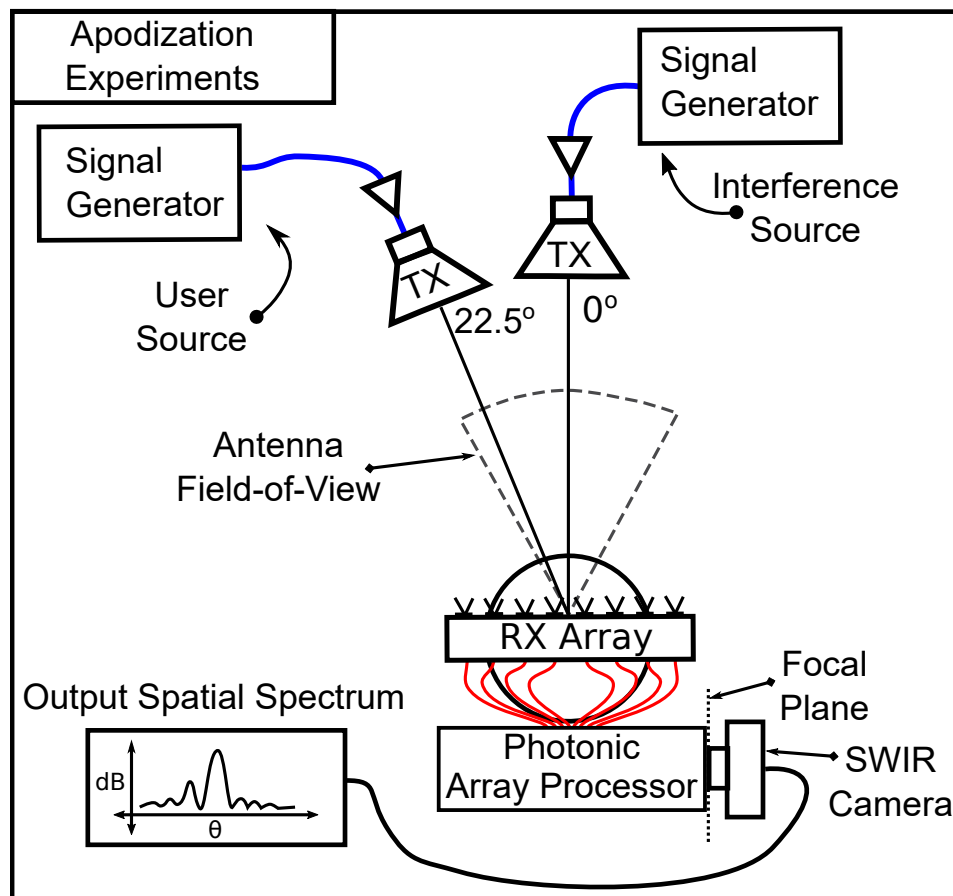


Figure 5.2: Schematic Overview of the Experimental Setup for the Apodization Experiments

of the array can be verified. The array is initially calibrated with a flat amplitude

profile which produces no appreciable apodization of the array side-lobe response. It was found that each elemental channel had drastically different optical insertion losses, therefore, calibration is absolutely necessary, even when no apodization is applied. The calibration of the amplitudes of each element is facilitated via measurement of the signal levels of each individual element at the output of the photonic array processor. The measurements are made using a logarithmic SWIR detector. A flat amplitude and phase calibration results in the expected -13.3 dB peak side lobe levels. Figure 5.4 shows the array response at the photonic beam-space beam-former's focal plane with both measured and simulated data overlaid and seen to be in good agreement. The grating lobe pattern that is evident within Fig. 5.4 is due to the spacing of the optical fiber bundle, as discussed in Section 3.1. We next wish to show that the side-lobe levels can be apodized via application of a weighted distribution to the input optical carrier laser source as hypothesized and simulated in Section 2.3.5.

5.2.2 Experimental Validation of Apodization Via Weighting of the Master Laser

As discussed in Section 2.3.5.2, the optimum method for applying an amplitude profile—when considering effects to system prime-power efficiency—is to avoid attenuation and instead opt for efficient distribution of the laser. The one draw-back of this approach is that it only allows a single apodization profile to be used, thus for the purposes of experimentation, input laser powers to the modulators at each element are adjusted via a set of variable attenuators. When no side-lobe apodization is desired the eight laser inputs are equalized to provide a flat amplitude distribution across the array, which results in an array response like that seen in Fig. 5.4. When side-lobe apodization is required, a symmetric amplitude distribution can be applied across the master laser inputs. In turn, the amplitude distribution of the optical sidebands that carry the RF signal information is affected proportionally. This results in a tapered beam profile at the output of the photonic beam-space array processing system. In order to demonstrate the concept, a set of amplitude weights was calculated using the

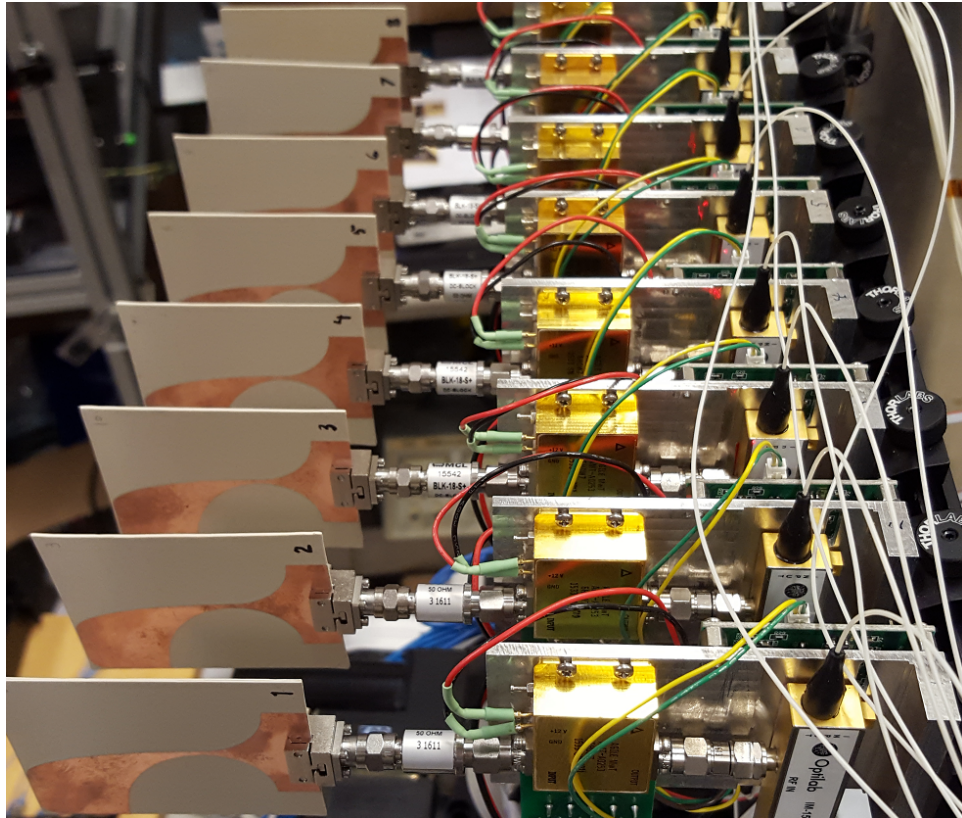


Figure 5.3: Picture of 8-element array used for spatial isolation experiments as reported in [54]. © IEEE 2017.

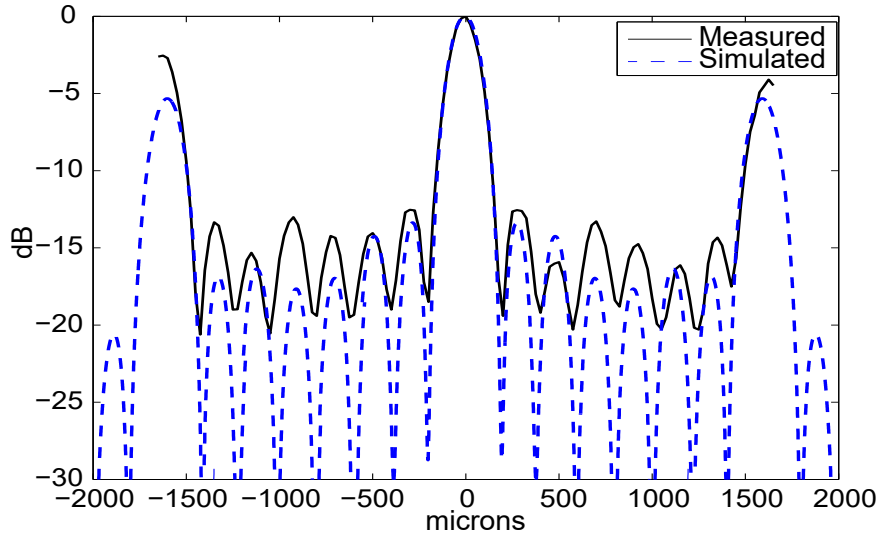


Figure 5.4: Overlay of simulated and measured data for a bore-sight RF source incident on the 1x8 prototype array [54]. © IEEE 2017..

Taylor synthesis technique [40]. A desired sidelobe level for the experiments was chosen to be -35 dB from the main-beam peak. The calculated weights, shown in Table 5.1, were set using attenuators in-line with each modulator. Specific choice of weighting functions is dependent on system isolation requirements and the technique presented is compatible with any amplitude weighting. A recent survey of potentially useful apodization functions can be found in [72]. The resulting beam-space output is shown in Fig. 5.5 along with the ideal response. Clearly, the measured response is limited by a root-mean-square (RMS) side-lobe floor as it fails to approach the ideal, desired side-lobe levels. Even still, the results of Fig. 5.5 show a marked improvement in the overall side-lobe level of the array response. The peak sidelobes have been reduced by 8.2 dB.

To illustrate the importance of side-lobe apodization in terms of achievable spatial isolation, a second source at 22.5 degrees off-bore-sight was turned on with an amplitude set to be 14 dB below that of the source at bore-sight. The scenario described above results in the measured beam-space outputs shown in Fig. 5.6. Comparison of Fig. 5.6a to Fig. 5.6b shows that the apodized array allows for the previously

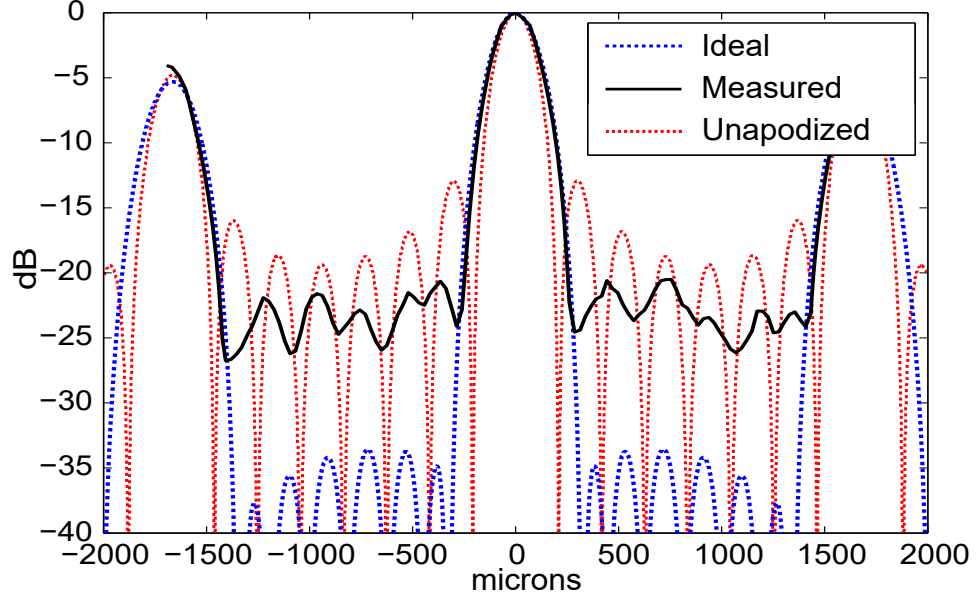


Figure 5.5: Measured prototype array response for a bore-sight RF source when the array is apodized via the amplitude profile listed in Table 5.1, overlaid with the Ideal response of the given weighting profile along with an unapodized reference.

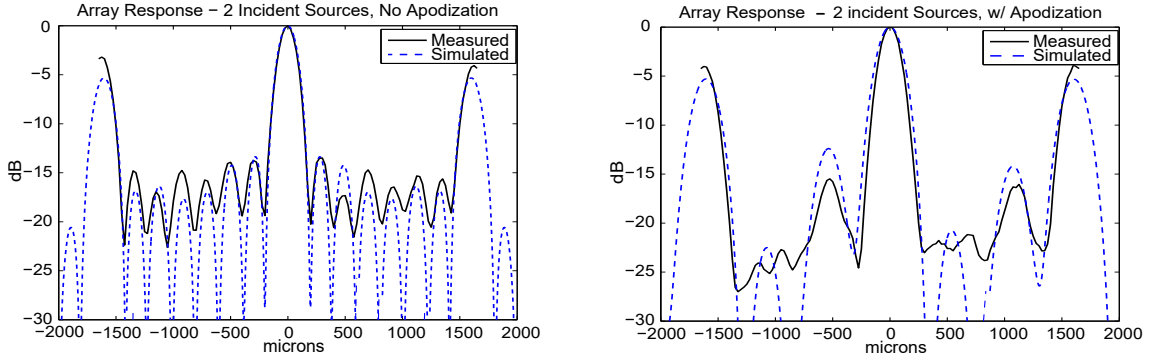
Table 5.1: Input Laser Weighting for Each Optical Modulator

MZM_n	1	2	3	4	5	6	7	8
(Ratio)	.213	.475	.791	1	1	.791	.475	.213
(dB)	-6.7	-3.2	-1.0	0	0	-1.0	-3.2	-6.7

undetected source at 22.5 degrees to be resolved at the output of the beam-space processing chain with a peak-to-side-lobe ratio of 7.5 dB such that it might be sampled with a high-speed photo-detector, enabling recovery of the desired signal. The initial results, shown in Fig. 5.5, indicate the presence of some un-mitigated amplitude and phase errors within the beam-forming system. If no errors were present, the measured apodized beam pattern would match the ideal perfectly.

5.2.3 Analysis of Error Sources within the Photonic Array Processing Chain

In order to verify the existence of an RMS side-lobe floor, and measure the level precisely, a number of additional experiments were carried out.



(a) Beam-former output of array response without apodization (b) beam-former output of array response with apodization profile from Table 5.1

Figure 5.6: Measured and simulated photonic beam-space beam-former response with two incident sources. From [54]. © IEEE 2017.

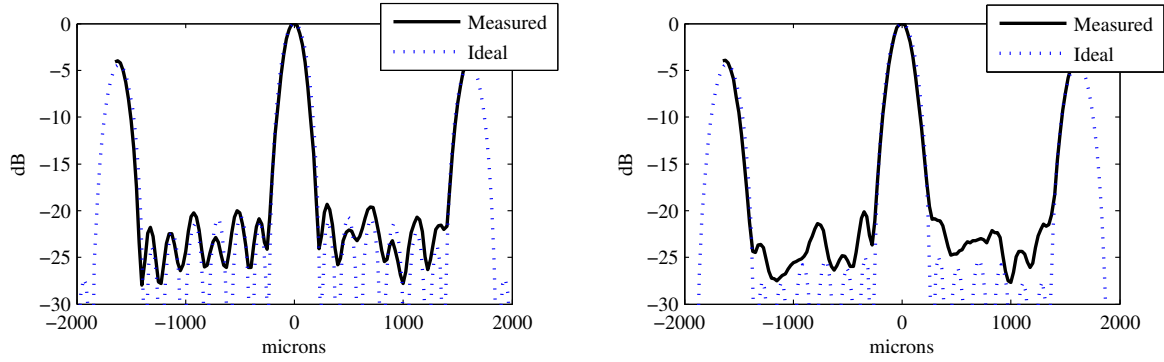
5.2.3.1 Additional Tapering Experiments

A number of additional apodization profiles were generated in order to measure the resulting beam-patterns in an effort to determine the source of the side-lobe floor seen during the initial experiments. The relative amplitude offsets for each channel are shown in Table 5.2. The results for each of the tapering functions are shown separately in Figs. 5.7a, 5.7b, and 5.7c so that they may be compared to the ideal array response in each case. Inspection of the measured results in Fig. 5.7a shows that the weighting

Table 5.2: Table of different amplitude weighting functions used for experimentation to validate the proposed apodization method. Tapering functions are applied via a weighted distribution of the feed laser. *The -27 dB taper mimics the realized weights using commercial splitters as discussed in Section 2.3.5.2.

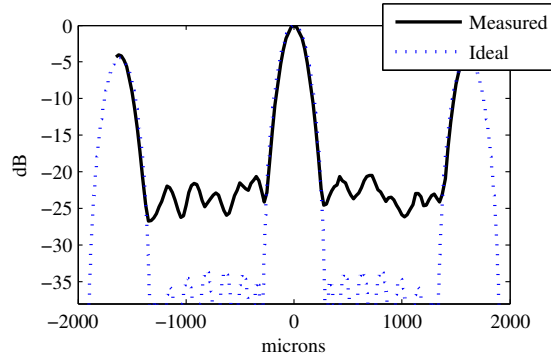
MZM_n	1	2	3	4	5	6	7	8
-22 dB	0.56	0.64	0.87	1.00	1.00	0.87	0.64	0.56
-27 dB*	0.38	0.58	0.86	1.00	1.00	0.86	0.58	0.38
-35 dB	0.21	0.48	0.79	1.00	1.00	0.79	0.48	0.21

of the master laser produces the desired beam-pattern. However, as the taper functions become more aggressive, as in Fig. 5.7b and Fig. 5.7c, the measured results begin to deviate from the ideal cases until an average sidelobe floor is evident at approximately -23 dB. The -35 dB taper produces a beam-pattern that is limited exclusively by the



(a) Measured beam-pattern at the output of the photonic beam-space array processor with master laser distribution according to the first row of Table 5.2. At this mild tapering the results are close to the ideal for our small experimental array.

(b) Measured beam-pattern at the output of the photonic beam-space array processor with master laser distribution according to the weights shown in the second row of Table 5.2.



(c) Measured beam-pattern at the output of the photonic beam-space array processor with master laser distribution according to the weights shown in the third row of Table 5.2. The measured result is far from the ideal due to an apparent root-mean-square (RMS) sidelobe floor of -23 dB.

Figure 5.7: Overview of the measured results (black traces) and simulated ideal results (dotted blue traces) for each of the amplitude profiles listed in Table 5.2.

RMS sidelobe floor as seen in Fig. 5.7c as originally reported in [54]. The high average sidelobe level can be caused by a number of defects within the antenna array system, all of which can be reduced to a set of tolerances for amplitude and phase errors across the array channels. Of particular interest are any errors introduced from the photonic components themselves as discussed next.

5.2.3.2 Array Error Analysis for Photonic Array Processor

As seen in Fig. 5.7c, the measured array output does not match the ideal aperture illumination function. The peak sidelobe levels are as much as 14.5 dB out of spec from ideal. The root-mean-square (RMS) sidelobe level measures approximately 23 dB below the main beam peak, with the peak sidelobe level being 20.5 dB down. Since the array errors are random in nature, it is desirable to determine the statistics of the errors affecting the prototype photonic system. Once the statistics are known (or estimated), they can be applied to the numerical simulations discussed in previous sections to better understand how the photonic beam-forming technique will scale to arbitrary arrays and tapers.

5.2.3.3 Determination of Error Statistics

Precise determination of the statistics of small arrays is difficult, if not impossible, since simplifications via the Central Limit Theorem are not necessarily valid [6]. However, an approximation of the peak sidelobe errors may be determined by following a method similar to [73]. The first step is to define the array pattern with errors to be

$$F_e(\phi, \theta) = \sum_1^N (1 + \delta_{a,n}) \cdot A_n \cdot e^{j\delta_{\phi,n}} \cdot e^{-j\frac{2\pi}{\lambda_r f} \cdot n \cdot d \cdot (\cos(\phi) \sin(\theta) - \cos(\phi_s) \sin(\theta_s))}, \quad (5.1)$$

where $\delta_{a,n}$ is the amplitude error (applied as a multiplicative error), $\delta_{\phi,n}$ is the phase error (in radians), ϕ_s and θ_s are desired steering angles as defined in Fig. 2.7. Assuming

that the array errors are small and that the array pattern is Rician distributed, the variance of the array errors can be approximated as:

$$\sigma^2 \approx \frac{1}{2} \cdot (\sigma_{\delta_a}^2 + \sigma_{\delta_\phi}^2) \cdot \sum_1^N A_n^2, \quad (5.2)$$

where $\sigma_{\delta_a}^2$ and $\sigma_{\delta_\phi}^2$ are the variances of the amplitude and phase errors respectively, and A_n represents the desired illumination at each element of the array. If it is assumed that the amplitude and phase errors are zero-mean, σ_{δ_a} and σ_{δ_ϕ} can be taken to represent the RMS error levels. It will be further assumed that the illumination functions are normalized such that the sum over the elements is equal to unity. Note, this assumption is in contrast to the treatment given in Section 1.1.1.5, however; the scaling only effects overall array gain, and not the relative side-lobe levels that are of the main concern here. From here, the constant probability sidelobe model in [74] is used to determine the ratio of the illumination function to the achieved (measured) sidelobe levels as:

$$R_s = \frac{\sum_1^N A_n^2}{S_m}, \quad (5.3)$$

where S_m is the measured or achievable sidelobe level given errors. The set of curves generated via the constant probability sidelobe model are used to determine the value of the scaled array error variance to guarantee a sidelobe level equal to our observed levels with a 90% probability.

The most aggressive illumination function used for the previously presented experiments was a -35 dB Taylor window function. The sum of the squares of the illumination yields a -8.18 dB value, while the measured sidelobe level was approximately -20.5 dB, thus

$$R_{s_{-35}} = 12.32 \text{ dB}. \quad (5.4)$$

The measured ratio of designed-to-achieved sidelobe levels for the -35 dB Taylor weighting experiments is

$$\frac{S_{designed}}{S_m} = -14.5 \text{ dB}. \quad (5.5)$$

Using the value in (5.5) as a lookup parameter within the constant sidelobe probability model yields

$$\frac{1}{2} \cdot (\sigma_{\delta_a}^2 + \sigma_{\delta_\phi}^2) \cdot R_s \simeq -6.7 \text{ dB}. \quad (5.6)$$

By inserting the result in (5.4) into (5.6) and reducing, one can arrive at

$$\frac{1}{2} \cdot (\sigma_{\delta_a}^2 + \sigma_{\delta_\phi}^2) \simeq -19.02 \text{ dB}. \quad (5.7)$$

The expression in (5.7) can be then used to determine a set of RMS error values that lead to the ratio of designed to achieved sidelobe levels in (5.5). Thus, the relation in (5.7) can be used to determine the RMS phase errors upon direct measurement of the RMS amplitude errors.

The RMS amplitude errors of the elemental channels was measured directly at the input to the beam-space processor system via an optical spectrum analyzer (OSA). The OSA allows for direct measurement of the optical carrier and the RF side-bands about-the-carrier in a manner similar to an RF spectrum analyzer. Data was collected on the OSA for several minutes and statistics were calculated on the side-bands, since the continuous spatial spectrum of the RF sideband is what results at the output of the beam-former. From the measurements, it was discovered that

$$\sigma_{\delta_a, \text{measured}} = 0.039, \quad (5.8)$$

thus, the amplitude error tolerance, ϵ_{δ_a} , is estimated to be

$$\epsilon_{\delta_a} \simeq \pm 0.59 \text{ dB}. \quad (5.9)$$

By substituting (5.8) into (5.7) and solving for σ_{δ_ϕ} yields

$$\sigma_{\delta_\phi} \simeq 0.153 \text{ r} \simeq 8.8 \text{ degrees}. \quad (5.10)$$

An ensemble of simulated array pattern outputs using the statistical values in (5.8) and (5.10) in conjunction with a -35 dB Taylor illumination function across the master laser inputs to the modulators is shown, in Fig. 5.8, to be in good agreement with measured results.

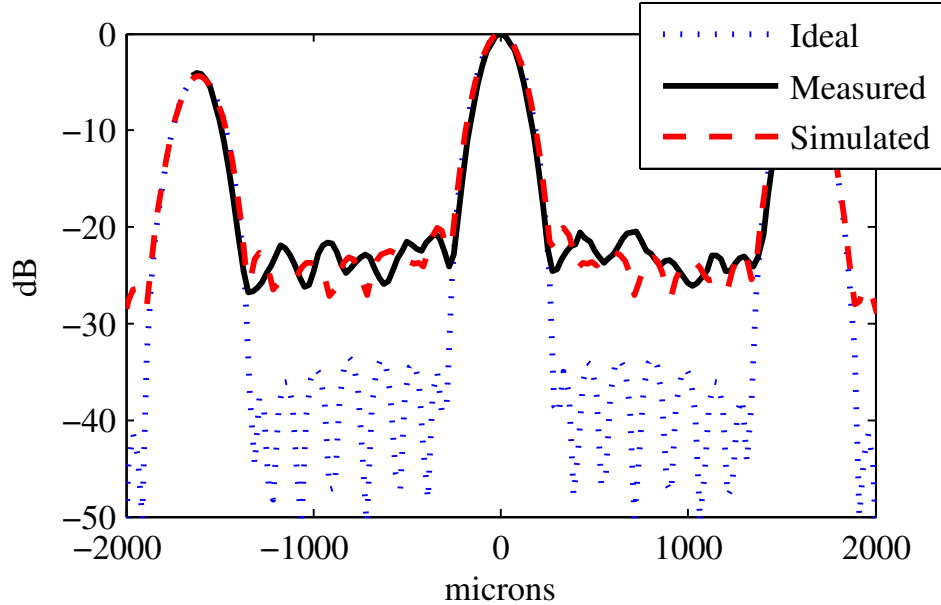


Figure 5.8: A plot of the measured beam-former output (solid, black) overlaid with a simulated output (dashed, red) that includes the RMS errors as measured in (5.8) and derived in (5.10). The measured results were initially reported in [54].

5.2.3.4 Discussion of Error Sources

With the nominal statistics of the array errors having been measured and/or otherwise estimated, it is prudent to discuss likely sources of error so that the array and beam-former performance can be improved in future designs. That being said, the errors, as measured, are reasonable for a large array. It is safe to assume that average sidelobe level performance will improve upon construction of a larger array, assuming the existing errors hold constant [75]. There is, however, an important design detail that limits the practical size of the array that can be beam-formed using a particular instance of the photonic array processor. The sidelobe structure and apparent floor is directly affected by the size of photo-detectors used to sample the Fourier-plane output.

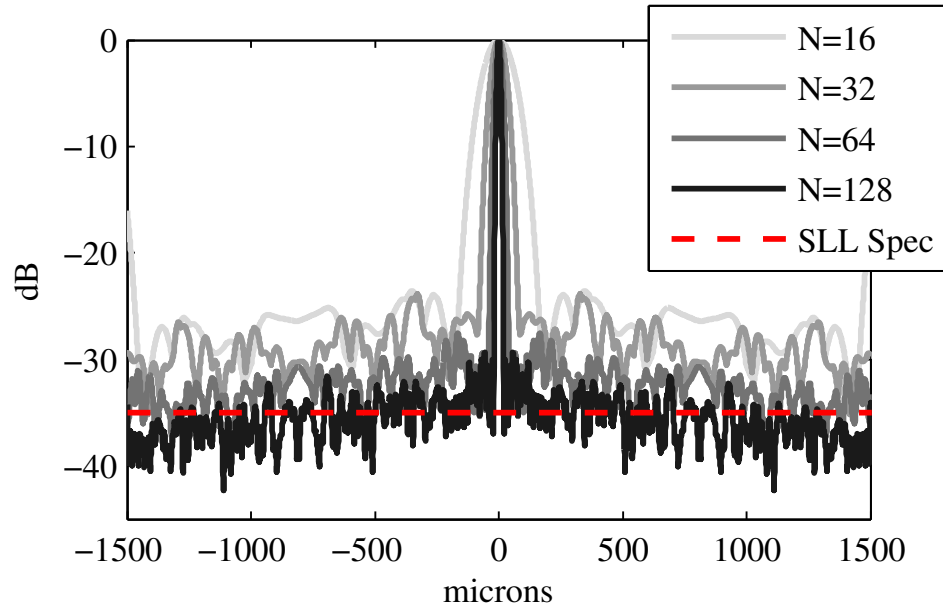
5.2.3.4.1 Sampling Array Effects on Effective Side-lobe Levels

The phenomena just introduced is due in large part to the effective spatial averaging that occurs across the unit area of a given photo-detector. There is some optimization of the relationship between array size and pixel-size that can be performed

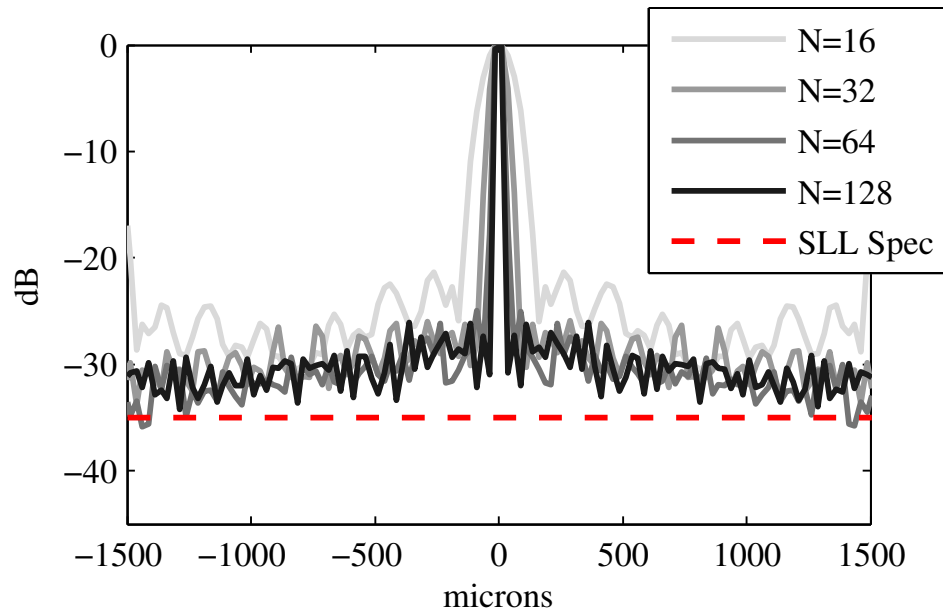
via changes to the magnification, but this optimization is limited by the physical size of the sampling array and the effective field-of-view that is imaged. That is, one can only magnify the output spatial spectrum until it falls off of the detector array. With these limits in mind, once the distance between adjacent sidelobes reaches a point where multiple side-lobes are incident onto a single detector (or pixel), the sampled result is a spatial integration of the array pattern over the surface area of the pixel. This integration effect causes a sidelobe floor in the antenna array pattern upon sampling. Examples of the photo-detector integration effect on the worst-case sidelobe floor for an ensemble of array patterns can be seen in Fig. 5.9. Thus, it is important to consider the overall antenna beam-width (and therefore, the total number of input array elements) when constructing the optical processor and the output plane detector array. Some simulated outputs for the 128 element case across two (2) widely available detector pixel configurations are shown in Fig. 5.10. Keeping all else constant, careful construction of the detector array and other back-end beam-space processing is required in order to ensure the desired RMS sidelobe performance can be reached.

5.2.3.4.2 Photonic Phase Modulation Effects on Effective Side-lobe Levels

Returning again to the front-end error sources, it was initially postulated that the modulator bias controllers were producing a sinusoidal amplitude variation due to the dither tone that is used on the bias. However, for the single-arm modulators used, the dithering should not affect the side-band, only the carrier. This fact was verified via measurements using an OSA and the next stage of the photonic chain was analyzed. At the next stage, it was discovered that a significant portion of the amplitude variation occurs after the phase modulator that is used to maintain channel-to-channel coherence. This is likely due to Residual Amplitude Modulation (RAM) within the 1x8 phase modulator, first studied for its negative effects in spectroscopy [76]. This additional modulation is due to imbalances in the sidebands of the phase modulated laser signal. Several mechanisms that cause these imbalances have been studied including the input beam-intensity profile, input laser frequency, polarization mis-matches



(a) Simulated aperture patterns incident on the photo-detector array. These patterns have not yet been spatially integrated by the physical photo-detector area and increasing the array size reduces the contribution of the array errors to the average sidelobe level.



(b) Simulated aperture patterns after the photo-detector array, showing the effects of photo-detector size (holding errors and optical chain constant) on achievable sidelobe level. For a given error budget, optical chain and detector array, there is a limit to achievable sidelobe level regardless of array size.

Figure 5.9: Simulated outputs of worst-case patterns for different aperture sizes ($N = 16, 32, 64,$ and 128 antenna elements) given existing error budget.

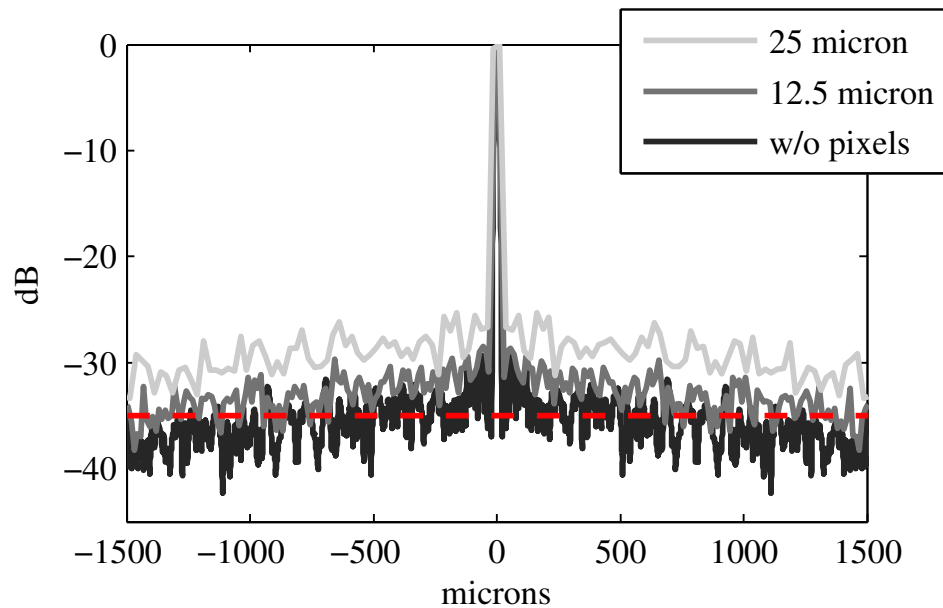


Figure 5.10: Simulated outputs of worst-case aperture patterns, for a 128 element array, as captured when using with two (2) different commercially available pixel pitches (pixel pitch = $25\mu m$ and $12.5\mu m$). Also shown is an ideal, no pixelation, case for the existing system error budget. The RMS sidelobe levels for the depicted worst-case patterns are -29 dB, -33 dB and -36 dB, respectively.

and photo-refractive defects within the modulator itself [76–78]. Measurements of the side-band voltage over time at both the array element MZM and the phase control loop modulator are shown in Fig. 5.11. The results in Fig. 5.11 are normalized to the expected value and any linear trends have been removed. The traces were taken over the same amount of time, however; they are not simultaneously captured. Thus, no direct correlation can be made between time deviations within the traces, but it is clearly shown that the phase control modulator introduces a larger amplitude ripple over all time. A potential source for RAM in the phase modulator is in how the input fibers are coupled to the optical wave-guides of the modulator. This coupling is less than ideally aligned and will be corrected in any future system design revisions. The phase control modulator’s design and subsequent packaging is also suspected to cause cross-talk between the channels due to a common ground on the bias. Thus, when one channel is providing a bias signal, some of the signal leaks to the abutting channels, leading to a phase error. This issue is seen as the most significant as it causes unintentional phase offsets in adjacent channels, contributing to both amplitude and phase errors within the array processing system. It is believed that replacement of the existing 1x8 phase modulator with discrete phase modulators is a candidate for improving the amplitude ripple in the phase control loop until a better 1x8 design can be developed.

5.2.3.4.3 System Phase Error Budgeting for Low-Side-lobe Performance

The calculated phase error budget for the system is divided among several design elements: the antenna element spacing, LNA phase characteristics and the optical phase control modulator. If we augment the relationship in (5.2) with a term to encompass the antenna element positional errors we arrive at:

$$\sigma^2 \approx \frac{1}{2} \cdot (\sigma_{\delta_a}^2 + \sigma_{\delta_\phi}^2 + k_{rf}^2 \cdot \sigma_p^2) \cdot \sum_1^N A_n^2, \quad (5.11)$$

where σ_p^2 is the standard deviation of the element positional error in all translational axes (assumed to be equal) [79,80]. The prototype array’s elements are hand positioned

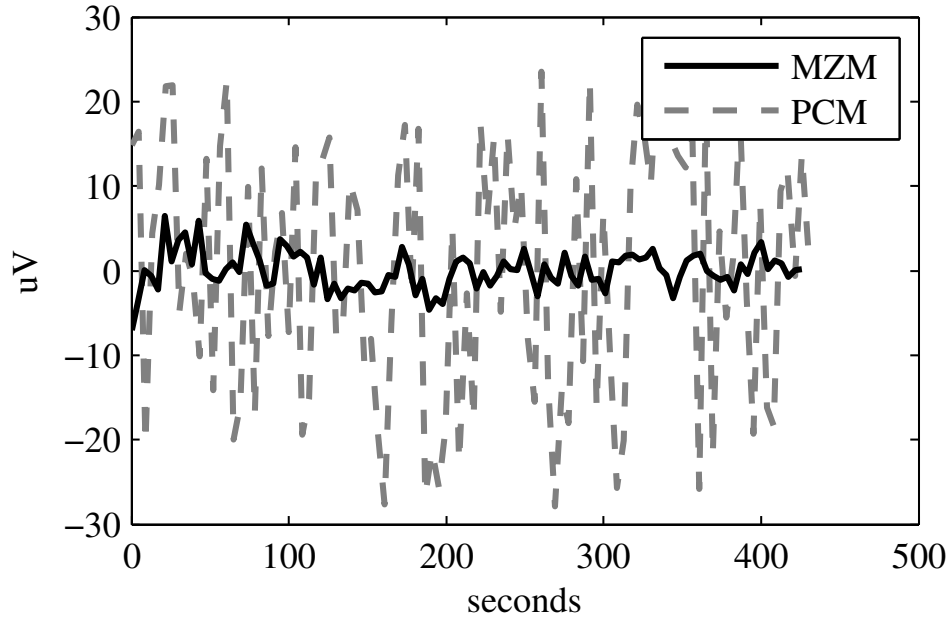


Figure 5.11: Measured RF sideband amplitude, versus time, for a single element’s Mach-Zehnder Modulator and corresponding phase control modulator. The plots clearly show that the phase control modulator has significantly more amplitude ripple than the MZM.

with the aid of a steel rule and movable mounting brackets. This was done to allow for a number of array element positions and array lengths to be studied over various incident radio frequencies. If we assume the positional error to be uniform over $\pm 0.5mm$, due to the inherent precision of the steel rule, we can calculate $\sigma_p = \frac{0.001}{\sqrt{12}} \approx 0.000289$. Using the newly calculated value for positional error and assuming an RF of 17 GHz, we can re-calculate the value for phase error contributions to sidelobe level in (5.11) as $\sigma_{\delta_\phi} = 0.1138 \approx 6.5degrees$. Thus, the phase errors due to the photonic system can be isolated to be approximately equal to a best-case 6.5 degrees RMS value, with the bulk of this error being attributed to the 1x8 phase control modulator. Finally, the LNA’s are not phase matched and only a rough channel-phase calibration is performed before collecting data from the array, however, the bulk of the phase and amplitude error is believed to stem from the phase-control circuit and its associated phase modulator, making a re-design of the existing phase modulator vital to achieving significant

performance improvements in future systems using apodization.

5.3 Significant Outcomes from the Apodization Experiments

The experiments presented within this Chapter showed the ability of the photonic array processor to generate a continuous, weighted, spatial spectrum from an unweighted input array. This result is significant since it validates the ability of the proposed system concept to detect and display the angular locations of incident signals via the relation derived in Section 2.3.4 using the imaging techniques described in Section 3.1, all in real-time. It is noted that the entire spatial spectrum (i.e., beam-space) is projected onto a detector array that is less than 5,000 microns across in the presented experiments. Furthermore, the fiber bundle that is used to transfer the up-converted signals is orders of magnitude smaller in diameter than an associated bundle of RF coaxial cables or wave-guides making the remoting of beam processing functions more amenable to space-constrained applications.

The results of the initial apodization experiments lead to an investigation into error sources that cause an apparent RMS side-lobe floor in the beam-space data. A number of system errors were measured, estimated and/or otherwise calculated in an effort to understand the shortcomings of a prototype system. These investigations led to the discovery of Residual Amplitude Modulation (RAM) within the optical phase control loop's electro-optical phase modulator. The phase modulator was shown to be the cause of considerable amplitude modulation compared to the rest of the RF and optical chains. This RAM signal contributes significantly to the overall sidelobe level performance of a photonic beam-formed system and will require mitigation for the proposed technique to generate low sidelobe arrays with a small number of elements.

Finally, the measured errors that exist in today's system, were shown to be sufficient to produce arrays with sidelobes well below -35 dB as the number of elements becomes greater than 128. This result also led to the discovery of the sampling effects of various detector configurations. It is therefore important to carefully design the optical processing chain along with the output detector array due to a spatial integration

phenomena that occurs across the physical size of the photo-detectors. As the size of the array increases it is necessary to reduce the size of the photo-detectors, or increase the magnification of the optical system to compensate. Future systems with large element numbers are more likely to require lens systems with increased magnification due to limitations in the manufacture and usage of smaller photo-detectors. The lessons-learned in precise sampling of the beam-space are carried forward into the next set of experiments—discussed in Chapter 6—where the down-conversion, spatial-sampling, digitization and processing of a full-dimension beam-space of a critically sampled input array is undertaken.

Chapter 6

RECOVERY OF A PHOTONICALLY-GENERATED FULL-DIMENSION BEAM-SPACE FOR MULTI-FUNCTION APPLICATIONS

A natural follow-on to the initial experiments in the imaging and capture of an apodized spatial spectrum for the purposes of increasing spatial isolation of two or more adjacent channels is to attempt to recover the signals that are incident in each of the channels using the optical heterodyning and beam-space sampling concepts introduced in Chapter 2.

6.1 Dual-Beam multi-function Experiments

Initial multi-function experiments were performed in a manner similar to those reported in [81], where selected spatial channels were isolated using optical heterodyning and high-speed photo-detectors. The experimental setup is shown in Fig. 6.1. Here the TTG is fed directly by the Radar Waveform generation components of the PXIe Cart. This provided a high-SNR signal for the initial attempts at processing. At this point, no extraordinary efforts were made to sample an orthogonal beam-space. One beam-output was sent to the VSA for communications processing, while a second beam-output was sent to the Radar Processing LabView program resident on the PXIe Chassis. The output from the SWIR camera can be used to show the AoA of the individual signals, as shown in Fig. 6.2. The Comms and Radar signals were configured such that the Radar signal would down-convert to a 62.5 MHz IF, while the communications signal would down-convert to an IF of 118 MHz. This ensures that the signals do not interfere, even if the sampled beams are not orthogonal. The sampled waveform and spectrum is shown in Fig. 6.3a, where the raised-cosine spectral shape of

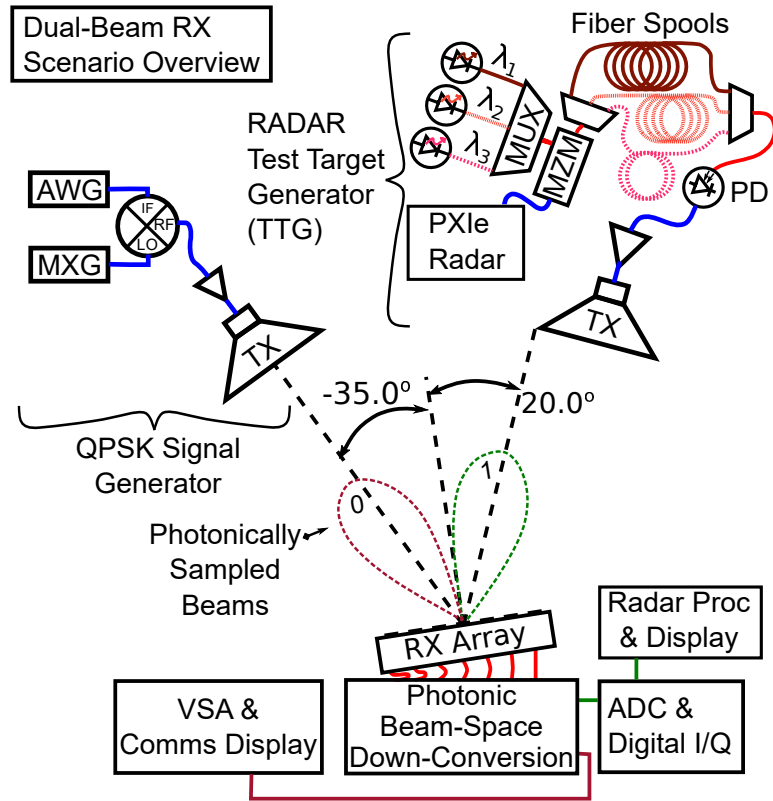


Figure 6.1: Experimental overview of the Dual-beam multi-function experiments.

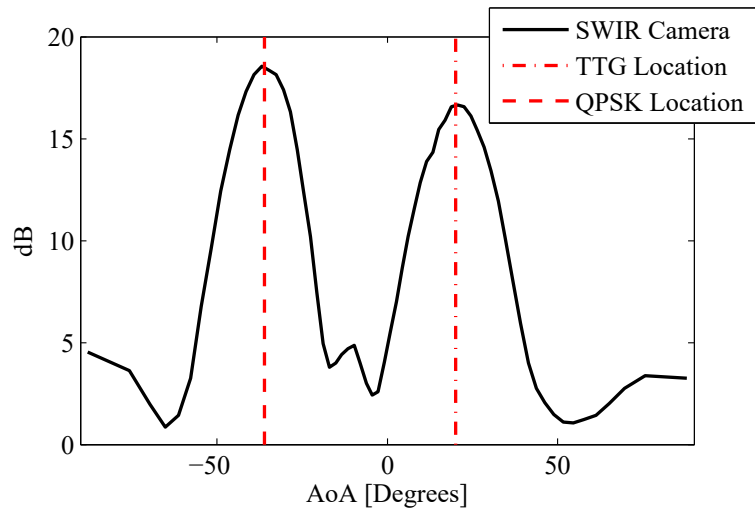


Figure 6.2: AoA measurements from SWIR output of the Photonic Array Processor. High-speed photo-detectors were aligned with each beam output location to show that signal recovery of separate signal types was possible.

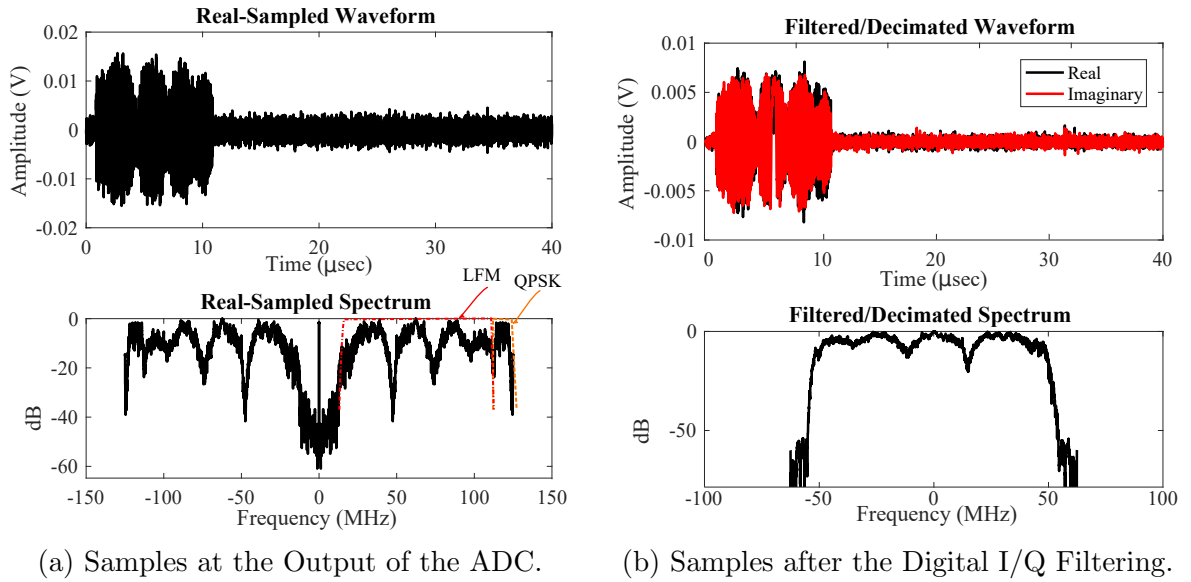


Figure 6.3: Plots of the waveforms and associated spectra of the captured outputs from the beam directed toward the Radar Test Target Generator.

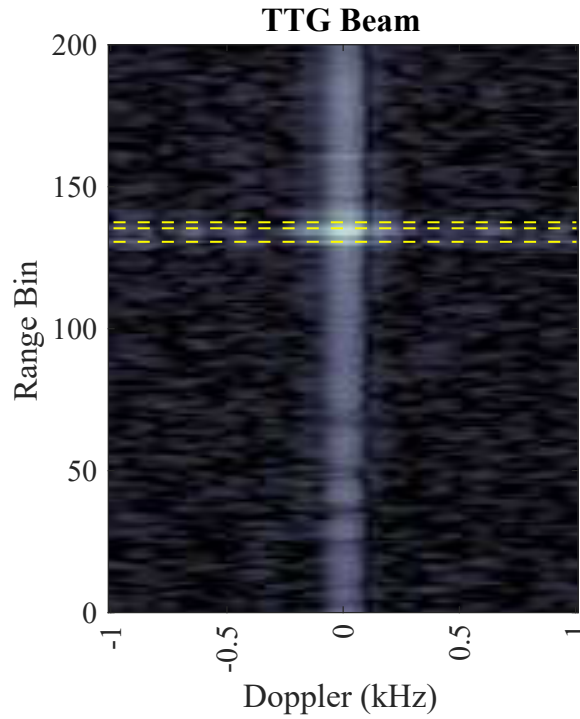


Figure 6.4: Range/Doppler Processed output of multiple radar pulses from the TTG as sampled from Beam "1" (directed toward the TTG). True Target locations are labeled with yellow-dotted lines.

the communications signal is evident adjacent to the 100 MHz chirp spectrum. Upon digital base-band translation and filtering as discussed in Section 3.2, the final output signal and spectrum that is processed by the radar processor is shown in Fig. 6.3b. The final digital I/Q samples are then stored until several pulses are collected. Upon collection of multiple pulses, the radar processor can perform both range and Doppler processing on the data. The resulting “Range/Doppler” plot is shown in Fig. 6.4. The Range/Doppler plot shows three test targets generated by the TTG. Currently, the TTG does not simulate moving targets, thus the targets remain at the zero-Doppler or “DC” position. Any Doppler response in the map is due to Doppler side-lobes and/or spurs/interference and not target motion.

Simultaneously, the VSA is processing the communications information that is set at the 118 MHz IF. The output screen capture from the VSA is shown in Fig. 6.5, where the QPSK signal was recovered with an SNR of 17 dB. Thus it was shown that

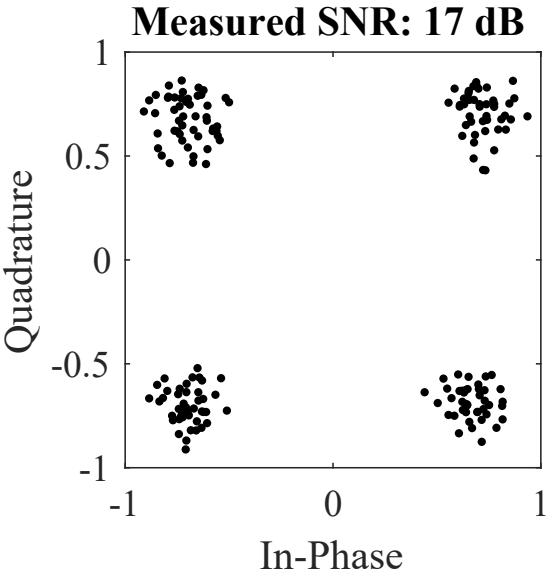


Figure 6.5: Recorded QPSK constellation from the VSA, connected to Beam “0.” The QPSK signal was recovered simultaneously with the radar signal from the TTG, each in a separate spatial channel.

two different signals could be spatially isolated, sampled and processed simultaneously,

however, they were set to separate center frequencies, such that they would be somewhat isolated upon down-conversion to IF. The next set of experiments placed both signals at the same RF and attempted to capture the entire beam-space. The signals were placed such that they not only interfered in frequency, but also spatially due to side-lobe energy.

6.2 Full-Beam-Space Multi-function Experiments

The final set of experiments required the sampling and recovery of the entire field-of-view of the input RF array. This is done most efficiently via the formation of the orthogonal beam-space introduced in Section 1.1.2. This experiment set out to validate the hypothesis that the continuous spatial spectrum that is generated by the photonic array processor could in fact be sampled precisely enough such that an output equivalent to that of a DFT beam-former could be recovered.

6.2.1 Sampling and Calibration of Orthogonal Beam-Space Locations

Ideally, a focal-plane array of high-speed photo-detectors with a fine pitch would be placed in the optical processor’s output plane such that a grid of beam-locations could be down-converted and sampled across the full field-of-view (FoV) of an input RF antenna. Such a device would allow for AoA processing and adaptive beam-forming techniques to be applied on arbitrary clusters of beams around focal plane locations with high incident intensities. In other words, if every pixel of a SWIR camera were capable of sampling the IF signal that is generated when an optical LO is introduced at the focal plane, the irradiance map could be used to cue processing of any pixel/beam location in the output plane. A suitable digital read-out circuit that selected “beam-pixels” for processing would also need to be developed. Currently, no commercially available, large-format, devices exist that would meet any useful bandwidth specification for a 2D array application. To allow for maximum flexibility in processing, it is otherwise beneficial to sample a set of orthogonal beam positions. For the uniform

linear RF array used in experimentation, this can be readily accomplished with a commercial linear SWIR photo-detector array. For the initial experiments, a Hamamatsu



Figure 6.6: Picture of the beam-sampling photo-detector array used for experimentation.

G12430 Series photo-detector array was chosen for its large pixels of $200\mu m$ in diameter, with a pitch of $250\mu m$, shown in Fig. 6.6. The photo-detectors have a nominal bandwidth of 60 MHz, though it was discovered to possess an adequate response up to 125 MHz. However, some of the wide-band radar data shows a slight roll-off due to the photo-detector response. Initially, this choice of large photo-sensitive area was made to guarantee that the maximum amount of beam-energy is converted to the IF signal at the output. This works well when single, spatially separated, beams are processed specifically for the recovery of a given signal, particularly when the beam-space is apodized to match the span of the photo-detectors. However, when the desire is to capture a set of beams that can be processed together, in an adaptive sense, the size of the pixels can allow unwanted leakage or cross-talk between the beams, as will be shown later. Furthermore, for adaptive processing it is desired to have orthogonal beams, but the large photo-sensitive area causes an effective broadening of the beams and alters the overall side-lobe structure. These effects tend to reduce the overall orthogonality of the beam-space and must be compensated for in processing. Compensation of such effects will be discussed later in a section on performance and design considerations.

For the signal recovery results presented in subsequent chapters, the beam-sampling array is placed such that we capture beam-locations associated with the ideal orthogonal beam angles shown in Table 6.1. For any given array-size and optical chain, the appropriate beam-sampling locations can be calculated via the relation in (2.69). These beam-locations are associated with a set of M beam-space steering vectors as defined in (1.24). Clearly, the photo-detector array, with a pitch of $250\mu m$, will not

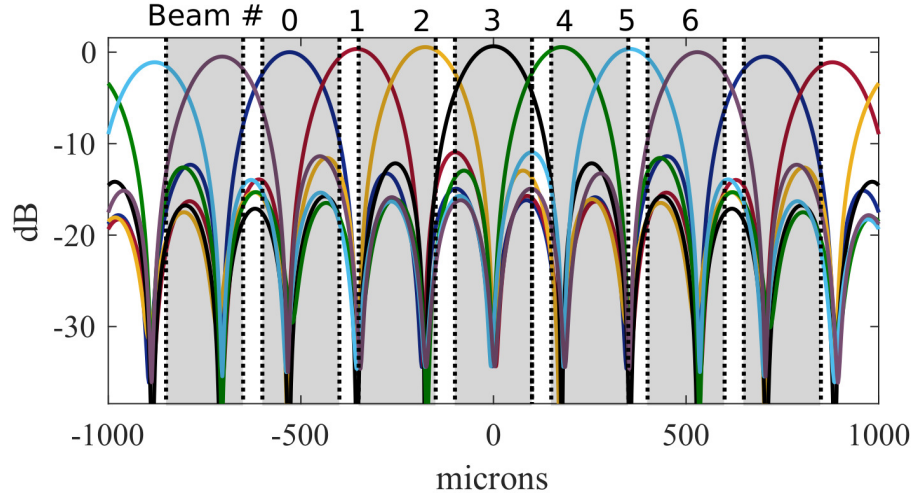


Figure 6.7: Simulated, unity magnification output for the experimental setup discussed. The sampling photo-detector locations are highlighted in gray. Clearly, for a fixed pitch, commercial array, like the one used here, some optical adjustments are necessary.

allow for unambiguous sampling of the desired beam locations. This effect is simulated in Fig. 6.7. For this reason, we must attempt to adjust magnification until we achieve good alignment.

Table 6.1: Sine-space and Fourier-space locations of 7 Beam Positions for the 7-elements used as the input to the Photonic Beam-Space Receiver. The Fourier plane positions assume unity magnification.

Beam (unit-less)	θ_{RF} (degrees)	u_{sine} (unit-less)	u_o (microns)
0	-59	-0.857	-603.9
1	-34.85	-0.571	-402.6
2	-16.6	-0.286	-201.3
3	0	0	0
4	16.6	0.286	201.3
5	34.85	0.571	402.6
6	59	0.857	603.9

In any case, the position of the sampling array along with the magnification and alignment of the optical system must be adjusted to achieve the best possible beam-sampling at the focal plane. That is, we endeavor to fill each high-speed pixel with only a single beam-position, in practice, this turns out to be easier with slightly

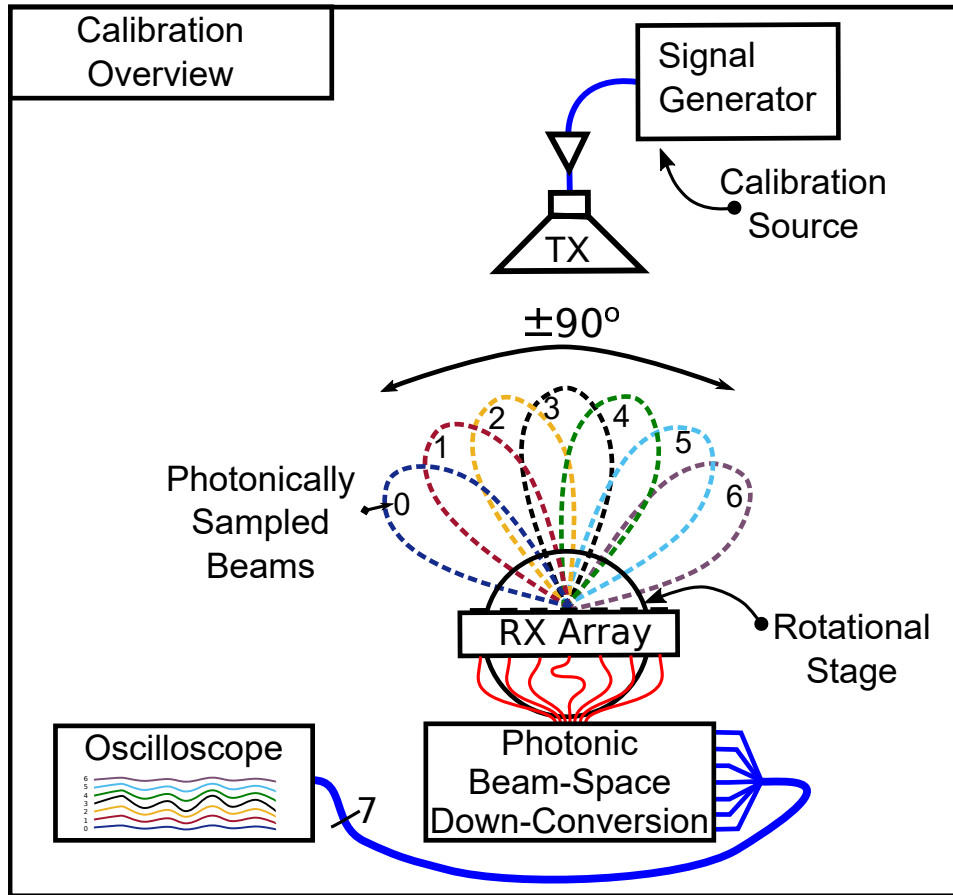


Figure 6.8: Overview of the Calibration setup and procedure for aligning the beam-sampling photo-detector array.

smaller pixels and future versions of the system will likely implement a beam-sampling PD array with smaller pixels and relative pixel pitch. We note that system sensitivity must also be considered when choosing an optimum pixel size, since less output current is likely yielded from smaller pixels. For now, we must find a near optimum alignment for the existing experimental system. The alignment procedure currently uses the output of each of the photo-detectors to determine when the signal is maximized. Thus, the outputs of the beam-sampling photo-detectors are sent to the NI-5171R, as described in Section 4.1.2, where each of the 14-bit ADC data streams are viewed at once on an oscilloscope display. The notional setup is shown in Fig. 6.8, where the calibration source utilizes a single horn from the radar TTG pictured in Fig. 4.8.

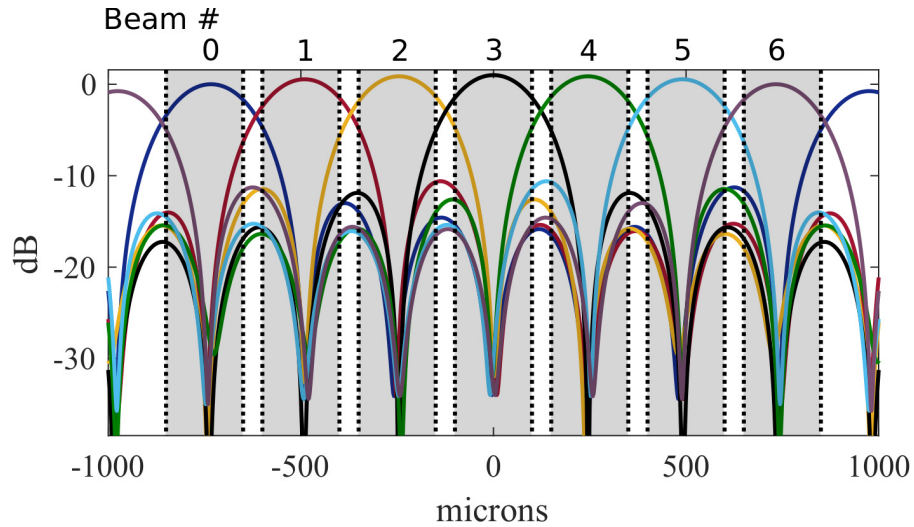


Figure 6.9: Simulated, 38% magnification output for the experimental setup discussed. The sampling photo-detector locations are highlighted in gray. Here the alignment of the fixed, 250 μm pitch detector array is much more well matched to the desired beam-locations.

With a known continuous wave (CW) tone incident on the receiver bore-sight beam, the beam-sampling array is translated, by micro-positioners, within the focal plane. The bore-sight beam channel is viewed along with each adjacent beam-channel and coarse alignment is complete when the signal is maximized in the central beam’s output channel. With the bore-sight channel maximized, further translations—within the large pixel itself—along with magnification adjustments are necessary to ensure that each of the adjacent channels is equalized. An ideal calculation of required magnification yields the magnified output beam-space as simulated in Fig. 6.9, where the detectors align reasonably well with the intended beams.

Once the beam-sampling photo-detector array is aligned to the desired beam locations, a calibration sweep of the antenna is performed using a continuous wave (CW) source. A picture of the calibration source, as viewed from the RF array, is shown in Fig. 4.8. The sweep allows the photo-detector channels or beam-ports to be stored and analyzed in order to generate a simple calibration table. It also allows for visualization of the sampled beam-space. The output of one such calibration sweep is shown in Fig. 6.10. The large photosensitive area of the beam-sampling array

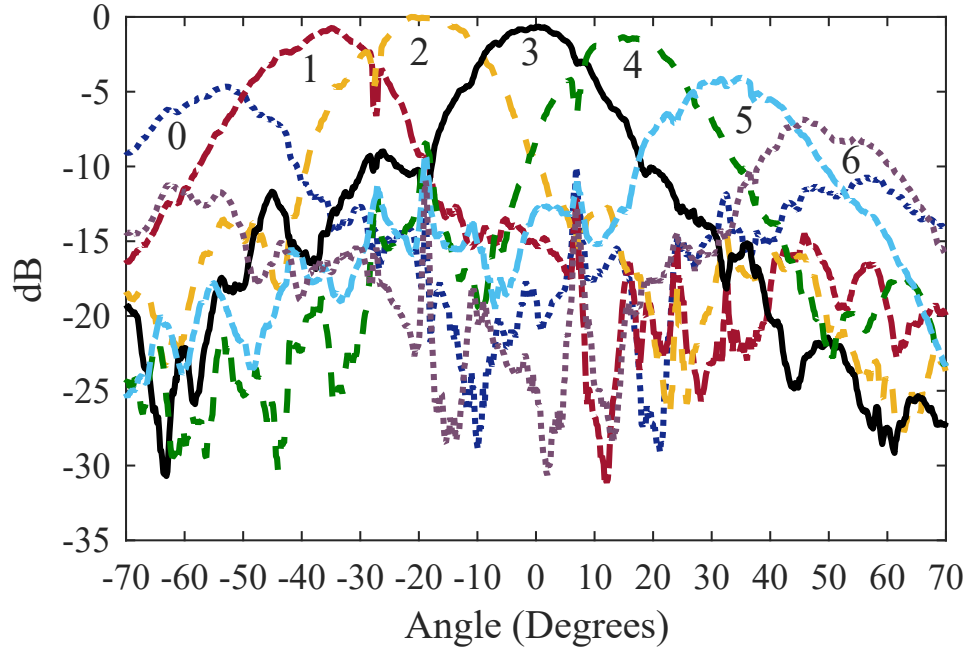


Figure 6.10: Beam-sampling photo-detector array outputs, as measured over a 140-degree calibration sweep. The calibration sweep of the RF antenna across a known source allows visualization of the beam-sampling photo-detector array’s beam-space. The beams are labeled within the diagram according to the first column in Table 6.1.

pixels makes manual alignment of the photo-detectors with desired beam locations challenging, thus some calibration is still required to account for alignment errors. An asymmetric amplitude roll-off of the beam-space is evident in Fig. 6.10 and must be calibrated out. The asymmetry was discovered to be due to optical beam alignment errors between the fiber-bundle terminations and the lens-let array at the input to photonic array processor. Alignments within the prototype are performed by hand via a set of micro-positioner stages, future versions of the system will feature bonded components that do not require manual alignment, eliminating several sources of error.

Even with reasonable alignment of the photo-detectors, the beam-space output in Fig. 6.10 shows that the outermost beams suffer from what appear to be grating lobes. This is likely due to the following factors:

1. Coupling of adjacent beams and potentially optical grating lobes due to the width of the photo-detectors

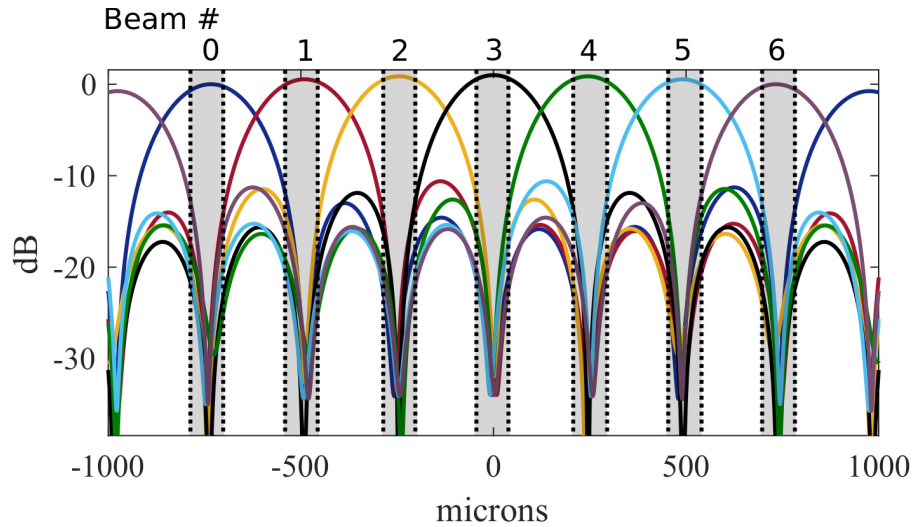


Figure 6.11: Graphical depiction of the potential advantages of the usage of a photo-detector array with smaller pixels. The hypothesized array shown also has a smaller pixel-to-pitch ratio which aids in reductions of channel cross-talk.

2. Slight mis-alignment of the entire array of photo-detectors such that none of them is sampling the main-response axis of any beams
3. Large scan angles when using small arrays (ours is effectively 7 elements) can cause elevated lobes at the opposite angle to the scan.

A number of calibration passes were performed in an attempt to reduce the influence of photo-detector mis-alignment (items 1 and 2 above). The results in Fig. 6.10, represent the best achievable alignment for the current system. It is believed that the usage of smaller detectors, while reducing the amount of out field energy that is collected for a given beam, will significantly reduce any cross coupling between beams. The gray-shaded region of beam “6” in Fig. 6.9 serves as an example where the grating lobe of beam “0” has energy incident on the photo-detector for beam “6”. Reducing the photo-detector diameter to less than $100\mu\text{m}$ would better ensure that the main response of beam “6” is all that is detected as shown in Fig. 6.11. Smaller detectors will also make it easier to align the array to the main-response axes of the beam positions since it will allow the beam roll-off to be detected more readily using the oscilloscope technique outlined earlier. Furthermore, the additional separation between adjacent

pixels will prevent spill-over and other coupling effects that hinder performance of the photo-detector array in and of itself. The final issue of array size can only be mitigated

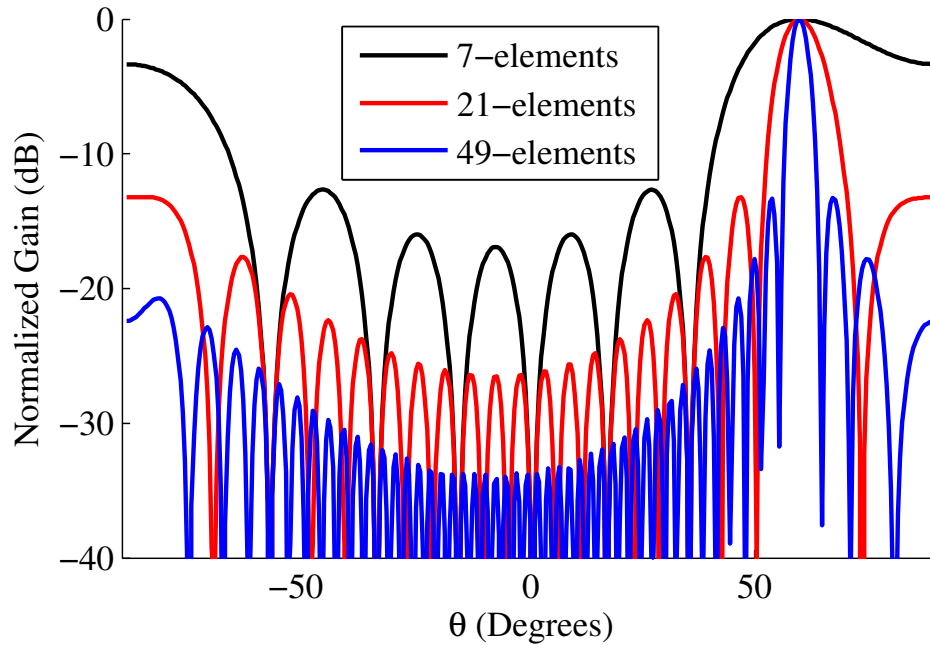


Figure 6.12: Comparison of 3 arrays of increasing numbers of elements when scanned to a large angle off bore-sight.

by building a larger array, or potentially by constraining the element pattern. An example pattern of a 7-element array at a wide scan angle is shown in Fig. 6.12, where the elevated side-lobes are evident for the 7-element array when compared to the larger arrays.

6.2.1.1 Orthogonality of the Sampled Beam-space

The beam-width (3 dB) of the calibrated results averaged to a value of approximately 19.6 degrees. However, the beam-width (3 dB) for the 7-element array used at the input is approximately 16.6 degrees. Thus, the spatial integration effect of a large photo-detector, as discussed in Section 5.2.3.4.1, has caused a 3-degree broadening of the bore-sight beam. Each subsequent beam will have additional broadening due to the decreasing projected area of the array. The calculated beam-locations for the array setup used in experimentation are provided in Table 6.2 along with the ideal

beam angles. The outer-most beams, while symmetric, are the farthest from the ideal

Table 6.2: Ideal vs Measured beam locations after sampling via high-speed photo-detectors.

Beam (unit-less)	θ_{Ideal} (degrees)	θ_{Actual} (degrees)	$\Delta\theta$ (degrees)
0	-59	-50	9
1	-34.85	-33.91	0.94
2	-16.6	-15.05	1.55
3	0	1.405	1.405
4	16.6	16.25	-0.35
5	34.85	35.52	0.67
6	59	50.77	-8.23

locations, however; this is to be expected and has to do with the construction of the input array. The element pattern, in an ideal sense, should have a cosine shape, where $E_z(x, y) = \cos\left(\frac{\pi x}{L_p}\right)$ and L_p is the patch side-length [82]. This is often approximated by the relation given in (1.7) for the purposes of system-level simulation. The element pattern effectively re-shapes the main-lobe response when steered at extreme angles. This effect is seen in Fig. 1.4, where the peak of the 60° beam, actually appears to align better with an angle that is closer to 53°. The rest of the beams are also slightly mis-aligned. This is largely due to an imperfect relationship of magnification and the pitch and pixel size of the sampling array as previously discussed. The net effect is to produce a set of beams at the output that are no longer considered orthogonal.

6.2.1.1.1 Beam-space Whitening

There are many processing techniques that take advantage of the orthogonality for a given beam-space output. Thus, for situations where the beam-space is not perfectly orthogonal, such as the case where some mis-alignment occurs, or the beam-space is apodized for low-sidelobe performance, the transformations performed on the beam-space data vectors must use a whitened, or “orthogonalized” beam-space steering matrix. The whitened beam-space matrix is given by the following:

$$\mathbf{B}_{wbs} = \mathbf{B} [\mathbf{B}^H \mathbf{B}]^{-\frac{1}{2}}. \quad (6.1)$$

The newly whitened component beams will have an altered sidelobe structure, likely by several dB [25]. This whitened version of the measured beam-space matrix will be used extensively during the experiments discussed in the following sections.

6.2.2 Full-Dimension Beam-Space Experimental Setup

With the alignment and calibration of the recovered beam-space complete and the beam-space matrix estimated, a set of experiments were conducted where the Radar and communications signal spectra were both centered at the same IF upon down-conversion. This ensured that any non-spatially isolated signal would be subjected to in-band interference upon subsequent down-conversion, sampling, and filtering. To further exacerbate the potential for interference, the signals were placed such that they straddled the set of sampled beam-positions as shown in Fig. 6.13. This ensures that the side-lobes of each signal appear in each of the adjacent beams. Recall, from Section 1.1.2, that any signal not incident along the main axis of a beam will impart side-lobe energy into all of the beams within the orthogonal beam-space. Furthermore, the discovery, in Section 6.2.1, that the sampled beam-space is both broadened by the photo-detectors and slightly mis-aligned, only serves to increase the chance for cross-coupling of the signals.

The Radar signal for these trials was also being transmitted from atop the receive array in a mono-static fashion. This provided additional opportunity for reflected echoes to arrive along a variety of beam-angles. Thus, the TTG now received the transmitted signal over-the-air, amplified and delayed the signal, then re-transmitted it back to the receive array. The QPSK signal was setup just as before, using a AWG that was up-converted to an RF. These experiments had both signals centered on a 12 GHz RF carrier.

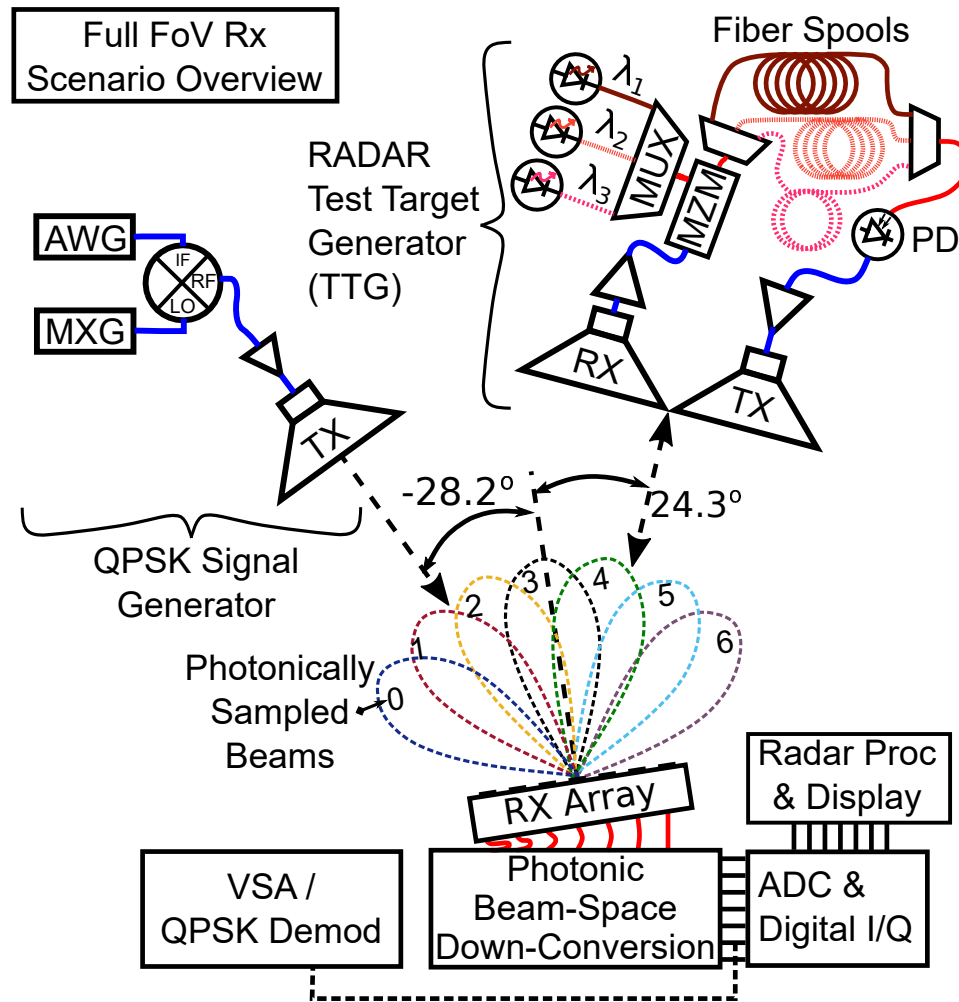
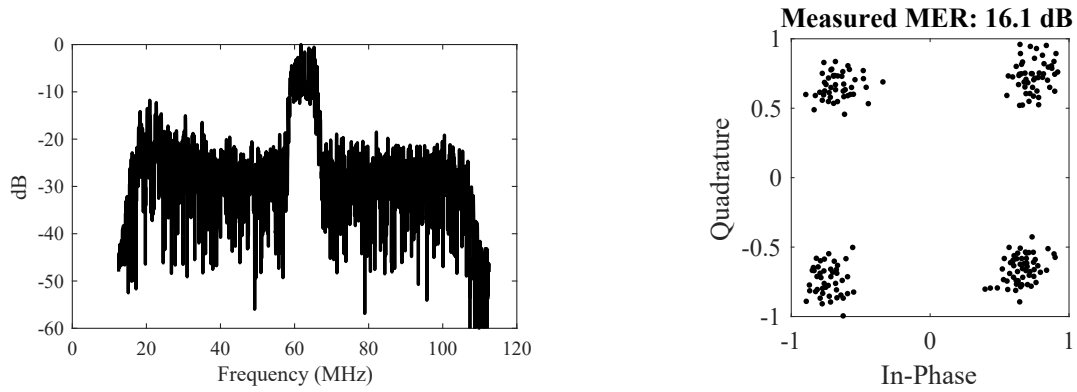


Figure 6.13: Schematic overview of the experimental setup used for the Full-Dimension Beam-space recovery experiments. Not shown is the Radar Transmit Horn. It sits atop of the receive array in a quasi-monostatic fashion as seen in Fig. 4.1.

6.2.3 QPSK Signal Recovery

If the location of the desired communications signal is assumed to be known precisely, or is discovered to be stationary, the sampled beam-locations can be physically adjusted to optimize the signal power entering the Photonic Array Processor. This was done during the prior experiment discussed in Section 6.1. However, for the beam-sampling scheme discussed here, the output from Beam 1 is instead optimized for orthogonality with its neighboring beams. The output of Beam 1 is then split off to a Vector Signal Analyzer where the signal is filtered, demodulated and processed for

a QPSK signal, just as before. The spectrum of beam 1, as displayed on the VSA, is



(a) Detected communications signal spectrum output from the VSA. The raised cosine spectrum of the 10 MHz QPSK signal, centered at 62.5 MHz, is immediately evident.

(b) Recovered QPSK constellation from sampled beam sent to the VSA. A slight skew in the constellation is evident from the in-band interference of the radar signal, though it is still recovered with acceptable SNR due to the separate root-raised cosine matched filter.

Figure 6.14: Recovered spectrum and constellation of a QPSK signal incident on the array at the same time as a Radar signal. Both signals are in-band.

shown in Fig. 6.14a. The VSA is setup with the parameters of the root raised cosine filter along with the expected symbol rate, samples per symbol and the bit-encoding scheme (i.e. Gray Encoding [55]). The VSA is then used to recover the QPSK constellation as seen in Fig. 6.14b. The constellation shown in Fig. 6.14b was recovered with a calculated Modulation Error Ratio (MER) of 16.1 dB, consistent with the Carrier-to-Noise ratio that is apparent in the spectrum shown in Fig. 6.14a. The MER is a receiver-data driven measurement that uses the relative offset of the data from a true constellation diagram and is directly related to the Signal-to-Noise Ratio (SNR). The reported MER fluctuated between 15.5 dB and 17.2 dB over the duration of several minutes of data recording. Thus, even under non-ideal beam-sampling conditions, the outputs of the beam-sampling photo-detector array allow for recovery of the QPSK signal.

6.2.4 Radar Signal Recovery

The radar signal processing is performed in near-real-time on the National Instruments PXIe chassis. Each of the 7 sampled beam outputs is digitized on the aforementioned 8-channel reconfigurable oscilloscope card and processed via a combination of Field programmable Gate Array (FPGA) and Single Board Computer (SBC) nodes. The usage of the compute nodes affords a greater amount of control over the collection and processing of the sampled output beams. The additional control and flexibility allowed for investigations of beam-space processing techniques to improve the performance of the radar processing, particularly in the presence of additional in-band signals, like the QPSK signal used in these experiments. For the purposes of radar processing, it is assumed that the transmit steering vector of the radar system is known a-priori, as in a typical mono-static radar case. The radar signal returns from the TTG were aligned between two adjacent beams in the sampled beam-space with an associated steering vector of $\mathbf{v}(24.3^\circ)$, as shown in Fig. 6.13. This once again represents a non-ideal case for direct signal recovery from the sampled beams themselves. Each beam-output is processed using the range correlation processing on each returned pulse. Once a set of pulses are collected, a Doppler Fast Fourier Transform (FFT) is taken across the pulses to form the Range/Doppler maps associated with the signals incident at each beam angle. The effect of non-ideal signal locations and beam-sampling is evident within the Range/Doppler outputs for each beam, shown in Fig. 6.15. The returns from the 3 point target responses due to the radar signal are seen in virtually every channel. Also seen in the channels are a set of constant-Doppler tones that spread vertically in range. These tones are due to the interference from the communications signal. A typical goal for a radar application would be to maximize the signal to noise along the direction of the transmit steering vector, while attempting to suppress any incident energy from unwanted directions. Thus, we wish to use the SWIR to estimate the location of any unknown and possibly interfering signals so that they might be suppressed, while simultaneously maximizing the signal in the

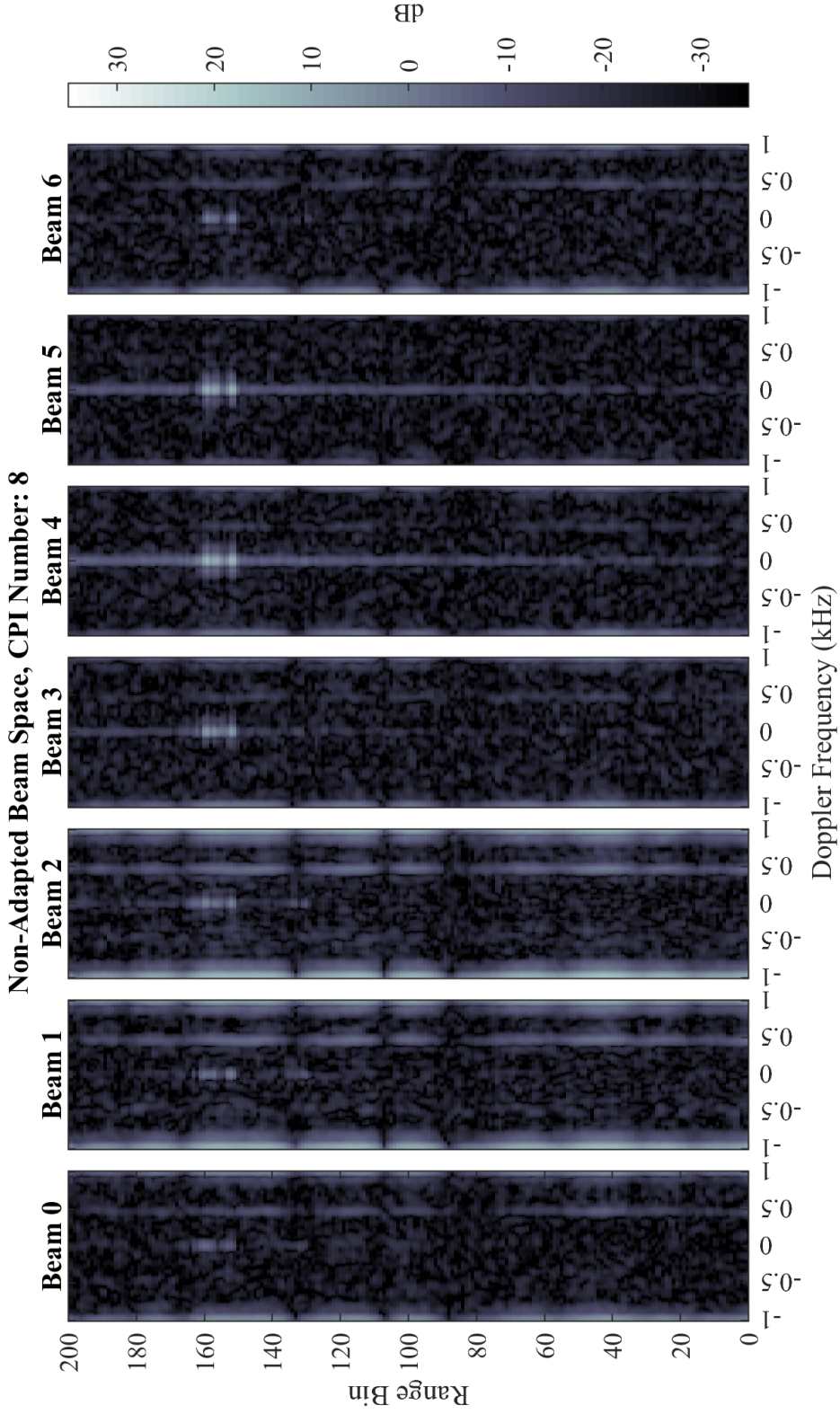


Figure 6.15: The output range/Doppler plots of a single coherent interval for each sampled beam location in the beam-space. The presence of 3 targets from the test-target generator can be seen as three point-target responses along zero-Doppler (at range bins 152, 156, and 159) along with in-band interference from the communications signal (most prevalent in beams 1 and 2) seen as a set of Doppler tones.

direction of the transmitted radar signal. In the experiment shown, the interfering signal is stationary and is defined as the the cooperative QPSK signal described earlier. However, in many cases the interfering signals will be unknown in both quantity and angle-of-arrival. It is therefore necessary to develop a method to estimate the location of interference when using the Photonic Array Processing techniques described thus far.

6.2.5 Estimation of Quantity and Angle-of-Arrival of Interference Sources

There are a number of potential advantages to using the outputs of the photonic array processor when real-time operation of an adaptive array are considered. A particular advantage of the photonic beam-space sampling approach is the ability to capture the continuous beam-space on an imaging SWIR camera. For the full-dimension experiments presented here, the output of the SWIR has several peaks as shown in Fig. 6.16. These peaks can be used as a coarse location estimate in real-time. Furthermore, the signal power of the incident signals can be estimated directly from the SWIR output as part of the peak search operation. This is seen as useful since the signals can be prioritized for the application of adaptive weights to either re-steer toward, or place nulls in, the directions of the prioritized responses. The output of the SWIR device can be fed directly to a processor where a simple peak-search operation can be performed in near real-time to provide estimates of the AoA of signals across the full field of view with latencies that are on the order of 8-10 milliseconds for the currently used device.

6.2.5.1 Latency of SWIR-Based AoA Estimates

Reduction of latency and/or convergence time for any adaptive technique is of the utmost importance if a particular algorithm is to be used in a real-time system. For the photonic array processor prototype, with a sampling rate of 250 Msps, and $N = M = 7$, at least 11 samples are required to meet the 3 dB SINR loss criteria using the relation in (3.48). The total sampling time required for the 11 samples is therefore 44 nanoseconds. With this in mind, Fig. 6.17 shows advantages to the real-time

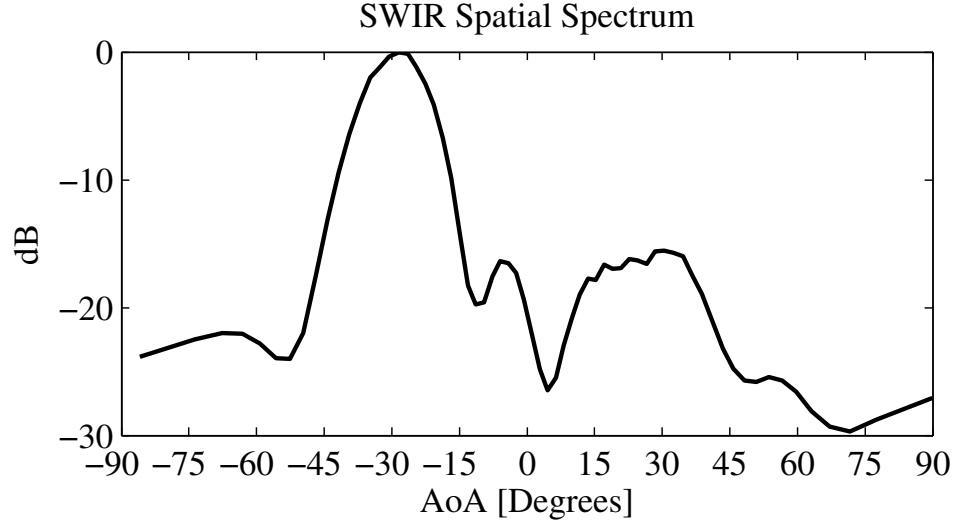


Figure 6.16: Captured snapshot of the SWIR measurement of the irradiance pattern at the output of the photonic array processor. This effectively measures the input spatial spectrum with resolution limited by the size of the array.

photonic beam-forming/AoA estimation approach presented for arrays with greater than 116 elements. With a future change to a high-speed SWIR sensor technology, capable of read-out speeds approaching 40 KHz [83], the array size cross-over point in Fig. 6.17 is reduced to 17 elements for the minimum latency curve and 9 elements for high-latency curve. The results presented in Figs. 6.18, 6.19, and 6.20, show the difference in AoA performance for varying numbers of samples, K , used for the estimate of \mathbf{R}_x during the subject experiments. The SWIR values are constant, with a mean latency of 8.5 milliseconds, due mainly to the usage of a 2-D camera array with substantially higher pixel count than necessary for the existing prototype. The covariance and sub-space based methods, for $M = 7$, have nominal latencies of 3.1, 5.9, and 10.3 microseconds for $K = 11$, 29, and 59, respectively. Therefore, even modest sized arrays making usage of a high-speed SWIR output as an AoA estimator would achieve significant benefit to initial AoA estimation times since the measurement latency depends only on the SWIR readout speed and not the values of M and K . It is reasoned that future versions of the technology should be developed using state-of-the-art SWIR detectors, with detector size optimized for the array configuration, in

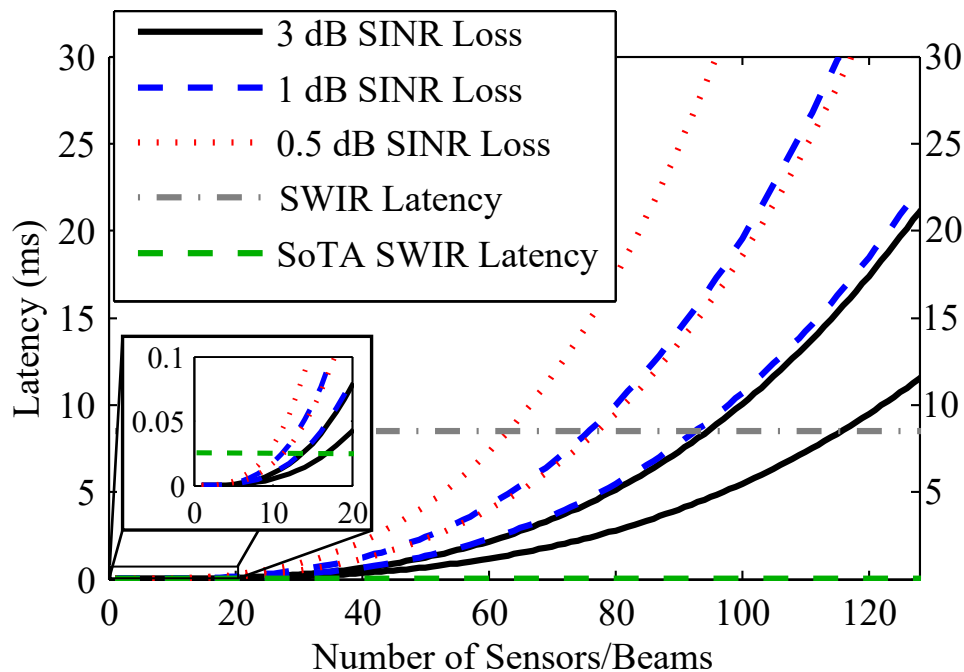


Figure 6.17: Family of curves depicting the first order estimate of processing latency when using a covariance-based AoA estimation or adaptive filtering approach, including the latency of the SWIR measurements. Each pair of curves depict a bounded region of expected latency assuming use of a Virtex-7 class of FPGA. The horizontal lines depict the AoA latency of the current SWIR camera in the photonic array processor prototype along with a latency value for a commercial state of the art (SoTA) SWIR sensor with 39 kHz read-out speeds. The intersection points show array sizes where advantages in latency can be gained from the presented photonic beam-space estimation approach. The inset is zoomed over the region of 0 to 20 to allow better visualization of the high-speed SWIR benchmark.

order to further improve the latency (even for small arrays).

6.2.5.2 AoA Estimation Using the SWIR Measurement of the Spatial Spectrum

If a particular application requires additional angular resolution of incident signals and can tolerate additional computational latency, the sample covariance matrix, $\hat{\mathbf{R}}_x$, can be estimated as discussed in Section 3.4 and any of the spatial spectrum estimation techniques reviewed in Section 3.4.1 can be applied to the sampled beam-space data. The sampled beam-space data vectors were used to calculate the sample covariance matrix for three separate values of K as defined in (3.48). The first dataset used only 11 samples, the second used 59 and the third dataset used 512. The 512 sample dataset was used as an “ideal” estimation case. Multiple frames of data were then ran through several of the estimation techniques to generate the plots shown in Fig. 6.18, Fig. 6.19 and Fig. 6.20. Only a single capture of the SWIR output is shown as a “truth” trace of what the input spatial spectrum resembled prior to sampling with the high-speed photo-detector array. The flattened peak is that of the pulsed radar signal, with the flat-top manifesting as a side-effect of the SWIR integration time and the chosen pulse rate of the radar. The opposite peak is located at -28.49° , a mere 0.29° from the actual location of the QPSK signal.

In general, the Fourier-based techniques perform on par with the SWIR output and are noticeably un-affected by the duty-factor of the radar signal. Both Capon and MUSIC detect and locate the two incident signals on every trial. The Pisarenko method introduces many false peaks and has a wide variance in AoA estimates. This is likely due to the fact that it only projects onto a single eigenvector and due to the finite nature of the data snapshots, it is unlikely that the smallest eigenvector truly represents the noise-subspace. The performance of MUSIC, which uses the entire estimated noise subspace, performs much more robustly across the trials. An interesting result from the Maximum Entropy Method was discovered, particularly when using a principle components version that operated on the estimated signal subspace. As seen in the

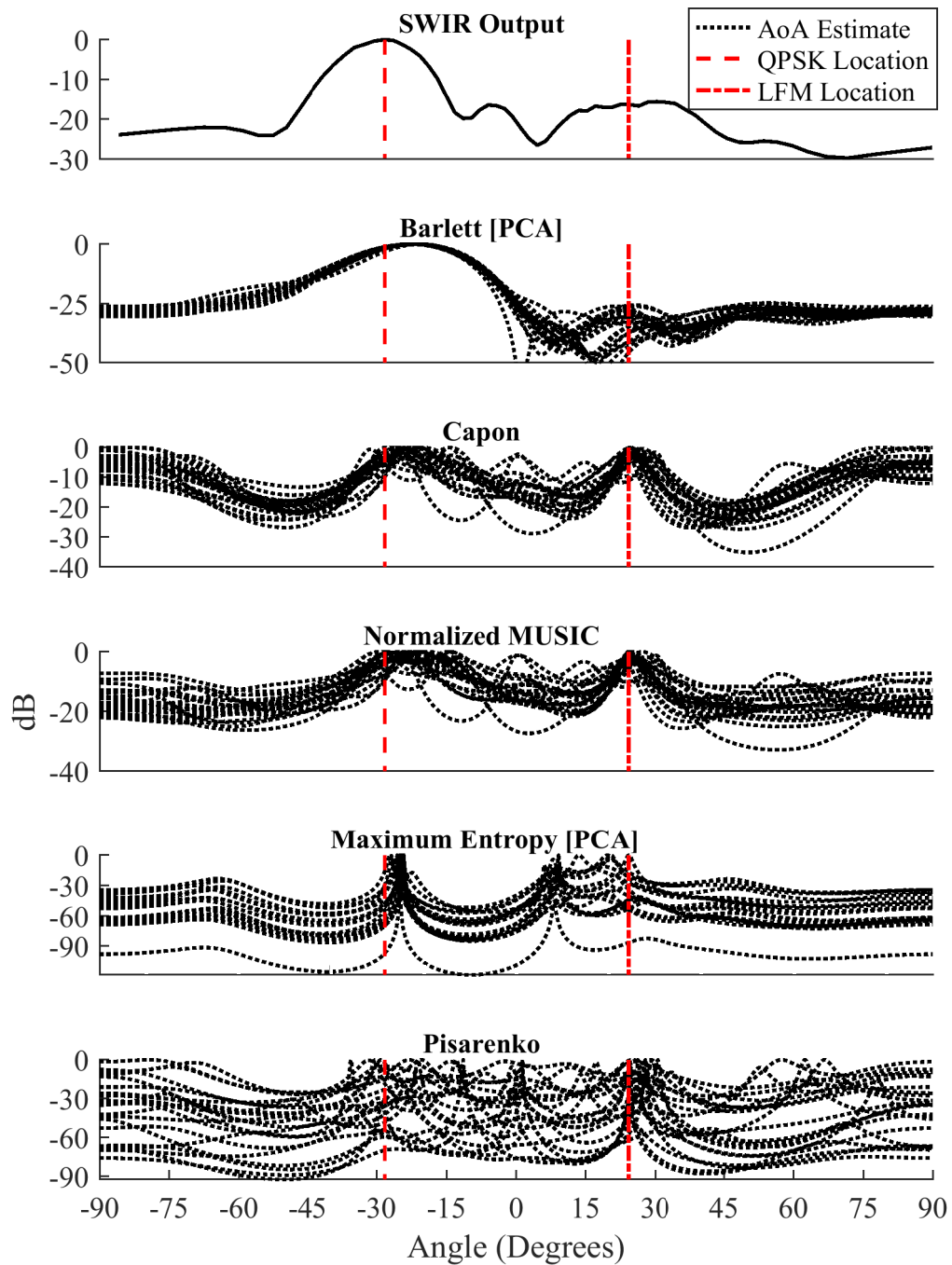


Figure 6.18: Overlay of 50 trials of Angle-Estimation using 11 samples to estimate the sample covariance.

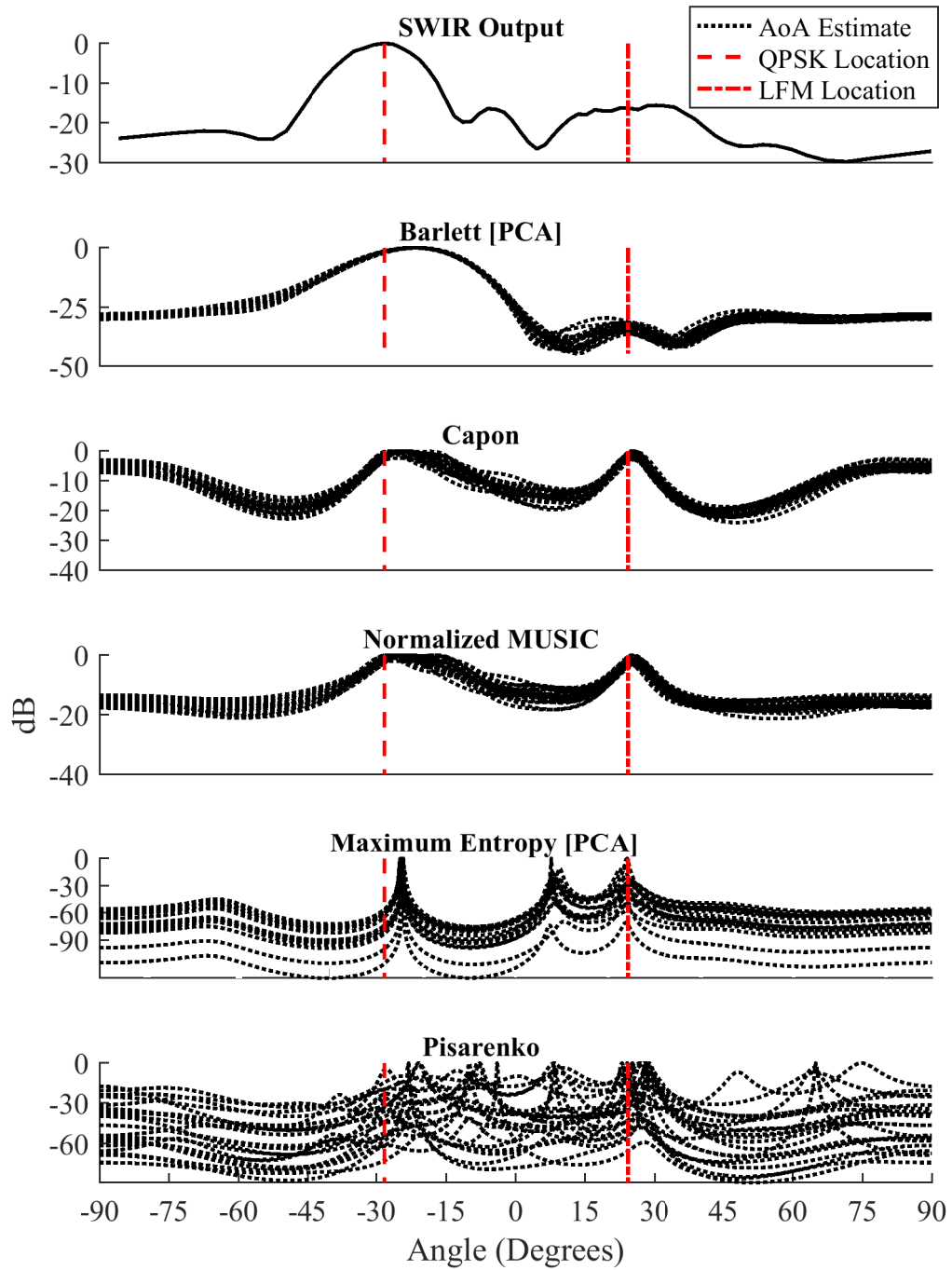


Figure 6.19: Overlay of 50 trials of Angle-Estimation using 59 samples to estimate the sample covariance.

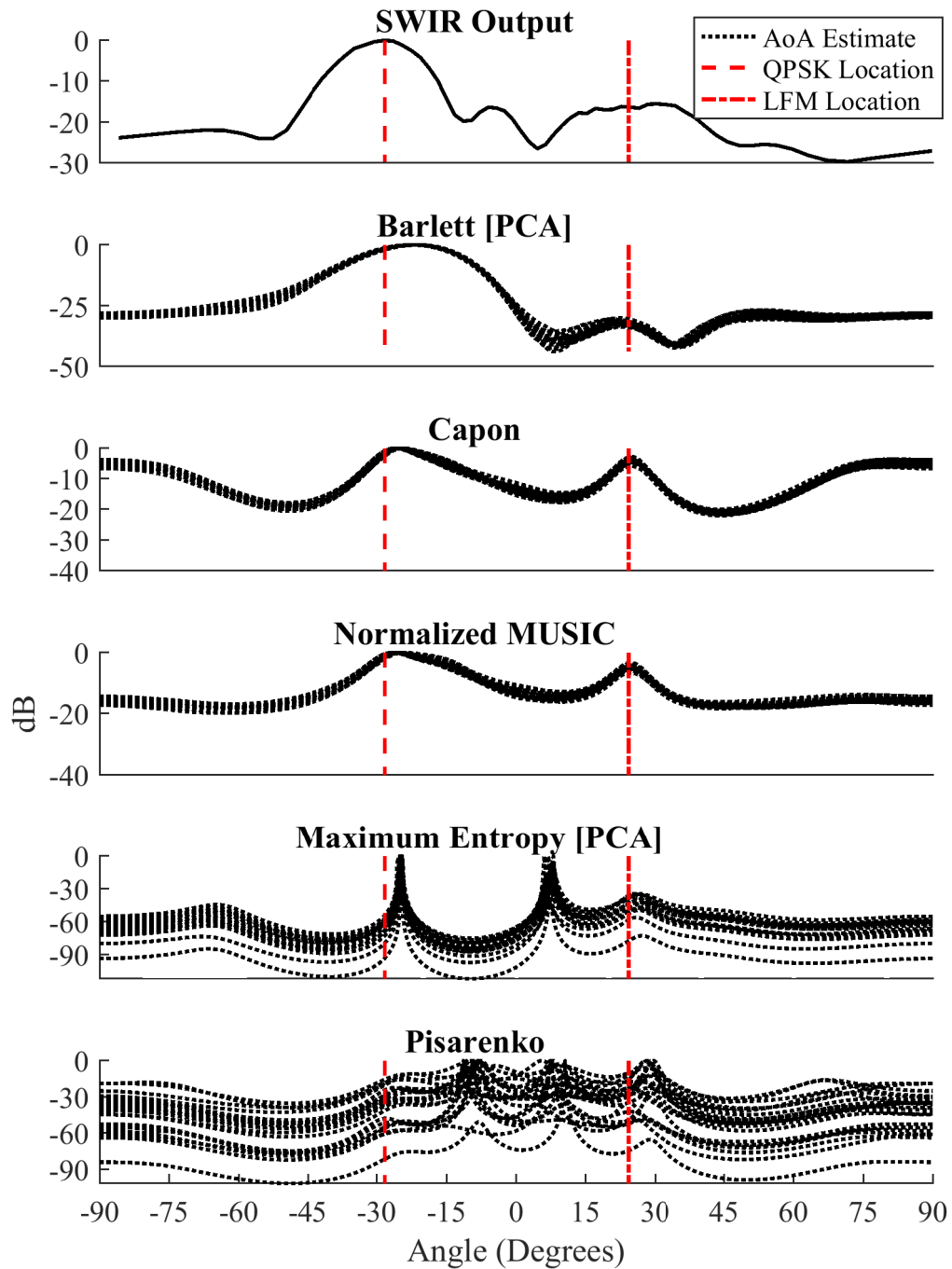


Figure 6.20: Overlay of 50 trials of Angle-Estimation using 512 samples to estimate the sample covariance. Using this many samples is seen as an ideal estimate.

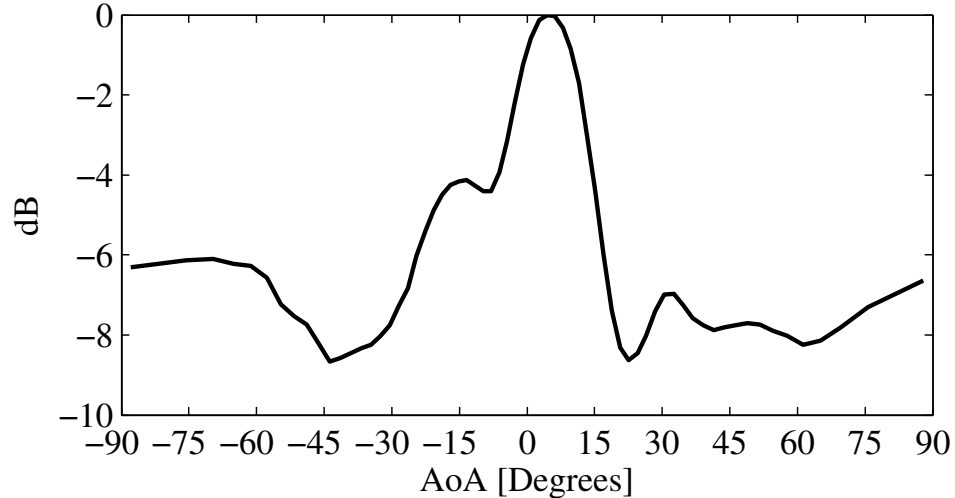
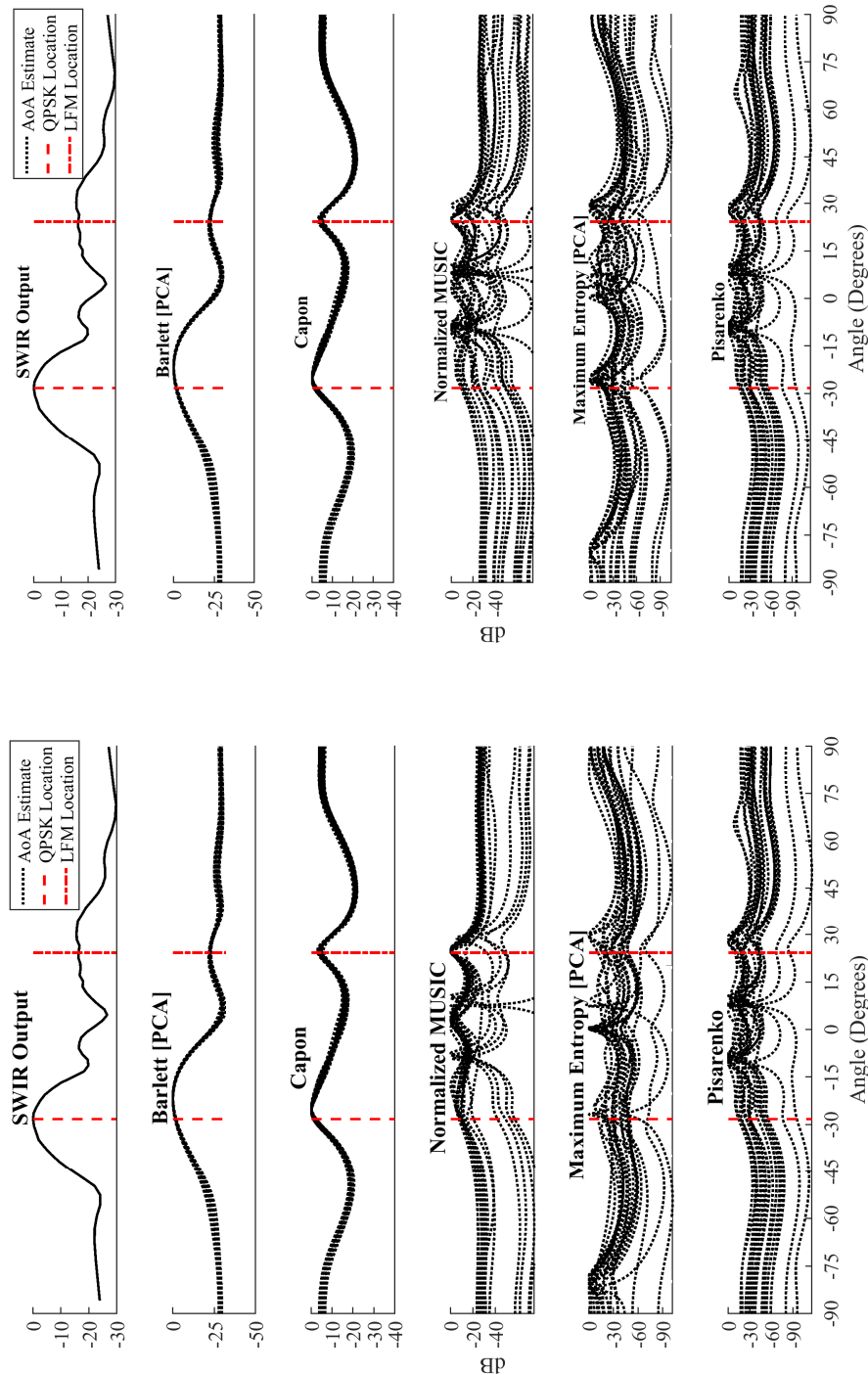


Figure 6.21: Plot showing the measured response at the output of the photonic array processor in the absence of any RF signals. The apparent beam pattern is due to the leakage of the optical carrier through the thin-film filter stack meant to reject it. This signal is 20-30 dB or more below the RF signals in most cases presented, yet certain sub-space estimation methods seem to detect and locate its presence in the data.

Figs. 6.18, 6.19, and 6.20, the Max Entropy plot regularly detects a third signal near 7 degrees. This was initially puzzling until it was discovered that the leakage of the optical carrier became offset from bore-sight upon applying a flat amplitude calibration on the input laser. The attenuators act as time-delay units, effectively changing the pattern of the carrier leakage. The carrier was subsequently measured on the SWIR output in the absence of any signals. The measured carrier response was discovered to be located with a peak at approximately 6.7 degrees, as seen in Fig. 6.21. This is believed to be the signal that is detected by the Maximum Entropy Method. No other method was able to detect the presence of the carrier signal with nearly as much probability. A secondary benefit of the measured SWIR output when used in conjunction with covariance and eigen sub-space methods is in estimation of the size of the signal sub-space. Two popular algorithms for estimating the dimensionality of the signal sub-space were provided in Section 3.4.1, namely Akaike's Information-Theoretic Criterion (AIC) and the Minimum Description Length (MDL). The peak search of the SWIR detector output is found to be an effective bound on the estimates

from these criteria and is used during the trials that resulted in Figs. 6.18, 6.19, and 6.20. Both AIC and MDL have been used with some success in this work, however, it is worth noting that the SWIR output aided in bounding the results when the incident signals were of high SNR. The AIC is known to over-estimate the signal space [64] and during the trials presented here it never estimated less than 5 signals, with a mean signal estimate of 5.78. Similarly, MDL failed to ever estimate the number of signals to be less than 4, with an average signal estimate of 5.2. Performance of the noise-subspace techniques when using an unconstrained estimate from either MDL or AIC, suffered greatly due to the lack of eigenvectors left to span the noise space. This is particularly an issue when a small number of degrees of freedom are being used, as when using a small array. The potential reason for the high estimates is believed to be due to the high potential for multi-path in the laboratory environment, in-fact double bounced returns from the forward and backward wall of the laboratory were evident within some of the radar data. To address this shortcoming, an updated MDL criterion was presented in the literature, which uses a computationally intensive search in the estimation [84]. The additional latency introduced by the exhaustive search required in [84] can be reduced by using the SWIR output as a set of seed locations to search over, thus reducing overall latency of such techniques and producing a more reliable estimate. When using the SWIR as a bound on the estimates the number of signals was not estimated over 3. Results for trials using only the idealized covariance estimate (i.e., using 512 samples) are shown for both MDL and AIC in Figs. 6.22a and 6.22b, respectively. Both MUSIC and the principle component version of MEM are affected by the over-estimation, as expected.

Thus, it has been shown that the SWIR output provides a constant-latency estimate of the number and AoA of incident signals, regardless of array size. It is important to point out that the angular resolution of the SWIR output will increase with increasing N , due to the decreased beam-width of a larger input array. The optically down-converted beam-space data outputs from the photonic array processor can also be used to provide estimates of increased resolution, beyond that possible with



(a) Signal-space estimation via MDL.

(b) Signal-space estimation via AIC.

Figure 6.22: Comparison of Angle-Estimation performance over multiple trials using two popular estimates of the signal-subspace parameter, D . $K = 512$ for both subplots.

simple beam-forming. A number of beam-space spatial spectrum estimation methods were shown to be compatible with the sampled beam outputs. Finally, the SWIR was shown to be a fair estimator of the signal sub-space, which can be used to improve performance of sub-space spectral estimators. The next section discusses performance of a low-latency digital re-steering of the array using the beam-space data vector and the estimate of the interfering signal location and power via the SWIR output.

6.2.6 Beam-Space Adaptivity Via SWIR Measurements of the Interference Spatial Spectrum

The ability to measure the continuous spatial spectrum at the Fourier plane of the photonic array processor allows for the direct measurement of the locations of any incident sources in the environment. This ability can be put to good use in estimating the location of large interference sources, without the need to use any covariance-based estimation techniques. The low-latencies with which these estimations are possible allow the photonic array processor to apply adaptive weighting to the captured beam data in near-real-time. Thus, if the location of a desired signal is known, any additional peaks on the SWIR output can be assumed to be due to interference. With this in mind an idealized interference covariance can be formed without much computation, only the generation of a set of steering vectors is required giving

$$\hat{\mathbf{R}}_{SWIR} = \hat{\sigma}_n^2 \mathbf{I} + \sum_{p=1}^{P_{SWIR}} A_p \mathbf{v}(\theta_p) \mathbf{v}^H(\theta_p), \quad (6.2)$$

where \mathbf{I} is the identity matrix augmented with a noise estimate (here left equal to 1), P_{SWIR} represents the total interference peaks measured on the SWIR output, A_p is the measured amplitude of the peak, and θ_p represents the estimated AoA of the p^{th} peak. The weights can then be determined directly by solving

$$(\mathbf{B}^* \hat{\mathbf{R}}_{SWIR} \mathbf{B}) \mathbf{w}_{SWIR} = \mathbf{B}^* \mathbf{v}(\theta_s), \quad (6.3)$$

where the superscript, $()^*$, denotes the conjugate of the elements, and $\mathbf{v}(\theta_s)$ is a steering vector in a desired look direction applied as a constraint to the adapted pattern. With some manipulation this results in

$$\mathbf{w}_{SWIR} = \hat{\mathbf{R}}_{SWIR_{BS}}^{-1} \mathbf{B}^* \mathbf{v}(\theta_s), \quad (6.4)$$

where, $\hat{\mathbf{R}}_{SWIR_{BS}} = (\mathbf{B}^* \hat{\mathbf{R}}_{SWIR} \mathbf{B})$, is the beam-space transformation of the estimated interference covariance.

For the experimental data discussed here, the single interference peak can be estimated at a location of -28.49° . If desired, additional degrees of freedom may be used to slightly widen the estimated covariance. This can be done by simply adding in symmetric measurements offset from the peak. It was discovered that adding in additional peak measurements of $\pm 1^\circ$ from the initially measured peak provided exceptional cancellation performance of greater than 20 dB in all trials that were run. The set of adapted beam-patterns using a number of techniques described in Section 3.4.2 along with two variants of the technique described above are shown in Fig. 6.23. The MVDR,

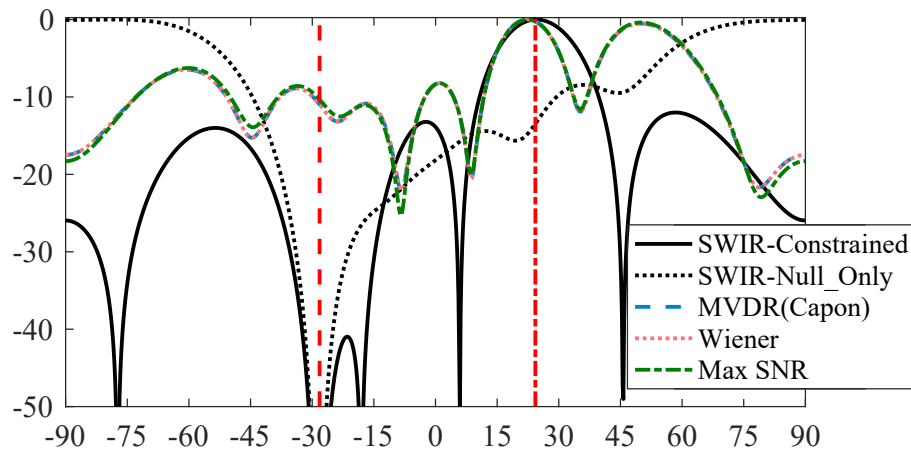
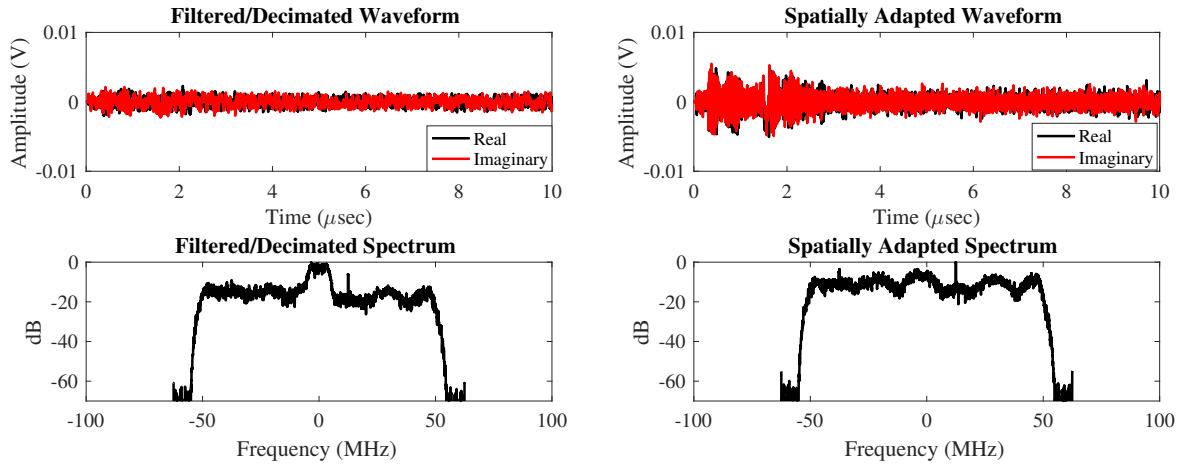


Figure 6.23: Plots showing a comparison of various adaptive filtering techniques.

Wiener and Maximum SNR derived weights all rely on the estimate of the sample covariance and, thus, require additional latency in the weight formation. They also will have varying performance across a given data-set as the sample covariance is constantly updated with new samples. For any given estimate of the covariance, MVDR, Wiener

and Max SNR perform similarly, as expected. The two, SWIR-derived, patterns remain steady across multiple samples as long as the signal peaks remain present in the SWIR data. For the QPSK signal used in these experiments, the SWIR peak in the direction of the QPSK signal is 20 dB greater in amplitude than the peak in the direction of the known radar signal and remains constant for the duration of the experiments. The solid black pattern in Fig. 6.23 is formed via the weights derived in (6.4), while the dotted black pattern attempted to steer a null in the direction of the interference by augmenting the measured sample covariance by the interference estimate given by the SWIR. The “Null-Steered” version of the SWIR derived weights was therefore susceptible to the same errors in covariance estimation as MVDR, Wiener, and Max SNR. It does, however, guarantee a steered null, but fails to ensure that gain remains in the desired direction. Thus, the constrained version of the SWIR derived weighting scheme is seen to have superior performance in terms of synthesizing an ideal adapted beam-pattern. With the usage of the synthesized covariance, only the application of the adapted weights themselves causes latency in the processing chain. Application of weights is necessary for all of the techniques employed making the SWIR derived weighting approach the most efficient in terms of overall latency.

Taking the adaptive weights used to generate the pattern, shown as the black trace within Fig. 6.23, and applying them to the collected beam-space sample data, provides the results seen in Fig. 6.24. A direct comparison of the spectra of the quiescent and adapted beams that are steered toward the TTG are shown in Fig. 6.25, where the 10 MHz QPSK spectrum can be seen to vanish in the adapted output spectrum. This is due to the application of a spatial null in the direction of the QPSK signal. After collection of multiple pulses of spatially filtered data, the resulting range/Doppler plots from each beam-output can be summed to form an adapted beam Range/Doppler output as shown in Fig. 6.26. The data shown in Fig. 6.26 is the spatially-weighted version of the initially processed results shown in Fig. 6.15. Thus, for the experiments shown, usage of the SWIR output to provide a low-latency estimate of interference sources along with beam-space adaptivity, can provide adaptive weights



(a) Waveform and Spectrum of Sample Data prior to adaptive spatial filtering. (b) Waveform and Spectrum of sample data after adaptive spatial filtering.

Figure 6.24: Comparison of sampled waveform data before and after adaptive spatial filtering is applied to the data streams. The output in (b) shows the removal of the 10MHz QPSK spectrum. The Radar echo return pulse is also more easily detected, visually, in the waveform graph.

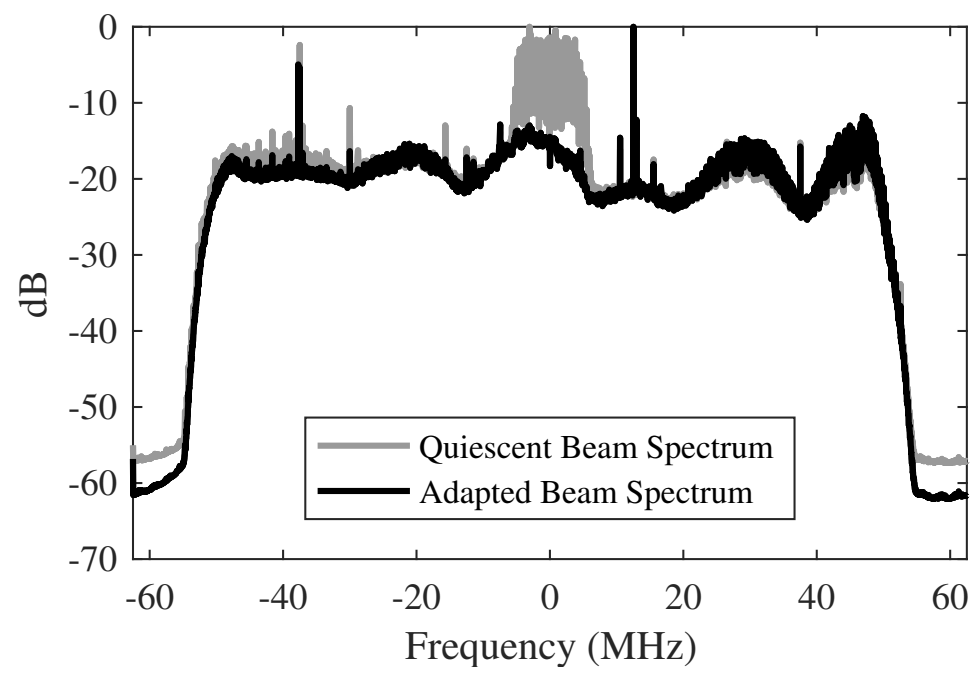


Figure 6.25: Output spectrum of the quiescent and adapted beams steered toward the direction of the radar signal. Greater than 20 dB suppression of the QPSK spectrum has been achieved.

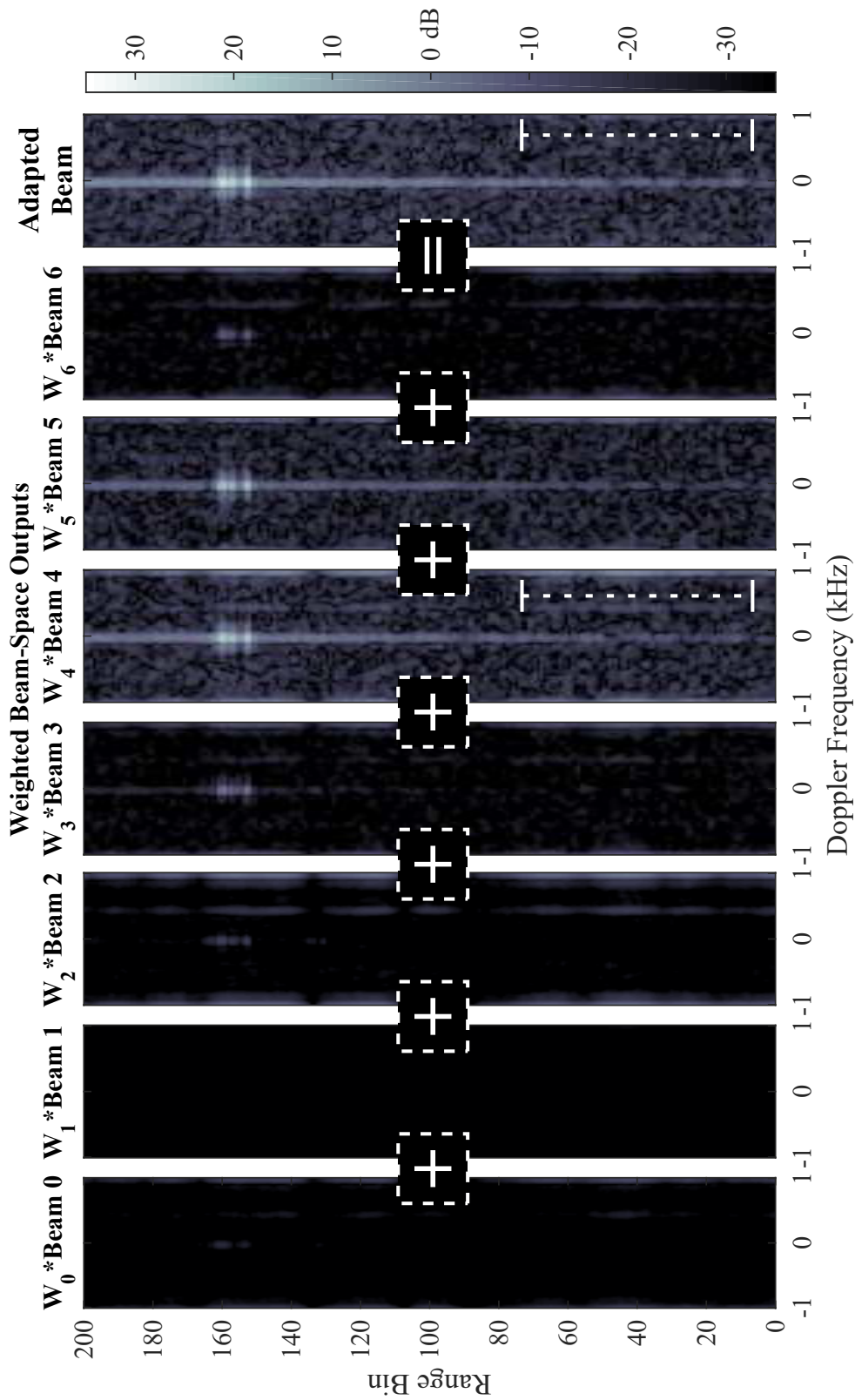


Figure 6.26: The outputs from beam-space sampling array may be weighted to steer a beam towards signal peaks evident on the SWIR output. The beams have been weighted toward the signal at 24 degrees while attempting to adapt a null on the interfering signal at -28 degrees. The weighted beams are summed to form an adapted beam output. The white-dotted lines call attention to the interference signal, suppressed in the adapted output.

with results better than sample covariance based weighting schemes. The results shown here have spatially-nulled the interference beyond its initial 20 dB of interference-to-signal ratio, leaving the adapted output of the beam-space data free of the constant Doppler spurs that were evident prior to applying any adaptive beam-space weights.

6.3 Significant Outcomes from Multi-function Experimentation

Based on the results for various sampled beam-space experiments that have been achieved to date, and the small array sizes that have been used thus far for experimentation, it has been discovered that robust results are obtained within the field-of-view that encompasses approximately $\pm 50^\circ$. This is due in part to the unreliable beam performance outside of this region, coupled with the fact that the large detector sizes in current use allow significant cross-talk in the outer beams of the beam-space. However, the first demonstrations of simultaneous functionality (i.e., communications and Radar signal recovery) of a photonic beam-space receive array have been recorded. To the knowledge of the author, this feat is unique to the work presented here. Moreover, several lessons on the design of a beam-space sampling photo-detector array have been learned, along with several methods to align and calibrate such a device so that a full beam-space can be sampled at the output of the photonic array processor described herein. With the beam-space sampling array in place, it was shown that the photonic array processor allows for the simultaneous down-conversion of any location within the beam-space. The down-conversion process has the advantage of using a single LO signal for the entire beam-space, thus reducing errors associated with clock distribution and skew. This is seen as a significant advantage, especially across a large input array. The down-converted outputs were then shown to be useful for recovery of both In-phase and Quadrature signal components which allows for the multi-functional processing to be undertaken. Additionally, it was shown that the beam-space outputs can be used in a variety of spatial spectral estimation techniques in order to identify possible location of incident signals. The key finding here being that the ability to image the entire spatial spectrum through the use of a commercial SWIR camera enabled a robust, low-latency

estimate of possible interference sources such that a set of adaptive weights for the beam-space outputs could be generated in an effort to null the interference. Finally, a new method of weighting a beam-space dataset, based on the SWIR data estimates was shown to out-perform traditional, covariance based techniques, in both potential latency as well as null-depth as shown in Fig. 6.23.

Chapter 7

CONCLUSIONS AND FUTURE WORK

The research performed throughout the course of this work has provided the community with a new understanding of the possible uses of RF photonics as they pertain to Array theory and processing. These techniques are wholly different from the traditional focus on RF photonic True-time delay beam-steering. Here, the techniques initially pioneered for passive RF imaging have been augmented for use in the remote processing of arrays of arbitrary sizes. Specifically, Chapter 2 of this work outlined the theory of array remoting via an array of electro-optic modulators where it was shown that an arrayed approach has the potential to offer substantial gain when compared to a single-receiver link of similar components. The remoted array elements can then be passed to an optical array processor, often referred to as the photonic array processor within the text, that allows for the measurement of the phase across the elements as well as the irradiance pattern of the spatial frequency spectrum. The phase measurements are used to compensate for phase mismatches among the elements such that they can maintain coherence. The coherent optical field is sent through a Fourier transforming lens system, generating a continuous spatial spectrum at the output. The theory of how an incident signal of a given angle is translated onto the output plane of the processor was derived along with several methods to taper, or apodize, the output response function. Finally, the introduction of a single optical local oscillator signal at the input to the processor was shown to allow for the down-conversion of any point within the spatial spectrum (also referred to as a Beam-space) with the addition of a high-speed photo-detector at the output plane.

Chapter 3 discussed the precise methods for the measurement of the irradiance pattern of the continuous spatial spectrum at the output of the photonic array processor. The irradiance pattern is shown to be equivalent to the amplitude of the far-field radiation pattern of the re-radiated optically up-converted electric-field. It is the re-radiation of the up-converted RF element fields that allows the optical processor to “image” the RF environment. The discussion continued with methods for determining the useful region of a given output image, as well as some shortcomings to the Fourier Imaging approach when it comes to wide-band inputs. The discussion is continued via introduction of the techniques used in the prototype system to down-convert the beam-space and sample and filter the data such that the real-sampled beam-space can be converted to a set of complex samples. This ability is fundamental to the usage of the system for both communications and radar functions. The basic techniques used to process both a communications signal and a radar signal are presented along with the necessary background for how a set of sampled beams can be processed in tandem for use in a number of adaptive filtering and spatial spectrum estimation techniques.

Chapter 4 discussed the multitude of experimental hardware that was developed, augmented or otherwise utilized throughout the course of this work. The experimental system consisted of two separate “carts”, one holding the RF receive array and associated photonic back-end that was the focus of the discussion in Chapter 2 as well as Section 3.1, while the other served as the Radar waveform generator, digitizer and beam-space adaptive processor. The experiments also used a number of test sources, namely a specially designed photonic test target generator, and a communications signal emulator. A significant amount of effort went into the design, control and coordination of myriad components across the two carts. The work performed in interfacing, data recording and processing was paramount to the success of the experiments presented in the final chapters of this Thesis.

Chapters 5 and 6 discuss the setup, operation and outcome of several experiments. The initial experiments of Chapter 5 were devised to prove the ability to taper the output beam-space by altering the input laser signal to the up-conversion stages

of the array processor. The results were promising and have been featured in several technical reports and publications [54, 81, 85]. The results of the initial apodization experiments also led the discovery of several sources of phase and amplitude error specific to the photonic components used within the system as well as a number of potential pitfalls to be avoided when scaling the technology to larger arrays. These discoveries will undoubtedly lead to enhanced versions of the system in the future as will be discussed in the section on future work. The experiments discussed in Chapter 6 concentrated on the simultaneous detection and recovery of disparate signals in two spatially isolated channels (i.e., separate beam positions). The demonstrations are the first of their type, with two separate signals being recovered from two separate beams and simultaneously down-converted using a single optical LO and have been featured in several publications [86, 87]. The approach was tried with several apodization profiles applied and significant lessons on the alignment of beam-sampling photo-detectors with desired spatial locations were learned. These lessons were applied to prove the possibility of sampling a full set of orthogonal beam positions for use in later adaptive processing experiments. The later experiments showed that the ability to “image” the beam-space in real-time with a SWIR detector, while simultaneously down-converting an orthogonal sampling of that same beam-space, could be used to develop a powerful, low-latency, adaptive weighting scheme. The latency was shown to be superior than that of a state-of-the-art FPGA for array sizes over 118 elements using the current detectors, with potential improvement to include array sizes as small as 9 elements. It was further shown that the application of the proposed weighting scheme, to the collected beam-space data, effectively nulled the SWIR-detected interference signal completely, while maintaining array gain along the desired look direction.

7.1 Future Work

The performance of the prototype equipment shows significant potential for use in future communications and radar applications. However, there are specific areas of investigation that can offer tremendous improvements in capability moving forward:

1. Integration of RF gain and RF photonic conversion stages to allow for critically sampled arrays of arbitrary size (and potentially frequency),
2. Reduction of RAM and other deleterious phase and amplitude effects imparted by the phase-coherence control mechanism and associated phase modulators,
3. Ability to rapidly apply apodization profiles and maintain relative amplitudes across array elements in an automated fashion,
4. Integration of SWIR spatial spectrum measurements into an adaptive control loop with low latency and convergence,
5. Integration of Spatial Spectrum Measurement detectors and Beam-space sampling detectors, a “Foveal Detector,”
6. Multiplexing of disparate RF Arrays onto a single Photonic Array Processor back-end for wide-band access.

7.1.1 Integrated RF-Photonic Receiver Module

The existing prototype uses bulk RF and bulk-fiber connectorized components eliminating the chances of building a critically sampled array without the usage of bulky interposers. With the coming advances in photonic integration [26], it is likely possible to integrate all of the components necessary for the up-conversion stage of the system. Integration at this level would alleviate the current challenges in achieving matched lengths of fiber for each channel, a feat that does not scale well with array size. It also may allow for the integration of the phase and amplitude controls necessary to maintain coherence and/or various apodization profiles.

7.1.2 Reduction of Error Sources

Certainly, integration of various components at the chip level can eliminate some sources for error, however it may also introduce some. The attempted to integrate the phase control modulators that are used to maintain coherence across the channels is

a good example of where integration can lead to unintended consequences. Thus, care must be taken in the design of future phase control systems to ensure that significantly less coupling across the channels and residual amplitude modulation within each channel are produced. Additional experiments using discrete phase modulators on each channel should be performed to ensure that errors are due to the modulator and not due to some oscillation in the phase control loop. The original phase control design was optimized for non-coherent imaging of passive millimeter wave energy, and thus it should likely be re-optimized for the coherent recovery of an RF array beam-space.

7.1.3 Application of real-time laser amplitude control

Currently, laser amplitude profiles are adjusted by hand, and while they are found to remain stable for days once adjusted, the initial calibration can take an hour or better to perform. For this reason a set of variable attenuators with a tapped feedback mechanism have been ordered to investigate methods to rapidly converge on a set of desired amplitude weights across the array. It is hoped that the variable optical attenuator (VOA) system will allow for real-time equalization of the optical channels along with rapid adaptation of the amplitudes. This capability along with the existing phase-control loop can be used to test the ability to apply complex weighing profiles across the array in real-time. This is seen as a necessary step to achieving a truly low-latency adaptive output capability.

7.1.4 Photonically Driven Adaptive Array Control

Assuming the ability to simultaneously apply amplitude and phase weights across the channels is proven by the usage of the VOA along with the existing prototype hardware, the logical next step is to apply the weights calculated from the SWIR camera estimates of an ideal interference source covariance directly to the array elements.

The adaptive technique described in Chapter 6 is seen as a unique capability that is only afforded by the usage of elemental optical up-conversion of an RF array.

The real-time aspect of the measurement is important, and with updated components, to further improve latency, could potentially be combined with the feed-back loop used for maintaining phase coherence across the channels. The current FPGA used for the phase-control loop could be updated to perform peak-search and weight estimation operations, allowing the entire process to occur in near-real-time. This combination would allow for the weighting to be applied in the element-space, rather than the beam-space, such that a set of desired look-directions could be maintained with constant gain, while any interference sources could be mitigated in real-time. This ability, along with the ability to re-steer the beam-space as discussed in Section 3.1.2, could allow recovery of the adapted beams directly at the output, further reducing the latency associated with achieving a spatially filtered output data set.

7.1.5 Foveated Sensing using Coherent Optical Up-Conversion

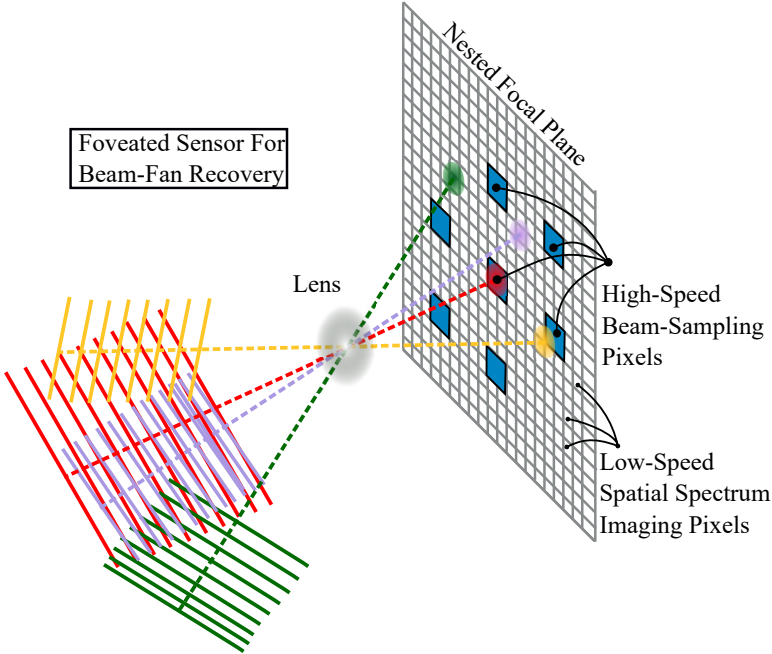


Figure 7.1: Graphic depiction of a potential layout for a nested array of photo-detectors. Such an array would allow the collapse of two separate functions within the photonic array processor to a single optical path.

It was shown in this thesis that only an orthogonal (or even approximately-orthogonal) set of beam-output locations is required to be recovered in order to form an adapted array response toward any direction within the RF array's useful field-of-view. For this reason it should be possible to design a focal plane array of sensors such that two embedded grids of pixels are overlaid. This could be thought of as a foveated type of sensor where a cluster of high-speed photo-detectors are meant to enable sampling and recovery of an orthogonal beam-space, while the surrounding, low-speed pixels were used to estimate signal locations for adaptive weight generation. Development of an array such as the one pictured in Fig. 7.1 would allow for one less lens and optical chain in the system. Currently a separate lens path is required for each function (i.e. Beam sampling and Spatial Spectrum Measurement).

7.1.6 Switched-inputs for Wide-band Operation

The photonic system used for experiments accepts RF inputs across the 5 GHz to 25 GHz band before the optical filters used start to block the RF side-band of interest. Furthermore, the beam-forming lens system operates across an even greater range within the limits of tolerable beam-squint. To avoid issues of beam-squint across a single, wide-band, array, it may be possible to multiplex the signals from many separate, narrow-band arrays instead. To test this theory a number of optical switches are being procured to allow for separate RF arrays, each with their own up-conversion stages to be switched into the photonic array processor as needed. This capability could lead to the discovery of novel methods to multiplex multiple arrays, perhaps via separate optical polarizations or separate master-laser wave-lengths. Such a system would allow for coherent recovery of signals across disparate arrays and could lead to several novel applications of the technology moving forward.

BIBLIOGRAPHY

- [1] K. F. Braun. Electrical oscillations and wireless telegraphy. In Stig Lundqvist, editor, *Nobel Lectures, Physics, 1901-1921*, volume 1. Elsevier Publishing Company, 1998.
- [2] R. M. Wilmotte. History of the directional antenna in the standard broadcast band for purpose of protecting service area of distant stations. *IRE Transactions on Broadcast Transmission Systems*, PGBTS-7(1):51–55, Feb 1957.
- [3] H. T. Friis and C. B. Feldman. A multiple unit steerable antenna for short-wave reception. *Proceedings of the Institute of Radio Engineers*, 25(7):841–917, July 1937.
- [4] R. M. Page. The early history of radar. *Proceedings of the IRE*, 50(5):1232–1236, May 1962.
- [5] C. A. Fowler. Old radar types never die; they just phased array or ... 55 years of trying to avoid mechanical scan. *IEEE Aerospace and Electronic Systems Magazine*, 13(9):24A–24L, Sept 1998.
- [6] Allen J. L. and et. al. Phased array radar studies, 1 july 1960 to 1 july 1961. Technical Report 236, MIT Lincoln Laboratory, 1961.
- [7] F. C. Ogg. Steerable array radars. *IRE Transactions on Military Electronics*, MIL-5(2):80–94, April 1961.
- [8] C. Fulton, M. Yeary, D. Thompson, J. Lake, and A. Mitchell. Digital phased arrays: Challenges and opportunities. *Proceedings of the IEEE*, 104(3):487–503, March 2016.
- [9] P. S. Hall and S. J. Vetterlein. Review of radio frequency beamforming techniques for scanned and multiple beam antennas. *IEE Proceedings H - Microwaves, Antennas and Propagation*, 137(5):293–303, Oct 1990.
- [10] W. Hong, Z. H. Jiang, C. Yu, J. Zhou, P. Chen, Z. Yu, H. Zhang, B. Yang, X. Pang, M. Jiang, Y. Cheng, M. K. T. Al-Nuaimi, Y. Zhang, J. Chen, and S. He. Multi-beam antenna technologies for 5g wireless communications. *IEEE Transactions on Antennas and Propagation*, PP(99):1–1, 2017.

- [11] J. Bulter and R. Lowe. Beamforming matrix simplifies design of electronically scanned antennas. *Electronics Design*, pages 170–173, 1961.
- [12] J. Blass. Multidirectional antenna - a new approach to stacked beams. In *1958 IRE International Convention Record*, volume 8, pages 48–50, March 1960.
- [13] F. Press. The need for fundamental research in seismology: A summary of the report from the panel on seismic improvement. *Transactions of the American Geophysical Union*, 40(3), September 1959.
- [14] F. Bryn. Optimum signal processing of three-dimensional arrays operating on gaussian signals and noise. *Journal of the Acoustic Society of America*, 34:289–297, 1962.
- [15] R. J. Greenfield J. Capon and R. T. Lacoss. Off-line signal processing results for the large aperture seismic array. Technical Note 1966-37, MIT Lincoln Laboratory, 1966.
- [16] R. J. Greenfield J. Capon and R. T. Lacoss. Design of seismic arrays for efficient on-line beamforming. Technical Note 1967-26, MIT Lincoln Laboratory, 1967.
- [17] H. W. Briscoe and P. L. Fleck. Data recording and processing for the experimental large aperture seismic array. *Proceedings of the IEEE*, 53(12):1852–1859, Dec 1965.
- [18] S. P. Applebaum. Adaptive arrays. Technical Report SPL-769, Syracuse University Research Corporation, June 1964.
- [19] S. Applebaum. Adaptive arrays. *IEEE Transactions on Antennas and Propagation*, 24(5):585–598, Sep 1976.
- [20] P. Barton. Digital beam forming for radar. *Communications, Radar and Signal Processing, IEE Proceedings F*, 127(4):266–277, August 1980.
- [21] B. D. Van Veen and K. M. Buckley. Beamforming: a versatile approach to spatial filtering. *IEEE ASSP Magazine*, 5(2):4–24, April 1988.
- [22] L. C. Godara. Application of antenna arrays to mobile communications. ii. beam-forming and direction-of-arrival considerations. *Proceedings of the IEEE*, 85(8):1195–1245, Aug 1997.
- [23] H. Krim and M. Viberg. Two decades of array signal processing research: the parametric approach. *IEEE Signal Processing Magazine*, 13(4):67–94, Jul 1996.
- [24] H. Singh and R. M. Jha. Trends in adaptive array processing. *International Journal of Antennas and Propagation*, 2012, 2012.
- [25] H. L. Van Trees. *Optimum Array Processing*. John Wiley and Sons, Inc., 2002.

- [26] K. Kincade. Aim photonics moves ahead. *SPIE Professional*, April 2016.
- [27] C. A. Schuetz. Optical techniques for millimeter-wave detection and imaging. Doctoral dissertation, University of Delaware, August 2007.
- [28] Vincent J. Urick, Jason D. McKinney, and Keith J. Williams. *Fundamentals of Microwave Photonics*. John Wiley and Sons, Inc., 2015.
- [29] C. A. Balanis. *Antenna Theory: Analysis and Design*. Wiley, 4 edition, 2016.
- [30] R. G. Priest. Analysis of fiber interferometer utilizing 3 x 3 fiber coupler. *IEEE Transactions on Microwave Theory and Techniques*, 30(10):1589–1591, 1982.
- [31] B. Moslehi, J. W. Goodman, M. Tur, and H. J. Shaw. Fiber-optic lattice signal processing. *Proceedings of the IEEE*, 72(7):909–930, 1984.
- [32] Janet L. Brooks, Robert H. Wentworth, Robert C. Youngquist, Moshe Tur, Byoung Yoon Kim, and H. J. Shaw. Coherence multiplexing of fiber-optic interferometric sensors. *Journal of Lightwave Technology*, LT-3(5), October 1985.
- [33] Z. Cao, Q. Ma, A. B. Smolders, Y. Jiao, M. J. Wale, C. W. Oh, H. Wu, and A. M. J. Koonen. Advanced integration techniques on broadband millimeter-wave beam steering for 5g wireless networks and beyond. *IEEE Journal of Quantum Electronics*, 52(1):1–20, Jan 2016.
- [34] C.A. Schuetz and al. et. Applications of photonics for spatial and spectral processing of microwave and millimeter-wave signals. In *Proceedings of IEEE AVFOP*, 2015.
- [35] Y. Fu, X. Zhang, B. Hraimel, T. Liu, and D. Shen. Mach-zehnder: A review of bias control techniques for mach-zehnder modulators in photonic analog links. *IEEE Microwave Magazine*, 14(7):102–107, Nov 2013.
- [36] J. W. Goodman. *Introduction to Fourier Optics*. Roberts and Company Publishers, 2005.
- [37] R.D. Martin, C.A. Schuetz, D.W. Prather, and T.E. Dillon. Controlling the phase of optical carriers, April 2012. US Patent 8,159,737.
- [38] Meng Xue, Jun and Karim Adil. Microwave photonic link with carrier suppression for increased dynamic range. *Fiber and Integrated Optics*, 25(3):161–174, 2006.
- [39] J. C. Deroba, S. Shi, C. A. Schuetz, and D. W. Prather. A novel photonic beam-space receiver for multi-function radar. In *Proc. SPIE*, volume 9829, 2016.
- [40] T. T. Taylor. Design of line-source antennas for narrow beamwidth and low side lobes. *Transactions of the IRE on Antennas and Propagation*, 3:16–28, January 1955.

- [41] A. J. Seeds and et. al. Coherent terahertz photonics. *Opt. Express*, 21(19):22988–23000, Sep 2013.
- [42] A. Theodore Forrester, William E. Parkins, and Edward Gerjuoy. On the possibility of observing beat frequencies between lines in the visible spectrum. *Phys. Rev.*, 72:728–728, Oct 1947.
- [43] A. Theodore Forrester, Richard A. Gudmundsen, and Philip O. Johnson. Photoelectric mixing of incoherent light. *Phys. Rev.*, 99:1691–1700, Sep 1955.
- [44] A. E. Siegman, S. E. Harris, and B.J. McMurtry. Optical heterodyning and optical demodulation at microwave frequencies. In J. Fox, editor, *Optical Masers*, XIII, pages 511–528. Wiley, 1963.
- [45] O. E. DeLange. Optical heterodyne detection. *IEEE Spectrum*, 5(10):77–85, Oct 1968.
- [46] J. Fred Holmes and Badih J. Rask. Optimum optical local-oscillator power levels for coherent detection with photodiodes. *Appl. Opt.*, 34(6):927–933, Feb 1995.
- [47] G. J. Schneider, J. A. Murakowski, C. A. Schuetz, S. Shi, and D. W. Prather. Radiofrequency signal-generation system with over seven octaves of continuous tuning. *Nature Photonics*, 7(2):118–122, February, 2013.
- [48] W. M. Waters and B. R. Jarrett. Bandpass signal sampling and coherent detection. *IEEE Transactions on Aerospace and Electronic Systems*, AES-18(6):731–736, Nov 1982.
- [49] D. W. Rice and K. h. Wu. Quadrature sampling with high dynamic range. *IEEE Transactions on Aerospace and Electronic Systems*, AES-18(6):736–739, Nov 1982.
- [50] C. M. Rader. A simple method for sampling in-phase and quadrature components. *IEEE Transactions on Aerospace and Electronic Systems*, AES-20(6):821–824, Nov 1984.
- [51] R. L. Mitchell. Creating complex signal samples from a band-limited real signal. *IEEE Transactions on Aerospace and Electronic Systems*, 25(3):425–427, May 1989.
- [52] G.A. Shaw and S.C. Pohlig. I/q baseband demodulation in the rassp sar benchmark. Project Report ESC-TR-95-053, MIT Lincoln Laboratory, 1995.
- [53] J. McClellan and T. Parks. A unified approach to the design of optimum fir linear-phase digital filters. *IEEE Transactions on Circuit Theory*, 20(6):697–701, November 1973.

- [54] J. C. Deroba, G. J. Schneider, C. A. Schuetz, and D. W. Prather. Smart antenna using element-level photonic up-conversion to generate an apodized beam-space for increased spatial isolation. *IEEE Antennas and Wireless Propagation Letters*, 16:2274–2277, 2017.
- [55] J.G. Proakis. *Digital Communications*. Electrical engineering series. McGraw-Hill, 2001.
- [56] F. Gardner. A bpsk/qpsk timing-error detector for sampled receivers. *IEEE Transactions on Communications*, 34(5):423–429, May 1986.
- [57] K. Mueller and M. Muller. Timing recovery in digital synchronous data receivers. *IEEE Transactions on Communications*, 24(5):516–531, May 1976.
- [58] M. Skolnik. *Radar Handbook, Third Edition*. Electronics electrical engineering. McGraw-Hill Education, 2008.
- [59] L. E. Brennan and L. S. Reed. Theory of adaptive radar. *IEEE Transactions on Aerospace and Electronic Systems*, AES-9(2):237–252, March 1973.
- [60] N. R. Goodman. Statistical analysis based on a certain multivariate complex gaussian distribution (an introduction). *The Annals of Mathematical Statistics*, 34(1):152–177, 03 1963.
- [61] M. S. Bartlett. Smoothing periodograms from time series with continuous spectra. *Nature*, 161:686–687, 1948.
- [62] J. Capon. High-resolution frequency-wavenumber spectrum analysis. *Proceedings of the IEEE*, 57(8):1408–1418, Aug 1969.
- [63] J. P. Burg. Maximum entropy spectral analysis. Doctoral thesis, Stanford University, May, 1975.
- [64] M. Wax and T. Kailath. Detection of signals by information theoretic criteria. *IEEE Transactions on Acoustics, Speech, and Signal Processing*, 33(2):387–392, Apr 1985.
- [65] V. F. Pisarenko. The retrieval of harmonics from a covariance function. *Geophysical Journal of the Royal Astronomical Society*, 33:347–366, 1973.
- [66] K. M. Buckley and X. L. Xu. Spatial-spectrum estimation in a location sector. *IEEE Transactions on Acoustics, Speech, and Signal Processing*, 38(11):1842–1852, Nov 1990.
- [67] R. Kumaresan and D. W. Tufts. Estimating the angles of arrival of multiple plane waves. *IEEE Transactions on Aerospace and Electronic Systems*, AES-19(1):134–139, Jan 1983.

- [68] D. Johnson and S. DeGraaf. Improving the resolution of bearing in passive sonar arrays by eigenvalue analysis. *IEEE Transactions on Acoustics, Speech, and Signal Processing*, 30(4):638–647, Aug 1982.
- [69] M. Kaveh and A. Barabell. The statistical performance of the MUSIC and the minimum-norm algorithms in resolving plane waves in noise. *IEEE Transactions on Acoustics, Speech, and Signal Processing*, 34(2):331–341, Apr 1986.
- [70] I. S. Reed, J. D. Mallett, and L. E. Brennan. Rapid convergence rate in adaptive arrays. *IEEE Transactions on Aerospace and Electronic Systems*, AES-10(6):853–863, Nov 1974.
- [71] Xilinx. Vivado design suite release 2017.2 - performance and resource utilization for complex multiplier v6.0. Online, 2017. Last Accessed, 20170629.
- [72] A. W. Doerry. Catalog of window taper functions for sidelobe control. Sandia Report SAND2017-4042, Sandia National Laboratories, 2017.
- [73] J. K. Hsaio. Effects of errors on the side-lobe level of a low-side-lobe array antenna. NRL Report 8485, Naval Research Laboratory, 1981.
- [74] J. K. Hsaio. Array sidelobes, error tolerance, gain and beamwidth. NRL Report 8841, Naval Research Laboratory, 1984.
- [75] L. Rondinelli. Effects of random errors on the performance of antenna arrays of many elements. In *1958 IRE International Convention Record*, volume 7, pages 174–189, March 1959.
- [76] Edward A. Whittaker, Manfred Gehrtz, and Gary C. Bjorklund. Residual amplitude modulation in laser electro-optic phase modulation. *J. Opt. Soc. Am. B*, 2(8):1320–1326, Aug 1985.
- [77] Juna Sathian and Esa Jaatinen. Dependence of residual amplitude noise in electro-optic phase modulators on the intensity distribution of the incident field. *Journal of Optics*, 15(12):125713, 2013.
- [78] C. Ishibashi, J. Ye, and J. L. Hall. Analysis/reduction of residual amplitude modulation in phase/frequency modulation by an eom. In *2002 Summaries of Papers Presented at the Quantum Electronics and Laser Science Conference*, pages 91–92, May 2002.
- [79] H. S. C. Wang. Performance of phased array antennas under error conditions. In *IEEE Aerospace Applications Conference*, pages 25 pp.–, Feb 1989.
- [80] H. S. C. Wang. Performance of phased-array antennas with mechanical errors. *IEEE Transactions on Aerospace and Electronic Systems*, 28(2):535–545, Apr 1992.

- [81] D. W. Prather and et. al. Optically-upconverted, spatially-coherent phased array antenna feed networks for beam-space mimo in 5g cellular communications. *IEEE Transactions on Antennas and Propagation*, October 2017. Accepted for Publication.
- [82] M. Skolnik. *Antenna Engineering Handbook*. McGraw-Hill Education, fourth edition, 2007.
- [83] Hamamatsu. G10768 series - near infrared image sensor with 1024 pixels and high-speed line rate. Online, July, 2015. Last Accessed, 20170629.
- [84] M. Wax and I. Ziskind. Detection of the number of coherent signals by the mdl principle. *IEEE Transactions on Acoustics, Speech, and Signal Processing*, 37(8):1190–1196, Aug 1989.
- [85] J. C. Deroba and et. al. Spatial-spectrum measurement from tapered radio-frequency arrays via photonic up-conversion and fourier processing. Being Prepared for Submission.
- [86] J. C. Deroba and et. al. Multi-function photonic array processor with optical beam-space down-conversion. Submitted for Publication.
- [87] C.A. Schuetz, G. J. Schneider, J. Murakowski, S. Shi, J. C. Deroba, and D. W. Prather. Imaging flash-radar realized using photonic spatial beam processing. *IEEE Microwave Magazine*, April 2018. Invited for Publication.

Appendix A

DERIVATION OF A CLOSED-FORM ARRAY RESPONSE FOR A UNIFORMLY ILLUMINATED LINEAR ARRAY

Beginning with the relationship in (1.6) and setting $A_n = 1$ for all n , we have:

$$AF(\theta) = \sum_{n=0}^{N-1} e^{j\Delta\phi_n} e^{-j\phi_s} = \sum_{n=0}^{N-1} e^{j\frac{2\pi}{\lambda_{rf}} nd_{ant}[\sin\theta - \sin\theta_s]}. \quad (\text{A.1})$$

Recognizing the relation in (A.1) as a particular geometric series, we can use the finite sum formula given by

$$\sum_{k=a}^b r^k = \frac{r^a - r^{b+1}}{1 - r}, \quad (\text{A.2})$$

along with the substitutions of $a = 0$ and $b = N - 1$ to arrive at the following formula that is relevant to our summation in (A.1):

$$\sum_{k=0}^{N-1} r^k = \frac{1 - r^N}{1 - r}. \quad (\text{A.3})$$

Thus, let $x = \frac{2\pi d_{ant}}{\lambda_{rf}} (\sin\theta - \sin\theta_s)$ which leaves us with the following simplified form of the array factor,

$$AF(\theta) = \sum_{n=0}^{N-1} e^{jn x}. \quad (\text{A.4})$$

Using the relation in (A.3), we now have the following set of trigonometric manipulations to (A.4):

$$AF(\theta) = \frac{1 - e^{jNx}}{1 - e^{jx}} \quad (\text{A.5})$$

$$= \frac{1 - \cos(Nx) - j \sin(Nx)}{1 - \cos x - j \sin x}, \quad (\text{A.6})$$

taking the squared magnitude of both sides provides,

$$|AF(\theta)|^2 = \frac{(1 - \cos(Nx) - j \sin(Nx)) \cdot (1 - \cos(Nx) + j \sin(Nx))}{(1 - \cos x - j \sin x) \cdot (1 - \cos x + j \sin x)} \quad (\text{A.7})$$

$$= \frac{1 - 2 \cos(Nx) + \cos^2(Nx) + \sin^2(Nx)}{1 - 2 \cos(x) + \cos^2(x) + \sin^2(x)} \quad (\text{A.8})$$

$$= \frac{2 - 2 \cos(Nx)}{2 - 2 \cos(x)} \quad (\text{A.9})$$

$$= \frac{1 - \cos(Nx)}{1 - \cos(x)}, \quad (\text{A.10})$$

remembering that

$$\sin^2(x) = \frac{1}{2}(1 - \cos(2x)), \quad (\text{A.11})$$

so if we substitute, $y = 2x$, such that $x = \frac{y}{2}$ above, we arrive at

$$2 \sin^2\left(\frac{y}{2}\right) = 1 - \cos(y), \quad (\text{A.12})$$

such that we can reduce (A.10) to

$$|AF(\theta)|^2 = \frac{2 \sin^2\left(\frac{Nx}{2}\right)}{2 \sin^2\left(\frac{x}{2}\right)}. \quad (\text{A.13})$$

Finally, taking the square root and replacing x leaves us with

$$\begin{aligned} \sqrt{|AF(\theta)|^2} &= \sqrt{\frac{2 \sin^2\left(\frac{Nx}{2}\right)}{2 \sin^2\left(\frac{x}{2}\right)}} \\ AF(\theta) &= \frac{\sin\left(\frac{Nx}{2}\right)}{\sin\left(\frac{x}{2}\right)} \\ AF(\theta) &= \frac{\sin\left(Nd_{ant} \frac{\pi}{\lambda_{rf}} [\sin \theta - \sin \theta_s]\right)}{\sin\left(d_{ant} \frac{\pi}{\lambda_{rf}} [\sin \theta - \sin \theta_s]\right)}, \\ AF(\theta) &= \frac{\sin\left(Nd_{ant} \frac{\pi}{\lambda_{rf}} [\sin \theta_s - \sin \theta]\right)}{\sin\left(d_{ant} \frac{\pi}{\lambda_{rf}} [\sin \theta_s - \sin \theta]\right)}, \end{aligned} \quad (\text{A.14})$$

which is equivalent to the result in (1.4) when $\theta_s = 0$.

Appendix B

DERIVATION OF ARRAY BEAM-WIDTH

Beginning with the final relation in (A.14) we have:

$$\begin{aligned}
 AF(\theta) &= \frac{\sin\left(Nd_{ant}\frac{\pi}{\lambda_{rf}}[\sin\theta_s - \sin\theta]\right)}{\sin\left(d_{ant}\frac{\pi}{\lambda_{rf}}[\sin\theta_s - \sin\theta]\right)}, \\
 &\approx \frac{\sin\left(Nd_{ant}\frac{\pi}{\lambda_{rf}}[\sin\theta_s - \sin\theta]\right)}{\left(Nd_{ant}\frac{\pi}{\lambda_{rf}}[\sin\theta_s - \sin\theta]\right)},
 \end{aligned} \tag{B.1}$$

where we have approximated the array factor via a true sinc function. We wish to derive an angle, offset from the maximum response, θ_{3dB} , that is 3 dB down from the peak response. It is convenient to first determine the value for the argument of the sinc function that produces the desired -3dB output value, therefore we must solve

$$\frac{\sin x}{x} = 10^{\frac{-3}{20}} = .70795, \tag{B.2}$$

for x . This is done most simply with a commercial solver or by plotting the function via any numerical software one might have available. The value for x can be found to be approximately equal to ± 1.39 . Taking this result along with the initial argument in (B.1) we can construct the following relations with respect to the angle, θ :

$$\frac{\pi Nd_{ant}}{\lambda_{rf}} \left[\sin\theta_s - \sin\left(\theta_s + \frac{\theta_{3dB}}{2}\right) \right] = -1.39 \tag{B.3}$$

$$\frac{\pi Nd_{ant}}{\lambda_{rf}} \left[\sin\theta_s - \sin\left(\theta_s - \frac{\theta_{3dB}}{2}\right) \right] = 1.39, \tag{B.4}$$

where we have considered both sides of the beam. To solve for the beam-width we can subtract equations (B.3) and (B.4), to arrive at a single relation:

$$\begin{aligned}
 \frac{\pi Nd_{ant}}{\lambda_{rf}} \left[\sin\theta_s - \sin\left(\theta_s + \frac{\theta_{3dB}}{2}\right) - \sin\theta_s + \sin\left(\theta_s - \frac{\theta_{3dB}}{2}\right) \right] &= -2.78 \\
 \frac{\pi Nd_{ant}}{\lambda_{rf}} \left[\sin\left(\theta_s - \frac{\theta_{3dB}}{2}\right) - \sin\left(\theta_s + \frac{\theta_{3dB}}{2}\right) \right] &= -2.78,
 \end{aligned} \tag{B.5}$$

which can be further reduced using the trigonometric identity,

$$\sin(a) = \sin(b) = 2 \cos\left(\frac{a+b}{2}\right) \sin\left(\frac{a-b}{2}\right), \quad (\text{B.6})$$

to leave us with

$$\begin{aligned} \frac{2\pi N d_{ant}}{\lambda_{rf}} \cos\left[\frac{(\theta_s - \frac{\theta_{3dB}}{2}) + (\theta_s + \frac{\theta_{3dB}}{2})}{2}\right] \sin\left[\frac{(\theta_s - \frac{\theta_{3dB}}{2}) - (\theta_s + \frac{\theta_{3dB}}{2})}{2}\right] &= -2.78, \\ \frac{2\pi N d_{ant}}{\lambda_{rf}} \cos[\theta_s] \sin\left[\frac{-\theta_{3dB}}{2}\right] &= -2.78. \end{aligned} \quad (\text{B.7})$$

Taking the small angle approximation allows one to further reduce the relation above

$$\frac{2\pi N d_{ant}}{\lambda_{rf}} \cos[\theta_s] \left[\frac{\theta_{3dB}}{2}\right] = 2.78, \quad (\text{B.8})$$

$$\frac{\pi N d_{ant}}{\lambda_{rf}} \cos[\theta_s] \theta_{3dB} = 2.78, \quad (\text{B.9})$$

$$\theta_{3dB} = \frac{2.78 \cdot \lambda_{rf}}{\pi N d_{ant} \cos[\theta_s]}, \quad (\text{B.10})$$

$$\theta_{3dB} = \frac{0.886 \cdot \lambda_{rf}}{L_{ant} \cos[\theta_s]}, \quad (\text{B.11})$$

which produces the familiar result for the 3 dB beam-width of an un-tapered array. A more general form may be written as

$$\theta_{3dB} = \frac{k_{ant} \cdot \lambda_{rf}}{L_{ant} \cos[\theta_s]}, \quad (\text{B.12})$$

where k_{ant} is a factor related to the efficiency of a particular aperture illumination function (i.e., amplitude taper profile).

Appendix C

JACOBI-ANGER EXPANSION

The Jacobi-Anger Expansion appears in many texts dealing with signal processing theory, electromagnetic theory and other disciplines where complex exponentials are common. It is useful in simplifying a number of equations related to both phase and frequency modulation as well as in expansions of plane waves to cylindrical waves. The identity relates a complex exponential with a sinusoidal phase function to an infinite sum of Bessel functions. There are several, real-valued forms that have been used when simplifying a number of equations in Chapter 2 of this thesis. An introduction to the Jacobi-Anger Identity and some simple derivations of the real-valued relations are offered below.

We begin with the complex relation:

$$e^{jx \cos \theta} = \sum_{n=-\infty}^{\infty} j^n J_n(x) e^{jn\theta}, \quad (\text{C.1})$$

substituting $\theta = \theta - \frac{\pi}{2}$, provides the alternate form as

$$e^{jx \sin \theta} = \sum_{n=-\infty}^{\infty} J_n(x) e^{jn\theta}, \quad (\text{C.2})$$

, where $J_n(x)$ is a Bessel function of order, n . If we apply the Bessel function identity that states

$$J_{-n}(x) = (-1)^n J_n(x) \quad (\text{C.3})$$

to the equation in (C.1), we can see that the terms in the sum that are symmetric about zero can be summed in order to reduce the bounds from $[-\infty, \infty]$, to $[1, \infty]$. Doing so for several values makes the pattern more clear:

$$\begin{aligned}
n = \pm 1 &\rightarrow jJ_1(x)e^{j\theta} + (-1)(-j)J_1(x)e^{-j\theta} = jJ_1(x) [e^{j\theta} + e^{-j\theta}] = 2jJ_1(x) \cos(\theta), \\
n = \pm 2 &\rightarrow (-1)J_2(x)e^{j2\theta} + (1)(1)J_2(x)e^{-j2\theta} = 2J_2(x) \cos(2\theta), \\
n = \pm 3 &\rightarrow -jJ_3(x)e^{j3\theta} + (-1)jJ_3(x)e^{-j3\theta} = 2(-j)J_3(x) \cos(3\theta),
\end{aligned} \tag{C.4}$$

and with $n = 0$, we have

$$n = 0 \rightarrow J_0(x), \tag{C.5}$$

which allows us to write the relation in (C.1) as

$$e^{jx \cos \theta} = J_0(x) + 2 \sum_{n=1}^{\infty} j^n J_n(x) \cos(n\theta). \tag{C.6}$$

Using the result in (C.6), we can arrive at identities for sinusoidal phase modulations.

We begin by using the Euler Identity on the left half of (C.6), such that:

$$e^{jx \cos(\theta)} = \cos(x \cos(\theta)) + j \sin(x \cos(\theta)) = J_0(x) + 2 \sum_{n=1}^{\infty} j^n J_n(x) \cos(n\theta) \tag{C.7}$$

From here, noticing that the real and imaginary parts of $e^{jx \cos(\theta)}$ can be calculated from the result above. Some manipulation provides the final form for some real-valued identities as:

$$\begin{aligned}
Re \{ e^{jx \cos(\theta)} \} &= \cos(x \cos(\theta)) = J_0(x) + 2 \sum_{n=1}^{\infty} (-1)^n J_{2n}(x) \cos(2n\theta) \\
Im \{ e^{jx \cos(\theta)} \} &= \sin(x \cos(\theta)) = -2 \sum_{n=1}^{\infty} (-1)^n J_{2n-1}(x) \cos([2n-1]\theta).
\end{aligned} \tag{C.8}$$

Appendix D

PERMISSIONS

In reference to IEEE copyrighted material which is used with permission in this thesis, the IEEE does not endorse any of the University of Delaware's products or services. Internal or personal use of this material is permitted. If interested in reprinting/republishing IEEE copyrighted material for advertising or promotional purposes or for creating new collective works for resale or redistribution, please go to http://www.ieee.org/publications_standards/publications/rights/rights_link.html to learn how to obtain a License from RightsLink.

If applicable, University Microfilms and/or ProQuest Library, or the Archives of Canada may supply single copies of the dissertation.